UNIVERSITY OF UDINE
hic sunt futura

www.uniud.it

PhD Programme in Industrial and Information Engineering

XXXVI Cycle

Supervised Machine Learning Approaches for Structural Integrity: Residual Stress Evaluation and Defect-based Fatigue Modelling

PhD Candidate
Alessandro Tognan

Supervisor
Professor Enrico Salvati

Year 2024

Abstract

Assessing the performance of structural materials is imperative to guarantee the integrity, service continuity, durability and load-bearing capacity of engineered parts. Amongst numerous failure mechanisms, fatigue is reportedly one of the most detrimental and catastrophic since it gradually and relentlessly damages structural components until they suddenly collapse. The fatigue performance evaluation is rendered convoluted by numerous concomitant impacting factors. In this respect, the scientific community has widely recognised the critical role of residual stress (RS) and manufacturing defects, which alter the local stress state induced by externally applied cyclic loads and lead to scattered fatigue response. Therefore, the key objective here is to route the development of a comprehensive fatigue design setting with the aim of including RS and defects in future engineering practice. Hereby, diverse supervised Machine Learning (ML) techniques are harnessed while prioritising probabilistic aspects to enhance the robustness of the proposed approaches. To incorporate RS, users must ascertain the trustworthiness of their evaluations. However, this stage is frequently hampered by deterministic and heavily user-dependent data regularisation protocols applied during the pre-processing of input data. To address this issue, Gaussian Process Regression is exploited as a stochastic regularisation technique. To showcase its potency, this technique is applied to the Contour Method, whose potential and cost-effectiveness are incredibly attractive. Although entrenched Continuum Solid Mechanics theories can capture the influence of defects on fatigue, they often restrict the number of explanatory defect descriptors, usually to a characteristic length. Moreover, the related models hinder an exhaustive quantification of the involved uncertainties. Therefore, traditional fatigue models are revisited and opportunely treated through the lens of ML. Specifically, defect-based approaches to estimating the finite fatigue life and fatigue endurance of metallic materials are conceived and appropriately addressed through diverse variants of Neural Networks, and Logistic Regression. The present work, therefore, provides the research & engineering community with systematic ML-supported predictive tools, thus constituting a step towards an integrated framework for probabilistic design against fatigue.

Selected Journal Papers

The present dissertation thesis is based on the following published papers.

1. **A. Tognan**, A. Patanè, L. Laurenti, E. Salvati. A Bayesian Defect-based Physics-guided Neural Network Model for Probabilistic Fatigue Endurance Limit Evaluation. In: *Computer Methods in Applied Mechanics and Engineering*. (2024). doi: 10.1016/j.cma.2023.116521.

2. **A. Tognan**, E. Salvati. Probabilistic defect-based modelling of fatigue strength for incomplete datasets assisted by literature data. In: *International Journal of Fatigue* (2023). doi: 10.1016/j.ijfatigue.2023.107665.

3. E. Salvati, **A. Tognan**, L. Laurenti, M. Pelegatti, F. De Bona. A defect-based physics-informed machine learning framework for fatigue finite life prediction in additive manufacturing. In: *Materials & Design* (2022). doi: 10.1016/j.matdes.2022.111089.

4. **A. Tognan**, L. Laurenti, E. Salvati. Contour Method with Uncertainty Quantification: A Robust and Optimised Framework via Gaussian Process Regression. *Experimental Mechanics* (2022). doi: 10.1007/s11340-022-00842-w.

5. **A. Tognan**, L. Sandnes, G. Totis, M. Sortino, F. Berto, Ø. Grong, and E. Salvati. Evaluation and Origin of Residual Stress in Hybrid Metal and Extrusion Bonding and Comparison with Friction Stir Welding. *International Journal of Mechanical Sciences* (2022). doi: 10.1016/j.ijmecsci.2022.107089.

Contents

List of Figures

List of Tables

List of Abbreviations

AM	Additive Manufacturing
ADVS	Advancing Side
BI	Bayesian Inference
BM	Base Material
B-PGNN	Bayesian Physics-guided Neural Networks
B-PINN	Bayesian Physics-informed Neural Networks
CM	Contour Method
CMM	Coordinate Measuring Machine
CT	Computed Tomography
EH	El Haddad
ELBO	Evidence Lower BOund
FE	Finite Element
FIP	Fatigue Indicator Parameter
FM	Fracture Mechanics
FIM	Filler Material
FSW	Friction Stir Welding
GP	Gaussian Process
GPR	Gaussian Process Regression
HMC	Hamiltonian Monte Carlo
HYB	Hybrid Metal and Extrusion Bonding
KRR	Kernel Ridge Regression
KT	Kitagawa-Takahashi
LPBF	Laser Powder Bed Fusion
LEFM	Linear Elastic Fracture Mechanics
LR	Logistic Regression
MAP	Maximum a Posteriori
ML	Machine Learning

MLE	Maximum Likelihood Estimation
NN	Neural Network
PDE	Partial Differential Equation
PINN	Physics-informed Neural Network
PPgNN	Probabilistic Physics-guided Neural Networks
RF	Random Forest
RS	Residual Stress
ReLU	Rectified Linear Unit
RETS	Retreating Side
SLM	Selective Laser Melted
SVD	Singular Value Decomposition
SVM	Support Vector Machines
VI	Variational Inference
WEDM	Wire Electrical Discharge Machine
XRD	X-ray Diffraction

1. Introduction

Modern engineering applications have increasingly demanded lightweight, cost-effective, sustainable mechanical products while meeting strict performance standards. Needless to say, this process can become an endeavour as designers are committed, at the same time, to ensuring structural functionality together with integrity, which ranges from adequate load-bearing capacity to reliability even in case of unpredicted off-design conditions. Nonetheless, confidently certifying these qualities is of capital importance to supply sound and durable mechanical products, thus preventing unforeseen failures and eventually undesired disruptions [1].

Amongst the well-established failure mechanisms, fatigue is reportedly responsible for approximately 80% of all structural collapses [2], often leading to catastrophic accidents [3]. Fatigue refers to the premature damaging of materials due to the action of cycling mechanical load. Generally, the fatigue failure phenomenon consists of three principal stages. The first one involves crack nucleation, primarily from the free-surface of mechanical parts, due to the progressive damage accrual. The applied cyclic load makes the crack propagate throughout the whole second stage. The third stage commences when the crack reaches a critical length beyond which unstable crack propagation occurs [4].

It is well-established how fatigue crack nucleation and incubation range most of the in-service lifespan of the exerted mechanical components. Furthermore, these early stages of fatigue life are significantly influenced by the material's microstructure [5, 6]. Relatively recently, the so-called Fatigue Indicator Parameters (FIPs) have been introduced to quantify the driving force for crack formation at the grain scale. A non-exhaustive list of input features typically incorporated into the FIP is stress, strain, microstructure, loading mode(s), and failure mechanism(s). The FIP aims to model the impact of these features on the failure probability of components subjected to cyclic loads. Additionally, FIPs offer a practical measure whereby microstructures can be compared in terms of their tendency to form and propagate

microstructurally short fatigue cracks [7, 8]. Intriguingly, it has been demonstrated that FIPs can ultimately be correlated with experimental fatigue life upon an appropriate calibration [9].

Although the scientific and engineering community has largely investigated the nuances of fatigue throughout the last two centuries, a complete comprehension of the related failure mechanism is yet to be reached. This is, in a word, paradoxical [10]. Alongside microstructural features, researchers have identified several factors that influence fatigue performance [2, 11], amongst which the present thesis deliberately investigates residual stress (RS) and manufacturing defects exploiting supervised Machine Learning (ML) computational techniques.

Throughout the thesis, much emphasis is devoted to probabilistic aspects, as it is believed that a superior level of reliability of structures can be attained by quantifying the uncertainties as well as the errors involved in the characterisation of RS and fatigue behaviour. In fact, deterministic protocols guarantee a certain safety margin covering uncontrolled load conditions or material inhomogeneities, by introducing the renowned "safety factor" in the design process, thus eventually resulting in bulky and expensive components. Unlike deterministic protocols, a thorough quantification of the uncertainties in the characterisation process shall enable the probabilistic assessment of structural integrity, thus matching the requirements of modern engineering while enabling the optimal exploitation of primary resources, environment, and energy consumption [12, 13].

The forthcoming sections are thus dedicated to introducing essential background knowledge crucial for the remainder of the dissertation. The introduction initially focusses on RS and their influence on fatigue. Additionally, an overview of manufacturing defects and their impact on fatigue is provided. Following this, a dedicated section widely reviews the current state-of-the-art of ML with reference to its application to RS evaluation and fatigue modelling. The chapter concludes with outlining the structure and objectives of the dissertation.

1.1. Residual Stress

RS is "locked-in" stress affecting materials and structures irrespective of any externally applied load. Specifically, RS is *self-equilibrating* stress, that is, regions of tensile and compressive stress coexist as to balance each other, thus nullifying force

and moment resultants. RS ensues from any manufacturing process as an elastic response to incompatible local strains. The material, however, is meant to ensure continuity, thus originating RS [14]. This peculiar phenomenon is primarily triggered by non-uniform plastic deformations, surface modifications and treatments, and severe thermal gradients [15]. Notably, the latter particularly regards welding and additive manufacturing (AM). Besides fabrication, RS may develop throughout the whole in-service life of structural components as well [16].

RS is conventionally classified into three classes according to the length scale over which it equilibrates. Type I refer to RS acting on the macro-scale, Type II pertains to intergranular RS (meso-scale), and Type III concerns RS at intragranular level (micron-scale) [17, 18]. Due to its latent, multi-scale, and tensorial nature, evaluating RS is often rather challenging, particularly for bulky materials. Consequently, RS is often neglected during the design process of structural components, although deemed to cause catastrophic in-service disruptions [14, 16]. RS has severe consequences for structural integrity depending upon its sign, location, and magnitude. The main effect of RS is to alter the local state of stress induced by applied external loads when components are exerted. This scenario is rendered even more convoluted as RS impacts structural integrity according to its length scale. Whilst Type I RS is responsible for the distortion of mechanical components, Type II and III RS generally condition the fatigue performance [19]. Tensile is thought to be detrimental in most of the instances, specifically when the applied loads already induce a tensile stress state. Whilst compressive RS is generally considered beneficial [20]. In regards to fatigue, tensile RS promotes the initiation of cracks and accelerates their propagation, notably in the neighbouring region of the free-surface of components. Hence, the load-bearing capacity is considerably reduced, and premature failures may occur [21]. By contrast, compressive RS can induce crack-closure and stress shielding phenomena [22, 23].

In order to mitigate RS, particularly when it is predominantly tensile in nature, a stress-relief annealing treatment is commonly applied [24, 25]. This post-fabrication operation typically entails subjecting a mechanical part or assembly to a controlled thermal cycle. The workpiece is gradually heated until it reaches the intended target temperature, which is then maintained for a calibrated time span. The workpiece is eventually cooled down to room temperature, and the process ends. It is worth remarking that during the heating stage the temperature of the workpiece must not

exceed the material's recrystallization temperature, as the treatment would alter the microstructure and condition mechanical properties. Additionally, non-thermal techniques are also available, as widely reviewed in [21]. As quickly mentioned earlier, the fatigue response can benefit from the introduction of compressive RS. For this reason, surface compressive RS is deliberately introduced using, for instance, shock/shot peening [26–30]. Similarly, other methods exists to produce compressive RS to balance tensile RS in those part's region where it is expected to develop, such as cold-hole expansion [31].

A graphical tool to intuitively capture the influence of RS on the fatigue behaviour is the Haigh diagram [1, 32, 33], see Figure 1.1. This diagram allows for visualising the fatigue endurance limit (also known as fatigue limit) as a function of the amplitude σ_a (the ordinate) and the mean stress σ_m (the abscissa) of the applied cycle stress. For the sake of the explanation, let us assume that Haigh's diagram involves a given material characterised through a uniaxial tensile fatigue test, whereas the fatigue limit is referred to the prescribed number of cycles to failure N_w^*. Theoretically, the fatigue endurance limit, i.e. the black solid line, would extend from the alternating fatigue limit σ_{af}^* (occurring at $\sigma_m = 0$) to the ultimate tensile strength σ_u (occurring at $\sigma_a = 0$, i.e. static failure). However, since the applied stress must not exceed the material's yield stress, the solid black line must interrupt at the intersection with the yield line and eventually run along it until σ_y, i.e. the yield stress. This eventually gives a piece-wise linear curve representing the fatigue limit, which encloses the locus of bearable stress combination that the material can withstand up to N_w^* cycles to failure, i.e. the admissible region. In this respect, let us consider a given allowable stress combination in terms of mean stress σ_m^* and stress amplitude σ_a^* in the absence of RS. The representative state of the load is, therefore, (σ_m^*, σ_a^*). Leaving σ_a^* unaltered, if compressive RS $\sigma_{\mathrm{RS}}^- < 0$ were present, the mean stress would be shifted toward $\sigma_m^* + \sigma_{\mathrm{RS}}^-$. Nonetheless, the representative point $(\sigma_m^* + \sigma_{\mathrm{RS}}^-, \sigma_a^*)$ would still be admissible, and the material's fatigue life is expected to be at least N_w^*. By contrast, if the tensile RS stress $\sigma_{\mathrm{RS}}^+ > 0$ affected the material, the representative load state would turn out to be $(\sigma_m^* + \sigma_{\mathrm{RS}}^+, \sigma_a^*)$, thus being no longer admissible. Hence, the material is anticipated to fail prior to N_w^*.

The length scale over which the RS would be resolved typically suggests the most suitable method for probing RS. There exists a number of experimental techniques to probe RS, which, in turn, can be categorised into three broad categories: non-

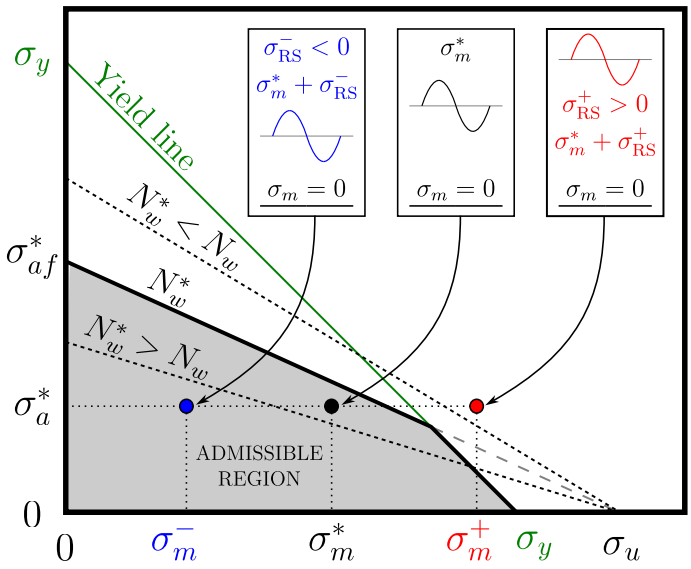

Figure 1.1. Haigh's diagram. Herein, the fatigue endurance limit (the black solid line) is referred to the number of cycles to failure N^*_w. The ordinate and the abscissa denote the applied stress amplitude σ_a and mean stress σ_m, respectively. Furthermore, σ_{af} is the alternating fatigue limit. Whilst σ_y and σ_u denotes are the yield and ultimate tensile strength, respectively. Alongside, the yield line is depicted in green. Additionally, σ^*_m and σ^*_a describe the cyclic loading condition. Finally, σ^+_{RS} and σ^-_{RS} represent tensile and compressive RS.

destructive, semi-destructive and destructive [18, 34, 35]. Non-destructive methods allow for the evaluation of RS by quantifying small changes of physical quantities or structural parameters at atomic or molecular length scales, hence Type III. Laboratory neutron X-ray diffraction (XRD) [36], synchrotron diffraction [19], and spectroscopy-based [37], is a non-exhaustive list of non-destructives methods. Alongside, semi-destructive techniques are also available for evaluating Type I, II, and III RS, such as hole-drilling [38], ring-core milling [39] and FIB-DIC [40]. This family of techniques relies on the stress relaxation phenomenon occurring when a new free surface is created within the material containing residual stress. To fully exploit this effect, either the evolution of displacement (or strain) during the cutting process is evaluated and used as an input to numerical models for the back-calculation of RS present before the creation of the new free-surface. In particular, stress-free surfaces are created by specimen sectioning or by progressive material removal. The last class

of RS evaluation methods is known as destructive. These methods are based upon the same working principle of the semi-destructive methods, i.e. stress relaxation, although in this case its application completely compromises the structural integrity of the examined material or mechanical part. Destructive methods generally permit resolving RS at millimetre scale (Type I). The Contour Method (CM), for instance, belongs to this class [41]. Upon selecting the suitable evaluation method, much attention ought to be devoted to appropriately defining the so-called interrogation (or sampling) volume, mainly when dealing with inter- and intra-granular RS [16]. The larger the volume, the more grains are sampled, so RS is smeared over a wider region, thus making the measurement less sensitive to noisy fluctuations occurring at finer scales [34]. Nevertheless, larger sampling volumes reduce the spatial resolution of the measurement. In extreme instances, no RS would be retrieved for excessively larger volumes with a characteristic size longer than the desired length scale [18, 42]. This suggests the existence of an optimal size for the interrogation volume across scales, but its determination is still an open issue. Another issue worth mentioning regards data regularisation, which affects the RS evaluation techniques, particularly those involving the back-calculation of RS (e.g., Contour Method, hole-drilling, and FIB-DIC). Essentially, regularisation involves a thorough smoothing of the experimentally measured input data (displacement/strain) to remove unintended oscillation and artefacts, thus obtaining meaningful RS distributions and making the assessments robust to noise. Although well-accepted regularisation methods exist [43], exploiting more advanced data-driven paradigms may represent a viable strategy to address this issue even in a probabilistic fashion. Additionally, data-driven methods would allow for including other pertinent features that may play a significant role in influencing RS, e.g. manufacturing parameters, that traditional computational protocols would neglect.

1.2. Manufacturing Defects

"Defects" represents a broad term to identify diverse forms of impurities, irregularities, inhomogeneities that originate from any manufacturing process, ranging from consolidated ones, e.g. casting, welding and sintering, to those more innovative, e.g. AM [2, 44–46]. Defects of different natures may primarily arise from uncontrolled manufacturing conditions and intricate thermal histories. For instance,

the entrapment of gas droplets during casting, welding, and AM can generate gas porosity [2]. Lack-of-fusion areas are distinctive defects of AM due to the incomplete melting of the feed material [46]. Welding and laser-based AM method shares a common type of defects, i.e. keyholes, which are essentially cavities [45, 47, 48]. On top of that, the presence of defects seems to be unavoidable in most of the cases, although post-fabrication treatments can attenuate their presence [30, 49, 50].

It is well-established that defects have a modest effect on material's static mechanical properties while they hugely impact fatigue response [2, 46]. From an experimental standpoint, defects have been identified as the foremost cause of scattered fatigue data in AM as well as traditional manufacturing processes [2, 11, 51]. Figure 1.2 schematically portrays a typical dataset conformation encountered in fatigue characterisation. In particular, the left and right panels show a fictitious experimental fatigue dataset, i.e. applied cyclic load $\Delta\sigma$ vs number of cycles to failure N, of a hypothetically defect-free and a defect-laden material, respectively. With particular regard to AM, for instance, despite judiciously selecting the process parameters to control defectivity, the experimental evidence demonstrates considerably irregular fatigue response of the produced materials [52, 53].

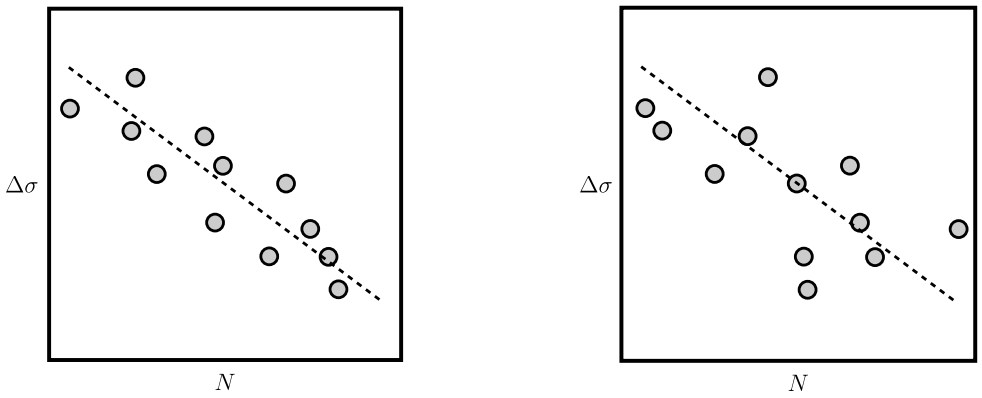

Figure 1.2. Scatter in fatigue data (plots in log-log scale). (a) In the hypothetical absence of defects. (b) In the presence of defects. Circle markers represent the acquired fatigue data in both panels.

Regardless of their origin, the reason for this unpredictable fatigue behaviour stems from defects inducing undesired stress/strain intensification inside the fabricated material. Therefore, defects may trigger fatigue crack initiation and prop-

agation, thus leading to unforeseen collapses [29, 54, 55]. The severity of this intensification strictly depends upon the defect's geometry, morphology, and location. For instance, lack-of-fusion defects generally possess flattened irregularly shaped and large extension which induces more intense stress concentration than gas pores, typically sphere-like [56]. Fatigue is also highly sensitive to the location of the defects besides their geometry and morphology. In fact, defects in the vicinity of the part's free-surface are more likely to trigger fatigue failure [57]. Thus, a precise characterisation of defect is of paramount importance to comprehend their impact on fatigue. Over the last years, the extensive combination of X-ray computed tomography (CT) and fractographic investigations permitted the precise characterisation of defects in numerous manufacturing contexts [58]. More recently, AM has fostered the post-processing of the information retrieved from CT scans and fractographies to compute relevant defect descriptors with the aim of attaining superior fatigue characterisation and predictions [59]. Nonetheless, the current state-of-the-art fatigue and Fracture Mechanics (FM) models impede their full exploitation.

Semi-empirical models, e.g. S-N curves or Basquin's, have represented the golden standard for fatigue characterisation since the dawn of this discipline. Indeed, these models have demonstrated excellent versatility when applied to engineering design against fatigue failure [60, 61]. However, S-N data often incorporates scatter due to crucial microstructural features impacting fatigue – defects above all. Although the resulting model can still be employed in the context of both traditional and AM materials, one can take into account such features and compensate for the scatter prior to fitting the models, thus making the resulting model more robust and reliable. To do so, it is possible to invoke FM, which already brought substantial progress while enabling practitioners to garner an insightful understanding of fatigue failure. [2]. As long as defects can be modelled as cracks, there exist many models, yet semi-empirical that can correlate material defectivity to the fatigue. Upon associating defects with a representative crack length, the fatigue behaviour can be modelled via Paris' law [4], whereas the fatigue endurance limit can be estimated by the El Haddad (EH) curve [62], which is commonly visualised on the well-established Kitagawa-Takahashi (KT) diagram [63]. Intriguingly, Sheridan has lately demonstrated how FM concepts can be exploited to curb the scatter of fatigue data, thus obtaining more reliable fatigue predictions [64, 65]. Therein, the Stress Intensity Factor (SIF) ΔK range was adopted to replace $\Delta\sigma$ resulting in reduced scatter.

This is schematically shown in Figure 1.3 with reference to the synthetic dataset illustrated in Figure 1.2. However, it is important to state that this approach should be verified for different classes of metals as it intrinsically assumes that the initial ΔK does not change over time, which is a potentially impactful assumption. This approach proved its effectiveness in the context of AM materials [66, 67]. Despite this, FM models restricts the number of defects descriptors that can be accounted for to the aforementioned characteristic length. Since semi-empirical models appear, once again, limiting, more sophisticated predictive model ought to be conceived to tackle this caveat.

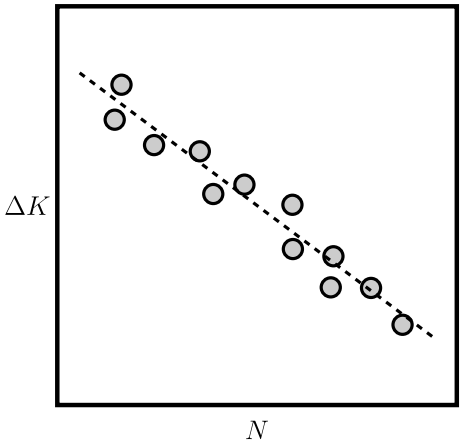

Figure 1.3. Sheridan's $\Delta K - N$ representation (in log-log scale) of the synthetic fatigue dataset given in Figure 1.2.

1.3. State-of-the-art of Machine Learning Applications to Relevant Structural Integrity Problems

When dealing with RS evaluation and fatigue characterisation, practitioners funnel their effort through collating experimental observations to acquire adequate knowledge of the examined phenomenon. Regarding RS, the data is processed complying within standard computational procedures depending upon the selected evaluation method. As concerns fatigue, the data is generally used to fit a semi-

empirical model. In both cases, therefore, the data harvesting usually culminates in a so-called *surrogate model* that describes – under certain hypotheses – the investigated phenomenon. In practice, the construction of these models reduces to determining some unknown parameters upon the acquired data, which are eventually linked to the desired output, e.g. RS or fatigue. Once the parameters are identified, the user is conferred with the ability to forecast the model elsewhere.

Users often wish to augment such consolidated models with additional relevant input features, e.g. manufacturing parameters or diverse defect's traits. Although this approach might deviate from traditional ones, it allows for gaining further insight into RS and fatigue. The augmentation can certainly be conducted within the old-fashioned setting of regression analysis. Still, the synergic fusion of Computer Science and Statistics has been offering more efficient ways to do so, i.e. ML [68]. Over the two decades, ML has experienced a sudden outbreak, thanks to the increasing deployment of computational resources [69]. At present, ML has reached a mature condition so that it can be exploited to easily manage highly non-linear and complex tasks.

Essentially, ML algorithms attempt to recognise data patterns over the processed *training* dataset, e.g. the experimental data. Technically, this operation is called learning or training, and it aims to identify the unknown parameters of the surrogate model. The given data can either be "labelled" with real numbers or integers, depending upon the nature of the examined problem. In this case, the user provides the algorithms with examples of targets that are expected beforehand. For this reason, ML is said to be *supervised*. As opposed, when input data are not labelled, ML is *unsupervised*, in the sense that the algorithm autonomously discovers the data targets [70]. Once this stage is accomplished, the surrogate model is built, and one can predict unseen data. Supervised ML comprises two popular branches, i.e. regression and classification. The former addresses modelling and predicting continuous data, i.e. inputs are labelled with real numbers. Whilst the latter serves the same purpose, it handles problems where the input data is categorised by discrete labels, e.g. integers [71].

In numerous research fields involving data analytics, the need for flexible and interpretable models often calls for probabilistic modelling. For this reason, probabilistic ML has increasingly sparked interest compared to its deterministic counterpart, offering several advantages. One of the most striking features of probabilistic

approaches resides in naturally handling noisy data by incorporating measures of uncertainty, such as those of aleatoric nature. Besides this, epistemic uncertainty is also automatically taken into account. Importantly, unlike deterministic models, probabilistic ones provide distributions over possible outcomes rather than point-valued estimates, thus allowing users to rapidly assess the reliability of the predictions. Furthermore, probabilistic models can deal with data scarcity by returning higher uncertainty for data predicted in regions with a lower density of training data. On top of that, Bayesian approaches provide further benefits. For instance, practitioners can model their initial belief, usually referred to as prior knowledge, about the model's parameters, which is then updated through the training data. This distinctive characteristic makes Bayesian models scalable with the dimensionality of the dataset and tolerates sparse data [71, 72].

Regarding the exploitation of ML in the context of RS, the literature would seem to lack applications for data regularisation purposes. Instead, the research community primarily focussed on training ML surrogate models with the aim of optimising manufacturing process parameters to attenuate the unintended presence of RS [35]. For instance, Neural Networks (NNs) and genetic algorithm were utilised to establish correlations between RS – evaluated via X-ray diffraction – and different combinations of turning process parameters in regards to Inconel 718 [73, 74]. A similar methodology has been proposed in [75]. X-ray diffraction data were also used to instruct an NN to correlate the process parameters of a surface modification treatment as well as the chemical composition with the induced RS in regards to Ni-based alloys [76]. A more computational study has been presented in Ref. [77] with regard to AISI52100. Therein, turning-induced RS were simulated at different cutting conditions. The results were then coupled with an NN to connect RS with the process parameters and find the optimal cutting conditions that mitigate RS. Analogously, NN and Random Forest (RF) surrogate models were trained upon numerical simulations to predict RS in wire-arc AM samples. The models allowed to rank the influence of the process parameters on the resulting RS distribution as well [78]. Another prominent application concerns the prediction of surface RS in end milled specimens by Gaussian Process Regression (GPR) [79].

In the context of fatigue, supervised ML approaches have recently gained popularity to overcome the limitations of FM models. Specifically, a wealth of defect-based surrogate models have been conceived to attain a comprehensive defect-based as-

sessment of fatigue performance [80–82]. For instance, the finite fatigue life of Laser Powder Bed Fusion (LPBF) Ti-6Al-4V was assessed through a drop-out NN receiving defect characteristics and surface roughness details as inputs [83]. RF algorithm and Support Vector Machine (SVM) were used to devise defect-based models to predict the finite life of an LPBF AlSi10Mg and Selective Laser Melted (SLM) Ti-6Al-4V, respectively [84, 85]. SVM constituted a powerful defect-based predictive model to predict the finite fatigue life of LPBF 17-4 PH stainless steel as well [86]. Therein, a sensitivity analysis was also conducted, whereby the influence of the descriptors on the predicted fatigue life was quantified. Given the versatility of ML approaches, a few researchers considered several AM process parameters along with defect descriptors as the inputs of an NN. The NN was then used to forecast the fatigue life of LPBF AlSi10Mg, SLM AlSi10Mg, and SLM Ti-6Al-4V [87–89]. ML methods have been applied outside the field of AM as well. In this respect, the fatigue life of 13Cr-5Ni stainless steel and a KSFA90 were predicted using NN, RF and SVM trained on defect data [90]. In addition, Kernel Ridge Regression (KRR), and GPR have been employed to surrogate defect-based model for finite fatigue life in regards to Ti-based alloys [91, 92]. SVM and KRR were also utilised to investigate the fatigue performance of a set of Inconel 718 specimens according to their defectivity [93].

1.4. Objectives and Structure of the Dissertation

This dissertation pursues the ambitious objective of gaping crucial deficits in fatigue modelling, amongst which I decidedly concentrated on those related to defects and RS. With particular regard to defects, the focus here is on the defect-based ML prediction of the finite fatigue life and estimation of the fatigue endurance limit of metallic alloys. As concerns RS, the attention is drawn to the CM, where ML is applied to enhance the robustness of the RS evaluations.

To address the objectives that this dissertation sets, Chapter 2 elucidates the necessary experimental and theoretical background. The CM evaluation procedure is illustrated with particular emphasis on both the practical implementation and input data processing. Following, current fatigue models based on Linear Elastic FM (LEFM) are presented. Subsequently, Bayesian Inference (BI) is introduced as the ground for the ML methods exploited throughout the dissertation. In this respect,

ML methods focus on GPR, Logistic Regression (LR), NNs, Physics-Informed NNs (PINNs), Bayesian NNs (BNNs), Bayesian PINNs (B-PINNs).

Chapter 3 introduces an outstanding limitation in the CM evaluation technique regarding the pre-processing of the input displacement data. This is shown with reference to a solid-state butt weld considered as a case study. Traditionally, the input data undergoes spline-fit prior to the back-calculation of the RS. However, this fitting necessitates the *arbitrary* selection of a few fitting parameters. Albeit guidelines have been proposed to this end, there is no general consensus about this selection, which, in turn, remains left to the user's experience and confidence.

Chapter 4 is devoted to tackling the limitation of the CM just outlined. This is motivated by the necessity of both assessing the goodness of the RS assessments and neatly integrating the appealing potential of CM evaluations within a unified probabilistic fatigue design framework. Specifically, the traditional spline-fit is replaced with GPR, which automatically determines the optimal fitting parameters and provides the user with a built-in quantification framework.

Chapter 5 addresses a central issue affecting the mere data-driven ML approaches reviewed at the end of Section 1.3. ML currently seems to be the sole option to enable the full exploitation of defect descriptors typically retrieved from CT and fractography that the traditional FM approach would neglect. Nonetheless, it might happen that ML algorithms capture data patterns that do not obey the physics of the observed phenomenon when insufficient training data is supplied. Therefore, Chapter 5 tackles this limitation by utilising the recent PINN paradigm, where the learning stage on the training data is seamlessly informed by the physical laws governing the underlying phenomenon. In this context, a defect-based PINN is developed to predict the fatigue life of metallic alloys, whereby consolidated concepts of FM are cast into a Basquin-like law to constrain the training of the PINN.

Chapter 6 is dedicated to the development of an ML tool for estimating the fatigue endurance limit of defective metallic alloys in a probabilistic manner. As quickly mentioned earlier, under appropriate hypotheses of FM, the EH curve can be invoked to describe the fatigue endurance limit. Nevertheless, such a curve requires the knowledge of two distinctive parameters, whose identification is often made challenging by a number of factors. It is thus demonstrated how these parameters can indirectly be estimated given an adequate amount of fatigue tests at different defect sizes and load magnitudes. To do so, the phenomenological behaviour of the

EH curve is morphed into an ML classification problem through LR. Maximum a Posteriori estimation (MAP) is then leveraged to obtain the probabilistic appraisals of the parameters sought. Finally, an appropriate statistical post-processing was performed to retrieve the EH curve at different failure probabilities.

Chapter 7 complements the work on the MAP identification of the EH curve just outlined. Therein, the key objective is to devise a Bayesian Physics-guided NN (B-PGNN) model for predicting whether metallic specimens retaining defects collapses when subjected to cyclic loading. In this case, the EH curve is selected as the semi-empirical model that informs the training stage. As schematically shown in Figure 1.2, defects are well-known to generate scatter in fatigue data, which eventually incorporate aleatory and epistemic uncertainty. Thanks to the Bayesian treatment of the problem, these uncertainties are intrinsically accounted for. Hence, the B-PGNN holds the potential to predict the failure probability of defective metallic materials while forecasting the uncertainty over such prediction. It should be mentioned that B-PINNs have already been presented elsewhere [94]. Although B-PINNs shares many aspects with the conceived B-PGNN, their implementations slightly differ – this shall be clarified later, though.

Finally, Chapter 8 synthesises the conclusions of this dissertation while emphasising the advancement that this research brought about and the related prospective future extensions.

2. Experimental and Theoretical Background

In order to address the objectives that the present research pursues, it is essential to introduce sufficient background knowledge. Initially, both the theoretical aspects and practical implementation of the CM are illustrated. Subsequently, a detailed overview of fatigue and FM is given, showing how to incorporate defectivity into fatigue modelling. BI is then presented to guide the reader through the explanation of probabilistic ML methods, such as GPR and LR. The foundation of NNs and PINNs are shown. Finally, the notions of BI and PINNs are merged to introduce B-PINNs.

2.1. Contour Method Evaluation of Residual Stress

2.1.1. Theoretical Preliminaries

The essential background of Continuum Mechanics used in the current section is briefly condensed herein, which shall help understand the back-calculation of the RS using the CM.

Let us consider a three-dimensional domain $\Omega \in \mathbb{R}^3$, whose local state of stress is described through Cauchy's symmetric second-order tensor $\mathbf{T}$. According to a generic reference frame $S = \{O, x_1, x_2, x_3\}$, $\mathbf{T}$ can be represented by a 3×3 matrix as:

$$\mathbf{T} = \begin{bmatrix} \sigma_{11} & \tau_{12} & \tau_{13} \\ \tau_{12} & \sigma_{22} & \tau_{23} \\ \tau_{13} & \tau_{23} & \sigma_{33} \end{bmatrix} \tag{2.1}$$

Let Γ be a plane intersecting Ω, and assume $\mathbf{n} = \begin{bmatrix} n_1 & n_2 & n_3 \end{bmatrix}^\top$ as the outward

normal vector of Γ. One can retrieve the stress acting with respect to $\mathbf{n}$ as:

$$\mathbf{t} = \mathbf{T}\,\mathbf{n} = T_{ij}\,n_j \tag{2.2}$$

where the summation over j is implicit. The local state of strain of Ω can be represented by the second-order strain tensor $\mathbf{E}$ whose representation according to S is:

$$\mathbf{E} = \begin{bmatrix} \varepsilon_{11} & \gamma_{12} & \gamma_{13} \\ \gamma_{12} & \varepsilon_{22} & \gamma_{23} \\ \gamma_{13} & \gamma_{23} & \varepsilon_{33} \end{bmatrix} \tag{2.3}$$

The entries of $\mathbf{E}$ can be related to the displacement field $\mathbf{u} = \begin{bmatrix} u_1 & u_2 & u_3 \end{bmatrix}$ of Ω stemming from the application of external loads:

$$\mathbf{E} = \frac{\nabla\mathbf{u} + \nabla\mathbf{u}^\top}{2} \tag{2.4}$$

where $\nabla\mathbf{u}$ is the displacement gradient, namely $\nabla\mathbf{u} = \partial u_i/\partial x_j \,\forall\, i,j \in \{1,2,3\}$ Finally, $\mathbf{T}$ and $\mathbf{E}$ are linked with each other through a constitutive law, expressed by the fourth-order tensor $\mathbb{C}$, namely $\mathbf{E} = \mathbb{C}\mathbf{T}$. As it shall be clearer later, the constitutive law for linear elastic materials is considered:

$$\mathbf{E} = \frac{1-\nu}{E}\,\mathbf{T} - \frac{\nu}{E}\,\mathrm{tr}(\mathbf{T})\,\mathbf{1} \tag{2.5}$$

where ν is Poisson's ratio, E is Young's modulus, $\mathrm{tr}(\square)$ computes the trace of a tensor, and $\mathbf{1}$ is the identity tensor.

2.1.2. General Framework

Amongst the family of destructive techniques, an effective and elegant method to obtain full-field RS maps was developed about twenty years ago at the Los Alamos National Laboratories, namely the CM. The present section summarises the stages of the application of the CM, in agreement with [41].

Consider a sample Ω arranged according to the reference frame $S = \{O, x, y, z\}$, as shown in Figure 2.1(a). Let us assume that inhomogeneous RS is distributed over the internal surface Γ predominantly aligned with respect to the z-direction. If $\mathbf{e}_z = \begin{bmatrix} 0 & 0 & 1 \end{bmatrix}^\top$ is the outward normal vector of Γ, then such RS turns out to be

$\sigma_{zz}(x,y) = \mathbf{T}\,\mathbf{e}_z \,\forall\, x,y \in \Gamma$ (Eq. (2.2)).

Initially, the sample undergoes a precise cut along Γ, thus giving two halves Ω^{P1} and Ω^{P2} having cut surface Γ^{P1} and Γ^{P2}, respectively. The RS normal to the cut surface is relieved, i.e. $\sigma_{zz}^{P1}(x,y) = \sigma_{zz}^{P2}(x,y) = 0$. Consequently, Γ^{P1} and Γ^{P2} experience an out-of-plane relaxation, see Figure 2.1(b). The respective relaxation is then experimentally measured in terms of displacement, thus acquiring the topography of Γ^{P1} and Γ^{P2}. These topographies are labelled as $u_z^{P1}(x_i,y_i)\,\forall\, x_i,y_i \in \Gamma^{P1}, i = 1,2,\dots \mathsf{D}_1$ and $u_z^{P2}(x_i,y_i)\,\forall\, x_i,y_i \in \Gamma^{P2}, i = 1,2,\dots \mathsf{D}_2$, where (x_i,y_i) is the point at which the surface was probed, and D_1 and D_2 are the total number of acquired points for Γ^{P1} and Γ^{P2}, respectively.

The topographies are subjected to a specific pre-processing, which entails aligning (Figure 2.1(c)) and averaging them over a common grid whose points are denoted by (x_g,y_g):

$$u_z(x_g,y_g) = \frac{u_z^{P1}(x_g,y_g) + u_z^{P2}(x_g,y_g)}{2} \tag{2.6}$$

The resulting topography, $u_z(x_g,y_g)$, is fitted, thus providing its surrogate version $\tilde{u}_z(x,y)$ which can be extrapolated at any desired point (x,y).

Figure 2.1(d) shows the Finite Element (FE) stage of the CM. Specifically, an FE model of half-specimen is designed. In this instance, the nodes (x_m,y_m) form the mesh grid over the modelled cut surface Γ. Since the RS is hypothesised to give rise to negligible plastic deformation, the material is modelled as linear elastic. Subsequently, the fitted topography (Eq. (2.6)) is changed in sign and applied as a displacement boundary condition over the modelled cut surface Γ. Computationally, $\tilde{u}_z(x_m,y_m)$ is prescribed for u_z at each mesh node (x_m,y_m) of Γ. Additional boundary conditions are applied to suppress rigid body motions while avoiding a structurally indeterminate model. In summary, the FE simulation aims to solve the following

Continuum Mechanics problem numerically:

$$\begin{cases} \operatorname{div} \mathbf{T} = \mathbf{0} & \text{in } \Omega \\ \mathbf{E} = \frac{1-\nu}{E}\,\mathbf{T} - \frac{\nu}{E}\operatorname{tr}(\mathbf{T})\,\mathbf{1} & \text{in } \overline{\Omega} \\ \mathbf{E} = \frac{\nabla\mathbf{u}+\nabla\mathbf{u}^{\top}}{2} & \text{in } \overline{\Omega} \\ \mathbf{T}\,\mathbf{n} = \mathbf{0} & \text{in } \partial\Omega \\ u_z = \tilde{u}_z & \text{over } \Gamma \\ u_y = 0 & \text{at } P \\ u_x = u_y = 0 & \text{at } Q \end{cases} \tag{2.7}$$

where $\partial\Omega$ and $\overline{\Omega} = \Omega \cup \partial\Omega$ are the boundary and closure of Ω, respectively. Once the simulation is accomplished the RS present prior to the cut is retrieved over Γ, namely $\sigma_{zz}(x, y)$, Figure 2.1(e).

2.1.3. Practical Implementation

The protocol of the CM has been progressively honed, thus reaching a well-established condition. Nevertheless, special care must be taken when setting both the experimental and numerical steps of its application. In this regard, guidelines have been laid out to help support users when performing the CM [95, 96].

As concerns the cut, Wire Electrical Discharge Machines (WEDM) are deemed to be the optimal facilities to carry out this essential stage. WEDM is a non-contact machining facility which uses an electrically charged moving wire to ablate the sample's material. Given their limited intrusiveness, WEDMs possess the natural tendency to avoid the introduction of additional RS, especially those due to plasticisation effects [97]. Therefore, the cutting process, in principle, does not interfere with the RS already present inside the examined specimen. Further attention ought to be drawn to the selection of the cutting parameters, encompassing the wire's material and diameter. Besides, the aforementioned guideline recommend a low wire speed to avoid excessive roughness over the cut surface. Importantly, the tension of the wire must be thoroughly adjusted. Insufficient tension might compromise the planarity of the cut surfaces, thus leading to unintended concave or convex surfaces or cutting artefacts at the entry and exit sites of the wire. Moreover, the

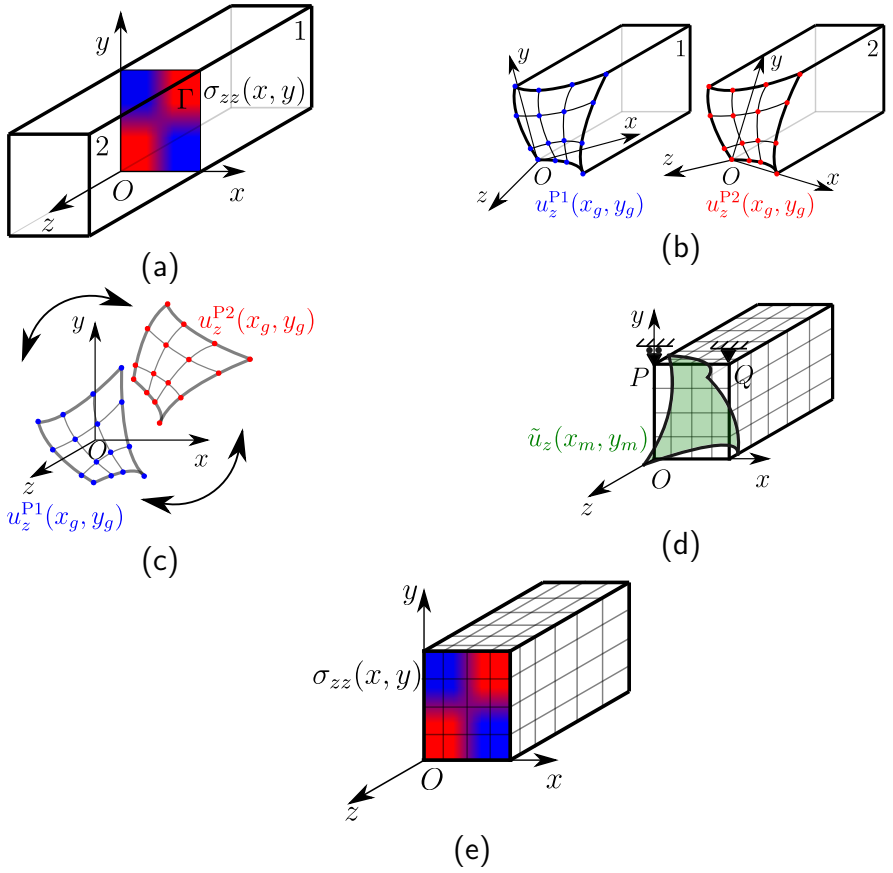

Figure 2.1. Stages of the CM. (a) Specimen preparation and cut. (b) Acquisition of the topographies. (c) Alignment of the topographies. (d) FE model of half-specimen. (e) FE back-calculation.

wire may experience uncontrolled vibrations, which, in turn, may cause wavy cut surfaces.

Despite several techniques available for experimentally acquiring the out-of-plane displacement of the cut surfaces, Coordinate Measuring Machines (CMMs) are broadly employed. Upon defining a raster scan pattern over the cut surfaces, CMMs exploit a contact probing system to measure the topographies. Such a grid must have an adequate nodal spacing to satisfactorily capture the gradient of the of the out-of-plane displacement.

The topographies are commonly smoothed via tensor-product surfaces, i.e. bi-

variate splines [98, 99]. Therefore, $u_z(x_g, y_g)$ (Eq. 2.6) is modelled as follows:

$$u_z(x_g, y_g) \simeq \tilde{u}_z(x, y) = \sum_{i=1}^{m} \sum_{j=1}^{n} C_{ij} \mathcal{P}_{i,r}(x) \mathcal{P}_{j,s}(y) \tag{2.8}$$

where $\mathcal{P}_{i,r}(x)$ and $\mathcal{P}_{j,s}(y)$ are the spline basis functions – polynomials, essentially – of degree r and s, respectively, C_{ij} constitutes the grid of the so-called control points of size $m \times n$. For the specific case of the CM, C_{ij} are identified upon the values of $u_z(x_i, y_i)$. The number of control points has to be carefully selected. Far too few points may over-smooth the topography as to remove the displacement gradients. Conversely, an excessive number of control points may lead to over-fitting, thus interpolating the noise typically included in the measurements. Therefore, the number of control points should be a good trade-off between preserving the peculiar traits of the topography and sufficiently filtering out the measurement noise.

2.1.4. Singular Value Decomposition for Aligning The Topographies

When experimentally measuring $u_z^{\mathrm{P1}}(x_i, y_i)$ and $u_z^{\mathrm{P2}}(x_i, y_i)$, the user is meant to specify a certain reference frame whereby the topographies are represented. However, such reference frame might be misaligned with respect to the preferential direction along which $u_z^h(x_i, y_i) \,\forall\, h = \mathrm{P1}, \mathrm{P2}$ are arranged. Singular Value Decomposition (SVD) can be leveraged to overcome this issue. In order to lighten the notation, the superscript h will be omitted in the following.

With reference to Figure 2.2, suppose that $u_z(x_i, y_i)$ is predominantly distributed according to the reference frame $S = \{O, x, y, z\}$. However, the user arbitrarily set $S' = \{O', x', y', z'\}$ for the acquisition which is not aligned with S. Lastly, assume $O \equiv O'$, without loss of generality.

Let D be the number of experimentally measured points of $u'_z(x'_i, y'_i)$ at (x'_i, y'_i) with respect to S', and let us gather the collected points into the following matrix:

$$\mathbf{W}' = \begin{bmatrix} x'_1 & y'_1 & u_z(x'_1, y'_1) \\ x'_2 & y'_2 & u_z(x'_2, y'_2) \\ \vdots & \vdots & \vdots \\ x'_{\mathsf{D}} & y'_{\mathsf{D}} & u'_z(x'_{\mathsf{D}}, y'_{\mathsf{D}}) \end{bmatrix} \in \mathbb{R}^{\mathsf{D} \times 3} \tag{2.9}$$

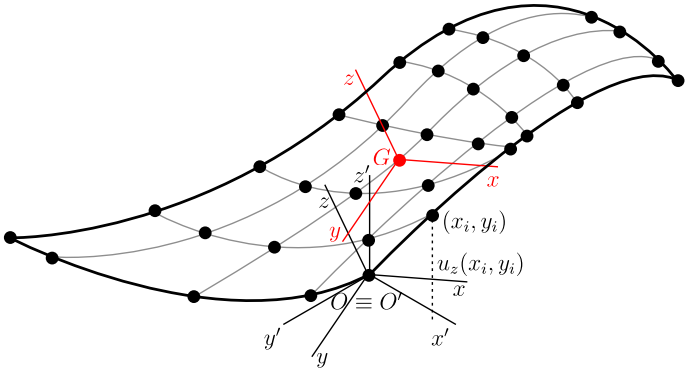

Figure 2.2. Schematic of a topography. Its preferential direction are represented by $S = \{O, x, y, z\}$, whilst $S' = \{O', x', y', z'\}$ is the user-defined reference frame for the acquisition of the points. Lastly, $S_G = \{G, x, y, z\}$ is the reference frame located at the centroid of the topography aligned with the preferential one.

Writing the i-th row of $\mathbf{W}'$ as $\mathbf{w}'_i = \begin{bmatrix} x'_i & y'_i & u'_z(x'_i, y'_i) \end{bmatrix}^\top$ allows Eq. (2.9) to be contracted in a block-partitioned fashion:

$$\mathbf{W}' = \begin{bmatrix} \mathbf{w}'_1 \mid \mathbf{w}'_2 \mid \cdots \mid \mathbf{w}'_{\mathsf{D}} \end{bmatrix}^\top \tag{2.10}$$

Considering the centroid G of $u'_z(x'_i, y'_i)$, let us define a new reference frame $S'_G = \{G, x'_G, y'_G, z'_G\}$ and translate $u'_z(x'_i, y'_i)$ to S_G. As a result, Eq. (2.10) transforms as:

$$\mathbf{W}^G = \begin{bmatrix} \mathbf{w}^G_1 \mid \mathbf{w}^G_2 \mid \cdots \mid \mathbf{w}^G_{\mathsf{D}} \end{bmatrix}^\top \tag{2.11}$$

The matrix $\mathbf{W}^G$ can directly be decomposed through SVD:

$$\mathbf{W}^G = \mathbf{Q}\mathbf{\Sigma}\mathbf{P} \tag{2.12}$$

where $\mathbf{P} \in \mathbb{R}^{\mathsf{D}\times\mathsf{D}}$ and $\mathbf{Q} \in \mathbb{R}^{3\times 3}$ are orthonormal matrices, and $\mathbf{\Sigma} \in \mathbb{R}^{\mathsf{D}\times 3}$ is the Singular Value matrix. The following change of basis is the carried out:

$$\mathbf{w}^{\text{SVD}}_i = \mathbf{P}\mathbf{w}^G_i \quad \forall\, i \in \{1, 2, \ldots, \mathsf{D}\} \tag{2.13}$$

This operation rotates $\mathbf{w}^G_i$ about the centroid G and automatically arranges the points according to their preferential directions. Therefore, a new reference frame

is automatically detected, i.e. $S_G = \{G, x, y, z\}$ (Figure 2.2). Finally, the points are translated back to O, thus giving $\mathbf{W} = \left[\mathbf{w}_1 \mid \mathbf{w}_2 \mid \cdots \mid \mathbf{w}_\mathsf{D}\right]^\top$, where $\mathbf{w}_i = \left[x_i \quad y_i \quad u_z(x_i, y_i)\right]^\top$ are expressed with respect to S. Besides minor manual adjustments, the resulting $\mathbf{W}$ might require a reflection if $\det \mathbf{P} = -1$.

2.2. Defect-based Fatigue Life Assessment

Fatigue is such a complex mechanical phenomenon whose systematical study was originally conducted by Wöhler circa 1850. His pioneering studies regarded the collection of experimental data to infer the fatigue life of railroad axles, i.e. what we currently call S-N data. Specifically, S-N data relates the applied stress range to the cycles to failure. However, a clear interpretation of S-N data was not readily available back then [11]. Only a few decades later, Basquin proposed a regression model to interpolate S-N data, thus providing a practical model for designing against fatigue failure. Upon collating sufficient experimental points, in terms of both applied cyclic stress $\Delta\sigma$ and the number of cycle to failure, N. Basquin's law formulates as [100]:

$$N = A\,\Delta\sigma^B \tag{2.14}$$

where A and B are the fitting parameters.

As experimentally observed, numerous metallic material possess an applied stress range $\Delta\sigma_w$, called fatigue (endurance) limit, below which the material is meant to (theoretically) withstand $N \to \infty$ cycles. In practice, however, this limit is usually referred to a prescribed number of cycles to failure N_w. Whether this fatigue endurance limit exists for every material is still a subject of debate [2]. When the fatigue endurance limit exists, Basquin's curve ought to be interrupted at $\Delta\sigma_w$ and extended horizontally, thus forming a "knee-point". A graphical overview of Basquin's curve along with its extension, is given in Figure 2.3 with reference to a synthetic fatigue dataset.

As already mentioned in Section 1.2, the curves shown in Figure 2.3 inherently incorporate scatter due to diverse microstructural sources, such as defects. A potential strategy to mitigate such a scatter before deploying the model is to reframe the fatigue assessment within FM, thus modelling defects as cracks and consequently making the predictions more robust. Specifically, assuming Linear Elastic FM (LEFM),

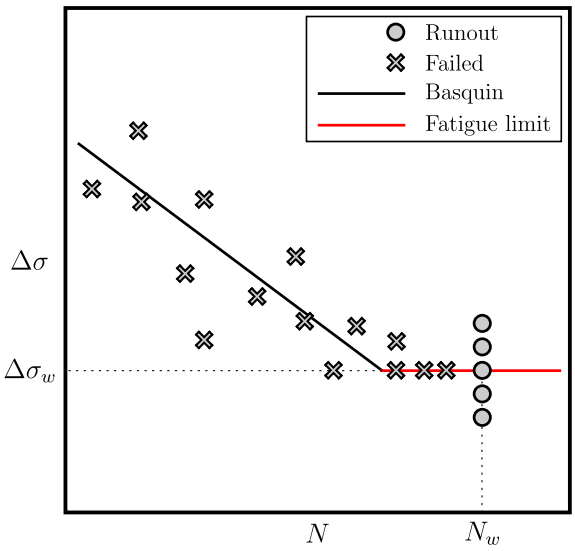

Figure 2.3. Schematic of the fatigue regimes commonly adopted for metallic materials exhibiting the knee-point (log-log scale).

i.e. when limited plasticity effects are involved, it is known that the severity of the stress field around the tip of a crack can quantified via SIF:

$$K = Y\sigma\sqrt{\pi\, a} \tag{2.15}$$

where Y is a dimensionless factor depending on the crack's geometry and load type, σ is the applied load, and a is the characteristic crack length [1]. Eq. (2.15) can easily be extended to handle cyclic loading:

$$\Delta K = Y\Delta\sigma\sqrt{\pi\, a} \tag{2.16}$$

where ΔK represent the SIF range corresponding to the applied stress range $\Delta\sigma$.

As discussed earlier, fatigued materials accumulate local damage leading to nucleation of cracks. Next, the crack experience a stable propagation up to a certain critical crack length. As experimentally shown by Paris [4], the long-cracks stage of fatigue life can be modelled through the following power law:

$$\frac{da}{dN} = C(\Delta K)^m \tag{2.17}$$

which links the fatigue crack driving force, i.e. ΔK, to the fatigue crack growth rate, i.e. da/dN. Additionally, C and m are the material's constants. The stage of the fatigue life when Eq. (2.17) holds is referred to as Paris' regime. Additionally, there exists a distinctive value of ΔK below which the fatigue cracks does not necessarily grow. This value is often called SIF range threshold, labelled as ΔK_{th}. Accordingly, one can compute an appraisal of the applied stress required to trigger fatigue crack growth, namely $\Delta\sigma_w$, by rearranging Eq. (2.16):

$$\Delta\sigma_w = \frac{\Delta K_{th}}{Y\sqrt{\pi\, a}} \tag{2.18}$$

Values such that $\Delta K < \Delta K_{th}$ denote the short-crack regime where LEFM cannot be applied, due to strong plasticity effects and the influence of the microstructure. At the opposite side of ΔK spectrum, for sufficiently high values of the SIF range, quasi-static failure occurs. Figure 2.4 shows a schematic of the regimes just described for a fictitious experimental dataset.

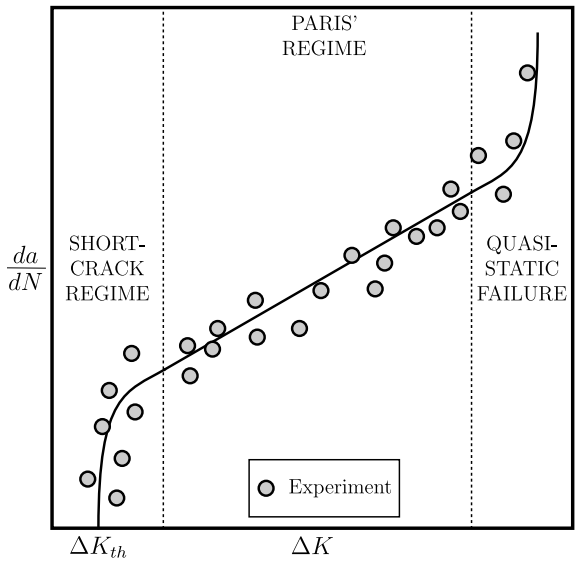

Figure 2.4. Schematic representation of the crack propagation regimes (log-log scale).

2.2.1. Finite Fatigue Life

As long as defects can be regarded as cracks, one can invoke LEFM to investigate their impact on fatigue. Thanks to Sheridan's clue [64, 65], the scatter of fatigue data is considerably reduced when replacing $\Delta\sigma$ with ΔK (Eq. (2.16)), thus obtaining a more truthful representation of the fatigue life. Hence, in order to ensure more robust predictions, Basquin's law is accordingly restated:

$$N = A\,\Delta K^{B} \tag{2.19}$$

where A and B differs from those in Eq. (2.14).

The fitting of Eq. (2.14) to the experimental data is currently regulated by the E739 ASTM standard [101]. Since Eq. (2.14) and Eq. (2.19) bear a close resemblance, the ASTM standard can be adapted to fit Eq. (2.19) as well and readily compute the confidence intervals for the resulting regression model. According to the ASTM standard, let us express Eq. (2.19) in logarithmic form, hence:

$$\log_{10} N = A + B\,\log_{10}\Delta K \tag{2.20}$$

where $A = \log_{10} A$ with abuse of notation. Upon collecting $(N_i, \Delta K_i)\,\forall\, i = 1, 2, \ldots, \mathsf{M}$ experimental data, the estimators of A and B are calculated via Ordinary Least Square method:

$$\begin{aligned}\hat{A} &= \overline{\log_{10} N} - \hat{B}\,\overline{\log_{10}\Delta K}\\ \hat{B} &= \frac{\sum_{i=1}^{\mathsf{M}}(\log_{10}\Delta K_i - \overline{\log_{10}\Delta K})(\log_{10}\Delta N_i - \overline{\log_{10} N})}{\sum_{i=1}^{\mathsf{M}}(\log_{10}\Delta K_i - \overline{\log_{10}\Delta K})^2}\end{aligned} \tag{2.21}$$

where:

$$\overline{\log_{10}\Delta K} = \frac{1}{\mathsf{M}}\sum_{i=1}^{\mathsf{M}}\log_{10}\Delta K_i \tag{2.22}$$

$$\overline{\log_{10} N} = \frac{1}{\mathsf{M}}\sum_{i=1}^{\mathsf{M}}\log_{10} N_i \tag{2.23}$$

Additionally, the unbiased estimator of the variance of the population turns out to

be:

$$s^2 = \frac{1}{\mathsf{M}-2}\sum_{i=1}^{\mathsf{M}}(\log_{10}\Delta N_i - \overline{\log_{10} N}) \tag{2.24}$$

Since the ASTM standard assumes $\hat{A}$ and $\hat{B}$ to be normally distributed, their confidence intervals can readily be obtained:

$$\begin{aligned}\hat{A} &\pm s\, t_{P,\alpha}\left(\frac{1}{\mathsf{M}} + \frac{\overline{\log_{10}\Delta K}^2}{\sum_{i=1}^{\mathsf{M}}(\log_{10}\Delta K_i - \overline{\log_{10}\Delta K})^2}\right)^{1/2}\\ \hat{B} &\pm s\, t_{P,\alpha}\left(\sum_{i=1}^{\mathsf{M}}(\log_{10}\Delta K_i - \overline{\log_{10}\Delta K})^2\right)^{-1/2}\end{aligned} \tag{2.25}$$

where $t_{P,\alpha}$ is the value of Student's t-distribution having $P = \mathsf{M} - 2$ degrees of freedom for α confidence level.

The regression model relies on the fundamental assumption that $\log_{10} N$ is normally distributed at every level of ΔK. This allows one to easily compute the confidence intervals of the regression model models:

$$\log_{10} N = \hat{A} + \hat{B}\log_{10}\Delta K \pm \sqrt{2F_{P_1,P_2,\alpha}}\, s\left(\frac{1}{\mathsf{M}} + \frac{(\log_{10}\Delta K - \overline{\log_{10}\Delta K}^2)}{\sum_{i=1}^{\mathsf{M}}(\log_{10}\Delta K_i - \overline{\log_{10}\Delta K})^2}\right)^{1/2} \tag{2.26}$$

where $F_{P_1,P_2,\alpha}$ is Fisher's distribution with $P_1 = \mathsf{M}$ and $P_2 = \mathsf{M} - 2$ degrees of freedom for α confidence level. Figure 2.5 shows an example of the results obtained from the application of the standard to fit a hypothetical fatigue dataset.

2.2.2. Fatigue Endurance Limit

When crack-like defect approximation holds, LEFM provides practitioners with two semi-empirical models to estimate and readily visualise the fatigue endurance limit of metallic alloys, namely the KT diagram and EH curve [63, 62].

Upon referring the fatigue endurance limit to a predefined number of cycles to failure N_w (typically $2 \cdot 10^6$ or 10^7) and assuming defects mainly subjected to Mode I cyclic load with limited plasticisation effects, the KT diagram allows one the ascertain whether cracks would propagate from pre-existing defects up to N_w. In the following, N_w will also be denoted as *runout threshold*. The KT diagram exploits the combination of two distinctive parameters, namely the SIF range threshold for

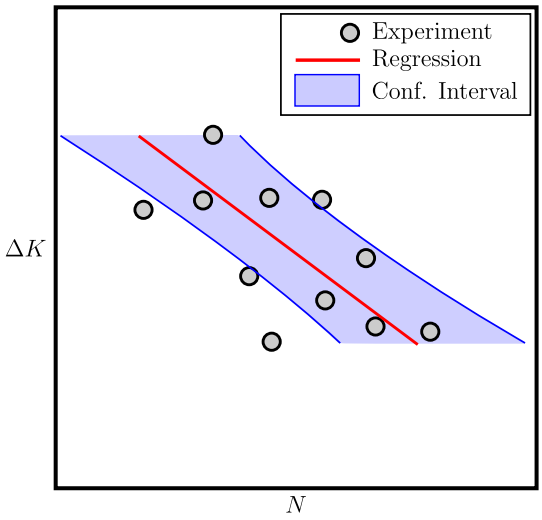

Figure 2.5. Overview of the regression model (log-log scale).

long cracks $\Delta K_{th,lc}$ and the fatigue endurance limit of the defect-free material $\Delta\sigma_w$ to outline outline the region of propagating and non-propagating crack. This typically results in a piece-wise linear curve; see Figure 2.6. From a practical perspective, if one collates experimental fatigue data and characterises the size a of the defect that triggered fatigue failure at different load conditions $\Delta\sigma$, the samples showing fatigue life $N \geq N_w$ and $N < N_w$ will predominantly be collocated beneath and above the curve associated with the KT diagram, respectively. This is shown, again, in Figure 2.6.

Later on, EH proposed its renowned curve as an alternative formulation for the fatigue limit aiming to provide a smooth transition over the entire range of a, se Figure 2.6. EH formulated a continuous curve described by:

$$\Delta\sigma = \sqrt{\frac{a_0}{a_0 + a}} \tag{2.27}$$

where a_0 is the so-called EH critical length:

$$a_0 = \frac{1}{\pi}\left(\frac{\Delta K_{th,lc}}{Y\Delta\sigma_w}\right)^2 \tag{2.28}$$

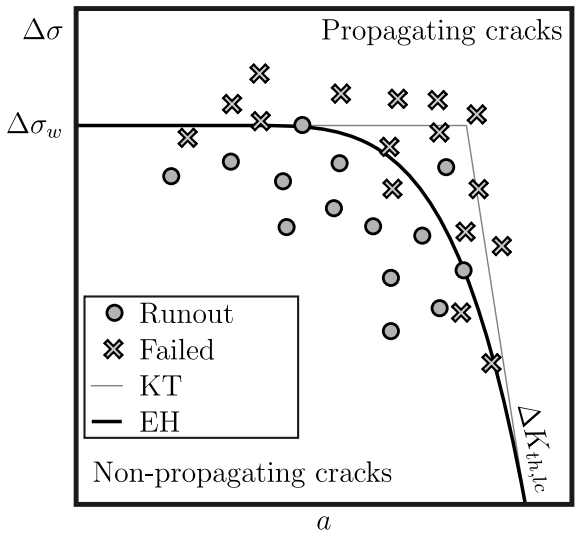

Figure 2.6. The El Haddad (EH) curve drawn on Kitagawa-Takahashi (KT) diagram in log-log scale. The figure reports a fictitious dataset for the sake of the illustration, and the piece-wise linear curve of the fatigue endurance limit having parameters $\Delta K_{th,lc}$ and $\Delta\sigma_w$, which is associated with the KT diagram.

Similarly to the aforementioned piece-wise curve depicted on the KT diagram, the EH curve outlines the fatigue endurance limit referred to a predefined runout threshold N_w. With particular regard to the present thesis, the EH curve can thought of as the optimal curve that separates the two considered classes, namely runout and failed. Thus, its phenomenological behaviour can be seen from ML classification standpoint; this shall be addressed afterwards.

2.3. Bayesian Inference

BI is a powerful technique enabling the construction of probabilistic predictive models [71]. Let $\mathcal{D} = \{(\mathbf{x}_i, y_i) | i = 1, 2, \ldots, \mathsf{N}\}$ the collected data whereby one wishes to fit the model:

$$y = \mathcal{G}_{\boldsymbol{\theta}}(\mathbf{x}) \tag{2.29}$$

which depends on some unknown parameters $\boldsymbol{\theta} \in \mathbb{R}^{\mathsf{P}}$. Whilst the input is assumed to be vectorial, i.e. $\mathbf{x}_i \in \mathbb{R}^N$, the output of the model is scalar to reflect the application of BI to the ML techniques throughout the next chapters.

BI commences with prescribing a *prior* (distribution) over $\boldsymbol{\theta}$, namely $\mathbb{P}[\boldsymbol{\theta}]$. Specifically, $\mathbb{P}[\boldsymbol{\theta}]$ is the prior knowledge of the user about the observed phenomenon. Therefore, tailoring $\mathbb{P}[\boldsymbol{\theta}]$ enables one to inject prior information about the parameters sought from a mechanistic model, for instance. The observed data $\mathcal{D}$ are used to construct the related *likelihood* (function) $\mathbb{P}[\mathcal{D}|\boldsymbol{\theta}]$, which represents the probability of generating the dataset $\mathcal{D}$ given a set of parameters $\boldsymbol{\theta}$. Typically, the likelihood is assumed as Gaussian for *regression problems*:

$$\mathbb{P}[\mathcal{D}|\boldsymbol{\theta}] = \prod_{i=1}^{\mathsf{N}} \frac{1}{\sqrt{(2\pi)}\sigma_n} \exp\left(-\frac{1}{2}\frac{(y_i - \mathcal{G}_{\boldsymbol{\theta}}(\mathbf{x}_i))^2}{\sigma_n^2} \right) \tag{2.30}$$

where σ_n is the variance of the random noise affecting the observations $y_i \in \mathbb{R}$, and $\mathcal{G}_{\boldsymbol{\theta}}(\mathbf{x}_i)$ is the predicted value. Whilst the Bernoulli likelihood is assumed for *binary classification problems*:

$$\mathbb{P}[\mathcal{D}|\boldsymbol{\theta}] = \prod_{i=1}^{\mathsf{N}} \mathcal{G}_{\boldsymbol{\theta}}(\mathbf{x}_i)^{y_i}(1 - \mathcal{G}_{\boldsymbol{\theta}}(\mathbf{x}_i))^{(1-y_i)} \tag{2.31}$$

where $y_i \in \{0, 1\}$ and $\mathcal{G}_{\boldsymbol{\theta}}(\mathbf{x}_i)$ are the ground-truth and predicted class, respectively. Once the likelihood is defined, $\mathbb{P}[\boldsymbol{\theta}]$ and $\mathbb{P}[\mathcal{D}|\boldsymbol{\theta}]$ are cast into Bayes' theorem:

$$\mathbb{P}[\boldsymbol{\theta}|\mathcal{D}] = \frac{\mathbb{P}[\mathcal{D}|\boldsymbol{\theta}]\,\mathbb{P}[\boldsymbol{\theta}]}{\mathbb{P}[\mathcal{D}]} \tag{2.32}$$

to compute the *posterior* (distribution) $\mathbb{P}[\boldsymbol{\theta}|\mathcal{D}]$. Additionally, $\mathbb{P}[\mathcal{D}]$ is called *evidence*, defined as:

$$\mathbb{P}[\mathcal{D}] = \int_{\boldsymbol{\theta}} \mathbb{P}[\mathcal{D}|\boldsymbol{\theta}]\,\mathbb{P}[\boldsymbol{\theta}] d\boldsymbol{\theta} \tag{2.33}$$

which represents the marginalisation of the likelihood with respect to $\boldsymbol{\theta}$. Bayes' theorem, therefore, updates the prior knowledge $\mathbb{P}[\boldsymbol{\theta}]$ to $\mathbb{P}[\boldsymbol{\theta}|\mathcal{D}]$ via after the observation of the dataset $\mathcal{D}$.

2.3.1. Parameter Estimation

Upon assembling the posterior as per Eq. (2.32), the expected value of $\hat{\boldsymbol{\theta}}$ is computed via Maximum a Posteriori Estimation (MAP):

$$\hat{\boldsymbol{\theta}} = \underset{\boldsymbol{\theta}}{\operatorname{argmax}}\ \mathbb{P}[\boldsymbol{\theta}|\mathcal{D}] \tag{2.34}$$

To facilitate numerical computations, the monotonicity of the logarithm is usually exploited, thus restating the last relationship as:

$$\hat{\boldsymbol{\theta}} = \underset{\boldsymbol{\theta}}{\operatorname{argmax}}\ \log \mathbb{P}[\boldsymbol{\theta}|\mathcal{D}] \tag{2.35}$$

which expands in agreement with Eq. (2.32):

$$\hat{\boldsymbol{\theta}} = \underset{\boldsymbol{\theta}}{\operatorname{argmax}}\ \log \mathbb{P}[\mathcal{D}|\boldsymbol{\theta}] + \log \mathbb{P}[\boldsymbol{\theta}] \tag{2.36}$$

where the evidence has been neglected since it is constant and so vanishes when maximising the log-posterior. As a special case, when a uniform distribution is prescribed over $\mathbb{P}[\boldsymbol{\theta}]$, the corresponding term in Eq. (2.36) vanishes as well:

$$\hat{\boldsymbol{\theta}} = \underset{\boldsymbol{\theta}}{\operatorname{argmax}}\ \log \mathbb{P}[\mathcal{D}|\boldsymbol{\theta}] \tag{2.37}$$

which is essentially Maximum Likelihood Estimation (MLE).

2.3.2. Full Computation of the Posterior

Although the estimation of the parameters can be accomplished by numerical optimisation strategies, the full computation of the posterior deserves further attention. In fact, the computation of the closed form $\mathbb{P}[\boldsymbol{\theta}|\mathcal{D}]$ is unfeasible in most of the cases. This section offers a concise overview of three methods frequently utilised to accomplish this task. Any of these techniques offers significant advantages over deterministic identification methods, such as Least Square, since they provide the full probability distribution $\mathbb{P}[\boldsymbol{\theta}|\mathcal{D}]$ of the parameters, instead of a point-valued appraisals.

Laplace Approximation. This method can be regarded as the simplest one. Although $\mathbb{P}[\boldsymbol{\theta}|\mathcal{D}]$ can assume any arbitrary distribution, this approximation involves a local Gaussian approximation of the posterior in the neighbourhood of $\hat{\boldsymbol{\theta}}$. Nevertheless, it ought to be mentioned that this method is primarily suitable for unimodal distribution [71, 102]. Practically, $\mathbb{P}[\boldsymbol{\theta}|\mathcal{D}]$ undergoes a local first-order Taylor's expansion about $\hat{\boldsymbol{\theta}}$:

$$\log \mathbb{P}[\boldsymbol{\theta}|\mathcal{D}] \approx \log \mathbb{P}[\hat{\boldsymbol{\theta}}|\mathcal{D}] + \underbrace{\nabla \log \mathbb{P}[\boldsymbol{\theta}|\mathcal{D}]\Big|_{\boldsymbol{\theta}=\hat{\boldsymbol{\theta}}}}_{=0} + \frac{1}{2}(\boldsymbol{\theta}-\hat{\boldsymbol{\theta}})^{\top}\mathbf{H}(\log \mathbb{P}[\boldsymbol{\theta}|\mathcal{D}])\Big|_{\boldsymbol{\theta}=\hat{\boldsymbol{\theta}}}(\boldsymbol{\theta}-\hat{\boldsymbol{\theta}}) \tag{2.38}$$

where $\nabla \log \mathbb{P}[\boldsymbol{\theta}|\mathcal{D}]$ vanishes as $\hat{\boldsymbol{\theta}}$ is a maximum for $\mathbb{P}[\mathcal{D}|\boldsymbol{\theta}]$. Whilst $\mathbf{H}(\log \mathbb{P}[\boldsymbol{\theta}|\mathcal{D}])\Big|_{\boldsymbol{\theta}=\hat{\boldsymbol{\theta}}}$ is the Hessian matrix of the posterior computed at $\hat{\boldsymbol{\theta}}$. This matrix will be denoted as $\mathbf{H}(\hat{\boldsymbol{\theta}})$ for the sake of conciseness. It is interesting to note that Eq. (2.38) tacitly endows $\mathbf{H}(\hat{\boldsymbol{\theta}})$ with role of covariance matrix, hence $\mathbf{H}(\hat{\boldsymbol{\theta}})$ must be positive (semi-) definite. However, since $\hat{\boldsymbol{\theta}}$ is a maximum, $\mathbf{H}(\hat{\boldsymbol{\theta}})$ is negative definite. This can be corrected by changing the sign of the second-order term:

$$\log \mathbb{P}[\boldsymbol{\theta}|\mathcal{D}] \approx \log \mathbb{P}[\hat{\boldsymbol{\theta}}|\mathcal{D}] - \frac{1}{2}(\boldsymbol{\theta}-\hat{\boldsymbol{\theta}})^{\top}\mathbf{H}(\hat{\boldsymbol{\theta}})(\boldsymbol{\theta}-\hat{\boldsymbol{\theta}}) \tag{2.39}$$

where, with abuse of notation, $\mathbf{H}(\hat{\boldsymbol{\theta}})$ is now positive definite. In addition, after this change of sign, $\mathbf{H}(\hat{\boldsymbol{\theta}})$ represents the Hessian matrix of $-\log \mathbb{P}[\boldsymbol{\theta}|\mathbf{x}]$ computed at $\hat{\boldsymbol{\theta}}$. Exponentiating both sides of Eq. (2.39) leads to:

$$\mathbb{P}[\boldsymbol{\theta}|\mathcal{D}] \approx \mathbb{P}[\hat{\boldsymbol{\theta}}|\mathcal{D}] \exp\left(-\frac{1}{2}(\boldsymbol{\theta}-\hat{\boldsymbol{\theta}})^{\top}\mathbf{H}(\hat{\boldsymbol{\theta}})(\boldsymbol{\theta}-\hat{\boldsymbol{\theta}})\right) \tag{2.40}$$

where the first multiplying factor can be set as the traditional normalisation constant for multivariate Gaussian distributions:

$$\mathbb{P}[\hat{\boldsymbol{\theta}}|\mathcal{D}] = \frac{1}{2\pi(\det \mathbf{H}(\hat{\boldsymbol{\theta}})^{-1})^{1/2}} \tag{2.41}$$

As a result, this leads to the final expression of the approximated posterior:

$$\mathbb{P}[\boldsymbol{\theta}|\mathcal{D}] \approx \frac{1}{2\pi(\det \mathbf{H}(\hat{\boldsymbol{\theta}})^{-1})^{1/2}} \exp\left(-\frac{1}{2}(\boldsymbol{\theta}-\hat{\boldsymbol{\theta}})^{\top}\mathbf{H}(\hat{\boldsymbol{\theta}})(\boldsymbol{\theta}-\hat{\boldsymbol{\theta}})\right) \tag{2.42}$$

Intriguingly, Laplace's approximation can be thought of as a special case of the forthcoming method.

Variational Inference (VI). The posterior $\mathbb{P}[\boldsymbol{\theta}|\mathcal{D}]$ can be approximated through VI as well. VI takes $\mathbb{Q}_{\boldsymbol{\lambda}}(\boldsymbol{\theta})$ from a given family of probability as the desired approximator. This $\mathbb{Q}_{\boldsymbol{\lambda}}(\boldsymbol{\theta})$ includes a number of parameters in $\boldsymbol{\lambda}$, which are determined by minimising a pseudo-distance between the approximator and the true posterior. For instance, if $\mathbb{Q}_{\boldsymbol{\lambda}}(\boldsymbol{\theta})$ is assumed to be Gaussian, then $\boldsymbol{\lambda}$ contains the mean vector and the covariance matrix of the distribution, namely $\boldsymbol{\lambda} = \begin{bmatrix}\boldsymbol{\mu} & \boldsymbol{\Sigma}\end{bmatrix}$. In this case, VI reduces to Laplace' approximation. As concerns the implementation, the identification of $\mathbb{Q}_{\boldsymbol{\lambda}}(\boldsymbol{\theta})$ is done by minimising the negative Evidence Lower BOund (ELBO) defined as [103–107]:

$$\text{ELBO} = \mathbb{E}_{\mathbb{Q}_{\boldsymbol{\lambda}}(\boldsymbol{\theta})}[\log \mathbb{P}[\mathcal{D}|\boldsymbol{\theta}, \mathcal{H}] - \log \mathbb{Q}_{\boldsymbol{\lambda}}[\boldsymbol{\theta}]] \tag{2.43}$$

Nevertheless, it is worth noting that the convergence to the true posterior is not always guaranteed, but VI generally necessitates limited computational requirements.

Hamiltonian Monte Carlo (HMC). This strategy is often employed to circumvent the potential lack of convergence of VI, albeit being more computationally demanding. HMC defines a set of Markov chains whose invariant is $\mathbb{P}[\boldsymbol{\theta}|\mathcal{D}]$, thus ergodically ensuring the convergence of the method. Interestingly, HMC relies on the concept of Hamiltonian Dynamics to boost the exploration of the parameter space [108]. To do so, trials of $\boldsymbol{\theta}$ are drawn from the so-called Canonical Ensemble:

$$\mathcal{C}(\boldsymbol{\theta}, \mathbf{p}) = \frac{1}{Z} \exp\left[-U(\boldsymbol{\theta})\right] \exp\left[-K(\mathbf{p})\right] \tag{2.44}$$

where $U(\boldsymbol{\theta})$ is the potential energy, $K(\mathbf{p})$ is the kinetic energy function of the vector of momenta $\mathbf{p} \in \mathbb{R}^{\mathsf{P}}$, and T is the temperature. Without loss of generality, T can be set to 1. For this specific application, $U(\boldsymbol{\theta})$ equals the negative posterior:

$$U(\boldsymbol{\theta}) = -\log \mathbb{P}[\boldsymbol{\theta}|\mathcal{D}] \tag{2.45}$$

whilst the kinetic energy is defined as:

$$K(\mathbf{p}) = \frac{1}{2}\mathbf{p}^\top \mathbf{M}\mathbf{p} \tag{2.46}$$

where $\mathbf{K}$ is the mass matrix, which actually serves as a covariance matrix, and it is typically assumed as diagonal, i.e. $\mathbf{K} = \text{diag}(K_1, K_2, \ldots, K_\mathsf{P})$. In agreement with Hamiltonian Dynamics, $(\boldsymbol{\theta}, \mathbf{p})$ are the coordinates of a mechanical system whose total energy is given by the Hamiltonian:

$$H(\boldsymbol{\theta}, \mathbf{p}) = U(\boldsymbol{\theta}) + K(\mathbf{p}) \tag{2.47}$$

which is hypothesised to be constant throughout the evolution of the system. The differentiation of Eq. (2.46)-(2.45) allows introducing the dynamics of sampling:

$$d\boldsymbol{\theta} = \mathbf{M}^{-1}\mathbf{p}\, dt \tag{2.48}$$

$$d\mathbf{p} = -\nabla U\, dt \tag{2.49}$$

where t is a pseudo-time variable. As suggested by Neal [109], discretising Eq. (2.48)-(2.49) can efficiently be carried out via the *leapfrog* scheme:

$$\begin{aligned} p_i(t+\varepsilon/2) &= p_i(t) - (\varepsilon/2)\, \nabla_{\theta_i} U(\boldsymbol{\theta}(t)) \\ \theta_i(t+\varepsilon) &= \theta_i(t) + \varepsilon\, \frac{p_i(t+\varepsilon/2)}{K_i} \\ p_i(t+\varepsilon) &= p_i(t+\varepsilon/2) - (\varepsilon/2)\, \nabla_{\theta_i} U(\boldsymbol{\theta}(t+\varepsilon)) \end{aligned} \tag{2.50}$$

which hold for each $i = 1, 2, \ldots, \mathsf{P}$, where p_i and θ_i are the i-th elements of $\mathbf{p}$ and $\boldsymbol{\theta}$. The last relationship allows one to define the Markov chains, i.e. trajectories in the $\boldsymbol{\theta} - \mathbf{p}$ space. In order to construct the states of such chains, samples of $\boldsymbol{\theta}^{(i+1)}$ and $\mathbf{p}^{(i+1)}$ are drawn to explore the parameter's space. Each new state $(\boldsymbol{\theta}^{(i+1)}, \mathbf{p}^{(i+1)})$ can be either accepted or rejected with respect to its ancestor $(\boldsymbol{\theta}^{(i)}, \mathbf{p}^{(i)})$. Whether a sample is accepted depends upon how much the Hamiltonian H (Eq. (2.47)) changes. In principle, H must remain constant across the states, but for the sake of the numerical implementation, H suffices to experience negligible variations. Therefore, a new state $(\boldsymbol{\theta}^{(i+1)}, \mathbf{p}^{(i+1)})$ is accepted if $|H(\boldsymbol{\theta}^{(i+1)}, \mathbf{p}^{(i+1)}) - H(\boldsymbol{\theta}^{(i)}, \mathbf{p}^{(i)})| \approx 0$. The sampling proceeds until Markov's chains converge to $\mathbb{P}[\boldsymbol{\theta}|\mathcal{D}]$. Once the convergence

is attained, additional trials are drawn to sample the posterior.

2.3.3. Making Predictions

Upon computing the posterior, or an approximation thereof, one may wish to forecast unseen data, namely:

$$y^* = \mathcal{G}_{\hat{\boldsymbol{\theta}}}(\mathbf{x}^*) \tag{2.51}$$

where y^* is the predicted valued associated with $\mathbf{x}^*$. In BI, the predicted value obeys the *predictive posterior* (distribution) defined as:

$$y^* \sim \mathbb{P}[\mathbf{x}^*|\mathcal{D}] = \int_{\boldsymbol{\theta}} \mathbb{P}[\mathbf{x}^*|\boldsymbol{\theta}]\mathbb{P}[\boldsymbol{\theta}|\mathcal{D}]\, d\boldsymbol{\theta} \tag{2.52}$$

Mathematically, the predictive posterior weights the value that the model predicts, $\mathbb{P}[\mathbf{x}_*|\boldsymbol{\theta}]$, through the posterior by integrating over the entire parameter space.

Unfortunately, Eq. (2.52) is, again, analytically intractable, thus approximation are pursued, for instance:

$$\mathbb{P}[\mathbf{x}^*|\mathcal{D}] \approx \frac{1}{\mathsf{M}} \sum_{j=1}^{\mathsf{M}} \mathbb{P}[\mathbf{x}^*|\boldsymbol{\theta}^{(j)}] \tag{2.53}$$

where $\boldsymbol{\theta}^{(j)} \,\forall\, j = 1, 2, \ldots, \mathsf{M}$ are samples drawn from the posterior $\mathbb{P}[\boldsymbol{\theta}|\mathcal{D}]$. Once $\mathbb{P}[\mathbf{x}_*|\mathcal{D}]$ is computed, it is possible to extract pertinent statistical descriptors, such as quartiles, the expected value (mean) $\mathbb{E}[y_*]$, the standard deviation (uncertainty) $\sqrt{\mathbb{V}[y_*]}$.

2.4. Gaussian Process Regression

GPR allows for constructing a probabilistic surrogate model of a given function f. Upon processing a training dataset, GPR assimilates the behaviour of f, conferring the ability to forecast f elsewhere while calculating the uncertainty over the prediction [102, 110].

Let $f : \mathbb{R}^N \to \mathbb{R}$ be a real-valued function one wishes to identify. Suppose the function was probed at $\mathbf{x}_i \,\forall\, i = 1, 2, \ldots, \mathsf{N}$, thus collecting $f_1, f_2, \ldots, f_{\mathsf{N}}$ noisy

observation of f. The resulting training dataset if given by:

$$\mathcal{D} = \{(\mathbf{x}_i, f_i) \mid f_i = f(\mathbf{x}_i), i = 1, 2, \ldots, \mathsf{N}\} \tag{2.54}$$

Let us define the regression model for f:

$$f_i = f(\mathbf{x}_i) + \varepsilon; \quad \varepsilon \sim \mathcal{N}(0, \sigma_n^2) \tag{2.55}$$

where ε is Gaussian noise with zero mean and variance σ_n^2, whose observations are independent and identically distributed (IID).

GPR commences with prescribing a Gaussian Process (GP) over f:

$$f \sim \mathrm{GP}(\mathcal{M}(\mathbf{x}), \mathcal{K}(\mathbf{x}, \mathbf{x}')) \quad \forall\, \mathbf{x}, \mathbf{x}' \in D \tag{2.56}$$

Specifically, a GPR is a collection of random variables such that any subset thereof is jointly Gaussian [102]. As can be seen in Eq. (4), a GP is fully defined by the mean $\mathcal{M}$, and the so-called kernel $\mathcal{K}$ – also known as covariance function. One of the most versatile kernels often encountered in the literature is Matérn's:

$$\mathcal{K}(\mathbf{x}, \mathbf{x}') = C\, \frac{2^{1-\xi}}{\Gamma(\xi)} \left(\frac{\sqrt{2\xi}\|\mathbf{x} - \mathbf{x}'\|}{l} \right)^{\xi} K_\xi \left(\frac{\sqrt{2\xi}\|\mathbf{x} - \mathbf{x}'\|}{l} \right) \tag{2.57}$$

where ξ, l are positive constants, K_ξ is the modified Bessel function, $\Gamma(\xi)$ is the Gamma function, and $\|\cdot\|$ denotes the Euclidean norm. Additionally, the constant C is introduced as a scaling factor for the kernel. The kernel $\mathcal{K}(\mathbf{x}, \mathbf{x}')$ includes a number of unknown parameters which are meant to be identified upon the training dataset, i.e. the *hyperparameters*. Referring to Eq. (2.57), these hyperparameters will succinctly be gathered into the vector $\boldsymbol{\theta} = \begin{bmatrix} C & l & \xi \end{bmatrix}^\top$.

GPR proceeds with the identification of the hyperparameters via MLE, see Eq. (2.37). Since the objective herein is the construction of a regression model, and f was tacitly modelled as an IID Gaussian random variable, MLE requires building the Gaussian likelihood (Eq. (2.30)) upon $\mathcal{D}$. With reference to [102], the likelihood is conveniently restated as:

$$\log \mathbb{P}[\mathcal{D}|\boldsymbol{\theta}] = -\frac{1}{2}\mathbf{f}^\top (\mathbf{V} + \sigma_n^2 \mathbf{I})^{-1} \mathbf{f} - \frac{1}{2} \log |\mathbf{V} + \sigma_n^2 \mathbf{I}| - \frac{n}{2} \log 2\pi \tag{2.58}$$

where $\mathbf{f} = \begin{bmatrix} f_1 & f_2 & \dots & f_{\mathsf{N}} \end{bmatrix}^\top$ and $\mathbf{V}$ is the covariance matrix:

$$\mathbf{V} = \begin{bmatrix} \mathcal{K}(\mathbf{x}_1, \mathbf{x}_1) & \mathcal{K}(\mathbf{x}_1, \mathbf{x}_2) & \dots & \mathcal{K}(\mathbf{x}_1, \mathbf{x}_{\mathsf{N}}) \\ \mathcal{K}(\mathbf{x}_2, \mathbf{x}_1) & \mathcal{K}(\mathbf{x}_2, \mathbf{x}_2) & \dots & \mathcal{K}(\mathbf{x}_2, \mathbf{x}_{\mathsf{N}}) \\ \vdots & \vdots & \ddots & \vdots \\ \mathcal{K}(\mathbf{x}_{\mathsf{N}}, \mathbf{x}_1) & \mathcal{K}(\mathbf{x}_{\mathsf{N}}, \mathbf{x}_2) & \dots & \mathcal{K}(\mathbf{x}_{\mathsf{N}}, \mathbf{x}_{\mathsf{N}}) \end{bmatrix} \tag{2.59}$$

which depends upon $\boldsymbol{\theta}$ through $\mathcal{K}$.

Once Eq. (2.58) is maximised, and the expected value of the parameters are known, i.e. $\hat{\boldsymbol{\theta}}$, these can be plugged into the kernel (Eq. (2.57)) so the user can predict f at any given point $\mathbf{x}^*$. Since Gaussian random variables are closed with respect to the conditional probability, the posterior distribution of $\boldsymbol{\theta}$ is still Gaussian with mean and variance given by:

$$\mathcal{M}_p(\mathbf{x}^*) = \mathcal{M}(\mathbf{x}^*) + \mathbf{V}(\mathbf{x}^*, \mathbf{x}) \left[\mathbf{V}(\mathbf{x}, \mathbf{x}) + \sigma_n^2 \mathbf{I}\right]^{-1} (\mathbf{y} - \mathcal{M}(\mathbf{x})) \tag{2.60}$$

$$\mathcal{K}_p(\mathbf{x}^*, \mathbf{x}^*) = \mathcal{K}(\mathbf{x}^*, \mathbf{x}^*) - \mathbf{V}(\mathbf{x}^*, \mathbf{x}) \left[\mathbf{V}(\mathbf{x}, \mathbf{x}) - \sigma_n^2 \mathbf{I}\right]^{-1} \mathbf{V}(\mathbf{x}, \mathbf{x}^*) \tag{2.61}$$

Accordingly, one can express the predicted value $f(\mathbf{x}^*)$ in terms of Eq. (2.60)-(2.61) and readily calculate the related 68% confidence interval:

$$f(\mathbf{x}^*) = \mathcal{M}_p(\mathbf{x}^*) \pm \sqrt{\mathcal{K}_p(\mathbf{x}^*, \mathbf{x}^*)}$$

where $\sqrt{\mathcal{K}_p(\mathbf{x}^*, \mathbf{x}^*)}$ is the uncertainty (standard deviation) of the prediction.

Figure 2.7 shows a schematic outcome of GPR applied to a scalar real-valued function $f : \mathbb{R} \to \mathbb{R}$, in solid black. The black dots are the noisy observation of f, i.e. f_i, whereas the red line is the expected value (Eq. (2.60)) retrieved from GPR. The shaded blue region is x-wise confidence interval at 68% confidence level whose width is $\mathcal{M}_p(\mathbf{x}^*) \pm \sqrt{\mathcal{K}_p(\mathbf{x}^*, \mathbf{x}^*)}$.

2.5. Logistic Regression

LR was conceived in the nineteenth century to model population growth and epidemic outspread [111]. Only recently, LR has received considerable attention as a probabilistic supervised ML classification technique [112].

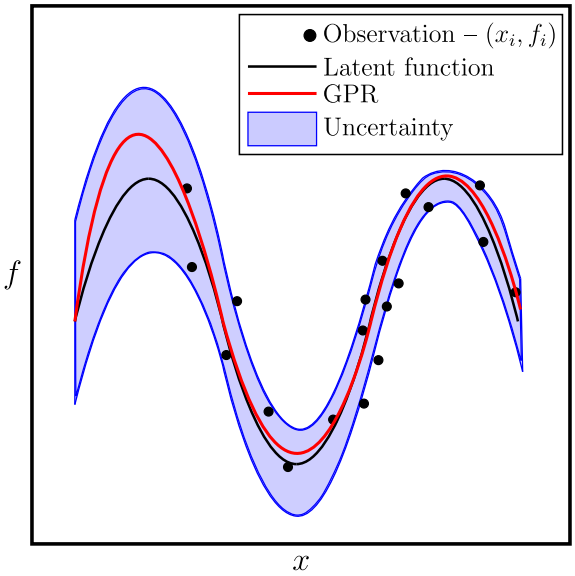

Figure 2.7. GPR applied to a scalar real-valued function $f : \mathbb{R} \to \mathbb{R}$. and the shaded blue region is x-wise confidence interval.

To facilitate the explanation, let us consider the following generic dataset $\mathcal{D}$:

$$\mathcal{D} = \{(\mathbf{x}_i, \mathcal{F}_i) \mid \mathcal{F}_i \in \{0, 1\};\ i = 1, 2, \ldots, \mathsf{N}\} \tag{2.62}$$

where each datum $\mathbf{x}_i$ is labelled through $\mathcal{F}_i$ which can either assume 0 or 1. For the sake of illustrating the background of LR, suppose $\mathbf{x}_i \in \mathbb{R}^2$ such that $\mathbf{x}_i = \begin{bmatrix} x_i & y_i \end{bmatrix}$. The resulting (schematic) dataset is portrayed in Figure 2.8. Therein, points with $\mathcal{F}_i = 0$ and $\mathcal{F}_i = 1$ are represented as blue and red circle markers, respectively. With reference to the two-dimensional setting just outlined, LR traditionally attempts to seek the straight line that optimally separates the two classes. Such a line is named as *decision boundary*, and it is depicted as the solid black line in Figure 2.8. In this instance, the decision boundary can be stated in its implicit form as:

$$\mathcal{H}(\mathbf{x}, \boldsymbol{\theta}) = x\,\theta_1 + y\,\theta_2 + \theta_3 \tag{2.63}$$

where $\boldsymbol{\theta}$ concisely indicates the aggregated vector of the parameters, i.e. $\boldsymbol{\theta} = \begin{bmatrix} \theta_1 & \theta_2 & \theta_3 \end{bmatrix}$, and x and y are the coordinate of a generic point. Eq. (2.63) can be demonstrated to be proportional to the signed distance to the decision boundary.

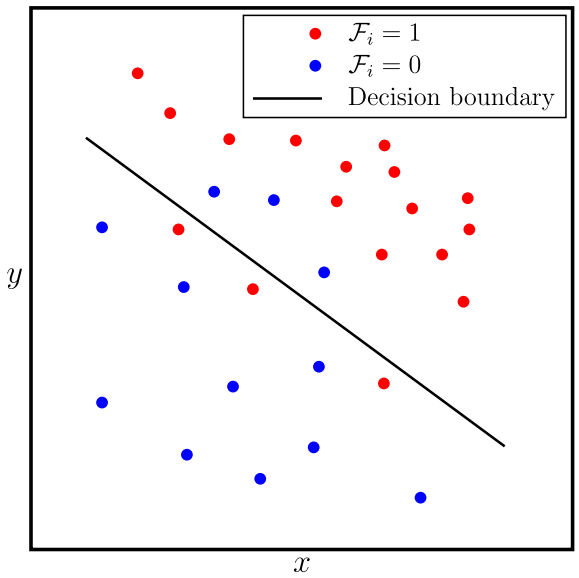

Figure 2.8. Graphical representation of the dataset $\mathcal{D}$ along with the decision boundary.

This signed distance plays a key role in the probabilistic modelling of LR, as it shall be discussed shortly.

LR entails transforming $\mathcal{F}_i$ into a Bernoulli random variable such that:

$$\mathcal{F}_i = \mathbb{P}[\mathbf{x}_i|\boldsymbol{\theta}]^k \left(1 - \mathbb{P}[\mathbf{x}_i|\boldsymbol{\theta}]\right)^{1-k} \quad k = 0, 1 \tag{2.64}$$

where $\mathbb{P}[\mathbf{x}_i|\boldsymbol{\theta}]$ represents the probability of predicted class. Generally, $\mathbb{P}[\mathbf{x}|\boldsymbol{\theta}]$ is modelled via the so-called log-odds ratio:

$$\log \frac{\mathbb{P}[\mathbf{x}|\boldsymbol{\theta}]}{1 - \mathbb{P}[\mathbf{x}|\boldsymbol{\theta}]} = \mathcal{H}(\mathbf{x}, \boldsymbol{\theta}) \tag{2.65}$$

If Eq. (2.65) is solved for $\mathbb{P}[\mathbf{x}|\boldsymbol{\theta}]$, the associated LR equation is promptly retrieved:

$$\mathbb{P}[\mathbf{x}|\boldsymbol{\theta}] = \frac{1}{1 + \exp[-\mathcal{H}(\mathbf{x}, \boldsymbol{\theta})]} \tag{2.66}$$

It is thus evident that LR connects the probability of the predicted class with the signed distance of $\mathbf{x}$ to the decision boundary $\mathcal{H}(\mathbf{x}, \boldsymbol{\theta})$. In particular, the last relationship "squashes" the values $\mathcal{H}(\mathbf{x}, \boldsymbol{\theta})$ into $[0, 1]$ to obey the axiomatic definition of

probability.

It should be mentioned that the parameters in $\boldsymbol{\theta}$ have been considered unknown thus far. In order to learn $\boldsymbol{\theta}$ upon the given dataset $\mathcal{D}$, the MLE of Eq. (2.37) is pursued while employing a Bernoulli likelihood. In this case, the predicted class $\mathcal{G}_{\boldsymbol{\theta}}(\mathbf{x}_i)$ and y_i of Eq. (2.37) are opportunely replaced with $\mathbb{P}[\mathbf{x}|\boldsymbol{\theta}]$ and $\mathcal{F}_i$, thus resulting in:

$$\mathbb{P}[\mathcal{D}|\boldsymbol{\theta}] = \prod_{i=1}^{\mathsf{N}} \mathbb{P}[\mathbf{x}_i|\boldsymbol{\theta}]^{\mathcal{F}_i}(1 - \mathbb{P}[\mathbf{x}_i|\boldsymbol{\theta}])^{(1-\mathcal{F}_i)} \tag{2.67}$$

It is worth mentioning that MLE succeeds if the likelihood exhibits a maximum. By contrast, when MLE fails, one can incorporate LR into the MAP framework (Section 2.3) to learn the parameters. This procedure involves casting Eq. (2.67) and an appropriate prior $\mathbb{P}[\boldsymbol{\theta}]$ into Bayes' theorem (Eq. (2.32)), and solving Eq. (2.34).

2.6. Neural Networks

2.6.1. Traditional Neural Network

NN refers to a broad class of surrogate models for both regression and classification tasks. NNs consist of a set of elementary units called neurons grouped by layer. Generally, NNs possess a sequence of layers. The first one is called the input layer, and it is devoted to receiving the input data. The last one is the output layer which gives the value of the predictions. When present, hidden layers, located between input and output ones, are liable for adding increasing non-linear predictive capabilities to the model [113].

Although there exist NNs of different nature, the focus here is on those *fully-connected*, where the neurons belonging to consecutive layers own connection with one another. Therefore, let us consider a fully-connected NN having an N_1-dimensional input layer, $l = 2, \ldots, L-1$ hidden layers with $N_2, \ldots, N_{L-1}$ each, and an N_L-dimensional output layer. In order to graphically visualise the distinctive NN architecture, an example is shown in Figure 2.9 where $N_L = 1$.

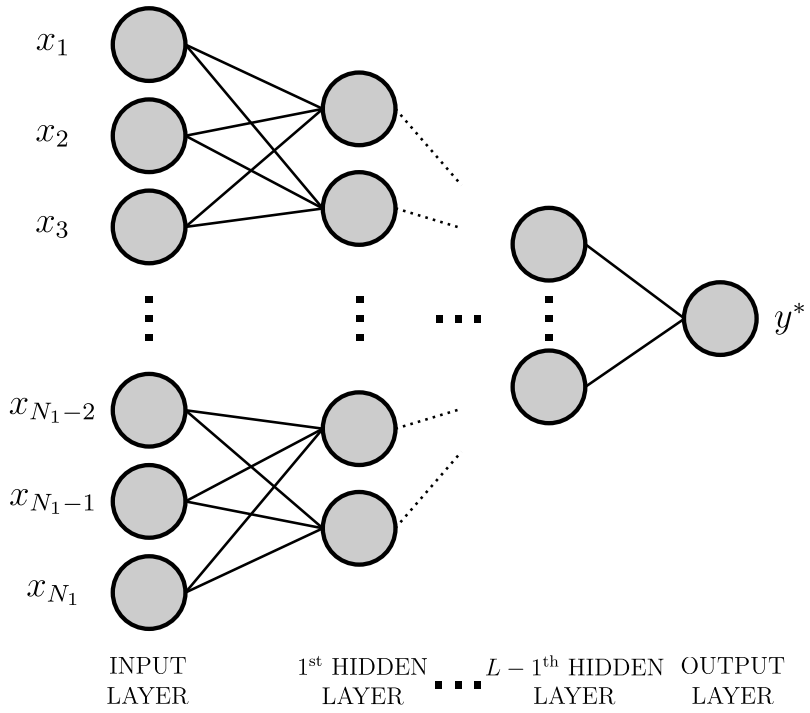

Figure 2.9. Schematic of a fully-connected NN having N inputs, $L-1$ hidden layers and a scalar output layer.

The input-output relationship of the l-th layer can recursively be stated as:

$$\begin{aligned} \mathbf{y}_1(\mathbf{x}) &= \mathbf{W}_1\mathbf{x} + \mathbf{b}_1 \\ \mathbf{y}_l(\mathbf{x}) &= \mathbf{W}_l\,\varphi_l(\mathbf{y}_{l-1}(\mathbf{x})) + \mathbf{b}_l \quad l = 2,\ldots,L \\ \mathcal{G}_{\boldsymbol{\theta}}(\mathbf{x}) &= \mathbf{y}(\mathbf{x}) \end{aligned} \tag{2.68}$$

where $\mathbf{x} \in \mathbb{R}^{N_1}$ is the input vector, $\mathbf{W}_l \in \mathbb{R}^{N_l \times N_{l-1}}$ and $\mathbf{b}_l \in \mathbb{R}^{N_l}$ are the weight matrix and the bias vector of the l-th layer, respectively. Additionally, the last entry of Eq. (2.68) describes the global input-output relationship of the NN where $\boldsymbol{\theta}$ stands for the aggregated vector of weights & biases. Therein, the subscript $l = L$ was omitted for conciseness. Lastly, φ_l denotes the activation function assigned to neurons of the l-th layer, which acts on $\mathbf{y}_l$ in an element-wise fashion. To explain the role of the activation functions it is worth concentrating on the k-th element of the vector $\mathbf{y}_l$ involved in the the l-th, i.e. $y_{l,k}$. Essentially, φ_l controls the fraction of $y_{l,k}$ that is supplied to the subsequent layer before being weighted through $\mathbf{W}_l$. Al-

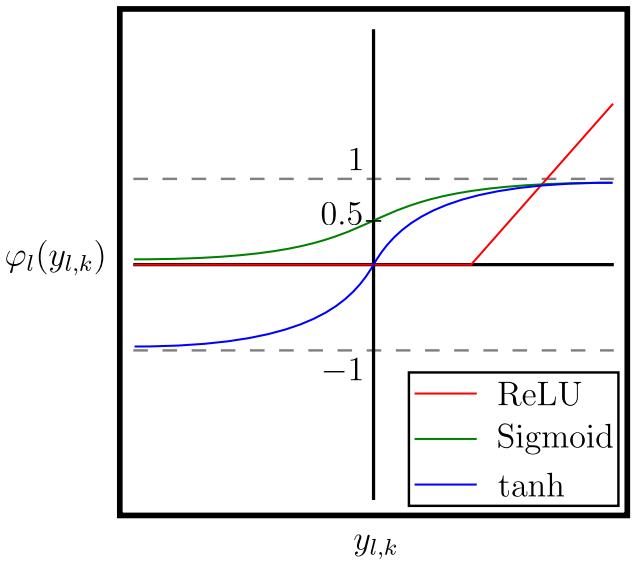

Figure 2.10. Schematic illustration of *ReLU*, *sigmoid*, and *tanh* activation functions.

though a number of activation functions are available, a few of the most popular are shown in Figure. 2.10, i.e. *Rectified Linear Unit (ReLU)*, *sigmoid*, *tanh*. ReLUs only transmit part of $y_{l,k}$ beyond a predefined threshold. This activation function is suitable for piecewise linear surrogate models in regression problems. Tanh activation functions can be adopted for regression as well, with the advantages of continuously rescaling into $[-1, 1]$ across $\mathbb{R}$ and allowing for switching the sign of $y_{l,k}$. Similarly, sigmoid rescale $y_{l,k}$, but into $[0, 1]$, thus making them the preferred choice for binary classification problems.

Suppose one obtained P samples from an observed phenomenon, thus collating the following dataset:

$$\mathcal{D} = \{(\mathbf{x}_i, \mathbf{y}_i \mid \mathbf{x}_i \in \mathbb{R}^{N_1}; \mathbf{y}_i \in \mathbb{R}^{N_l}; i = 1, 2, \ldots, \mathsf{P}\} \tag{2.69}$$

and they wish to fit the data with a surrogate NN model as per Eq. (2.68), i.e. $\mathbf{y} = \mathcal{G}_{\boldsymbol{\theta}}(\mathbf{x})$. Analogously to the ML methods examined thus far, the surrogation implies learning the parameter $\boldsymbol{\theta}$ upon observing $\mathcal{D}$ regardless of the problems' nature. To accomplish this task, the NN processes $\mathcal{D}$ and computes the prediction corresponding to $\mathbf{x}_i$, namely $\mathbf{y}_i^* = \mathcal{G}_{\boldsymbol{\theta}}(\mathbf{x}_i) \, \forall \, i = 1, 2, \ldots, \mathsf{P}$. Subsequently, the mismatch between the prediction $\mathbf{y}_i^*$ and the ground-truth $\mathbf{y}_i$ is used to calculate the loss function –

usually a squared error:

$$\mathcal{L} = \sum_{i=1}^{\mathsf{P}} \|\mathbf{y}_i^* - \mathbf{y}_i\|^2 \tag{2.70}$$

During the training, this loss function is then numerically minimised to seek the optimal parameters of the NN, i.e. $\hat{\boldsymbol{\theta}}$. This operation is typically done via back-propagation [114]. The process continues until $\mathcal{L}$ attains values below a user-defined threshold. Once the training is done, it is possible to forecast and prospective data $\mathbf{x}^*$ using the last relationship of Eq. (2.68), i.e. $\mathbf{y}^* = \mathcal{G}_{\boldsymbol{\theta}}(\mathbf{x}^*)$.

2.6.2. Physics-Informed Neural Networks

Fundamentally, a PINN couples a traditional NNs (Eq. (2.68)) with a Partial Differential Equations (PDE) that is supposed to govern the observed phenomenon. For instance, equilibrium or conservation laws are generally considered in the field of Solid and Fluid Mechanics. The PDE serves the purpose of guiding the training stage aiming to ensure the physical consistency of the predictions. In practice, a bespoke loss term is added to Eq. (2.70), which derives from the discrepancy between the NN predictions and those the PDE would give [115]. PINNs have mainly been developed to numerically solve PDE-driven problems [116, 117], and their application to engineering research is still scarce. Nevertheless, the framework of PINNs is incredibly versatile so that it can be easily adapted to handle problems other than PDEs. In this section, the classical settings of PINNs is outlined, whereas Chapter 5 demonstrates how to tailor this framework to deal with finite fatigue life modelling. Figure 2.11 is presented to support the following explanation.

Let us consider a NN described by Eq. (2.68). Alongside, let us define a N_1-dimensional domain $\Omega \subset \mathbb{R}^{N_1}$ whose boundary is Γ, and let:

$$\begin{cases} \mathcal{P}(\mathbf{y}(\mathbf{x})) = \mathbf{f}(\mathbf{x}) & \mathbf{x} \in \Omega \\ \mathcal{B}(\mathbf{y}(\mathbf{x})) = \mathbf{b}(\mathbf{x}) & \mathbf{x} \in \Gamma \end{cases} \tag{2.71}$$

be a boundary value PDE problem, where $\mathcal{P}$ is a generic differential operator, $\mathcal{B}$ is a generic boundary value operator, $\mathbf{y}(\mathbf{x})$ represent the solution of the PDE, $\mathbf{f}(\mathbf{x})$ is the forcing term, and $\mathbf{b}(\mathbf{x})$ is the prescribed value of the solution over Γ. Assume

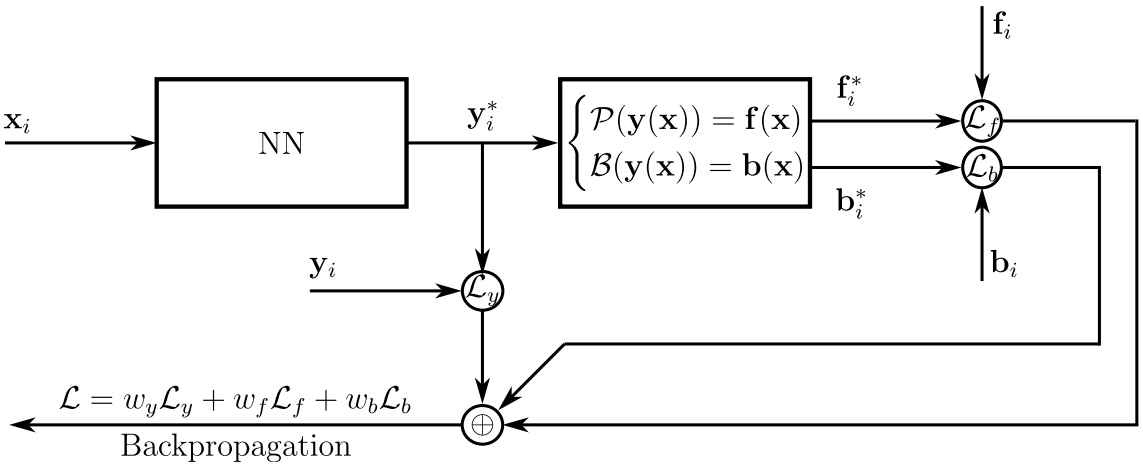

Figure 2.11. Block diagram of PINNs.

that one probed $\mathbf{y} \in \mathbb{R}^{N_L}$, $\mathbf{f} \in \mathbb{R}^{N_f}$, $\mathbf{b} \in \mathbb{R}^{N_b}$, thus acquiring the training dataset $\mathcal{D}$:

$$\begin{aligned} \mathcal{D} &= \mathcal{D}_{\mathbf{y}} \cup \mathcal{D}_{\mathbf{f}} \cup \mathcal{D}_{\mathbf{b}} \\ \mathcal{D}_y &= \{(\mathbf{x}_i, \mathbf{y}_i) \mid i = 1, 2, \ldots, \mathsf{P}_y\} \\ \mathcal{D}_f &= \{(\mathbf{x}_i, \mathbf{f}_i) \mid i = 1, 2, \ldots, \mathsf{P}_f\} \\ \mathcal{D}_b &= \{(\mathbf{x}_i, \mathbf{b}_i) \mid i = 1, 2, \ldots, \mathsf{P}_b\} \end{aligned} \tag{2.72}$$

The input data $\mathbf{x}_i$ is fed into the NN to compute the corresponding prediction $\mathbf{y}_i^*$. Next, $\mathbf{y}_i^*$ is supplied into $\mathcal{P}(\square)$ and $\mathcal{B}(\square)$ to calculate the corresponding forcing term and boundary condition, namely $\mathbf{f}_i^*$ and $\mathbf{b}_i^*$. The discrepancy between the predictions and the probed values originate the following losses:

$$\begin{aligned} \mathcal{L}_y &= \sum_{i=1}^{\mathsf{P}_y} \|\mathbf{y}_i^* - \mathbf{y}_i\|^2 \\ \mathcal{L}_f &= \sum_{i=1}^{\mathsf{P}_f} \|\mathbf{f}_i^* - \mathbf{f}_i\|^2 \\ \mathcal{L}_b &= \sum_{i=1}^{\mathsf{P}_b} \|\mathbf{b}_i^* - \mathbf{b}_i\|^2 \end{aligned} \tag{2.73}$$

Each contribution is combined through a weighted sum ($\oplus$, in Figure 2.11) to gen-

erate the total loss $\mathcal{L}$:

$$\mathcal{L} = w_y \mathcal{L}_y + w_f \mathcal{L}_f + w_b \mathcal{L}_b \tag{2.74}$$

where w_y, w_f, w_b are weights that balance each contribution. Similarly to NNs, $\mathcal{L}$ is backpropagated to compute the optimal parameters $\hat{\boldsymbol{\theta}}$ of the NN. In this instance, a hypothetical minimiser learns $\hat{\boldsymbol{\theta}}$ while seeking a trade-off between the data, i.e. $\mathcal{L}_y$, and the physics, i.e. $\mathcal{L}_f$ and $\mathcal{L}_b$, which compete against one another. As a special case, if $w_f = w_b = 0$ and $w_y = 1$, the physics constraint is suppressed, then the PINN reduces to a traditional NN. After accomplishing the training, unseen data are predicted as per traditional NN.

2.6.3. Bayesian Neural Networks

The potential of BI can be exploited in the context of NNs as well. Specifically, when the parameters of a NN (Eq. (2.68)), i.e. $\boldsymbol{\theta}$, are turned into random variables and trained via BI, the NN is said to be a Bayesian NN (BNN) [108, 118–120]. In this regard, each neuron possesses both biases and weights described by a probability distribution. A schematic representation is offered by Figure 2.12. Hence, differently from traditional NN, the output of the BNN turns out to be a probability distribution, automatically.

Briefly, according to the Bayesian treatment of the training, a prior is initially prescribed over the parameters, thus defining $\mathbb{P}[\boldsymbol{\theta}]$. Upon collating a training dataset $\mathcal{D}$, the likelihood is constructed, hence $\mathbb{P}[\mathcal{D}|\boldsymbol{\theta}]$. Finally, both $\mathbb{P}[\boldsymbol{\theta}]$ and $\mathbb{P}[\mathcal{D}|\boldsymbol{\theta}]$ are substituted into Bayes' theorem (Eq. (2.32)) and the parameters posterior $\mathbb{P}[\boldsymbol{\theta}|\mathcal{D}]$ is computed [121–123], mainly via HMC or VI (see Section 2.3.2). Once $\mathbb{P}[\boldsymbol{\theta}|\mathcal{D}]$ or its approximation is known, the predictions about prospective data are made using the predictive posterior shown in Eq. (2.52).

Thanks to BI, BNNs offer diverse advantages over traditional NNs. Users can develop NN models whose complexity depends upon the problem, not the amount of data [108]. Thus, small-data regimes can effortlessly be handled [124], especially when the size of the dataset is lower than the dimensionality of the problem [125].

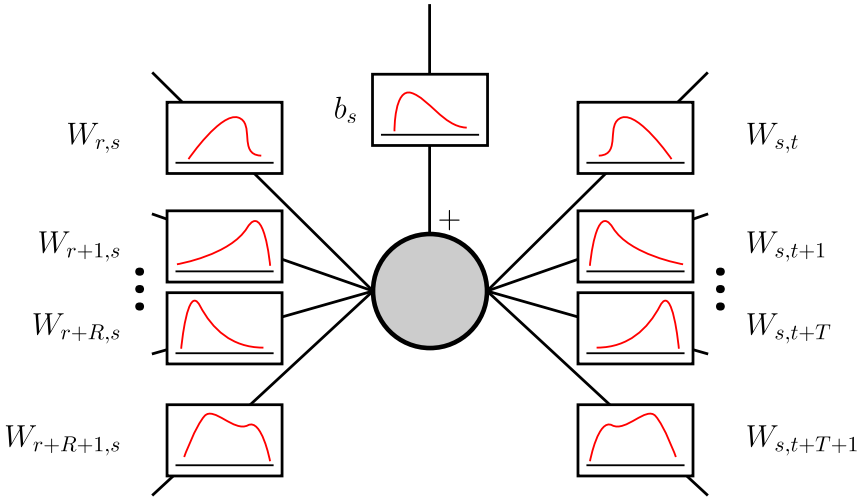

Figure 2.12. The s-th neuron of belonging to the generic l-th layer of a BNN. Herein, $W_{i,j}$ and b_s are the coefficients of the weight matrix and bias vector pertaining to the considered neuron and layer. The explict indication of the layer is dropped for brevity.

2.6.4. Bayesian Physics-Informed Neural Networks

Let us consider a BNN whose architecture is given in Eq.(2.68), and the PDE defined in Eq. (2.71). Analogously to PINNs, B-PINNs are BNNs whose training is constrained by physical or phenomenological models. Figure 2.13 illustrates a block diagram of a generic B-PINN where a PDE informs its physical branch, in agreement with Ref. [94] which addresses a regression problem.

The standard framework of B-PINNs assumes that the observations of the solution $\mathbf{y}_i$, forcing term $\mathbf{f}_i$, and boundary condition $\mathbf{b}_i$ are modelled as:

$$\begin{aligned} \mathbf{y}_i &= \mathbf{y}(\mathbf{x}_i) + \boldsymbol{\varepsilon}_i^y \\ \mathbf{f}_i &= \mathbf{f}(\mathbf{x}_i) + \boldsymbol{\varepsilon}_i^f \\ \mathbf{b}_i &= \mathbf{b}(\mathbf{x}_i) + \boldsymbol{\varepsilon}_i^b \end{aligned} \tag{2.75}$$

where each $\boldsymbol{\varepsilon}_i^y$, $\boldsymbol{\varepsilon}_i^f$, and $\boldsymbol{\varepsilon}_i^b$ is Gaussian noise with zero mean and covariance matrices $\boldsymbol{\Sigma}^y$, $\boldsymbol{\Sigma}^f$, $\boldsymbol{\Sigma}^b$, respectively. Consequently, the training dataset $\mathcal{D} = \mathcal{D}_y \cup \mathcal{D}_f \cup \mathcal{D}_b$ is straightforwardly defined in agreement with Eq. (2.72). Since the observations incorporate Gaussian noise and are independent of each other, the likelihood of $\mathcal{D}$

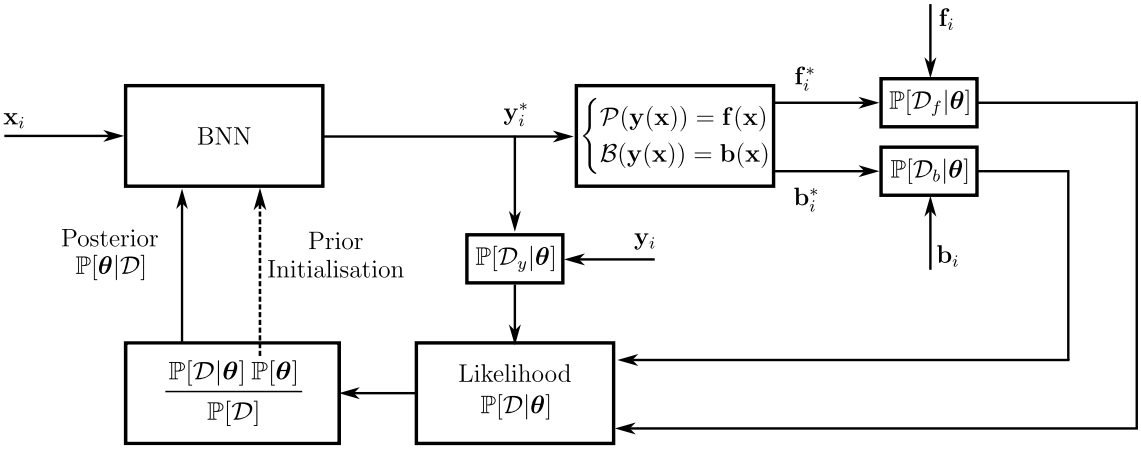

Figure 2.13. Schematic of a B-PINN

turns out to be:

$$\mathbb{P}[\mathcal{D}|\boldsymbol{\theta}] = \mathbb{P}[\mathcal{D}_y|\boldsymbol{\theta}]\mathbb{P}[\mathcal{D}_f|\boldsymbol{\theta}]\mathbb{P}[\mathcal{D}_b|\boldsymbol{\theta}] \tag{2.76}$$

where:

$$\begin{aligned}
\mathbb{P}[\mathcal{D}_y|\boldsymbol{\theta}] &= \prod_{i=1}^{\mathsf{P}_y} \frac{1}{\sqrt{(2\pi)^y \det \boldsymbol{\Sigma}^y}} \exp\left(-\frac{1}{2}\|\mathbf{y}_i^* - \mathbf{y}_i\|^2_{\boldsymbol{\Sigma}^y} \right) \\
\mathbb{P}[\mathcal{D}_f|\boldsymbol{\theta}] &= \prod_{i=1}^{\mathsf{P}_f} \frac{1}{\sqrt{(2\pi)^f \det \boldsymbol{\Sigma}^f}} \exp\left(-\frac{1}{2}\|\mathbf{f}_i^* - \mathbf{f}_i\|^2_{\boldsymbol{\Sigma}^f} \right) \\
\mathbb{P}[\mathcal{D}_b|\boldsymbol{\theta}] &= \prod_{i=1}^{\mathsf{P}_b} \frac{1}{\sqrt{(2\pi)^b \det \boldsymbol{\Sigma}^b}} \exp\left(-\frac{1}{2}\|\mathbf{b}_i^* - \mathbf{b}_i\|^2_{\boldsymbol{\Sigma}^b} \right)
\end{aligned} \tag{2.77}$$

In the last relationships, $\mathbf{y}_i^*$ are the predictions given by the sole NN, i.e. $\mathbf{y}_i^* = \mathcal{G}_{\boldsymbol{\theta}}(\mathbf{x}_i)$. Furthermore, $\mathbf{f}_i^*$ and $\mathbf{b}_i^*$ are the values of the forcing term and boundary condition obtained by supplying $\mathbf{y}_i^*$ into $\mathcal{P}(\square)$ and $\mathcal{B}(\square)$ (Eq. (2.71)), respectively. Lastly, $\|\square\|_{\boldsymbol{\Sigma}} = \sqrt{\square^\top \boldsymbol{\Sigma} \square}$ denotes the Mahalanobis distance with respect to $\boldsymbol{\Sigma}$. Evidently, the likelihood realises the penalisation between the ground-truth values ($\mathbf{y}_i$, $\mathbf{f}_i$, and $\mathbf{b}_i$) and the associated predicted values ($\mathbf{y}_i^*$, $\mathbf{f}_i^*$, and $\mathbf{b}_i^*$) similarly to the PINN's loss of Eq. (2.73). As concerns B-PINNs, however, such a penalisation is attained in terms of probabilities instead of mere mean squared error. Finally, $\mathbb{P}[\mathcal{D}|\boldsymbol{\theta}]$ and an opportune prior $\mathbb{P}[\boldsymbol{\theta}]$ is plugged into Bayes' theorem (Eq. (2.32)) to compute the posterior of $\boldsymbol{\theta}$. Such computation, which is, in fact, the training stage, is carried out

by the methods in Section 2.3.2, typically VI and HMC. Differently from NNs and PINNs, the predictions regarding prospective data are performed via the predictive posterior in agreement with BI; see Eq. (2.52).

2.6.5. Bayesian Model Selection

Designing the most suitable architecture of NNs, PINNs, BNNs, and B-PINNs is very often debated. Irrespective of the NN's nature, one can reframe the problem selection in a Bayesian fashion. In this way, one can probabilistically select the optimal number of hidden layers and neurons, and activation functions. This strategy is technically called Bayesian model selection [126, 127].

Initially, the designer is committed to considering a finite set of candidate architectures:

$$\mathcal{D}_C = \{\mathcal{G}_h : h = 1, 2, \dots, \mathsf{H}\} \tag{2.78}$$

where the h-th model $\mathcal{G}_h$ may possess any number of hidden layers, neurons per layer, and activation functions. Whilst the size of the input and output layer are fixed according to the designated task of the NN. In this respect, it is worth recalling Bayes' theorem (Eq. (2.32)) while explicitly including model's conditioning:

$$\mathbb{P}[\boldsymbol{\theta}|\mathcal{D}, \mathcal{G}_h] = \frac{\mathbb{P}[\mathcal{D}|\boldsymbol{\theta}, \mathcal{G}_h]\,\mathbb{P}[\boldsymbol{\theta}|\mathcal{G}_h]}{\mathbb{P}[\mathcal{D}|\mathcal{G}_h]} \tag{2.79}$$

where $\mathcal{D}$ is, again, the training dataset, and the evidence becomes:

$$\mathbb{P}[\mathcal{D}|\mathcal{G}_h] = \int_{\boldsymbol{\theta}} \mathbb{P}[\mathcal{D}|\boldsymbol{\theta}, \mathcal{G}_h]\mathbb{P}[\boldsymbol{\theta}|\mathcal{G}_h] d\boldsymbol{\theta} \tag{2.80}$$

Notice that while the integral is in general analytically intractable, it can numerically be approximated [126, 127]:

$$\mathbb{P}[\mathcal{D}|\mathcal{G}_h] \approx \frac{1}{\mathsf{Q}} \sum_{j=1}^{\mathsf{Q}} \mathbb{P}[\mathcal{D}|\boldsymbol{\theta}^{(j)}, \mathcal{G}_h] \tag{2.81}$$

where the sample $\boldsymbol{\theta}^{(j)}$ are drawn from $\mathbb{P}[\boldsymbol{\theta}|\mathcal{G}_h]$, and the likelihood can be computed according to Eq. (2.30) or (2.31) for regression or classification problems, respectively. The evidence is representative of the accuracy that the NNs attain with a

prescribed architecture. Therefore, the user intuitively selects the NN architecture that maximises the evidence:

$$\hat{\mathcal{G}} = \max_{\mathcal{G}_h \in \mathcal{D}_C} \mathbb{P}[\mathcal{D}|\mathcal{G}_h] \tag{2.82}$$

3. Contour Method Residual Stress Evaluation in Solid-state Welded Joints

The current chapter discloses the limitations of the CM's state-of-the-art while addressing a problem of scientific interest. Herein, the CM is applied to investigate RS in a novel solid-stated welded butt-joint.

3.1. Introduction

Solid-state welding refers to a broad class of welding techniques in which workpieces are joined below the melting point of the base material (BM) being welded. Solid-state welding techniques have been developed to overcome the main limitations affecting the traditional fusion welding. Because there is no material melting involved in solid-state welding, the thermal input is significantly lower than that of fusion welding, and the extent of heat-affected zone softening is reduced. Consequently, fewer microstructural changes occur within this softened zone, and the overall structural performance of the joint is typically improved. Solid-state welding also allows for joining both similar and dissimilar materials that are often considered difficult to fusion weld [128].

Amongst the family of solid-state welding, friction stir welding (FSW) has been particularly attracting attention in the last decades. This solid-state welding method was developed by The Welding Institute (TWI) of the UK in 1991. Basically, this technique employs a non-consumable rotating pin to join two facing workpieces (Figure 3.1(a)), usually plates. Due to the contact of the rotating pin and the sides of the material undergoing welding, a source of heat is generated by friction. As a consequence, the BM undergoes local softening and plastic deformations, which

eventually facilitate the two sides to merge together. As the pin travels along the weld direction, the material left behind experiences cooling until reaching room temperature. At this point, the welding process ends [129]. Throughout the years, FSW has evolved so that it can also handle joints in different configurations such as butt welds, T-butt and T-lap joints [129–131]. Many works in literature proved the capability of FSW to weld similar [132, 133], and dissimilar material pairs [134, 135]. Furthermore, FSW provides sound joints with limited defects and porosity [136]. Despite the significant advantages of FSW, it does not involve the use of any filler material (FIM), which would provide a gradual transition between the BMs being welded in several aspects.

About ten years ago, the development of the hybrid metal and extrusion bonding (HYB) enabled to combine the advantages of the FSW with the use of FIM. HYB relies on the processing principle of FSW, see (Figure 3.1(b)). However, continuous extrusion and injection of an aluminium FIM into the weld groove is utilised to consolidate the joint [137]. Further studies showed the great potential of HYB to weld together up to three dissimilar BMs, plus the FIM, and perform butt, slot and fillet welds. In addition, a set of equations were derived for tuning the HYB process parameters, such as FIM feed rate, pin rotation speed and overall energy consumption [138]. Therefore, HYB has become a mature technique in terms of process protocol and welding capability.

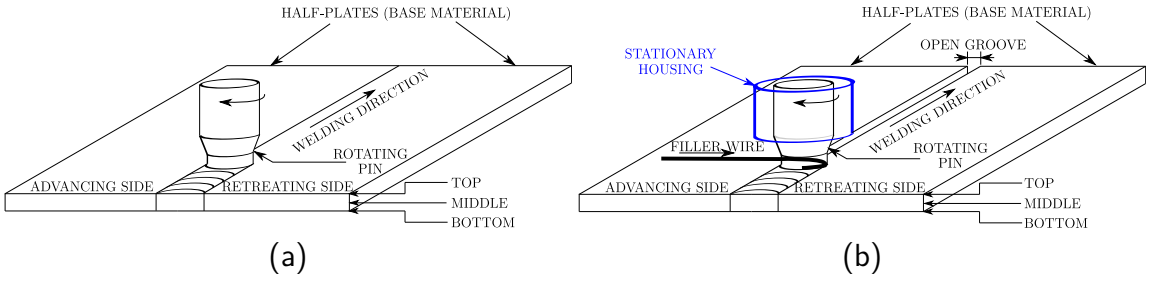

Figure 3.1. Schemes of the welding the processes. (a) Friction stir welding. (b) Hybrid metal and extrusion bonding, which relies on a continuous extrusions and injection of a filler wire into the open groove to consolidate the weld.

The beneficial effects of the FIM on the bending strength, tensile strength and fatigue life of a 2 mm thick similar AA6060-T6 HYB butt weld filled with AA6082-T4 were experimentally investigated [139, 140]. Therein, a minor kissing bond defect

between base and filler materials was unveiled, which promoted the crack initiation, especially during the three-point bending test. Nevertheless, the bending response of the joint approached that of the BM [139]. Furthermore, the yield stress (YS) evaluated through tensile tests was close to that reported for an equivalent FSW AA6082-T6 butt weld and superior to that of a FSW AA6061-T6 butt weld. Finally, the high-cycle fatigue property of this joint was characterised. After the removal of the kissing bond area, the joint exhibited the highest number of cycles to failure under constant amplitude loading, with respect to the comparable FSW and fusion welded joints considered in the literature [141].

Solid-state welding also aims at mitigating the thermal gradient effects involved, nevertheless it is impossible to completely eliminate them. Consequently, RS arises in correspondence of the weld heterogeneously distributed [129], giving rise to different RS types according to their length-scales [34, 142]. As a consequence, the influence of RS on the structural integrity has motivated the need of assessing RS also in welded structures [143–145]. Particularly for FSW, several studies have been performed exploiting different experimental methods: XRD [146], synchrotron XRD [147–149], neutron XRD [150, 151], FIB-DIC [148], and nanoindentation [151]. These techniques aim to investigate RS concerning the longitudinal, transverse and normal direction of the weld. Unfortunately, they are expensive, demanding and conditioned by the microstructure and weld material inhomogeneities. Despite this, XRD and neutron XRD have been recently used to investigate RS in an isothermal-FSW stainless steel plate [152]. Given that the dominant component of RS is that aligned with the weld direction, i.e. the longitudinal one, as investigated in [146, 147, 150, 152], it is of interest to study only this component.

According to Section 2.1, the CM evidently appears suitable to evaluate the longitudinal component of the RS. If the CM cut is orthogonally performed with respect to the direction of the of the weld, the longitudinal welding-induced RS is aligned with the outward normal of the cut surface. For this reason, the CM has been extensively employed to study RS in thin, thick, similar and dissimilar FSW joints. For instance, as concerned aluminium joints, the CM was applied to investigate RS in a 25.4 mm thick dissimilar FSW plate made of AA7050-T7451 and AA2024-T351 [153] and for the RS assessment of a 4 mm and a 8 mm similar AA6061-T6 FSW butt welds [154]. This experimental technique was also exploited to analyse the influence of welding process parameters on the arising of RS [155], where a

set of 4 mm thick similar AA2024-T3 butt welds were considered. Dissimilar joints were also studied using the CM. For instance, the RS assessment was performed on a 2 mm thick plate made of aluminium 5A06 and T2M pure copper [156]. Recently, the RS has been evaluated in a 5 mm thick plate made of AA7075-T6 and AA6061-T6 strengthened with SiO2 nanoparticles [74]. With regard to the FSW manufacturing technology, the CM was employed to investigate the RS induced by the innovative ultrasonic-assisted FSW. In this respect, 3 and 5 mm thick similar AA6061-T6 were considered as a case-study [157, 158].

Besides affecting the structural performance, RS induced by manufacturing processes is responsible for joint distortion as well [159, 160]. In the context of FSW, for instance, the joint distortion of a FSW butt weld on a 3 mm thick plate made of AA6065-T6 was analysed in [161]. This study showed that RS, which peaked at about 200 MPa at the advancing side, generated the peculiar "V-shaped" angular distortion along the traverse direction. A recent research attempted to determine the dependence of the joint distortions upon the FSW welding parameters, i.e. pin rotation speed and welding feed speed [162]. Therein, a set of three FSW butt welds were manufactured on 3 mm thick AA6005-T6 plates, and essentially an "A-like" shape joint distortion was detected. However, earlier findings revealed that for a particular selection of pin rotation speed and welding feed speed, respectively 1200 rpm and 282 mm/min, the joint distortion turned out to be essentially negligible [163]. This was observed on a 6.5 mm thick FSW butt welded AA6061-T6 plate.

This Chapter aims to study and compare the RS arising as a consequence of the two solid-state welding processes just outlined, i.e. FSW and HYB. This aspect is of fundamental importance in order to establish its structural integrity performance and to assess how it performs as compared with the more conventional solid-state weld, i.e. FSW. The full-field RS evaluation of the welds is conducted by employing the CM. Statistical evaluation of errors, due to the mismatch of the RS evaluated on two different faces obtained by the linear cut, is performed and presented. Alongside, a quantitative analysis of the distortion of the FSW and HYB joints is reported. The results of the experimental analysis and comparison between the two case-studies are presented and critically discussed, with particular emphasis on the consequence that RS may have on the integrity properties of the examined welds.

3.2. Fabrication of the Butt-welds

The FSW and HYB butt-welds considered herein were prepared using extruded profiles of the commercial aluminium alloy AA6082-T6 as the BM. For the particular case of HYB, a AA6082-T4 was employed as the FIM. Same materials were previously used by some of the authors of the present research and reported in the literature [164]. The nominal compositions of the base and filler materials are summarised in Table 3.1. The geometry of the plates is depicted in Figure 3.2, while their dimensions are reported in Table 3.2.

Table 3.1. Chemical compositions of the base and filler materials (wt%).

	Si	Mg	Cu	Fe	Mn	Cr	Ti	Zr	B	Other	Al
AA6082-T6 (BM)	1.00	0.65	0.03	0.20	0.50	-	0.02	-	-	-	Balance
AA6082-T4 (FIM)	1.11	0.61	0.002	0.20	0.51	0.14	0.043	0.13	0.006	0.029	Balance

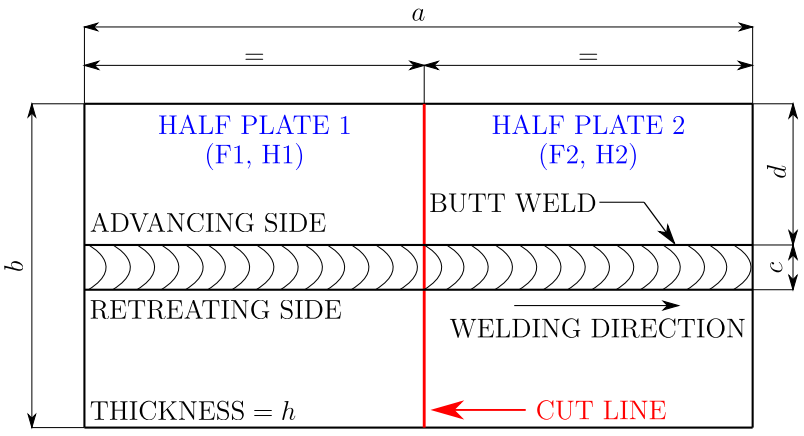

Figure 3.2. Scheme of the plates geometry. Each plate is characterised by a length a, a width b and a thickness h. The butt weld position is indicated by d, whereas its width is denoted by c. According to the CM procedure, the cut line in red, indicates the path followed to cut the plates in half. The cut provided the half-plates F1 and F2, and H1 and H2, for the case of FSW and HYB, respectively.

The employed process parameters used to fabricate the HYB weld are given in Table 3.3. Because of confidentiality issues, the authors could not share the FSW parameters. Nonetheless, the applied welding parameters for HYB and FSW were

Table 3.2. Plates dimensions (mm) in agreement with Figure 3.2.

	a	b	c	d	h
HYB	500	170	14	79	4.2
FSW	770	168	18	70	4

deemed to represent best-practice at the time when the butt welds were manufactured. In particular, the welding parameters were tuned to produce the butt welds meeting all the acceptance criteria for offshore use [164].

Table 3.3. Welding parameters for HYB. Those for FSW are not available due to confidentiality issues.

	Groove Width [mm]	Pin Rotation Speed [rpm]	Welding Feed Speed [mm/min]	Wire Feed Rate [mm/min]	Gross Heat Input [kJ/mm]
HYB	2	350	1080	7500	0.11

The mechanical integrity of two identical HYB and FSW joints were previously investigated through their longitudinal tensile testing [164], and the related results are summarised Table 3.4. Besides, the data regarding the yield stress and ultimate tensile stress can be found in [165–168]. Before being extruded to perform the HYB weld, the wire FIM underwent drawing that reduced its diameter from 1.6 mm to 1.4 mm. As a consequence, the FIM experienced work hardening. For this reason, at room temperature, the FIM is characterised by the highest yield stress as compared with the BM.

With regard to HYB, it should be noted that if the FIM was in the T6 condition, the high temperatures developed within the process zone of the weld would have triggered an overaging effect, which is well known to reduce the tensile strength of the material. Conversely, having the FIM in T4 condition implied that most of the major alloying elements, such as Mg and Si, were in solid solution prior to the welding operation. Therefore, the natural ageing was preserved after the whole process. This ensured superior tensile properties as compared with those that would have been obtained if the FIM was of the same type of the base material (BM). It this respect, the yield stress of the consolidated FIM turned out to be about 70 %

of that of the BM [164, 169].

Table 3.4. Mechanical properties of the joints with respect to the longitudinal direction of the weld (MPa).

	Yield stress	Ultimate tensile stress
HYB	163	254
FSW	175	281

3.3. Application of the Contour Method

The analysed plates were cut in half by means of the CDM Rovella 650© WEDM following the red line in Figure 3.2 at a cut speed of 5 mm/min. The WEDM was equipped with a 0.25 mm diameter brass coated wire whose core composition was CuZn36. The cut of the two plates, respectively HYB and FSW, produced four half-plates. According to Figure 3.2, H1 and H2 indicate the HYB half-plates, whereas F1 and F2 indicate the FSW half-plates. The index P is then defined, which can assume H1, H2, F1 and F2 to refer to a generic half-plate. Accordingly, the cut generated surface of the half-plate P will be denoted by Γ^P.

The measurement of the out-of-plane displacement of Γ^P was carried out using the Hexagon Global S© CMM with a contact probing system. The CMM had a resolution estimated to be 1 µm, whereas the probe was a 1 mm diameter ruby spherical tip. A reference frame $\{O, x, y, z\}$ similar to that in Figure 2.1(a) was defined such that the out-of-plane displacement of Γ^P is oriented with respect to the z-direction, and it will be denoted by u_z^P, according to Section 2.1.

In order to measure u_z^P the CMM followed a raster-scan pattern defined over Γ^P. Such a pattern covered a rectangular grid with a regular 0.75×0.25 mm grid-spacing regarding the x and y-direction, respectively. The grid nodes are identified by the couple of coordinates (x_i, y_i). The same grid-spacing was chosen for each pair of half-plates, given that their dimensions were similar. Thus, a set of four displacement maps was collected: $u_z^{\mathrm{H1}}(x_i, y_i)$, $u_z^{\mathrm{H2}}(x_i, y_i)$, $u_z^{\mathrm{F1}}(x_i, y_i)$, $u_z^{\mathrm{F2}}(x_i, y_i)$. In order to accurately match the axes of the Cartesian coordinate system for the experimental measurement and those of the numerical model, the SVD was exploited, see

Section 2.1.4.

Bivariate splines (Eq. (2.8)) were adopted to interpolate the acquired CMM data $u_z^P(x_i, y_i)$. These splines were of third- and second-order, and had 27 and 7 nodes both concerning the x- and y-direction, respectively. Differently from the traditional application of the CM (Section 2.1), the each pair of half-plates was separately analysed – this choice shall be clarified later though. Therefore, the interpolation of $u_z^P(x_i, y_i)$ provided the functions denoted by $\tilde{u}_z^{\mathrm{H1}}(x, y)$, $\tilde{u}_z^{\mathrm{H2}}(x, y)$, $\tilde{u}_z^{\mathrm{F1}}(x, y)$, $\tilde{u}_z^{\mathrm{F2}}(x, y)$.

In order to model the geometrical characteristics of the probed surfaces, the perimeter of the projection of $u_z^P(x_i, y_i)$ onto the x-y plane was computed, and this perimeter enclosed the surface Γ^P. Such a surface was then extruded to generate the three-dimensional solid body, with the actual length of the experimentally tested half-plates 3.2. Subsequently, the generation of the mesh was performed following two steps using Gmsh [170]. Firstly, a mesh was generated over the enclosed surface, where 28 and 160 elements were prescribed concerning the thickness and width of , respectively. The best-practice guidelines recommend to choose a FE size less than a quarter of the spline nodal spacing with respect to both x- and y-direction [95]. The selected number of elements along with the adopted spline nodal spacing complied with such an empirical rule. In addition, a selective mesh refinement was performed in the neighbourhood of the weld region, in order to better capture possible sharp variations of RS. Secondly, the mesh was extruded along the third direction by imposing a finer mesh near Γ^P and coarser far from Γ^P. These steps provided meshes counting 89600 volume elements.

The linear elastic FE simulation was carried out using code_aster [171], a FE open-source code and set according to Section 2.1. In this specific analysis, eight-node brick elements with linear shape functions were utilised in the FE analysis. These elements are called `HEXA8` according to code_aster nomenclature. Since the CM allow to probe RS at the macro scale, the studied aluminium alloys were assumed to be homogeneous and isotropic with Young's modulus and Poisson's ratio $E = 70000\,\mathrm{MPa}$ and $\nu = 0.3$, respectively. The FE simulation was repeated for each half-plate resulting in the following set of RS maps $\sigma_{zz}^{\mathrm{H1}}(x, y)$, $\sigma_{zz}^{\mathrm{H2}}(x, y)$, $\sigma_{zz}^{\mathrm{F1}}(x, y)$, $\sigma_{zz}^{\mathrm{F2}}(x, y)$.

Given that prior the WEDM cut, the couples of cut surfaces Γ^{H1} and Γ^{H2}, and Γ^{F1} and Γ^{F2} shared exactly the same stress state, in correspondence of the discrete surface the back-evaluated RS values must be coincident with each other. As a

consequence, it is appropriate to obtain a unique evaluation of RS for each plate. Thus, the RS estimator for a plate was defined as:

$$\sigma_{zz}^{\mathrm{HYB}}(x,y) = \frac{\sigma_{zz}^{\mathrm{H1}}(x,y) + \sigma_{zz}^{\mathrm{H2}}(x,y)}{2} \tag{3.1}$$

$$\sigma_{zz}^{\mathrm{FSW}}(x,y) = \frac{\sigma_{zz}^{\mathrm{F1}}(x,y) + \sigma_{zz}^{\mathrm{F2}}(x,y)}{2} \tag{3.2}$$

Besides, the standard deviation of the estimators for a generic plate was also computed:

$$U_{zz}^{\mathrm{HYB}}(x,y) = \mathrm{std}(\sigma_{zz}^{\mathrm{H1}}(x,y), \sigma_{zz}^{\mathrm{H2}}(x,y)) \tag{3.3}$$

$$U_{zz}^{\mathrm{FSW}}(x,y) = \mathrm{std}(\sigma_{zz}^{\mathrm{F1}}(x,y), \sigma_{zz}^{\mathrm{F2}}(x,y)) \tag{3.4}$$

Much attention was devoted to three critical paths over the surface Γ^P: the top (T), the middle thickness (M) and the bottom (B), see Figure 3.1. According to Eq. (3.5)-(3.6), an index K is defined, which can assume T, M and B, to refer to a generic path. Then the RS $\sigma_{zz}^P(x,y)$ was extracted along a line positioned at each path K. In the following, $\sigma_{zz}^P(K)$ and $U_{zz}^P(K)$, will denote the RS σ_{zz}^P and U_{zz}^P extracted along the path K. Therefore for each path K, the related RS estimator is:

$$\sigma_{zz}^{\mathrm{HYB}}(K) \pm U_{zz}^{\mathrm{HYB}}(K) \tag{3.5}$$

$$\sigma_{zz}^{\mathrm{FSW}}(K) \pm U_{zz}^{\mathrm{FSW}}(K) \tag{3.6}$$

Although the common protocol of the CM requires a single FE simulation is required, it does not provide a measure of uncertainty on the final result. The followed procedure slightly differed from such a protocol, given that the cut surfaces were independently analysed, thus maintaining the displacement maps as separated. As a consequence, two related FE were required for each pair of half plates. Although this was a slight, yet elaborated, variation to the common CM procedure, it directly provided the evaluation of the RS (Eq. (3.1)-(3.2)), along with a practical measure of uncertainty related to the repeatability (Eq. (3.3)-(3.4)), which, enables accounting for the RS distribution scatter across the examined samples.

3.4. Results and Discussion

3.4.1. Weld Distortions

According to the literature, research has been devoted to study the relationship between FSW-induced RS and the correspondent weld distortion. Identifying such a relationship, however, was out of the scope of the present research. Nevertheless, it is useful to report a qualitative analysis of the distortions of the welds and discuss how they compared with the results from the literature.

The boundary of the x-y plane projection of $u_z^P(x_i, y_i)$ was numerically post-processed to calculate the joint distortion of the considered samples, in correspondence of the cut surfaces Γ^P. Figure 3.3(a) shows the boundaries of Γ^{H1} and Γ^{F1}, whereas Figure 3.3(b) shows those of Γ^{H1} and Γ^{F1}. The HYB distortion was characterised by the deflection angle γ, evaluated with respect to the middle-thickness line Figure 3.3. The angle γ turned out to be equal to 181.62° for H1 and 181.07° for H2. The HYB half-plates exhibited a "V-shaped" distortion, which could be quantified by the peak-to-valley range of the middle-thickness lines. These ranges are about 1 mm and 0.8 mm for H1 and H2, respectively. Although Γ^{H1} and Γ^{H2} were the counterpart of each other, thus the peak-to-valley ranges should be equal, the authors believe that this discrepancy could be justified by an uneven RS relaxation effect. Moreover, the approximately 0.5° of distortion present between the two cut plates is negligible and can be due to several factors which are not strictly related to the RS evaluation conducted in this study, i.e. inhomogeneous plastic deformation in the transverse direction along the welding direction, CMM errors which become amplified through the calculation process. As far as F1 and F2 are considered, their joint distortion are so modest that it was not possible to detect them according to the CMM resolution (Figure 3.3). Therefore, at this qualitative level of analysis the deflection angle γ and the peak-to-valley range, can be assumed as 180° and 0 mm for both F1 and F2. This negligible distortion was also observed in the $306 \times 306 \times 6.5$ mm AA6061-T6 FSW butt weld analysed in [163]. Despite the plate geometry analysed in this work is slightly different to that of [163], the results are in good agreement with each other. Interestingly, a characteristic "V-shaped" distortion was also encountered with regard to a $600 \times 315 \times 3$ mm AA6065-T6 FSW butt weld found in the literature [161].

The higher HYB joint distortion may reasonably prompt to think that the HYB

plate accommodated higher RS than the FSW plate. Nevertheless, the authors of [162] identified an inverse relationship between joint distortion and RS for a FSW $220 \times 110 \times 3\,\text{mm}$ AA6005-T6 plate. From a practical viewpoint, they showed the more distortion the less RS. Thus, no qualitative results about RS can be fairly inferred with regard to the HYB butt weld.

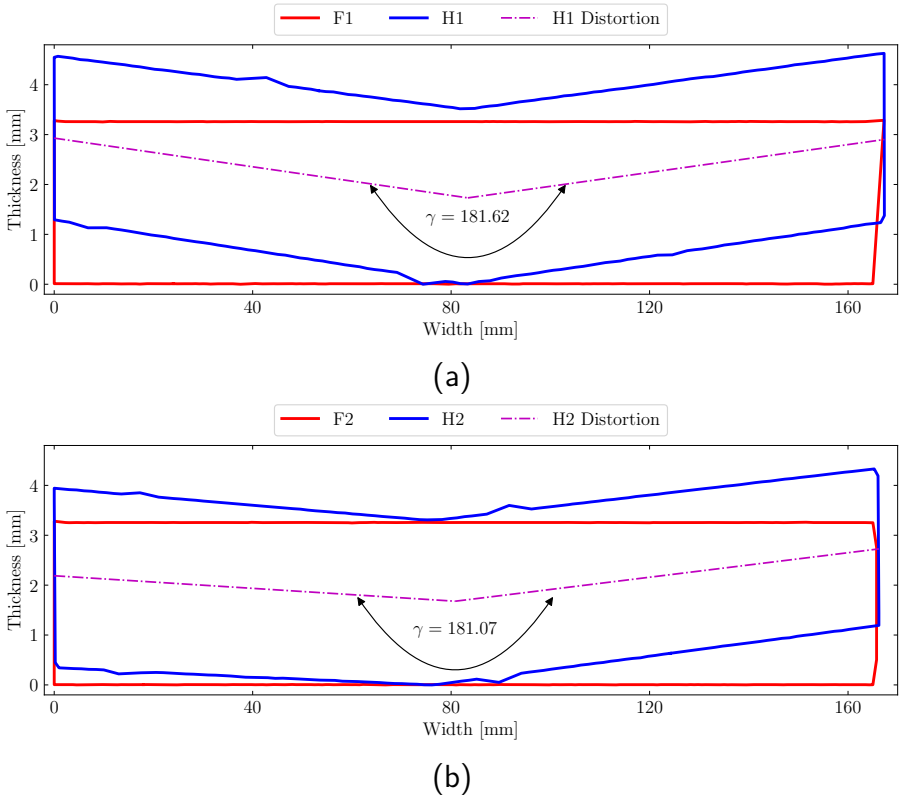

Figure 3.3. Boundaries of the cut surfaces Γ^P and characterisation of the transverse distortion for the HYB half-plates. The blue and the red lines represents the boundaries of the HYB and FSW half-plates, respectively. The purple dot-dashed line is the middle-thickness line of the HYB half-plates where the deflection angle γ was evaluated. (a) Boundaries of Γ^{F1} (red) and Γ^{H1} (blue). (b) Boundaries of Γ^{F2} (red) and Γ^{H2} (blue). The cut surfaces Γ^{H1} and Γ^{H2} exhibited a more pronounced traverse distortion as compared with their FSW counterpart Γ^{F1} and Γ^{F2}.

3.4.2. Residual Stress

Figure 3.4(a)-(d) show the displacement maps of the elastic relaxation $u_z^P(x_i, y_i)$, for H1, H2, F1 and F2. Since the z-position of the reference measurement plane x-y is arbitrary, the data were translated to the mean value of the correspondent [95]. Quantitatively, the relaxation ranged from $-0.07\,\text{mm}$ to $0.06\,\text{mm}$ for H1 and H2, and from $-0.05\,\text{mm}$, $0.04\,\text{mm}$ for F1 and F2. In addition, the measured relaxations $u_z^{\text{F1}}(x_i, y_i)$ and $u_z^{\text{F2}}(x_i, y_i)$ are consistent both in order of magnitude and in shape with those observed for the $300 \times 206 \times 4\,\text{mm}$ AA6061-T6 FSW butt welds in [154]. Herein, the weld region is enclosed between $x = 79\,\text{mm}$ and $x = 93\,\text{mm}$ for H1 and H2 half-plates, while for F1 and F2 this region lies between $x = 70\,\text{mm}$ and $x = 88\,\text{mm}$. Inside these regions it is possible to recognise $u_z^P(x_i, y_i) < 0$. This physically means that the material over each cut surface Γ^P relaxed due to the presence of tensile RS and therefore the cut surface was subjected to out-of-plane displacement pointed in the inward surface direction. Despite the shape of the relaxation of H1 and H2 is similar to that of F1 and F2, HYB half-plates show higher magnitudes of relaxation. Consequently, higher tensile RS was already expected to be present in H1 and H2. These qualitative observations are further corroborated by the CM evaluations.

The application of the CM provided the contours (Figure 3.5(a)-(d)) of the RS induced by the two solid-state welding methods employed, namely $\sigma_{zz}^P(x, y)$, for H1, H2, F1 and F2. All these contours clearly identify a predominant tensile RS inside the weld and milder compressive RS in the regions outside the weld. The RS distributions of F1 and F2 agree both in terms of trend and order of magnitude with other comparable CM evaluations for 4 mm thick aluminium FSW butt welds, already present in the literature [154, 155]. In particular, regarding the order of magnitude, RS over the cut surfaces varying from $-150\,\text{MPa}$ to $100\,\text{MPa}$ were reported in [155], and from $-50\,\text{MPa}$ to $100\,\text{MPa}$ were reported in [154]. Furthermore, the contour maps highlight higher RS in H1 and H2, thus confirming the initial observation with regard to the relaxation ranges. Although the contours give a global picture of the RS over the cut surface, they do not capture the RS distribution with respect to the plate width. For this reason, the aforementioned three paths, T, M and B, were drawn onto the cut surfaces Γ^P, see Figure 3.5(a)-(d). These paths were conceived to follow the distortion of the half-plates. Therefore, those regarding H1 and H2 show the distinctive "V-like" shape, while those for F1 and F2 are horizontal. The RS extracted along these paths, $\sigma_{zz}^P(K)$, are depicted in the

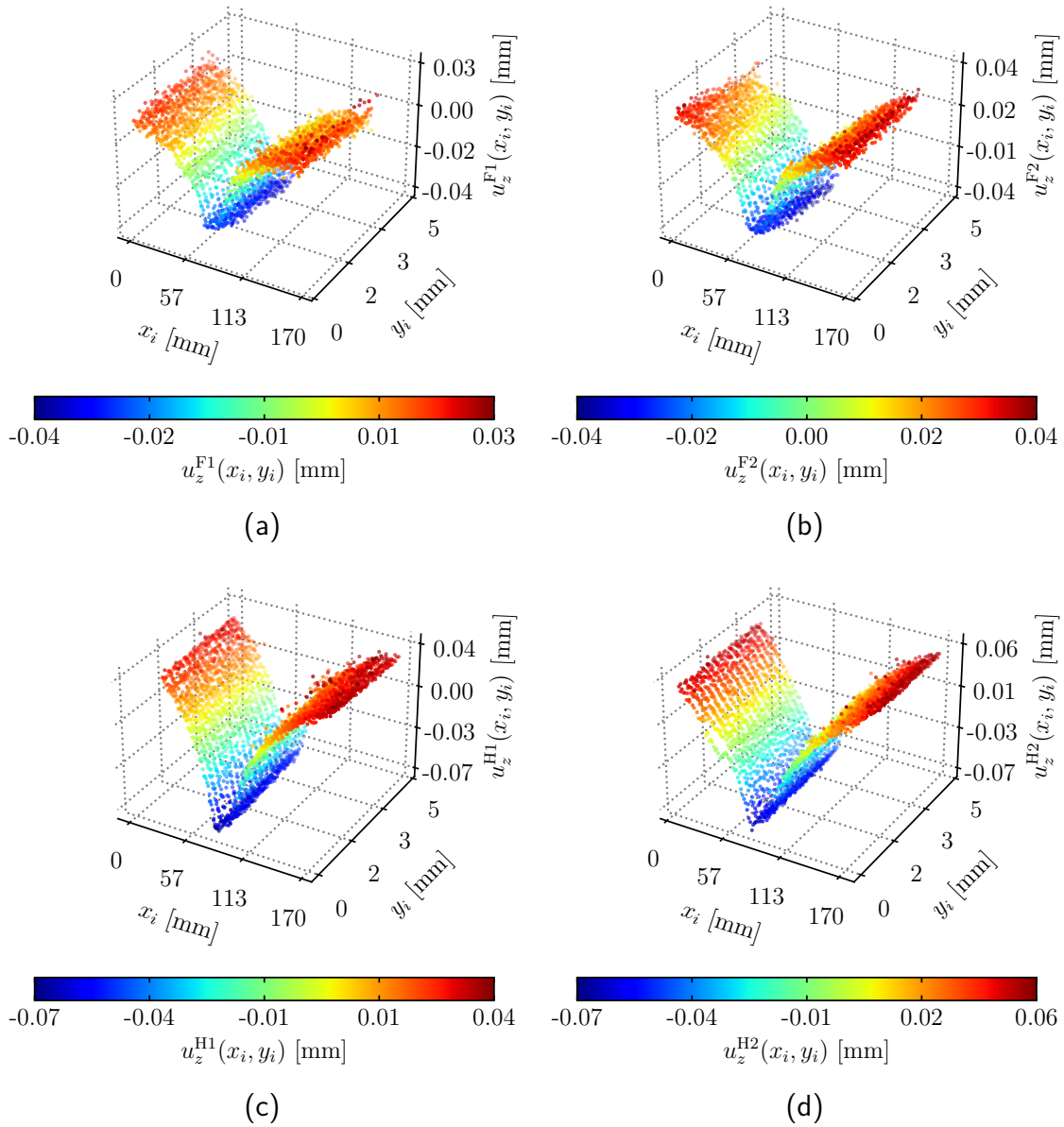

Figure 3.4. CMM-measured displacement maps $u_z^P(x_i, y_i)$ of the elastic relaxation of P-th cut surface. All the half-plates were subjected to a relaxation which forced the material inward the correspondent cut surface. (a) P=H1 (b) P=H2 (c) P=F1 (d) P=F2.

upper part of Figure 3.5(a)-(d), as well as the weld position and the indication of the advancing side (ADVS) and retreating side (RETS). The T and B paths, were taken slightly offset from the upper and the lower edges of the half-plate, given that inaccuracies might arise as a consequence of unstable spline interpolation at those boundaries. Moreover, the higher the spline order, the higher the instability is [172]. On the top of that, the RS evaluation might be less reliable near the perimeter of the cut surfaces for two main reasons: i) WEDM cutting artefacts; ii) a minor elastic deformation about the y-direction due to the elastic relaxation of the traverse component of RS.

The outcomes just outlined, however, only represent an intermediate result of the CM evaluation. In fact, these findings need to be combined using Eq. (3.1)-(3.2) along with the evaluation of the associated uncertainties given by Eq. (3.3)-(3.4) to obtain a more accurate evaluation of the RS fields for the two welds.

The evaluated RS, extracted along the K path, $\sigma_{zz}^{P}(K)$, are depicted in Figure 3.6 and in Figure 3.7, for the FSW and HYB half-plates, respectively. As far as the FSW butt weld is concerned, the paths revealed the classical "M-shaped" pattern. This qualitative trend agrees well with earlier experimental studies on aluminium butt welds, 3 mm thick [147], 4 mm thick [155], 8 mm thick [146], and also with steel butt welds 3 mm thick [150, 152]. Intriguingly, a similar "M-shaped" pattern was retrieved for the HYB butt weld. Generally, all the paths show high tensile RS within the weld and a steep decrease moving towards the BM, reaching a compressive RS state, similarly to what reported by other researchers [155]. The observed oscillations right outside the weld could have been arisen for two main reasons: i) the heterogeneous intrinsic RS present in the BM due to its manufacturing process (extrusion), thus producing low-frequency oscillations; ii) the interpolation of the CM measurement noise which generates high-frequency oscillations. The latter class of fluctuations would have been reduced if the CMM measurements had been smoothed more. However, this in practice cannot be carried out since it would smear the significant gradients of RS, particularly those in correspondence of the weld affected zone; for instance the "M-like" shape inside the weld would have been aliased. For this reason, it appears to be very important to judiciously choose the most appropriate interpolation functions. According to Eq. (3.5)-(3.6), the RS estimators and their associated interval bands are depicted in Figures 3.6-3.7. These bands account for the CM evaluation repeatability and represent the values in the range $\sigma_{zz}^{\mathrm{HYB}}(K) \pm$

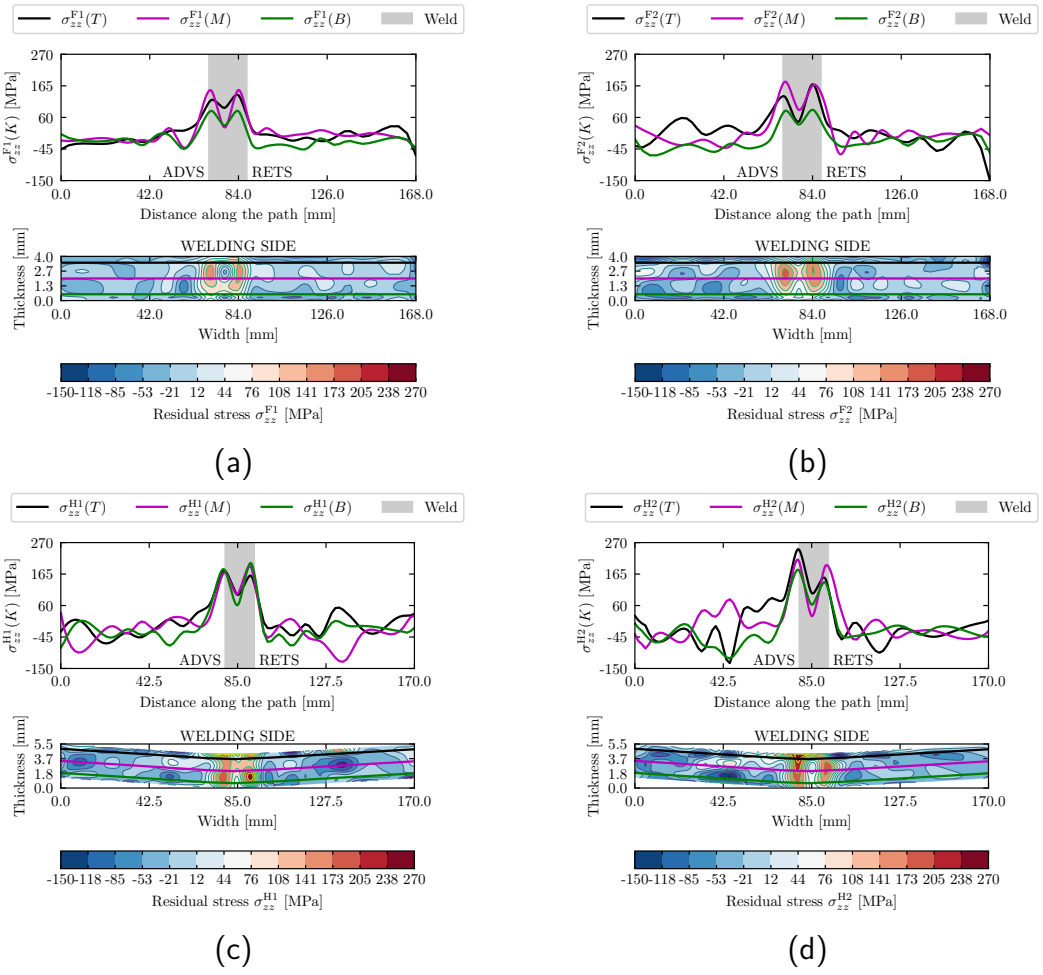

Figure 3.5. Results of the CM RS evaluation of each of the P-th cut surface. Each picture shows in its lower part the contour of the RS over the related cut surface Γ^P, namely $\sigma^{\mathrm{H1}}_{zz}(x, y)$. Three paths were drawn onto Γ^P to extract the RS data. With respect to the thickness of Γ^P, these path are located at its top (T), middle-thickness (M) and bottom (B). The RS extracted along the three paths are named for $K = T, M, B$, and are shown in the upper part of each picture. Black, purple and green were respectively associated to the T, M and B paths in order to distinguish the extracted RS data. In addition, the advancing side (ADVS), the retreating side (RETS) and the weld position are indicated. (a) $P = \mathrm{F1}$. (b) $P = \mathrm{F2}$. (c) $P = \mathrm{H1}$. (d). $P = \mathrm{H2}$.

$U^{\mathrm{HYB}}_{zz}(K)$ (Figure 3.6) and $\sigma^{\mathrm{FSW}}_{zz}(K) \pm U^{\mathrm{FSW}}_{zz}(K)$ (Figure 3.7). Therefore, the bands provide a confidence interval of approximately 68%. Given that narrower bands are

present on the edge of the ADVS and RETS, in such regions the evaluated $\sigma_{zz}^{\mathrm{FSW}}(K)$ and $\sigma_{zz}^{\mathrm{HYB}}(K)$ accurately predict the RS. However, wider bands were encountered in correspondence of the ADVS and RETS peaks. Although a better estimation of the confidence intervals, may improve the accuracy of the estimated errors, for instance by performing more WEDM cuts on the same butt weld, the computed confidence intervals are appropriate to discuss the following result. To date, the user could refer to [98], in which the uncertainty quantification of the CM was addressed.

With regard to FSW, the combination of the peripheral speed of the pin and the welding feed speed is generally responsible for asymmetries between the two observed tensile RS peaks in correspondence of the heat-affected zone, in terms of magnitude. Physically, the relative speeds between the rotating pin and the BM is different between the ADVS and RETS sides, respectively. This intrinsic feature of the FSW process, produces higher frictional heat at the RETS and consequently more severe temperature gradients at the ADVS. Therefore, higher RS should be expected at the ADVS [153–156]. Concerning the M and B paths, Figure 3.6(b)-(c), this behaviour is little intense, leading to comparable magnitudes of the two tensile peaks. However, the confidence interval of the M path does not preclude a more accentuated asymmetric behaviour. Conversely, the asymmetry is evident for the T path. Because of the analogy between HYB and FSW processes, the asymmetric tangential speed at the ADVS and RETS lead to the same conclusion for the HYB, conceptually. Nonetheless, such an asymmetry is exacerbated (Figure 3.7(a)-(c)).

A critical comparison between the two analysed welds can underline several similitudes and differences. The M path of the FSW joint is the most critical, followed by T and B, in terms of highest magnitudes of RS, see Figure 3.6(d). On the other hand, in the HYB joint the RS intensity within the weld is comparable, see Figure 3.7(d). Quantitatively, the predicted RS peaked along the path M at the ADVS and at the RETS at about $165 \pm 15\,\mathrm{MPa}$ and $155 \pm 5\,\mathrm{MPa}$ as concerns the FSW butt weld, whereas at $205 \pm 25\,\mathrm{MPa}$ and $180 \pm 5\,\mathrm{MPa}$ for the HYB butt weld. In order to provide an immediate comparison between these findings and those from the literature, Table 3.5 was reported to summarise the welding process, the material, the welding parameters and the magnitudes of the RS peaks detected along the middle-thickness path (M). The present findings regarding the FSW sample concur well with those reported in the literature concerning the butt welds performed on AA6061-T6 plates $270 \times 250 \times 8\,\mathrm{mm}$ and $300 \times 206 \times 4\,\mathrm{mm}$ plates, even though dif-

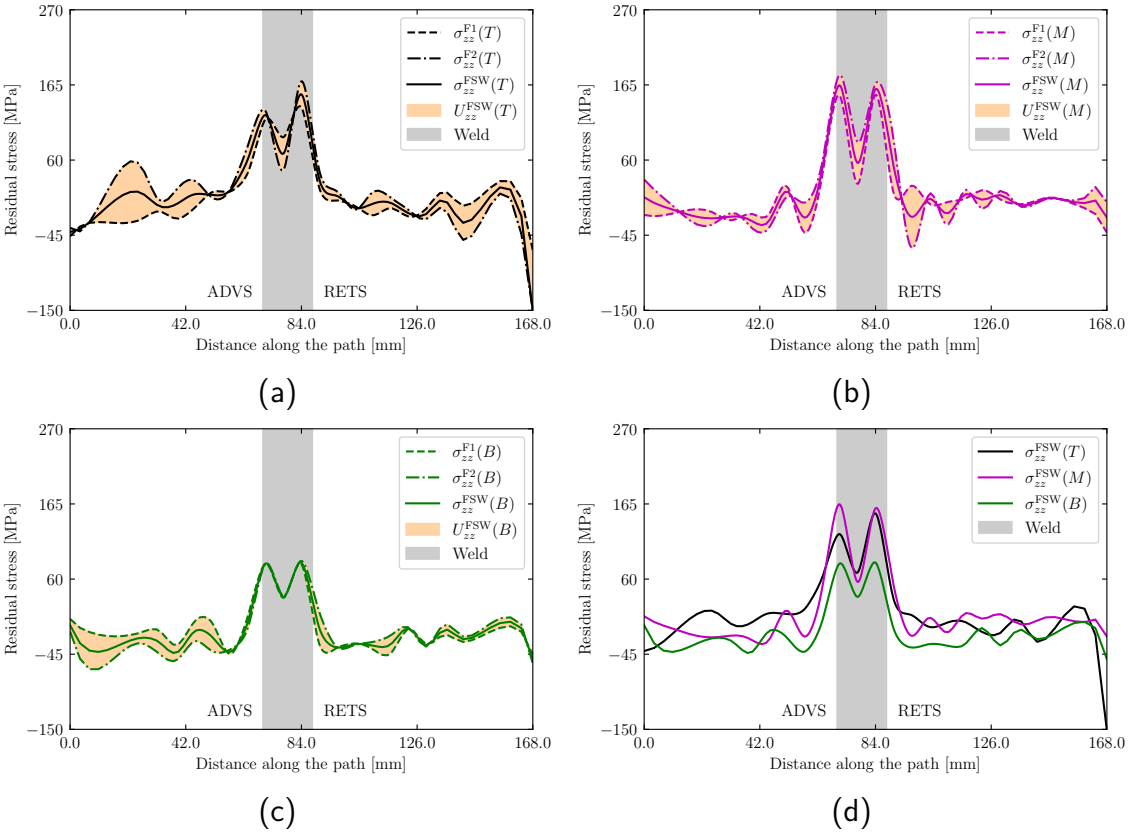

Figure 3.6. RS estimator for the K-path $\sigma_{zz}^{\mathsf{FSW}}(K)$ and associated uncertainty $U_{zz}^{\mathsf{FSW}}(K)$ computed from $\sigma_{zz}^{\mathsf{F1}}(K)$ and $\sigma_{zz}^{\mathsf{F2}}(K)$. The filled area enclosed between $\sigma_{zz}^{\mathsf{F1}}(K)$ and $\sigma_{zz}^{\mathsf{F2}}(K)$ graphically represents $U_{zz}^{\mathsf{FSW}}(K)$, thus corresponding to a confidence interval of about 68% for $\sigma_{zz}^{\mathsf{FSW}}(K)$. (a) $K = T$. (b) $K = M$. (c) $K = B$. (d) Comparison between the RS estimators $\sigma_{zz}^{\mathsf{FSW}}(K)$ evaluated along the path $K = T, M, B$. The ADVS, the RETS and the weld position are also indicated.

ferent aluminium alloys were involved [154]. In [154], although the classical "M-like" shape pattern was not clearly distinguishable, analogous paths were analysed. In the totality of RS profiles reported in the literature, the middle-thickness path (M) turned out to be the most critical, followed by T and B, for both the analysed 4 mm and 8 mm thick FSW butt welds, which agrees with the results presented herein. Notwithstanding the different thickness, the RS magnitudes reached at the ADVS and RETS were respectively 163 MPa and 100 MPa for the 8 mm thick plate, with a very good agreement with those found in the present study of the FSW. Similar

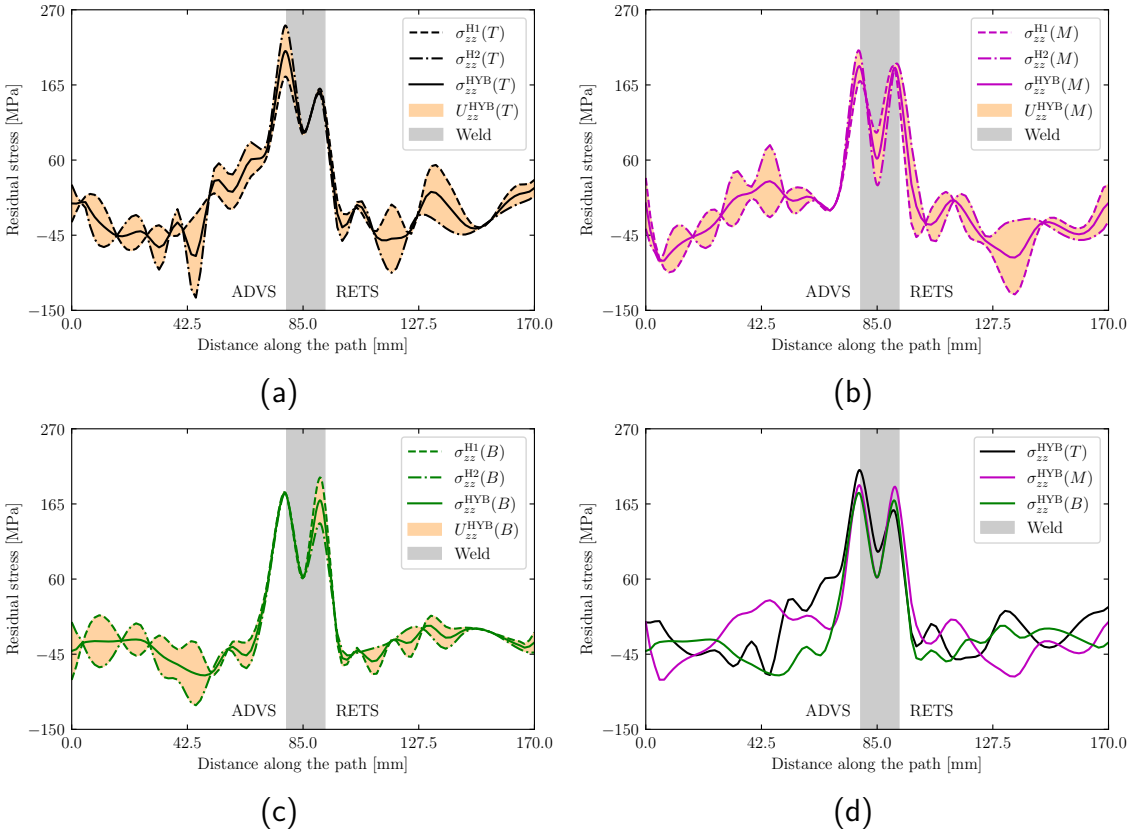

Figure 3.7. RS estimator for the K-path $\sigma_{zz}^{\mathrm{HYB}}(K)$ and associated uncertainty $U_{zz}^{\mathrm{HYB}}(K)$ computed from $\sigma_{zz}^{\mathrm{H1}}(K)$ and $\sigma_{zz}^{\mathrm{H2}}(K)$. The filled area enclosed between $\sigma_{zz}^{\mathrm{H1}}(K)$ and $\sigma_{zz}^{\mathrm{H2}}(K)$ graphically represents $U_{zz}^{\mathrm{HYB}}(K)$, thus corresponding to a confidence interval of about 68% for $\sigma_{zz}^{\mathrm{HYB}}(K)$. (a) $K = T$. (b) $K = M$. (c) $K = B$. (d) Comparison between the RS estimators $\sigma_{zz}^{\mathrm{HYB}}(K)$ evaluated along the path $K = T, M, B$. The ADVS, the RETS and the weld position are also indicated.

agreement was also found with regard to the 4 mm thick plate from the literature, the RS peaked at the ADVS and RETS at 154 MPa and 130 MPa, respectively. Additional support to this conclusion is provided by the results reported in [155], in which a full-factorial sensitivity analysis of FSW was addressed. The aim of the study was to establish the influence of the welding parameters on the induced RS. In particular, a set of AA2024-T3 200 × 30 × 4 mm FSW butt welds was analysed. Peak values of 145 MPa and 125 MPa were observed at the ADVS and RETS, respectively. Such values were retrieved by combining a fixed welding feed speed of

140 mm/min with different pin rotation speeds from 800 rpm to 1600 rpm. Despite the different material employed in [155], the reported peak values are remarkably close to those found in the present study.

Finally, from the cross-comparison between the HYB- and the FSW-induced RS along the T, M and B paths, it is evident that HYB produced higher RS magnitudes into the region affected by the joining process.

Apart from the continuous extrusion and injection of the filler material, HYB and FSW are two similar friction-driven welding methods. With regard to FSW, earlier studies has demonstrated the dependence of RS upon welding parameters and materials being welded [153–156, 74]. Although the present research was the first attempt to characterise RS in HYB, the authors believed that different materials (BM and FIM) and HYB welding parameters might influence the RS distribution as well.

It is worth observing that if unprocessed plates were involved, i.e. neither extrusion nor solid-state welding, in principle the CM would have provided null residuals stress over the WEDM cut surface. Nonetheless, measurement noise would have affected the CM evaluation by generating fluctuations in the final result. On the other hand, if the plates were extruded but not solid-state welded, only the RS inherited from the extrusion process would have been retrieved. Still, measurement noise might have affected the RS evaluation.

Table 3.5. Summary of the comparable CM evaluations of RS.

Welding process	Material	Butt-weld dimension [mm]	Pin rotation speed [rpm]	Welding feed speed [mm/min]	Wire feed rate [mm/min]	ADVS peak [MPa]	RETS peak peak [MPa]	Source
FSW	AA6061-T6	$300 \times 206 \times 4$	800	300	-	154	130	[154]
FSW	AA6061-T6	$270 \times 250 \times 8$	500	250	-	163	100	[154]
FSW	AA2024-T3	$200 \times 30 \times 4$	800-1600	140	-	145	125	[155]
FSW (this study)	AA6082-T6	$770 \times 168 \times 4$	-	-	-	165 ± 15	155 ± 5	Figure 3.6(b)
HYB (this study)	AA6082-T6 (Parent) AA6082-T4 (Filler)	$500 \times 168 \times 4$	350	1080	7500	205 ± 25	180 ± 5	Figure 3.7(b)

3.4.3. Origin of Residual Stress

Light onto the origin of longitudinal RS in welding, or more specifically in FSW, was already shed [173]. To interpret this phenomenon, it is useful to consider small element volume of the BM AA6082-T6 located at the edge of the weld nugget. As far as the FSW is concerned, the blue solid line in Figure 3.8 describes a schematic example of the temperature-stress history experienced by this volume. Figure 3.8 also reports for the BM examples of tensile, σ_y^+, and compressive, σ_y^-, yield stress curves as a function of the temperature (black solid line). Besides, $T_{\max}$ indicates the maximum temperature which is expected to occur within the weld nugget. In addition, T_{melt} is the melting temperature of the BM. Essentially, the approaching heat source (rotating pin) ensures that the considered volume of material increases its temperature (line AB in Figure 3.8) and expands. This thermal expansion is constrained by the surrounding material and therefore a compressive RS is generated within the material at the heat source (line AB). Due to the combination of high temperature and high compressive RS, the material reaches the compressive yield stress (point B) and deforms plastically (line BC). As the heat source overtakes the same volume of material (line BC), a cooling process begins (point C) which makes the material to shrink (line CD). This shrinkage is again constrained by the surrounding material and therefore tensile stress takes place in the weld (point D). Given that the contraction occurs in the linear elastic regime of the material, in this instance, the amount of tensile stress generated is higher than the compressive stress arose in the expansion stage. For this reason, tensile RS is originated at the end of the welding (point D). In the particular case of FSW, the heat source is not uniform within the welding due to the higher friction generated at the material/tool interface, and for this reason two tensile peaks are generally found (Figure 3.6).

Regarding the HYB technique, same considerations done for the FSW still hold. Yet, a significant difference is made by the presence of a second material (FIM) showing different elastoplastic properties (black dashed yield stress curve in Figure 3.7 when compared with the BM. It is important to remark that the FIM had undergone a drawing process before being employed in the welding process. Such a wire-pre-process introduces work hardening that increased its yield stress level. Nevertheless, the work hardening effect is cancelled as soon as the material enters the rotating pin, thanks to the dynamic recovery triggered by the temperatures reaching values as high as 400 °C [174]. Therefore, most of the ductility of the FIM

is regained and the yield stress becomes lower than that of the BM. Furthermore, $T_{\max}$ and T_{melt} are supposed to be equal for the FIM. The latter temperature is generally true, while the former might differ for the two processes. In fact, under some circumstances HYB might generate slightly lower temperatures than those of FSW [175]. Therefore, this physical interpretation can be considered valid as long as the difference between the maximum temperature due to HYB, and FSW, is negligible – it is the case of the present study. The red dashed line in Figure 3.8) represents a schematic temperature-stress cycle of a small volume of FIM AA6082-T4, which is located at the edge of the weld nugget. In this study, the FIM shows a substantially lower yield stress. This characteristic makes sure that during the material expansion stage (line $A'B$), the FIM builds up compressive stresses that are lower than what the BM would do (line AB). As a consequence, during the cooling stage (line $C'D'$), the constrained material shrinkage allows the RS to reach higher values of tension (point D').

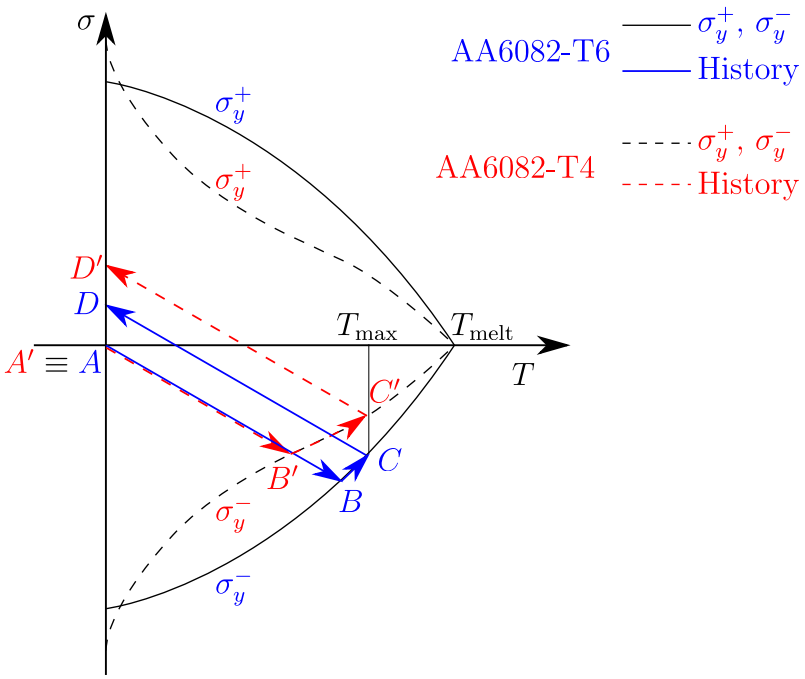

Figure 3.8. Temperature-stress cycles experienced by a small volume element of: BM AA6082-T6 (blue solid line $ABCD$) and FIM AA6082-T4 (red dashed line $A'B'C'D'$). In both cases, such a volume element is assumed to be located at the edge of the weld nugget. The yield stress vs. temperature curve of the two materials are reported.

3.5. Conclusions

This part of the dissertation considered a 4 mm thick AA6082-T6 HYB butt weld performed using an AA6082-T4 as the FIM, and a 4 mm thick AA6082-T6 FSW butt weld. Specifically, the full-field longitudinal RS state of these joints was evaluated employing the CM. In particular, this research has addressed for the first time the RS evaluation in a HYB butt weld.

The RS analysis unveiled similar RS distributions for both HYB and FSW butt welds, i.e. tensile RS in the weld region and milder compressive RS within the neighbouring regions of the weld affected zone. The RS distributions exhibited two tensile peaks respectively observed at the ADVS and the RETS of the FSW butt welds, describing the peculiar "M-like" shape RS pattern, also seen in other previous studies reported in the literature. Additionally, the "M-like" shape RS pattern was retrieved for the HYB butt weld. A key difference was revealed between the two welds, that is significantly higher tensile RS magnitudes present in the HYB, both at the ADVS and RETS. Quantitatively, the RS attained its maximum at the ADVS at 205 ± 25 MPa. By contrast, the FSW joint showed its maximum value of tensile RS at the ADVS as high as 165 ± 15 MPa. Additionally, this study showed a methodology to obtain an appraisal of the uncertainty involved in the RS assessment, which is, however, limitedly focussed on the repeatability of the CM evaluation. Although the guidelines in Ref. [95, 96] were followed to fit the displacement data, they still retain much arbitrariness in the selection of the fitting parameters. This, in turn, hampers the quantification of the uncertainties arising from this crucial stage of the CM. Therefore, a probabilistic and systematic strategy to address this limitation must be sought.

A physical interpretation has been proposed to explain the discrepancy in terms of RS magnitude between the analysed welds. In this respect, the higher RS in the HYB butt weld stemmed from the presence of the softer FIM, which is exclusively employed in HYB. In fact, the lower yield stress threshold of the AA6082-T4, as compared with the AA6082-T6, was responsible for a lower compressive RS when the material reached the maximum temperature during the process. Such a lower value then induced a higher tensile RS when the material cooled down and the constrained shrinkage process occurred.

Alongside, a qualitative analysis of the weld inherent transverse distortion was

performed, even though it was ancillary to the present RS investigation. Despite this, a distinctive "V-like" distortion for the HYB weld of approximately 1.4°was detected. On the other hand no significant joint distortion was observed for the FSW.

The results presented herein will definitively be helpful to develop new strategies to mitigate the presence of RS and thus improving the structural integrity performance of HYB welded structures.

4. Gaussian Process Regression Uncertainty Quantification for the Contour Method

The present chapter addresses the issues of quantifying the uncertainty arising from the fitting stage of the CM. In particular, GPR is harnessed to replace traditional splines. Since the uncertainty quantification reduces to a FE Monte Carlo simulation, which may be relatively computationally demanding, an optimisation strategy is presented to accelerate its accomplishment.

4.1. Introduction

Besides the numerous RS assessments for FSW joints and HYB butt-welds reviewed in the previous chapter, the CM has found a number of applications into a variety of problems where the evaluation of RS was sought. For instance, the CM was applied to investigate RS: due to different manufacturing processes [176–178]; due to surface treatments [179, 172]; in axisymmetrical components [180–182]; in fusion-welded materials [183–187]. Due to the relatively young age of the CM, however, little research has been devoted to the problem of uncertainties arising throughout the RS evaluation process.

Although and rough appraisal of the repeatably for the CM can be attained using the strategy presented in Section 3.3, the problem of uncertainty related to the numerical manipulation of the experimentally measured displacement data has been only preliminary addressed by Olson et. al [98]. The authors of [98] accounted for two crucial sources of error: (i) the uncertainty in the experimentally acquired displacement data; (ii) the uncertainty arising as a result of the displacement data interpolation and smoothing. These uncertainties propagate throughout the opera-

tional steps of the CM and eventually influence the results in terms of RS. Specifically, the source of error (i) can be separated as the sum of two contributions: the material surface roughness and the intrinsic measurement error of the used measuring machine (usually CMM), and thus being of stochastic nature. As such, this error can be quantified using a Monte Carlo approach, for a certain number of trials (numerical calculations), by adding a normally distributed random noise to the measured data. The error induced by (i) is then given by the standard deviation of RS from the Monte Carlo simulations. The source of error labelled as (ii) derive from the arbitrariness in selecting the bivariate spline parameters (nodes & degree, see Eq. (2.8)) to interpolate the out-of-plane displacement data [95, 96, 98]. Some identification strategies of the bivariate splines are proposed by the literature, based upon a trade-off between appropriately capturing the gradients of the measured out-of-plane deformation and filtering out the noise already expected in the experimental measurement. It is evident how the process is massively influenced by the operator's experience when selecting the fitting parameters involved, i.e. the degree of the tensor product surface and the number of nodes of the interpolation grid, see Eq. (2.8).

For this reason, a robust evaluation of the error due to the interpolation process becomes unrealistic in the present state-of-the-art. Assuming that the interpolation process was sufficiently accurate, possibly owing to the user's experience in the use of the CM, Olson et al. proposed to assess the model error by retrieving the standard deviation of the RS computed by the CM for different values of the spline fitting parameters [98]. Finally, the total error due to the contribution of error (i) & (ii) was essentially computed by taking their quadrature. Indeed, the method was applied on a set of five Al alloy samples. More recently, this approach has been successfully applied also to an aluminium T-section, a stainless steel dissimilar plate, a titanium electron beam welded plate, stainless steel and a nickel based alloy forged specimen [188].

As outlined before, the Olson et al. state-of-the-art approach to uncertainty quantification may be effective in some cases. Nevertheless, it would seem to lack robustness, thus highly affected by user's experience and confidence. Earlier research proposed a more sophisticated identification strategy of the fitting parameters [99]. Still, it appeared deterministic and influenced by user's experience and ability.

An advanced and powerful solution to tackle the central issue of the uncertainty

quantification involved in the CM is through GPR [102, 110] whose details are illustrated in Section 2.4. Additionally, this GPR can automatically account for the inherent uncertainty of the input dataset. Only in recent years, GPR has been applied to tackle engineering problems, demonstrating its effectiveness to model random phenomena pertinent to this field. For instance, the engineering research community applied GPR to predict the water inflow into tunnels [189], the maximum vertical displacement of a bridge subjected to uncertain load conditions [190], the mechanical response of marine structures [191], pile load bearing capacity [192], blast-induced ground vibration [193], and in control theory [194]. The application of GPR in solid mechanics is still extremely scarce, but its potential is incredibly attractive, particularly if applied to uncertainty determination problems or material response behaviour.

A GPR-based approach is developed herein to address the outstanding issue related to the uncertainty quantification of RS when employing the CM. Dedicated optimisation tools are used to minimise the influence of user's confidence on the numerical processing of the input displacement data [195], and to devise a robust and accurate calculation framework. Firstly, GPR is applied to fit the out-of-plane displacement of each half-plate obtained from the CMM measurement after the material cut, and to quantify the uncertainty of the fitting predictions. Following, each half-plate is independently analysed, thus deliberately differing from the traditional CM procedure; effects of this choice will be discussed. In this respect, each fitted displacement is used as a boundary condition in a separate numerical simulation to carry out the RS evaluation of the correspondent half-plate. In particular, a Monte Carlo approach is pursued to numerically perturb the boundary condition (prescribed displacement) according to the GPR-estimated uncertainty. This allowed for the appraisal of the uncertainty associated with the local perturbation. Eventually, the results of the Monte Carlo trials are statistically post-processed to obtain both the expected value of RS and its associated uncertainty. Alongside, an optimised open-source computational framework is set up to reduce the computation effort required to run the Monte Carlo simulations. In order to demonstrate the effectiveness of the presented methodology, a friction stir welded (FSW) aluminium plate is considered as a case study. Eventually, the performance of the proposed method is critically discussed, and the major improvements with respect to the previously used evaluation framework are highlighted.

4.2. Case Study: Friction Stir Welded Al Butt Joint

An AA6082-T6 FSW butt-welded plate was used to developed the present GPR-based uncertainty quantification framework for the CM. This plate was similar to that previously analysed in Chapter 3. Figure 4.1 shows the characteristics of the FSW butt-welded joint studied here such as, the dimensions of the analysed plate, the position of the ADVS & RETS, and the welding direction. Whilst Table 4.1 gives the chemical composition of the parent Al alloy.

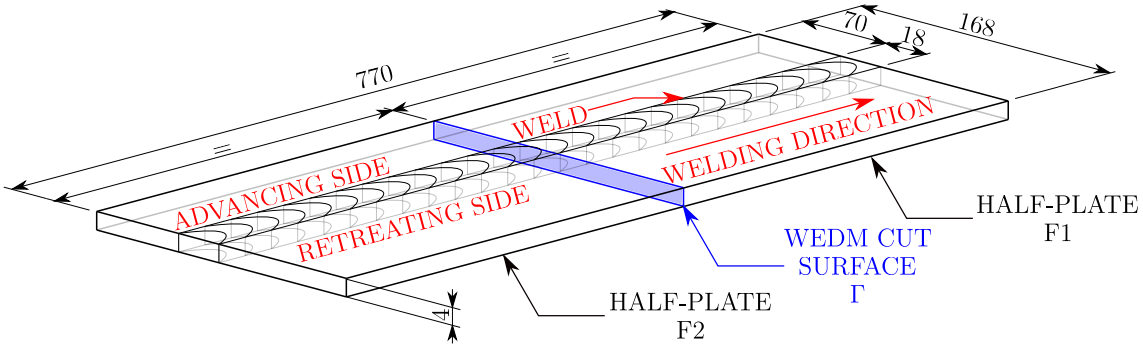

Figure 4.1. The FSW plate analysed to develop the GPR-supported uncertainty quantification approach (dimensions in mm). According to the CM procedure the plate was cut in half in correspondence of the WEDM cut surface Γ, which is indicated in blue.

Table 4.1. Chemical composition of the commercial AA6082-T6 (wt%).

	Si	Mg	Mn	Fe	Cu	Ti	Al
AA6082-T6	1.00	0.65	0.50	0.20	0.03	0.02	Balance

A CDM Rovella 650© WEDM was used to section the FSW plate along its cross section. The reference position of the cut surface is shown in Figure 4.1. The cut was performed using a wire of 0.25 mm diameter. The core of the WEDM wire was composed of CuZn36, whereas its external surface was brass-coated. The cut provided two half-plates, namely F1 and F2 (Figure 4.1) of equal length and two correspondent cut surfaces, Γ^{F1} and Γ^{F2}. Low-roughness of the cut surfaces was ensured by selecting a WEDM cutting speed of 5 mm/min.

The obtained surfaces Γ^{F1} and Γ^{F2}, exhibited the expected out-of-plane deformation promoted by this stress relaxation, and its measurement was carried out by

means of a Hexagon Global S© CMM equipped with a 1 mm diameter ruby spherical probe. Two identical raster-scan patterns were defined both Γ^{F1} and Γ^{F2}, which consisted of a regular grid whose nodal spacing was 0.75×0.25 mm. Following the defined raster-scan pattern, the CMM probed the cut surfaces Γ^{F1} and Γ^{F2} giving the displacement maps shown in Figure 4.2(a) and Figure 4.2(b). In Figure 4.2, the couple (x_i, y_i) refers to the coordinates of the grid node where the displacement value of $u_z^{F1}(x_i, y_i)$ and $u_z^{F2}(x_i, y_i)$ were sampled. The index h assumes either F1 or F2 to refer to the out-of-plane displacement of Γ^{F1} and Γ^{F2}, respectively.

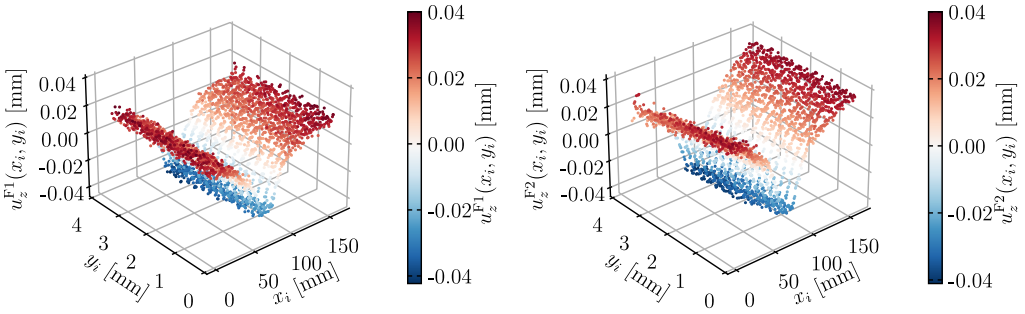

Figure 4.2. Maps z_h of the out-of-plane displacement elastic relaxation of the FSW half-plates. (a) $h = \text{F1}$ (2) $h = \text{F2}$.

4.3. Computational Procedure

4.3.1. Finite Element Model

Aiming at performing the CM evaluation of RS in the FSW plate, a three-dimensional FE model was realised, Figure 4.3. The dimensions and geometry of the model were chosen to comply with those of the obtained half-plates (Figure 4.1). The 3D domain was then discretised with 70200 tetrahedral elements opportunely distributed over the domain, using Gmsh [170]. In this instance, $\mathbf{x}_m$ indicates the mesh node lying on Γ^h, whose coordinates are (x_m, y_m). The simulation was set according to Section 2.1. Additionally, since a purely elastic relaxation is hypothesised,

the material was assumed as homogeneous and linear elastic. Therefore, $E = 70000$ MPa and $\nu = 0.3$ were adopted respectively as Young's modulus and Poisson's ratio.

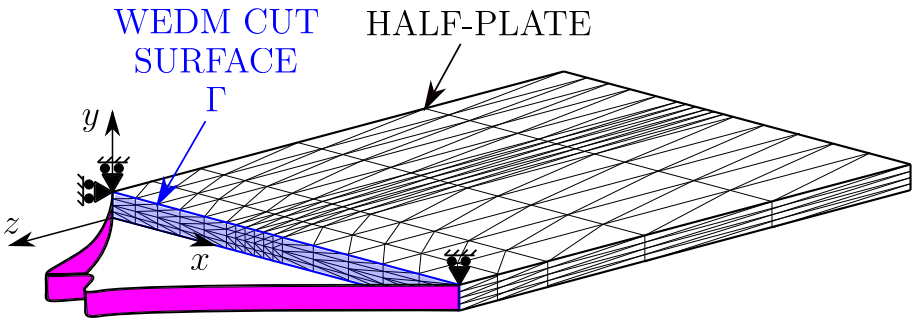

Figure 4.3. Exemplification of the FE model used for both the half-plates F1 and F2. The discretisation was performed using tetrahedral elements. The interpolated displacement (not to scale) is indicated in purple and it was applied on the cut surface Γ as a boundary condition. The additional boundary conditions prescribed on the corners of the cut surface are used to suppress rigid body motions. Note that the mesh is not representative of that employed in the present analysis.

Similarly to Chapter 3, the current application of the CM differed from its standard protocol [41] as the half-plates F1 and F2 were independently analysed. The method devised herein may overcome the possible arbitrariness of the averaging operation, provided that the presence of shear residual stress is negligible. Indeed, the method would compensate for the mismatch in terms of stress that the cut could have been induced since, in principle, each half-plate had shared the same RS state before the cut occurred.

4.3.2. Application of Gaussian Process Regression

The present section illustrates the application of GPR to interpolate the out-of-plane displacement maps obtained from the CMM measurements. For the sake of clarity, the following explanation will refer to a single half-plate. Nevertheless, in this case study the procedure was replicated identically to the counterpart.

Let us assume that the point of this topography form the dataset as indicated in Eq. (2.54). As shown in Section 2.4, the topography $u_z^h(x_i, y_i)$ is modelled according

to Eq. (2.55), hence:

$$u_z^h(\mathbf{x}_i) = f_h(\mathbf{x}_i) + \varepsilon; \quad \varepsilon \sim \mathcal{N}(0, \sigma_n^2) \tag{4.1}$$

where $\mathbf{x}_i = \begin{bmatrix} x_i & y_i \end{bmatrix}$, and σ_n^2 is the variance of the zero-mean noise ε. A GP was placed over f_h, see Eq. (2.56). Since no prior is available for the present model, the mean was assumed as $\mathcal{M} = 0$. This assumption is not limiting as most of the kernels used in practice are universal approximators: the space of functions that can be represented with a GP with a universal kernel is dense with respect to the space of continuous functions. Therefore, GPR holds the ability to approximate arbitrarily well any continuous function over a compact set [196]. Although various kernels are available in the literature [102], because of its universality and wide use [196], the squared exponential kernel was considered. This kernel is obtained from Matern's (Eq. (2.57)) upon setting $\xi \to \infty$, thus resulting in:

$$\mathcal{K}(\mathbf{x}_i, \mathbf{x}_j) = C \, \exp\left[- \frac{(\mathbf{x}_i - \mathbf{x}_j)^\top (\mathbf{x}_i - \mathbf{x}_j)}{l^2} \right]. \tag{4.2}$$

where C and l are the hyperparameters. In this case, the hyperparameters has a physical interpretations. Particularly, C represents how much the function f_h can span. By contrast, given two generic samples $u_z(\mathbf{x}_i)$ and $u_z(\mathbf{x}_j)$, l is the length scale that quantifies how much the correlation between these samples decreases as their relative distance $\sqrt{(\mathbf{x}_i - \mathbf{x}_j)^\top (\mathbf{x}_i - \mathbf{x}_j)}$ increases. For the sake of convenience, these are collected in the vector $\boldsymbol{\theta} = \begin{bmatrix} C & l \end{bmatrix}^\top$. Essentially, the application of GPR replaces the splines of Eq. (2.8) in the fitting stage of the CM.

The computational implementation of GPR was performed using the Python module scikit-learn [195]. Upon incorporating the additive noise $\sigma_n = 1$ µm for the input dataset, the optimised hyperparameters for f_1 and f_2 were identified by maximising the log-likelihood of the given dataset Eq. (2.58). Alongside, the identified hyperparameters for both f_1 and f_2 are given in Table 4.2.

It should be noted that σ_n quantifies the noise embedded in the experimental measurements. This assumption aimed to estimate the uncertainty due to the CMM resolution and the surface roughness of the cut surface. A potential strategy to estimate this value more accurately would be the roughness measurements of a WEDM cut on a stress-free component, which is directly linked with the WEDM process

Table 4.2. Hyperparameters for f_1 and f_2.

	C^* [mm^2]	l^* [mm]
f_1	0.0134	8.07
f_2	0.0193	8.68

parameters. Conversely, the CMM uncertainty is provided by the manufacturer. Through the newly proposed approach the user has the capability to promptly set different values of σ_n when this parameter in not known to evaluate its impact of the evaluated RS field.

Once the hyperparameters were computed, the prior mean and the kernel function were determined. Therefore, it was possible to make predictions at a new input $\mathbf{x}_m$, in terms of mean $\mathcal{M}_p(\mathbf{x}_m)$ and variance $\mathcal{K}_p(\mathbf{x}_m, \mathbf{x}_m)$ given by Eq. (2.60)-(2.61).

4.3.3. Computation of Residual Stress

Exploiting the hyperparameters in Table 4.2, the displacement map was forecast at every mesh node $\mathbf{x}_m$ belonging to the cut surface of the related half-plate. The predicted value of the z-displacement at $\mathbf{x}_m$ will be denoted by u_m – the superscript z of the out-of-plane displacement is implicitly assumed. This prediction is characterised by its expected value $\mathbb{E}[u_m]$ and its uncertainty $\sqrt{\mathbb{V}[u_m]}$, i.e. the standard deviation. According to Eq. (2.60))-(2.61), these quantities are given by $\mathbb{E}[u_m] = \mathcal{M}_p(\mathbf{x}_m)$ and $\sqrt{\mathbb{V}[u_m]} = \sqrt{\mathcal{K}_p(\mathbf{x}_m, \mathbf{x}_m)}$. Hence, the displacement boundary condition of the FE model shown in Figure 4.3 was prescribed by imposing $\mathbb{E}[u_m]$ at the related mesh node $\mathbf{x}_m$ along the z-direction.

The FE simulation was conducted exploiting the open source FE platform FEniCS [197, 198]. The distinctive code structure of the FEniCS solver allowed for the access and manipulation of the linear FE system of equations, according to the Direct Stiffness Method (or displacement based method):

$$\mathbf{K}\mathbf{u} = \mathbf{b} \tag{4.3}$$

where $\mathbf{K}$ is the model stiffness matrix, $\mathbf{u}$ is the unknown nodal displacement vector

and $\mathbf{b}$ is the known force vector. The expansion of Eq. (4.3) leads to:

$$\begin{bmatrix} k_{11} & k_{12} & k_{13} & k_{14} & \dots & k_{1s} & k_{1r} & \dots & k_{1N} \\ k_{21} & k_{22} & k_{23} & k_{24} & \dots & k_{2s} & k_{2r} & \dots & k_{2N} \\ k_{31} & k_{32} & k_{33} & k_{34} & \dots & k_{3s} & k_{3r} & \dots & k_{3N} \\ k_{41} & k_{42} & k_{43} & k_{44} & \dots & k_{4s} & k_{4r} & \dots & k_{4N} \\ \vdots & \vdots & \vdots & \vdots & \ddots & \vdots & \vdots & \vdots & \vdots \\ k_{s1} & k_{s2} & k_{s3} & k_{s4} & \dots & k_{ss} & k_{sr} & \dots & k_{sN} \\ k_{r1} & k_{r2} & k_{r3} & k_{r4} & \dots & k_{rs} & k_{rr} & \dots & k_{rN} \\ \vdots & \vdots & \vdots & \vdots & \vdots & \vdots & \vdots & \ddots & \vdots \\ k_{N1} & k_{N2} & k_{N3} & k_{N4} & \dots & k_{Ns} & k_{Nr} & \dots & k_{NN} \end{bmatrix} \begin{bmatrix} u_1 \\ u_2 \\ u_3 \\ u_4 \\ \vdots \\ u_s \\ u_r \\ \vdots \\ u_N \end{bmatrix} = \begin{bmatrix} b_1 \\ b_2 \\ b_3 \\ b_4 \\ \vdots \\ b_s \\ 0 \\ \vdots \\ 0 \end{bmatrix} \tag{4.4}$$

where the i-th row of the system is associated with a specific degree of freedom (DOF) of each node of the model, in total N. Note that the following explanation still holds regardless of the order of the rows in Eq. (4.4). For the sake of clarity, the DOFs of the problem are sorted as shown in Eq. (4.4), i.e. the non-zero $b_i \, \forall \, i = 1, 2, \dots, s$ at those DOFs where a displacement boundary condition was imposed. Conversely, the null entries $b_i \, \forall \, i = r, \dots, N$ correspond to the unconstrained DOFs. After the application of the boundary conditions, i.e. the displacement boundary condition and the additional boundary conditions to prevent rigid body motions (Figure 4.3), Eq. (4.4) is conveniently transformed as:

$$\begin{bmatrix} 1 & 0 & 0 & 0 & \dots & 0 & 0 & \dots & 0 \\ 0 & 1 & 0 & 0 & \dots & 0 & 0 & \dots & 0 \\ 0 & 0 & 1 & 0 & \dots & 0 & 0 & \dots & 0 \\ 0 & 0 & 0 & 1 & \dots & 0 & 0 & \dots & 0 \\ \vdots & \vdots & \vdots & \vdots & \ddots & \vdots & \vdots & \vdots & \vdots \\ 0 & 0 & 0 & 0 & \dots & 1 & 0 & \dots & 0 \\ k_{r1} & k_{r2} & k_{r3} & k_{r4} & \dots & k_{rs} & k_{rr} & \dots & k_{rN} \\ \vdots & \vdots & \vdots & \vdots & \vdots & \vdots & \vdots & \ddots & \vdots \\ k_{N1} & k_{N2} & k_{N3} & k_{N4} & \dots & k_{Ns} & k_{Nr} & \dots & k_{NN} \end{bmatrix} \begin{bmatrix} u_1 \\ u_2 \\ u_3 \\ u_4 \\ \vdots \\ u_s \\ u_r \\ \vdots \\ u_N \end{bmatrix} = \begin{bmatrix} 0 \\ 0 \\ 0 \\ \mathbb{E}[u_4] \\ \vdots \\ \mathbb{E}[u_s] \\ 0 \\ \vdots \\ 0 \end{bmatrix} \tag{4.5}$$

The $N \times N$ matrix on the left-hand side of Eq. (4.5) is the modified stiffness matrix, and it is named as $\mathbf{K}'$. The right-hand side of this equation consists of the modified

load vector, which is labelled as $\mathbf{b}'$. Herein, load is intended in its broad sense as it embodies the knowledge of the imposed nodal displacements $\mathbb{E}[u_m]$. For the particular problem presented here, the first three rows of Eq. (4.5) are associated to the constrained DOFs by the nodal boundary conditions employed to cancel rigid body motions, i.e. $u_i = 0 \,\forall\, i = 1, 2, 3$. The rows from 4 to s are related to the z-DOFs of the mesh nodes $\mathbf{x}_m$ belonging to the cut surface Γ^h. Therefore, the corresponding equations give $u_i = \mathbb{E}[u_i] \,\forall\, i = 4, \ldots, s$.

The numerical rearrangement just outlined enabled all the known quantities involved in the model to be gathered in a single vector, i.e. that on the right-hand side of Eq. (4.5). Such a unique characteristic of the system in Eq. (4.5) permitted a random disturbance vector to be introduced on the right-hand side of Eq. (4.5), thus perturbing the imposed boundary conditions:

$$\begin{bmatrix} 1 & 0 & 0 & 0 & \ldots & 0 & 0 & \ldots & 0 \\ 0 & 1 & 0 & 0 & \ldots & 0 & 0 & \ldots & 0 \\ 0 & 0 & 1 & 0 & \ldots & 0 & 0 & \ldots & 0 \\ 0 & 0 & 0 & 1 & \ldots & 0 & 0 & \ldots & 0 \\ \vdots & \vdots & \vdots & \vdots & \ddots & \vdots & \vdots & \vdots & \vdots \\ 0 & 0 & 0 & 0 & \ldots & 1 & 0 & \ldots & 0 \\ k_{r1} & k_{r2} & k_{r3} & k_{r4} & \ldots & k_{rs} & k_{rr} & \ldots & k_{rN} \\ \vdots & \vdots & \vdots & \vdots & \vdots & \vdots & \vdots & \ddots & \vdots \\ k_{N1} & k_{N2} & k_{N3} & k_{N4} & \ldots & k_{Ns} & k_{Nr} & \ldots & k_{NN} \end{bmatrix} \begin{bmatrix} u_1 \\ u_2 \\ u_3 \\ u_4 \\ \vdots \\ u_s \\ u_r \\ \vdots \\ u_N \end{bmatrix} = \begin{bmatrix} 0 \\ 0 \\ 0 \\ \mathbb{E}[u_4] \\ \vdots \\ \mathbb{E}[u_s] \\ 0 \\ \vdots \\ 0 \end{bmatrix} + \begin{bmatrix} 0 \\ 0 \\ 0 \\ N(0, \mathbb{V}[u_4]) \\ \vdots \\ N(0, \mathbb{V}[u_s]) \\ 0 \\ \vdots \\ 0 \end{bmatrix} \tag{4.6}$$

The non-zero entries of the disturbance vector are given by a Gaussian random noise having variance equal to $\mathbb{V}[u_m]$, over the prediction $\mathbb{E}[u_m]$. By defining $\mathbf{b}_p$ as the disturbance vector, Eq. (4.6) is contracted as follows:

$$\mathbf{K}'\mathbf{u} = \mathbf{b}' + \mathbf{b}_p \tag{4.7}$$

The system in Eq. (4.7) was repeatedly solved for both the half-plates F1 and F2 as in a standard Monte Carlo simulation. Aiming at optimising the overall computational process of the simulation, the LU-factorisation of $\mathbf{K}'$ was computed only once and then employed for the computation of the nodal displacements in each simulation of the Monte Carlo approach. Subsequently, through Eq. (4.3) the nodal

reaction were computed. Lastly, the RS was evaluated.

The total number of simulations M was arbitrarily set to 1000. Each i-th simulation provided the full-field RS over the correspondent cut surface Γ^{F1} and Γ^{F2}, namely $\sigma^{(i)}_{zz,1}(x,y)$ and $\sigma^{(i)}_{zz,2}(x,y)$. Following, $\sigma^{(i)}_{zz,1}(x,y)$ and $\sigma^{(i)}_{zz,2}(x,y)$ were collated in the set $R^{(i)}(x,y)$ (the dependence on the coordinates is omitted for each $\sigma^{(i)}_{zz,k}$ to lighten the notation, whereas it is kept for $R^{(i)}(x,y)$ to explicitly indicate the dependence of $R^{(i)}$ on the spatial coordinates):

$$R^{(i)}(x,y) = \{\sigma^{(1)}_{zz,1}, \sigma^{(1)}_{zz,2}, \sigma^{(2)}_{zz,1}, \sigma^{(2)}_{zz,2}, \ldots, \sigma^{(i)}_{zz,1}, \sigma^{(i)}_{zz,2}\} \tag{4.8}$$

As mentioned in Chapter 3, before the WEDM cut occurred, the cut surfaces Γ^{F1} and Γ^{F2} had been the counterpart of each other and, in principle, had shared exactly the same RS state. Hereafter, the cut surface will univocally be indicated as Γ. Furthermore, the related RS state of Γ at the i-th iteration will be denoted by $\sigma^{(i)}_{zz}(x,y)$ and its associated uncertainty by $U^{(i)}_{zz}(x,y)$. According to the set of results $R^{(i)}(x,y)$ (Eq. (4.8)), the expected RS stress (mean) $\sigma^{(i)}_{zz}(x,y)$ and $U^{(i)}_{zz}(x,y)$ were computed by means of:

$$\sigma^{(i)}_{zz}(x,y) = \mathbb{E}[R^{(i)}(x,y)] \tag{4.9}$$

$$U^{(i)}_{zz}(x,y) = \sqrt{\mathbb{V}[R^{(i)}(x,y)]} \tag{4.10}$$

where the operators $\mathbb{E}[\square]$ and $\mathbb{V}[\square]$ act as pointwise with respect to each mesh node $(x_m, y_m) \in \Gamma$. As common in the FE post-processing, $\sigma^{(i)}_{zz}$ and $U^{(i)}_{zz}$ were interpolated among the mesh nodes to obtain their full-field maps over Γ. Such an interpolation, was performed *after* the application of $\mathbb{E}[\square]$ and $\mathbb{V}[\square]$ (Eq. (4.9)-(4.10)). These computations, led to the final result:

$$\sigma^{(i)}_{zz}(x,y) \pm U^{(i)}_{zz}(x,y) \tag{4.11}$$

Given that $U^{(i)}_{zz}(x,y)$ is the standard deviation of the expected value of RS, it represents a confidence interval of approximately 68%.

The number of trials for the Monte Carlo simulation was set to 1000. However, the convergence of the simulation was periodically monitored through the following

residual indicator:

$$\gamma_i = \frac{\|\sigma_{zz}^{(i-1)}(x,y) - \sigma_{zz}^{(i)}(x,y)\|_1}{\|\sigma_{zz}^{(i-1)}(x,y)\|_1} \tag{4.12}$$

where $\sigma_{zz}^{(j)}(x,y)$ is the expected value in Eq. (4.9) calculated at the j-th iteration, and $\|\cdot\|_1$ is the 1-norm pointwisely computed with respect to each mesh node $(x_m, y_m) \in \Gamma$:

$$\|\sigma_{zz}^{(j)}(x,y)\|_1 = \sum_{m \in S} |\sigma_{zz}^{(j)}(x_m, y_m)| \tag{4.13}$$

Therefore, Eq. 4.12 gives:

$$\gamma_i = \frac{\sum_{m\in\Gamma} |\sigma_{zz}^{(i-1)}(x_m,y_m) - \sigma_{zz}^{(i)}(x_m,y_m)|}{\sum_{m\in\Gamma} |\sigma_{zz}^{(i-1)}(x_m,y_m)|} \tag{4.14}$$

In this regard, the convergence could be considered as reached when γ_i is less than a threshold value γ_{th} opportunely selected.

The developed computational framework is briefly illustrated in Algorithm 1. Additionally, Algorithm 1 allows for certain flexibility in computing RS. In this instance, if the uncertainty quantification were of marginal interest for the users, they would perform the GPR on the input displacement data, impose $\mathbf{b}_p = \mathbf{0}$ and run Algorithm 1 once. In this case, the convergence check would not be required. Alternatively, the user would perform GPR only to smooth the experimental dataset disregarding the uncertainty quantification and pursue the traditional CM procedure.

It is important to mention that the computation of the standard deviation as in Eq. (4.10) may overestimate the uncertainty compared to the standard CM procedure, in particular instances. Moreover, probed samples containing relevant amount of shear residual stress may induce an out-of-plane displacements mismatch between the two cut surfaces. In the present case-study, the residual shear stress is thought to play a negligible role, although not fully confirmed, so a first estimate of the sample repeatability error was sought. As introduced in Section 3.3, this error allows taking into account potential RS distribution scatter across the probed samples. This uncertainty could be reduced if more samples of the same plate were available. Unfortunately, this aspect could not be verified, given the limited number of data (only two cut surfaces). Therefore, a reliable estimate of the error due to the analysis of multiple samples, i.e. the repeatability error [199, 188] could not be accomplished.

In this instance, the overestimation of the uncertainty provided by Eq. (4.10) could be seen as a means to compensate for: i) the averaging uncertainty that is often underestimated or neglected when pursuing the standard CM procedure; ii) the mismatch in terms of RS that may arise over the cut surface of each half-plate as a result of the WEDM cut. Nevertheless, the authors' aim is to propose an alternative approach that is sufficiently flexible to be applied under different circumstances.

Algorithm 1 Monte Carlo Finite Element Simulation.

Require: Hyperparameters for both f_1 and f_2
Require: Suppress rigid body motions
Assemble Stiffness Matrix $\mathbf{K}$
Stiffness Matrix modification: $\mathbf{K} \rightarrow \mathbf{K}'$
LU factorisation of $\mathbf{K}'$
for $i \in \{1, 2, \ldots, \mathsf{M}\}$ **do**
    for $k \in \{1, 2\}$ **do**
        — **i-th iteration, k-th half plate** —
        GPR prediction of f_h
        Impose $\mathbb{E}[u_m] \, \forall \, \mathrm{DOF} \in \Gamma$
        Assemble load vector $\mathbf{b}$ ▷ Eq. (4.4)
        Modify load vector $\mathbf{b} \rightarrow \mathbf{b}'$ ▷ Eq. (4.5)
        Perturb $\mathbf{b}'$ by adding $N(0, \mathbb{V}[u_m]) \, \forall \, \mathrm{DOF} \in \Gamma$ ▷ Eq. (4.6)
        Solve linear system $\mathbf{K}'\mathbf{u} = \mathbf{b}' + \mathbf{b}_p$ ▷ Eq. (4.7)
        Compute nodal reactions through $\mathbf{K}\mathbf{u} = \mathbf{b}$ ▷ Eq. (4.3)
        Compute stress $\sigma^{(i)}_{zz,k}(x, y)$
        Gather data in $R^{(i)}(x, y)$ ▷ Eq. (4.8)
    end for
    Calculate the expected RS $\sigma^{(i)}_{zz}(x, y)$ ▷ Eq. (4.9)
    Calculate the uncertainty $U^{(i)}_{zz}(x, y)$ ▷ Eq. (4.10)
    Calculate the residual indicator γ_i ▷ Eq. (4.12)
    — **Check convergence** —
    if $\gamma \leq \gamma_{th}$ **then**
        Stop the simulation
    else
        Continue the simulation
    end if
end for

4.4. Results and Discussion

Figure 4.4 shows the GPR prediction used to process the measured out-of-plane displacement, f_1 and f_2 (Figure 4.2). In this figure, the z-axis reports the predicted value of the displacement, namely $\mathbb{E}[u_m]$, in correspondence of each mesh node (x_m, y_m) belonging to the cut surface Γ^h. The colour bar indicates the uncertainty of the prediction $\mathbb{E}[u_m]$, namely $\sqrt{\mathbb{V}[u_m]}$. Globally, the GPR-estimated uncertainty reaches values around 1.30 µm. However, at $x = 0$ and $x = 168$ mm for both Γ^{F1} and Γ^{F2}, higher values of uncertainty can be noticed. This deviation from the general trend of $\sqrt{\mathbb{V}[u_m]}$ could be attributed to a lack of data at the surface perimeter. Thus, the GPR was able to fit the edge-data but resulting in a higher level of uncertainty, as high as 2.2 µm.

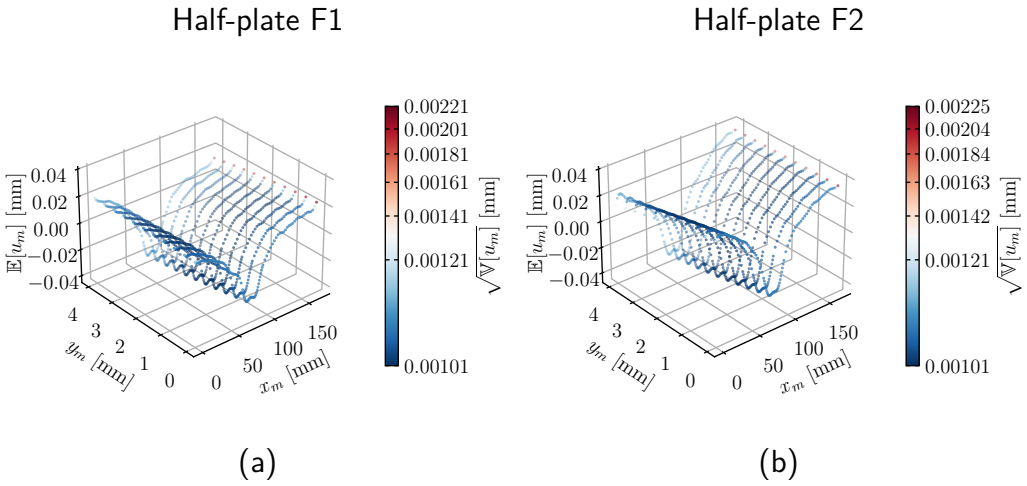

Figure 4.4. GPR prediction of the measured out-of-plane measurement f_h over the mesh nodes of Γ^h. (a) h = F1, half-plate F1. (b) h = F2, Half-plate F2. The colour bar displays the values of the uncertainty of the interpolation over the predicted values.

Referring to a plane section of the data set shown in Figure 4.4(a), taken at $y_m = 2$, Figure 4.5 aims to show more exactly the effectiveness of the GPR. In particular, the red dots refer to the measured experimental data of f_1 (Figure 4.2(a)), while the black dots represent the predicted value $\mathbb{E}[u_m]$. The error bars are the correspondent standard deviations of each mesh point, i.e. $\pm\sqrt{\mathbb{V}[u_m]}$. From the comparison reported in Figure 4.5 it is evident that the GPR successfully fitted the data on the mesh nodes. Besides, the GPR thoroughly reproduced the data trend

and filtered out the high frequency noise that affected the experimental measurement, while at the same time accounting for such a noise through the point-by-point estimate. Furthermore, it is interesting to note that the prescription of $\sigma_n = 1$ µm as the noise level allowed for the automatic detection of the outliers, i.e. the points resulted in being outside the error bars. These points were not meaningful for the regression task, and without GPR they should have been manually removed before the CM evaluation process.

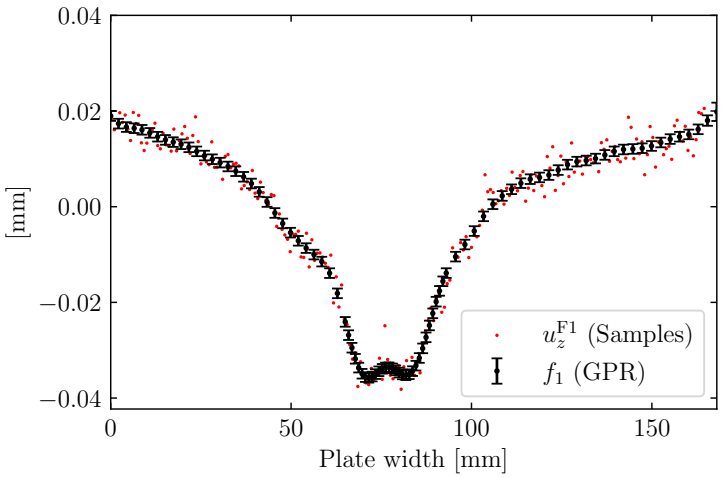

Figure 4.5. Plane section of the 3D map of $\mathbb{E}[u_m]$ (Figure 4.4(a)) taken at $y_m = 2$ and experimental data extracted at $y = 2$. The black dots represent the GPR prediction

The FE Monte Carlo simulation provided the set of results $R^{(\mathsf{M})}(x, y)$ (Eq. (4.8)). The expected value of the RS estimator $\sigma_{zz}^{(\mathsf{M})}(x, y)$ and its associated uncertainty $U_{zz}^{(\mathsf{M})}(x, y)$ were given by Eq. (4.9) and Eq. (4.10), respectively. Hereafter, the superscripted (M) will be dropped to lighten the notation. The contour of $\sigma_{zz}(x, y)$ and $U_{zz}(x, y)$ are depicted in Figure 4.6(a)-(b).

To help visualise the stress distribution within the plate cross-section and appreciate the relevant gradients, three horizontal lines scans (L) were defined over the cut surface Γ (Figure 4.6(a)). Specifically, $L = T$, $L = M$ and $L = B$ refer to the top, middle-thickness and bottom line, located at $y = 4$ mm, $y = 2$ mm, $y = 0$ mm, respectively. Accordingly, $\sigma_{zz}(L)$ indicates the expected value of the RS extracted along the path L. These paths allowed the "M-like" shape RS distribution to be unveiled, see Figure 4.6(c). The figure illustrates the comparison between $\sigma_{zz}(L)$.

Such a characteristic distribution of RS is aligned with earlier findings [154, 155], despite the different interpolation methodology adopted.

As far as the propagated uncertainty is concerned, Figure 4.6(b) shows that $U_{zz}(x, y)$ is less than 16 MPa over most of the cut surface, apart from localised areas near the perimeter of Γ. Most likely, these exceptions are due to edge cutting artefacts which are known to considerably affect measurements in thin parts [172]. Lastly, a considerably high uncertainty was encountered at the top-left corner of Γ. Within this restricted area, $U_{zz}(x, y)$ is about 47 MPa. This could be interpreted as being a result of a lack of data within this localised area. In particular, GPR extrapolates the displacement data at the perimeter of the cut surface, especially at corners, more than it would do over its interior, where a large amount of data is present. Consequently, GPR predicts displacements with higher uncertainty in such regions, giving rise to higher uncertainty in terms of stress as well. Despite this, the presented approach provided reliable results.

The uncertainty data were also extracted along the same line scans L and displayed in Figure 4.7(a)-(c) along with the expected value of the RS. In this figure the colour-filled bands stand for the interval $\sigma_{zz}(L) \pm U_{zz}(L)$, thus representing a confidence interval of about 68%.

From a structural integrity viewpoint, much attention should be devoted to the weld region. In particular, the line scan $\sigma_{zz}(M)$ revealed that $\sigma_{zz}(x, y)$ is characterised by comparable peak values at the ADVS and RETS; around 110 MPa. The developed strategy enabled the RS evaluation, i.e. $\sigma_{zz}(x, y)$, to be strengthened with a measure of uncertainty. Specifically, $U_{zz}(x, y)$ was estimated to be 20 MPa at both ADVS and RETS. Thus, at such regions it is possible to assert that the RS is 110 ± 20 MPa, with a confidence level of 68%.

From a computational perspective, the proposed evaluation approach appears to outperform spline interpolation commonly adopted in the CM. In particular, the GPR allows the optimal fitting parameters to be automatically identified. Furthermore, the GPR enables the user to effectively take into account measurement uncertainties and the influence of the roughness due to the WEDM cut. These features makes the devised GPR-supported approach way faster and less unwieldy in comparison with the consolidated spline-based one. With particular regard to the CM uncertainty quantification, the GPR-supported approach presented herein seems to introduce several advantages over that discussed in [98]. For instance, the

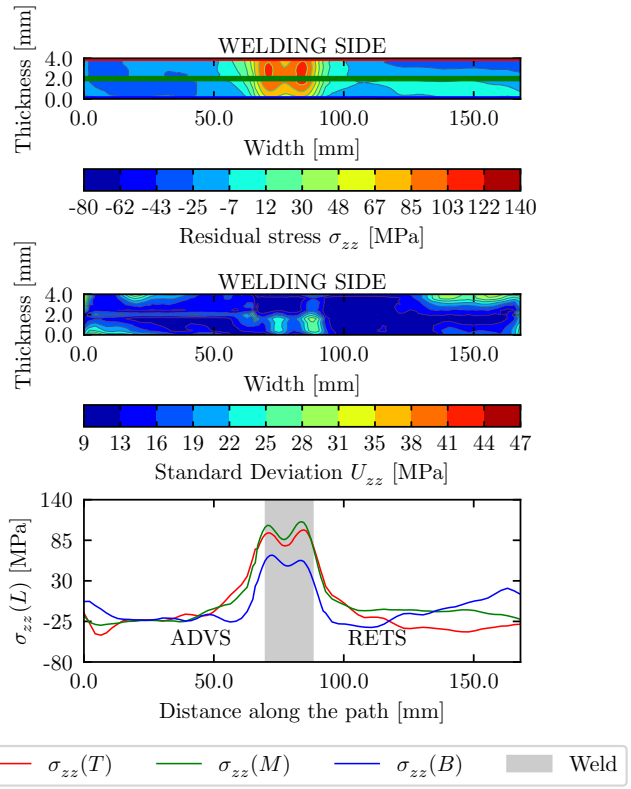

Figure 4.6. Result of the RS evaluation. (a) Contour of the residual stress estimator $\sigma_{zz}(x, y)$. (b) Contour of the uncertainty $U_{zz}(x, y)$ of the residual stress estimator. (c) RS extracted along the line scans in (a), respectively located at the top ($L = T$), middle ($L = M$) and bottom ($L = B$) of the cut surface. The shaded gray region indicates the position of the weld. The locations of the ADVS and RETS are also specified.

uncertainty due to the CMM measurement and interpolation were assumed as separated contributions in [98]. Therefore, the assessment of their correspondent errors required two independent sets of simulations which were eventually combined *after*. By contrast, the GPR combined both these uncertainties *before* the FE simulation, and therefore a single set of Monte Carlo FE simulation was necessary to quantify the uncertainties, allowing for a considerable reduction of the computational cost.

Moreover, the definition of the model error in [98] implies that several combinations of fitting parameters need to be surveyed to find those more suitable for the specific case study. Specifically, the users should choose, based upon their experi-

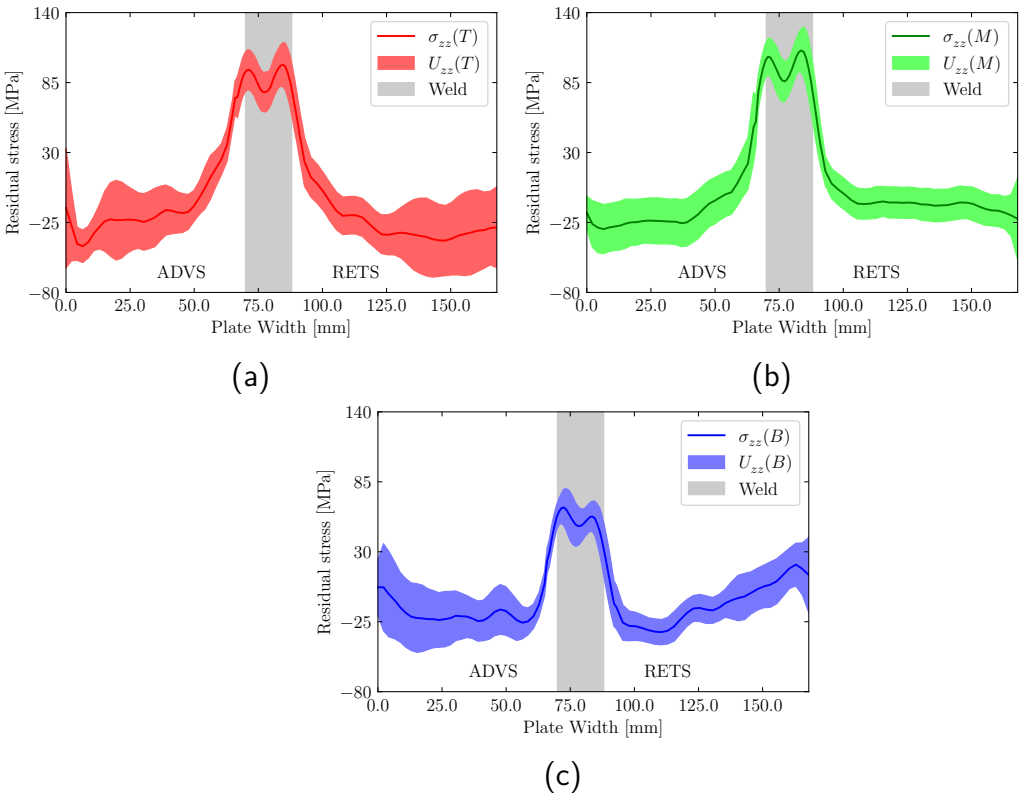

Figure 4.7. RS, $\sigma_{zz}(L)$ and uncertainty distribution $U_{zz}(L)$ extracted along the L line scan. (a) $L = T$ (b) $L = M$ (c) $L = B$. With regard to the line scan L, the colour-filled bands graphically represent $\sigma_{zz}(L) \pm U_{zz}(L)$, i.e. a confidence interval of 68%. The shaded gray region represents the position of the weld. Additionally, the locations of the ADVS and RETS are indicated.

ence, the most appropriate degree of the spline as well as the most suitable number of spline nodes (four parameters in total) to perform the interpolation of the measured data. Conversely, the GPR overcomes this main limitation by reducing the number of parameters involved in the fitting process (C and l, see Table 4.2) and determining them optimally and automatically via probabilistic modelling (see Section 2.4). Therefore, the probabilistic nature of the GPR makes the entire evaluation more robust against the user's experience and confidence as far as the data analysis is concerned.

An additional shortcoming, linked with the use of spline-interpolation, is the nu-

merical instability produced when attempting to fit the data in the proximity of the contour of the surface [172]. This instability is dramatically reduced when the GPR is employed since it is less prone to overfitting and numerical instabilities due to its probabilistic nature [102]. For this reason, it was possible to extract the data very close to the upper and lower edge of Γ (line scans in Figure 4.6(a)). Although the interpolation near the surface contour is always affected by the scarce experimental data available in these regions, the GPR approach can effectively quantify its uncertainty, given that GPR provides the uncertainty of the interpolation, i.e. $\sqrt{\mathbb{V}[u_m]}$ differently from spline fitting.

The entire simulation was carried out on a PC equipped with an Intel® Core™ i7-7500U CPU (@ 2.70 GHz) and 8 GB RAM. The simulation lasted approximately 2 and a half hours for 1000 iterations, whereas each of them took about 8 seconds. The aforementioned LU-factorisation (Section 4.3) of the modified FE stiffness matrix $\mathbf{K}'$ (Eq. (4.7)) led to a substantial reduction of the computational time for each Monte Carlo trial. Preparatory tests showed that if the LU-factorisation had not been adopted, the solution of each trial would have lasted 50 times longer.

Although the total number of simulations was set to 1000, the convergence indicator γ_i (Eq. (4.12)) suggests that the simulation could have been interrupted approximately after 100 trials, i.e. after about 15 minutes. In this instance, γ_i exhibited a drop of two orders of magnitude from the first trial to the hundredth, whereas γ_i decreased only about one order of magnitude until the thousandth trial (Figure 4.8(a)). Practically, this denotes a rapid convergence of the RS estimator $\sigma_{zz}^{(i)}(x, y)$. In order to further optimise the computational cost, a convergence control can be easily implemented on-line, i.e. during the Monte Carlo simulation. To this end, it suffices to define a convergence criterion for γ_i, such as $\gamma_i \leq \gamma_{th}$, where γ_{th} is a threshold. For instance, the convergence can be rationally considered to be achieved when γ_i has decreased by two orders of magnitude. Therefore, for the particular case of the present study, γ_{th} can be reasonably fixed to 0.1 (the red horizontal line in Figure 4.8(a)).

Aiming to display the rapid convergence of the RS estimator of (Eq. (4.9)), $\sigma_{zz}^{(i)}(x, y)$ extracted at $L = M$, i.e. $\sigma_{zz}^{(i)}(M)$, was stored at the iterations $i =$ 1, 10, 50, 100, 500, 1000 and eventually plotted on the same graph, (Figure 4.8(b)). As it can be seen, after the hundredth simulation the fluctuations become negligible, making the RS profiles overlapping. Henceforth, the convergence of the RS

estimator can be assumed as attained.

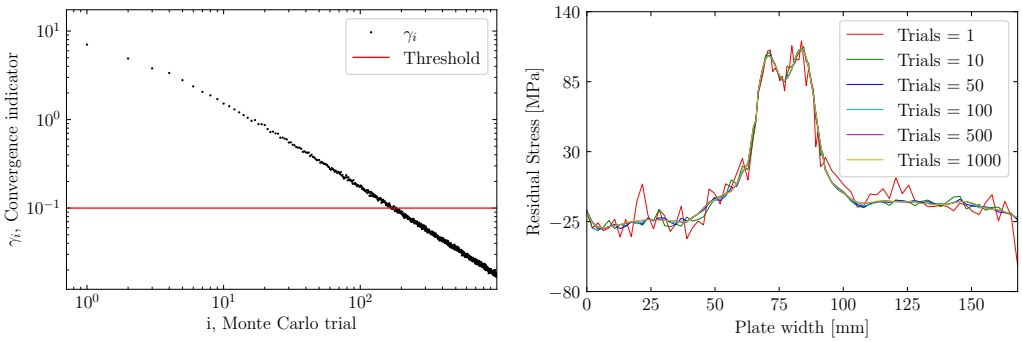

Figure 4.8. (a) Convergence indicator, γ_i, against the Monte Carlo trials, i. The red line indicates the convergence threshold $\gamma_{th} = 0.1$. (b) Qualitative Convergence graph. The RS $\sigma_{zz}^{(i)}(M)$ was stored at the following iterations $i = 1,\ 10,\ 50,\ 100,\ 500,\ 1000$.

4.5. Conclusions

The exploitation of GPR allowed for developing a comprehensive methodology to tackle the uncertainty quantification of RS when utilising the CM. Using Gaussian Process Regression (GPR), it was possible to circumvent the lack of robustness implied by the well-established spline-based interpolation and smoothing strategy of the experimental data of the CMM out-of-plane displacements. Specifically, the GPR was adopted given that the optimal fitting parameters can be stochastically and automatically determined. Therefore, this approach allowed for the minimisation of user's intervention which is inevitably reflected in the lack of uniqueness of the fitting process. Besides providing the data fitting, the GPR estimated the uncertainty that arose as a consequence of this procedure. Furthermore, the resulting uncertainty also embedded the sources of uncertainties associated with the intrinsic CMM measurement error, and the cut surface roughness inherited from the WEDM cut.

Given that the GPR condensed these sources of uncertainty along with the smoothed dataset, the latter was appropriately perturbed and fed into a single Monte Carlo FE simulation to estimate the associated uncertainty as concerned the RS. An effi-

cient strategy to compute the Monte Carlo simulation was developed by exploiting the LU-factorisation of the modified FE stiffness matrix. In particular, this matrix was computed only once and then employed for the solution of each Monte Carlo iteration. Finally, a convergence criterion was developed to stop the simulation when a satisfactory result was achieved. If this criterion is implemented on-line, then the evaluation of uncertainties becomes rapid and accurate, sufficiently rapid to be routinely employed.

Aiming to assess the performance and the effectiveness of this method, a 4 mm thick AA6082-T6 FSW was considered as a case study. The simulation provided the RS field along with the associated uncertainty quantification, thus providing additional information and also giving and appraisal of the reliability of the results. For this particular case study the method revealed, with a confidence level of 68%, that the RS in the FSW joint reached magnitudes as high as 110±20 MPa. The entire simulation can be performed, by implementing the proposed convergence criterion, within approximately 15 minutes with a standard low-budget personal computer.

Finally, it is important to note that the developed method has deviated from the standard CM procedure. In particular, the displacement input data from two surfaces from the same cut were not averaged before performing the Monte Carlo FE simulation. Therefore, two full-field RS maps were provided and eventually post-processed at the end of each trial. Additional errors could affect this strategy due to possible shear stress present over the cut surface, usually reduced by the averaging process. However, this effect was thought to be negligible in the analysed case-study. Without averaging the input data, the presented post-processing may, in turn, lead to an overestimation of the uncertainty. Nonetheless, the arbitrariness of the averaging operation envisaged by the standard protocol induces errors as well that are not accounted for.

The proposed strategy may represent a practical methodology that can help CM-users to routinely evaluate RS along with its associated uncertainty.

5. A Defect-based Physics-Informed Neural Network for Finite Fatigue Life Prediction in Additive Manufacturing

The present chapter adapts the PINN framework to devise an extremely flexible and accurate predictive tool to forecast the finite fatigue life of metallic materials plagued by defects. Concepts of FM are cast into a Basquin-like law to obtain a regression model for fatigue data that intrinsically account for the presence of defect. This model is then used to inform the physical side of the PINN, whilst its NN branch processes a predefined set of defect descriptors.

5.1. Introduction

The development of AM techniques has brought an unprecedented degree of geometry flexibility during the design process of mechanical components, which has been enabling the full exploitation of topology optimisation processes [200]. Nevertheless, structural performance – particularly fatigue – of AM materials is still an open issue that needs to be addressed in order to produce reliable engineering components [46]. Besides surface roughness finish, several interplaying microstructural factors rule the fatigue behaviour of these materials, distinctively from those produced by traditional manufacturing processes. Such influencing factors are largely caused by the nature of the process, which consists of a fast-moving heat source that inevitably produces high and inhomogeneous localised cooling speeds. Therefore, the resulting material is greatly influenced by the thermal history and heat fluxes, which are then reflected in the resulting inhomogeneous microstructure. Indeed, AM materi-

als usually show a textured microstructure linked to the heat flux directions, and even crystallographic phase gradients may be present in some cases [201]. Another important consequence of the poorly controlled thermal history across the length scales is the origin of RS [34]. When superior fatigue performance of AM products was sought, RS was mitigated via stress relief treatment [202]. Additionally, shock and shot peening has been applied in the context of AM, thus enhancing the fatigue load-bearing capacity of the manufactured parts [88, 203, 204].

Although thermal effects can also cause the nucleation of thermal cracks, the predominant presence of crack-like features in AM materials is due to the interplay of localised thermal gradients and dynamics of the material's melt pool producing gas/vapour jets [205] that can promote spatter effects, which are then the principal cause of pore gas formation [206]. Besides gas porosity, where insufficient localised heat is provided to the material to be melted, lack-of-fusion defects may arise [207].

Despite some specific post-processing thermo-mechanical treatments have been developed over the recent years to mitigate issues related to the presence of defects in AM materials (e.g. Hot Isostatic Pressing) [208], in some cases, these methods either cannot be employed practically or do not produce the expected effectiveness. In the last decade, FM concepts have been widely used to assess the fatigue endurance of AM parts considering material defects [52, 209–211], even in the elastoplastic regime [212], thanks also to the original idea of Murakami and his definition of the characteristic size of a defect [2]. Nevertheless, other approaches have also been used [213]. By means of extreme value statistics [214], Romano et. al lately employed the statistical distribution of porosity to infer the probability of failure invoking the KT diagram with the EH model cast within a Finite Element Methods framework [62, 215].

As mentioned in Chapter 1, the detection of defects characteristics in materials can be done through destructive and non-destructive methods. The former refers to material sectioning and optical metallurgical observations, while the latter appeals to non-invasive technique CT scan and fractography [53, 216]. In agreement with Section 1.2, it is worth emphasising that in the specific case of CT, such a technique enables fine morphology details to be captured for a large number of pores. Nonetheless, these details are not fully exploited when semi-empirical models are employed. Therein, the numerous reviewed applications of ML methods to defect-based fatigue evaluation demonstrates that these methods can potentially substitute

semi-empirical modelling for fatigue prediction when the available data is sufficiently high. On the other hand, semi-empirical models are the only possible choice if a prediction is sought while having only a limited dataset. Thus, in some cases, relevant influencing factors are either partially or completely neglected. The fundamental challenge is, therefore, the fusion of the two approaches with the aim to reinforce the prediction. Still, one method generally excludes the intervention of the other.

The recent advent of PINNs (Section 2.6.2), together with its incredible potential and features, seems to constitute a neat solution to this problem. In fact, such an approach appeared to be effective for the prediction of AM material porosity during manufacturing [217]. Another example is an application of NN to a Ti-6Al-4V AM alloy for the prediction of fatigue life, also considering probability, without considering any material microstructural characteristics such as defects [218]; in this case, the physics-informed approach was referred to as physics-guided. In the field of solid mechanics, these methods were also proposed to identify inhomogeneous elastic properties [219].

A novel ML approach – based on PINNs – is developed to forecast the finite fatigue life additively manufactured metallic materials. This approach enables for taking into account those morphological characteristics of the porosity present in the material that are not contemplated when using classic LEFM. By proposing and exploiting the capability of a novel semi-empirical modelling approach to fatigue life based on LEFM, the physics-informed section of the PINN model was employed to reinforce the training process of a properly structured NN. A case-study is eventually shown by analysing a relatively small dataset obtained from the literature regarding an AlSi10Mg alloy produced by selective laser melting, specifically containing material fatigue experimental data and morphological characteristics of the porosity present in the material. Importantly, the analysed samples did not undergo any thermal treatment after fabrication, so the effect of RS may be significant. The validation of the devised PINN model is then performed through the so-called K-fold cross validation, i.e. permutations of the samples excluded in the training process of the PINN. To this end, the predicted and actual results in terms of fatigue finite life of independent experimental test samples are compared for each generated fold. In order to prove the benefits offered by the PINN, the training and the validation is replicated using an equivalent NN, i.e. the same PINN where the LEFM physical constraint is deactivated. To this end, both qualitative and quantitative compari-

son are widely discussed along with a discussion on the implications and potential limitations of the proposed model.

5.2. Materials and Methods

5.2.1. Experimental Dataset

This investigation considers an experimental literature dataset kindly provided by Romano et. al. [52], particularly regarding those which underwent CT analysis. According to the authors, several cylindrical aluminium alloy (AlSi10Mg) samples were additively manufactured by means of an EOS M400® powder-bed machine, which relies on the selective laser melting (SLM) technology. The surface of the samples was turned to remove the intrinsic roughness of the SLM machining process. These samples were fabricated over a period of three years (2015 to 2017) employing the same process parameters, and the diameter of the gauge volume was not the same for all the tested samples: from 4 mm to 6 mm. Additionally, all the samples were fabricated using a layer thickness of 60 µm and a pre-heating of the platform of 200°C. Throughout the fabrication period, however, the machine's built-in system that recirculates the inert gas and removes the particles was upgraded to improve the quality of the material. Therefore, two different batches of samples were distinguished, namely P1 and P2. Specifically, the samples belonging to P1 and P2 were produced using the original and the upgraded recirculating system, respectively. Furthermore, regardless of the batch involved, two different built orientations were considered, namely vertical (V) and horizontal (H). It is important to highlight that none of the samples was heat treated after the manufacturing process.

Prior to fatigue testing, the samples underwent CT scans in order to reconstruct the accurate morphology and location of hidden, or partially hidden, defects. In this respect, details of the adopted gauge volume can be found elsewhere [52].

In order to characterise the fatigue behaviour of the material, the specimens were subjected to a cyclic load of constant stress amplitude $\Delta\sigma$ at a load ratio of $R = -1$. In this instance, $\Delta\sigma$ is the nominal externally applied load, whereas N is the corresponding number of cycles to failure N. Table 5.1 provides the outcomes of the fatigue experimental characterisation. After the fatigue testing, the samples were observed through fractography in post-mortem conditions to detect, where

identifiable, killer pores, i.e. the pores where the fatigue cracking was triggered. Table 5.1 reports in which samples this operation turned out to be successful.

Table 5.1. List of tested samples and fatigue details [52]. As concerns the built orientation, H and V stand for horizontal and vertical, respectively.

Sample	Batch P#	Built orientation	$\Delta\sigma$	N	Killer defect detectable?
1	1	H	400.0	474	YES
2	1	H	360.0	3432	YES
3	1	V	378.3	11465	NO
4	1	H	298.5	19806	NO
5	2	H	374.4	28201	NO
6	1	V	301.6	39538	NO
7	1	V	295.0	46255	YES
8	1	V	180.0	237485	NO
9	1	H	220.0	2622640	YES
10	1	V	156.0	3795336	NO
11	1	V	180.0	11352768	YES
12	1	V	200.0	15242310	YES

The morphology features that are considered pertinent to the present work are: the volume of the defects V, the external surface of the defects A, and the projection of A onto the plane normal to the direction of the applied load. The square root of this projection will be identified as $\sqrt{\text{area}}$ in the following sections concerning the LEFM model. According to the features A and V, the sphericity of the defects is computed as:

$$S = \frac{\pi^{1/3}\,(6V)^{2/3}}{A} \tag{5.1}$$

whereas the equivalent three-dimensional diameter of the defects is given by:

$$d = \sqrt[3]{\frac{6V}{\pi}} \tag{5.2}$$

Regarding the location of the defects, the CT scans permitted the distance between the defects and the free surface of the specimen to be assessed. Hereafter, such quantity will be denoted by h.

5.3. Development of a Fracture Mechanics-based Model

5.3.1. Stress Intensity Factor Evaluation

Due to the relatively small size of the defects generally found in AM materials, a LEFM approach is often used to assess the severity of the applied cyclic load concerning the fatigue life. The SIF K of Eq. (2.15), is widely employed to evaluate the crack driving force in LEFM. With particular regard to fatigue problems the SIF range presented in Eq. (2.16) is adopted accordingly.

When dealing with small cracks (up to ~ 1000 µm), compared with the characteristic cross section dimension of the probed material, Murakami demonstrated how even three-dimensional defects can be characterised by simply evaluating the square root of the projected area of the defect over a plane normal to the principal loading direction, $\sqrt{\text{area}}$; this characteristic is then considered as the equivalent crack length [2], i.e. $a \mapsto \sqrt{\text{area}}$. Therefore, for small defects, the SIF range (Eq. (2.16)) becomes:

$$\Delta K = Y \Delta\sigma \sqrt{\pi \sqrt{\text{area}}} \tag{5.3}$$

As widely reported by Murakami [2], Y turns out to be predominantly dependent on the distance between the centre of the defect and the sample free surface – for short cracks. In particular, Murakami proposed the following empirical condition to discriminate (sub-)surface defects and embedded cracks:

$$\frac{h}{r} < 1.25 \tag{5.4}$$

where h is the distance from the sample free surface of the defect centre, and r is the radius of the equivalent circular planar defect defined as:

$$r = \sqrt{\frac{\text{area}}{\pi}} \tag{5.5}$$

Therefore, according to LEFM, the crack coefficient turns out to be: $Y = 0.65$ for

(sub-)surface defects and $Y = 0.5$ for embedded (or bulk) cracks:

$$Y = \begin{cases} 0.65 & \text{if } \frac{h}{r} < 1.25 \\ 0.5 & \text{if } \frac{h}{r} \geq 1.25 \end{cases} \tag{5.6}$$

Particular Case of Sub-surface Defects. For a more precise evaluation of the ΔK, the equivalent crack length for sub-surface defects should be corrected to account for the fraction of material laying between the defect and the free surface that does sufficiently restrain the defect to open when the load is applied [2, 220]. To this end, an *effective area* (area_{eff}) is generally employed. The concept of the effective area stems from the relatively fast propagation of sub-surface cracks, preferentially towards the sample free surface, along with those directions where the crack driving force is predominant. In this scenario, fatigue crack growth occurs rapidly to form a secondary defect geometrical configuration (area_{eff}) and these fatigue cycles allowing for a crack to grow from area to area_{eff} are neglected; this is a generally accepted assumption [220].

Given the difficulty in achieving an accurate estimate of area_{eff} – especially when dealing with three-dimensional defects – the exact shape of the defect can be conveniently and efficiently replaced by accounting for the distance of the sample free surface h to the centre of the equivalent circular defect again by a planar circular crack with the equivalent radius, r, according to Figure 5.1. It is important to report that the centre of the equivalent circular defect is coincident with the centroid of the defect itself. By using these dimensions, an approximate value of the area_{eff} can be defined through the following equation:

$$\text{area}_{\text{eff}} = \frac{\pi r^2}{2} + 2\,h\,r = \text{area}\left(\frac{1}{2} + \frac{2h}{\pi r}\right) \tag{5.7}$$

In this way, the projected defect area is increased by maximum 1.3 times at the boundary between bulk and sub-surface defects ($h/r = 1.25$), and this multiplying factor turns out to be 1 when $h/r = \pi/4$ (limit of applicability of the present sub-surface defect). By substituting area_{eff} in Eq. (5.3), and assuming $Y = 0.65$ as per

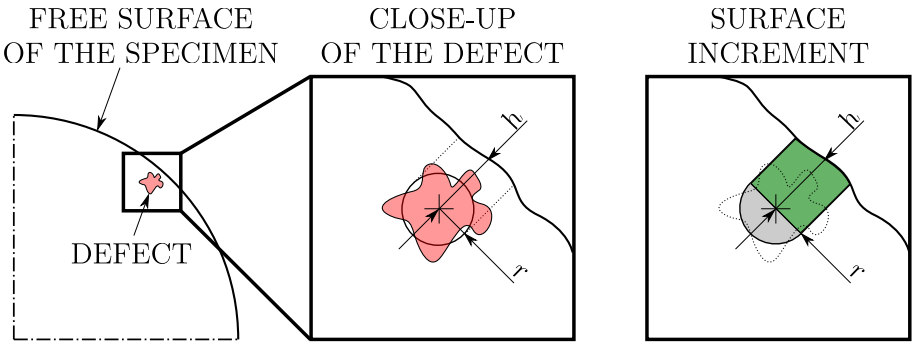

Figure 5.1. Graphical illustration of equivalent planar circular crack and its surface increment for sub-surface defects. The projected defect area is highlighted in red, and the radius of its area equivalent circular domain is r. The distance of the equivalent domain to the free surface is h. The effective area of the defect is approximatively given by the sum of half of the equivalent circular defect (in grey) and the portion of material connecting to the free surface (in green).

surface defects, the following expression can be written:

$$\Delta K^{\text{sub-surf}} = 0.65\left(\frac{1}{2}+\frac{2h}{\pi r}\right)^{1/4}\Delta\sigma\sqrt{\pi\sqrt{\text{area}}} \tag{5.8}$$

As can be seen, the last relationship maintains the same structure of Eq. (5.3). Therefore, a modified version of Y can be straightforwardly defined as:

$$Y^{\text{sub-surf}} = 0.65\left(\frac{1}{2}+\frac{2h}{\pi r}\right)^{1/4} \tag{5.9}$$

which accounts for the aforementioned defect surface increment. It is worth outlining that this handy estimation procedure might lead to either an overestimation or underestimation of the effective area depending upon the shape of the defect. In any case, this effect is deemed to be negligible herein.

Surface Cracks and Generalised Correction in SIF Calculation. The correction on the effective area decays when the boundaries of internal defects meet the material sample free surface. In this scenario, there is no need to consider an effective area of the defect, but the actual projected area can be used. As quickly mentioned

earlier, as it can be seen in Eq. (5.7), a further criterion must be implemented to discriminate this class of cracks, thus:

$$\frac{h}{r} \leq \frac{\pi}{4} \tag{5.10}$$

In summary, a modified version of Y, namely Y_{eff} is readily defined:

$$Y_{\text{eff}} = \begin{cases} 0.65 & \text{if } \frac{h}{r} \leq \frac{\pi}{4} \\ 0.65\left(\frac{1}{2} + \frac{2h}{\pi r}\right)^{1/4} & \text{if } \frac{\pi}{4} < \frac{h}{r} < 1.25 \\ 0.5 & \text{if } \frac{h}{r} \geq 1.25 \end{cases} \tag{5.11}$$

Hence, ΔK can promptly be evaluated through equation Eq. (5.3), where Y is now replaced by Y_{eff}:

$$\Delta K = Y_{\text{eff}} \Delta\sigma \sqrt{\pi\sqrt{\text{area}}} \tag{5.12}$$

5.3.2. Normalised Fatigue Driving Force

As discussed in Section 2.2, $\Delta K - N$ curve can be exploited to model the finite fatigue life. Nevertheless, additional assumptions are required to refine such model for the present investigation.

In a recent publication, Murakami showed how the normalisation of S-N curves using the fatigue limit $\Delta\sigma/\Delta\sigma_w$ can be effective to describe the finite fatigue life behaviour of different batches of samples belonging to the same parent material; different batches were referred to different sizes of defects [11, 221]. Herein, an analogous normalisation is proposed to deal with short cracks, with the goal of further reducing the scatter band of the master fatigue life curve. To this end, the normalisation is done by using the fatigue SIF threshold, ΔK_{th}. Therefore, $\Delta K/\Delta K_{th}$ becomes the normalised fatigue driving force. However, such normalisation is not straightforward given that in the short crack region, ΔK_{th} is strongly affected by the initial crack size as widely reported by Murakami and Ritchie [2, 222]. Specifically, this result is attributed to plastic deformations and crack closure effects [19, 223, 224]. Hence, the normalisation is alternatively done by evaluating ΔK_{th} according to the empirical law proposed by Murakami and Endo [225]. Therein, it was showed that ΔK_{th} can easily be found with remarkable accuracy for many metallic materials, and defect

sizes ranging from 10 µm to 1000 µm, through the following equation in which only the material Vickers hardness (HV) is used as the intrinsic material property:

$$\Delta K_{th} = C \times 10^{-3}(\mathrm{HV} + 120)\sqrt{\mathrm{area}}^{1/3} \tag{5.13}$$

where C is a constant that depends on the defect position, i.e. 2.77 for bulk cracks and 3.30 for sub-surface or surface cracks [2], following the same distinction discussed earlier. It is noteworthy that the units of ΔK_{th} and $\sqrt{\mathrm{area}}$ are $\mathrm{MPa}\sqrt{\mathrm{m}}$ and µm, respectively.

At this point, in order to fully exploit Murakami's relation, it is useful to normalise ΔK in the $\Delta K - N$ curve also with respect to the material intrinsic mechanical property HV and other remaining constants, therefore Eq. (5.13) can be rearranged as:

$$\frac{\Delta K_{th}}{C \times 10^{-3}(\mathrm{HV} + 120)} = \sqrt{\mathrm{area}}^{1/3} \tag{5.14}$$

Thus, the normalisation is done by dividing Eq. (5.12) as follows:

$$\frac{\Delta K}{\Delta K_{th}} C(\mathrm{HV} + 120) = \frac{Y_{\mathrm{eff}} \Delta\sigma \sqrt{\pi\sqrt{\mathrm{area}}}}{\sqrt{\mathrm{area}}^{1/3}} \tag{5.15}$$

It is worth noting that the constant 10^{-3} in the last equation vanishes, if it is decided to express $\sqrt{\mathrm{area}}$ in µm. Given that the coefficient C varies according to the same rule of Y_{eff} (Eq. 5.11), it is possible to include the functional relationship of both C and Y_{eff} into a single function Y^*:

$$Y^* = \begin{cases} 0.1970 & \text{if } \frac{h}{r} \leq \frac{\pi}{4} \\ 0.1970 \left(\frac{1}{2} + \frac{2h}{\pi r}\right)^{1/4} & \text{if } \frac{\pi}{4} < \frac{h}{r} < 1.25 \\ 0.1805 & \text{if } \frac{h}{r} \geq 1.25 \end{cases} \tag{5.16}$$

Eventually, the driving force of the fatigue life can be expressed as:

$$\frac{\Delta K}{\Delta K_{th}}(\mathrm{HV} + 120) = \frac{Y^* \Delta\sigma \sqrt{\pi\sqrt{\mathrm{area}}}}{\sqrt{\mathrm{area}}^{1/3}} \triangleq \delta K \tag{5.17}$$

Hereafter, this parameter will be often recalled as the *normalised SIF range*: δK.

5.3.3. Fatigue Curve Regression and Prediction Band

As mentioned in Section 2.2.1, Sheridan showed that traditional S-N curves can be restated in terms of with $\Delta K - N$ to reduce the scatter that fatigue data typically incorporates. Although this rationale is exploited herein as well, the normalised SIF range of Eq. (5.17) is employed instead. Therefore, Sheridan's model (Eq. (2.19)) is reformulated as:

$$N = A\,\delta K^{B} \tag{5.18}$$

Since the last relationship still retains the functional form of $\Delta K - N$ curves, the ASTM standard is, again, adapted to fit Eq. (5.18) to the data [101]. Therefore, the logarithm of both sides of Eq. (5.18) is firstly taken:

$$\log_{10} N = \hat{A} + \hat{B} \log_{10} \delta K \tag{5.19}$$

and expected value of the fitting coefficients, namely $\hat{A}$ and $\hat{B}$ is obtained by ordinary least squares method. Differently from the ASTM standard, which allows for evaluating the simultaneous *confidence* intervals for the sole regression line, the introduction of the empirical formulation of fatigue life is aimed at providing an interval in which the fatigue failure is expected to lay in – this shall be discussed in greater details in regards to the PINN calculation scheme. Such an interval is called a non-simultaneous two-sided *prediction* interval approach is fully exploited [226]. The calculation of the prediction interval is particularly useful since it provides a band which includes, with a given confidence, a single future observation. This distinctive interval takes into account both the random variability of a future observation and the epistemic variability of the regression estimates. As a particular case, if the sample size tends to infinity, the prediction interval converges to the scatter band of the sole regression. Accordingly, the model presented in Eq. (2.26) is modified to replace the confidence band with the prediction one, hence:

$$\log_{10} N = \hat{A} + \hat{B} \log_{10} \delta K \pm s\,\Delta P \tag{5.20}$$

in which s is, again, the square root of unbiased estimator of the variance (as per Eq. (2.24)), and ΔP is the semi-amplitude of the prediction interval, which is com-

puted through:

$$\Delta P = t_{n-2,\alpha/2}\sqrt{1+\frac{1}{\mathsf{P}}+\frac{(\log_{10}\delta K-\overline{\log_{10}\delta K})^2}{\sum_{i=1}^{\mathsf{P}}(\log_{10}\delta K_i-\overline{\log_{10}\delta K})^2}} \tag{5.21}$$

where $t_{n-2,\alpha/2}$ is the $\alpha/2$-quantile of Student's t-distribution having $n-2$ degrees of freedom, P is the sample size, and $\overline{\log_{10}\delta K}$ is the sample mean which is computed analogously to Eq. (2.22).

5.4. Application of PINNs

5.4.1. PINN for Predicting the Finite Fatigue Life

The present section outlines how to adapt the traditional setting of PINNs to deal with the semi-empirical model shown in Eq. (5.20), referred to as *LEFM fatigue model* in the following. In particular, the physical constraint of Eq. (5.20) shall enforces the training of a NN whose architecture is defined in Eq. (2.68). The objective is therefore to surrogate the model:

$$N = \mathcal{G}_{\boldsymbol{\theta}}(\mathbf{x}) \tag{5.22}$$

using a PINN, where $\mathbf{x}$ gathers any relevant defect descriptor. Figure 5.2 synthesises the block diagram of the devised approach. Conceptually, the NN branch elaborates the training data $\mathbf{x}_i$ and generates the loss $\mathcal{L}_{NN,i}$. Following, the related fatigue prediction N_i^* is fed into the LEFM model, thus originating the additional loss $\mathcal{L}_{M,i}$. These losses are combined (through $\oplus$) and backpropagated.

Before explaining the details of the implementation, it is worth describing how the dataset was structured to be appropriately employed across the branches of the B-PINN. Overall, the dataset comprises all the experimental information obtained from fatigue tests, CT analysis, and – if available – fractography measurements of the killer defect.

In regards to the outcomes of the fatigue tests, this part of the dataset is simply given by the collection of the applied stress range and the corresponding recorded fatigue life, i.e. $(\Delta\sigma_i, N_i)\,\forall\, i = 1, 2, \ldots, \mathsf{P}$ samples.

As far as the NN branch is concerned, the sole feature information obtained from

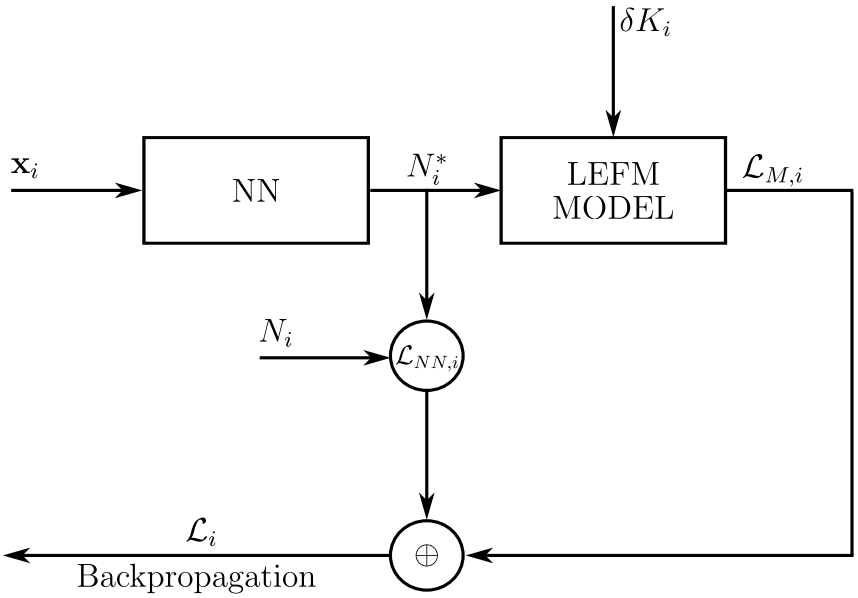

Figure 5.2. Conceptual representation of PINN. The input $\mathbf{x}_i$ is elaborated by the NN which estimates the output N_i^*. Then $\mathcal{L}_{NN,i}$ is computed according to N_i^* and the expected output N_i. Simultaneously, N_i^* is processed through the LEFM model, thus giving rise to an additional loss $\mathcal{L}_{M,i}$. Finally, $\mathcal{L}_{NN,i}$ and $\mathcal{L}_{M,i}$ are combined and backpropagated.

CT scans of each tested sample was used since the prediction is meant to be done before the sample is experimentally tested and thus the actual killer defect cannot be known beforehand. Therefore, a filtering operation is executed to prepare the relevant data which will be used as inputs to the NN. Such a filter relies on the identification of a number of defects l that gives rise to the largest magnitudes of δK and following sorting in ascending order, i.e. $\delta K_1, \delta K_2, \ldots, \delta K_l$. The size of l (also referred to as the number of potential killer defects) is chosen by the user – the case study reported in the next section will show how an appropriate value of l can judiciously be selected. Therefore, the i-th sample is associated with by l instances of each selected defect descriptor, i.e. $\sqrt{\text{area}}$, h, S, and d. Accordingly, the whole

set of inputs can be summarised as:

$$\begin{aligned}\sqrt{\mathbf{area}}_i &= \begin{bmatrix}\sqrt{\text{area}}_{1,i} & \sqrt{\text{area}}_{2,i} & \dots \sqrt{\text{area}}_{l,i}\end{bmatrix} \\ \mathbf{h}_i &= \begin{bmatrix}h_{1,i} & h_{2,i} & \dots & h_{l,i}\end{bmatrix} \\ \mathbf{S}_i &= \begin{bmatrix}S_{1,i} & S_{2,i} & \dots & S_{l,i}\end{bmatrix} \\ \mathbf{d}_i &= \begin{bmatrix}d_{1,i} & d_{2,i} & \dots & d_{l,i}\end{bmatrix}\end{aligned} \tag{5.23}$$

In order to fully define the input vector that the NN branch is meant to process, Eq. (5.23) is merged with the fatigue test data. Hence, the input vector of the i-th sample is readily defined as:

$$\mathbf{x}_i = \begin{bmatrix}\sqrt{\mathbf{area}}_i & \mathbf{h}_i & \mathbf{S}_i & \mathbf{d}_i & \Delta\sigma_i\end{bmatrix} \; \forall\, i = 1, 2, \dots, \mathsf{P} \tag{5.24}$$

Thereby, the dimension of the input layer of the NN (n. of input neurons) is $u \times l + 1$, where u is the number of defect characteristics (or features) used herein ($u = 4$ in this instance: $\sqrt{\mathbf{area}}_i$, $\mathbf{h}_i$, $\mathbf{S}_i$, and $\mathbf{d}_i$) and 1 refers to the applied load $\Delta\sigma_i$. Besides, N_i is the expected experimental output associated with $\mathbf{x}_i$.

As concerns the physical side of the PINN, by construction, the LEFM model, i.e. $\delta k - N$ diagram and its associated regression and prediction band, is identified upon h, and $\sqrt{\text{area}}$ along with fatigue test data, i.e. N, $\delta\sigma$. In this case, the retrieval of pertinent data prioritises actual killer defect information obtained from fractography. Thus, the dataset would ideally be formed as $(\sqrt{\text{area}}_i, h_i, \Delta\sigma_i, N_i)\, \forall\, i = 1, 2, \dots, \mathsf{P}$. However, if the information about the killer defect is missing for a certain i-th sample, then a number of l potential killer defects are exploited for this sample, whose data are retrieved from CT measurements. Upon collating this data, the LEFM model (Eq. (5.20)) is identified and can readily be used to inform the PINN, as it will be shown shortly.

Initially, the PINN processes $\mathbf{x}_i$ (Eq. (5.24)), thus computing the associated prediction N_i^* for each. The loss for the i-th sample is computed as a mean squared error between the predictions and the ground-truth value:

$$\mathcal{L}_{NN,i} = (\log_{10} N_i^* - \log_{10} N_i)^2 \tag{5.25}$$

The N_i^* are then fed into the LEFM model to compute the additional loss owing to

the physics. Given the logarithm of the first n.l normalised SIFs of the i-th sample, namely $\log_{10}\delta k_{1,i}, \log_{10}\delta k_{2,i}, \ldots, \log_{10}\delta k_{l,i}$, Eq. (5.20) can be used to predict the logarithm of the associated potential killers expected finite fatigue lives, namely $\log_{10} N^*_{1,i}, \log_{10} N^*_{2,i}, \ldots, \log_{10} N^*_{l,i}$. Reasonably, a loss function that penalises the difference between each $\log_{10} N^*_{j,i}$ (from the LEFM model) and $\log_{10} N^*_i$ (from the NN) should be sought. The definition of such a loss function exploits an important assumption of the model, i.e. $\log_{10} N$ for a fixed level of $\log_{10}\delta K$ follows a Gaussian distribution [101]:

$$\log_{10} N \sim \mathcal{N}(\log_{10}\hat{N}, s) \tag{5.26}$$

where $\log_{10}\hat{N}$ is given by Eq. (5.20) evaluated at $\log_{10}\delta K$, and s is the aforementioned square root of the unbiased estimator of the variance. Upon normalising the random variable $\log_{10} N$, Eq. (5.26) provides:

$$\log_{10} N \sim \frac{1}{\sqrt{2\pi}s}\exp\left[-\frac{1}{2}\left(\frac{\log_{10} N - \log_{10}\hat{N}}{s}\right)^2\right] \tag{5.27}$$

In view of defining a suitable loss function it is useful to normalise the values provided by Eq. (5.27) so that this function lays in $[0, 1]$. Hence the previous equation can be restated as:

$$\log_{10} N \sim \exp\left[-\frac{1}{2}\left(\frac{\log_{10} N - \log_{10}\hat{N}}{s}\right)^2\right] \tag{5.28}$$

Given that such a normal distribution describes what probability of occurrence of N is expected at a given δK, the aim is to exploit this phenomenological condition into the definition of the loss function for the physics constrains of the PINN.

Considering Eq. (5.28), one could recognise the squared difference between the expected fatigue life $\log_{10}\hat{N}$ and its potential prediction $\log_{10} N$, in the argument of the exponential function. This squared difference resembles a loss function, similar to what is implemented in NN back propagation process. Nevertheless, this form cannot be used as a loss function to enforce the physics constrains since the presence of the exponential penalises the predictions of $\log_{10} N_i$ when approaching the expected value $\log_{10}\hat{N}$. Consequently, it is proposed to revert the behaviour of the function displayed in Eq. (5.28) such that it can be effectively used as a loss function. The fundamental idea is to have a function that provides a null loss function at the mean value of the normal distribution and a loss function approaching a uni-

tary value far away from the mean value. To this end, the general form of the loss function driving the physics branch of the PINN framework is devised as follows:

$$\mathcal{L}_M = 1 - \exp\left[-\frac{1}{2}\left(\frac{\log_{10} N - \log_{10} \hat{N}}{s}\right)^2\right] \tag{5.29}$$

This equation can be readily adapted to handle the prediction given by the NN, $\log_{10} N_i^*$, and the expected value $\log_{10} N_{j,i}^*$ provided by the $\delta K - N$ model. Therefore, upon setting $\log_{10} N \mapsto \log_{10} N_i^*$, and $\log_{10} \hat{N} \mapsto \log_{10} N_{j,i}^*$ in Eq. (5.29) the loss function pertaining to the LEFM model for the i-th sample can readily be stated:

$$\mathcal{L}_{M,i} = \sum_{j=1}^{l}\left[1 - \exp\left[-\frac{1}{2}\left(\frac{\log_{10} N_i - \log_{10} N_{j,i}^*}{s}\right)^2\right]\right] \tag{5.30}$$

and the weighted sum of Eq. (5.25) and Eq. (5.30) is taken to define the loss for the i-th sample:

$$\mathcal{L}_i = w_{NN}\mathcal{L}_{NN,i} + w_M\mathcal{L}_{M,i} \tag{5.31}$$

where $w_{NN} \in [0,1]$ and $w_M \in [0,1]$ are the weights, which are meant to sum to 1, hence:

$$w_{NN} = 1 - w_M \tag{5.32}$$

The loss $\mathcal{L}_i$ related to each i-th sample is accumulated (as per Eq. (2.73)) and backpropagated. Clearly, Eq. (5.31) retains the same structure of Eq. (2.74).

Considering Eq. (5.30), it is worth emphasising that the loss provided from the physics side of the PINN, $\mathcal{L}_{M,i}$, is originated from the mismatch between the predictions given by the NN, $\log_{10} N_i^*$, and the expected value obtained from the regression line of the LEFM, $\log_{10} N_{j,i}$. From a practical standpoint, the additional contribution provided by $\mathcal{L}_{M,i}$ progressively instruct the PINN to make predictions closer to the regression line, until reaching a trade-off with the experimental input. At the end of the training process, the peculiar structure of $\mathcal{L}_{M,i}$ automatically ensures the predictions to lay inside the prediction band, upon rational choice of the weight w_M, thus complying with the semi-empirical law of the LEFM model, Eq. (5.20).

Aiming at evaluating the benefits and the accuracy of the PINN as compared with those of an equivalent fully NN one, two indicators were employed, namely the Root Mean Squared Error (RMSE) and the Coefficient of Determination (R^2). The

RMSE was defined as:

$$\text{RMSE} = \sqrt{\frac{\sum_{i=1}^{\mathsf{P}}(\log_{10} N_i - \log_{10} N_i^*)^2}{\mathsf{P}}} \tag{5.33}$$

where N_i is the experimental fatigue life, whereas N_i^* is the associate prediction, and P is the sample size. Whilst R^2 was defined as:

$$R^2 = 1 - \frac{\sum_{i=1}^{\mathsf{P}}(\log_{10} N_i - \log_{10} N_i^*)^2}{\sum_{i=1}^{\mathsf{P}}(\log_{10} N_i - \overline{\log_{10} N})^2} \tag{5.34}$$

where $\overline{\log_{10} N}$ is the mean of the population, according to Eq. (2.23).

Algorithm 2 is presented to show the summary of the calculation scheme illustrated thus far.

5.4.2. Application to a Case-study

To showcase the capabilities of the present PINN-based method, a case-study is presented. In order to pursue a more conservative approach, it was decided to pick the first three defects showing the highest SIF range, with the difference that the normalised SIF range (δK) was employed herein, therefore, $l = 3$ was assumed. This assumption is justified by the observations reported by Romano et al. [52], who systematically identified the two defects showing the highest SIF as the killer defects. It is fundamental to highlight that the selection of l is highly dependent on the distribution of defects giving rise to close SIF range values. For instance, if a certain batch of material shows two predominant defects, having much larger SIF ranges as compared with the remaining ones, then the use of $l > 2$ would not be the most appropriate choice.

The architecture of the NN consists of a 13-element input layer (according to the dimension of the input vector), a 16-neuron hidden layer, an 8-neuron hidden layer and a single-neuron output layer. Sigmoid activation functions were adopted regarding the neurons of both the first and second hidden layers. Additionally, at each neuron the bias parameter was trained according to the considered data fold. The architecture of the NN was accurately designed to provide predictions complying with the LEFM model, while at the same time keeping its complexity as low as possible and avoiding overfitting the training dataset. It should be noted,

Algorithm 2 Developed fatigue finite life PINN algorithm.

Require: CT-scan dataset: $\sqrt{\mathbf{area}}_i, \mathbf{h}_i, \mathbf{S}_i, \mathbf{d}_i \, \forall \, i = 1, 2, \ldots, \mathsf{P}$
Require: Fatigue dataset: $\Delta\sigma_i, N_i \, \forall \, i = 1, 2, \ldots, \mathsf{P}$
Require: Fractography dataset: $\sqrt{\mathbf{area}}_i, \mathbf{h}_i$
Require: l, i.e. the maximum number of potential killer defects
— **NN data preparation** —
for $i = 1, 2, \ldots, \mathsf{P}$ **do**
    Gather the l-th entries of $\sqrt{\mathbf{area}}_i, \mathbf{h}_i, \mathbf{S}_i, \mathbf{d}_i$ ▷ Eq. (5.23)
    Assemble NN input vector $\mathbf{x}_i = \left[\sqrt{\mathbf{area}}_i \quad \mathbf{h}_i \quad \mathbf{S}_i \quad \mathbf{d}_i \quad \Delta\sigma_i\right]$ ▷ Eq. (5.24)
end for
— **LEFM model preparation** —
for $i = 1, 2, \ldots, \mathsf{P}$ **do**
    if Killer detectable **then**
        Compute δK from fractography data
        Expand δK l times $\delta\mathbf{K}_i = \underbrace{[\delta K \; \delta K \; \ldots \; \delta K]}_{l-\text{times}}$
        Retrieve N_i
    else
        Compute $\delta K_1, \delta K_2, \ldots, \delta K_l$ from CT data
        Select the first l occurrences such that $\delta K_1 < \delta K_2 < \cdots < \delta K_l$
        Collate $\delta\mathbf{K}_i = [\delta K_1 \; \delta K_2 \; \ldots \; \delta K_l]$
        Retrieve N_i
    end if
    Collate $(\delta\mathbf{K}_i, N_i) \, \forall \, i = 1, 2, \ldots, \mathsf{P}$
    Do regression of $\log_{10} N = \hat{A} + \hat{B} \log_{10} \delta K \pm s \, \Delta P$ ▷ Eq. (5.20)
end for
— **Training** —
Accumulate & backpropagate $\mathcal{L}_i = \mathcal{L}_{NN,i} + \mathcal{L}_{M,i}$ ▷ Eq. (5.31)

however, that no rigorous procedures exist to design the architecture of the NN and thus the necessary number of layers and neurons. Some criteria were considered while structuring the present NN architecture. The fundamental idea is to gradually increase the complexness of the NN structure, Therefore, preliminary a structure without any hidden layers was tested to check whether the system could be predicted by a simple model. This operation was done by considering R^2, and it was decided to increase the complexity of the NN architecture (by adding more hidden layers) such that the R^2 turned out to be around 0.9 when considering both training and test datasets in the PINN framework; higher values were not considered to avoid overfitting. In the same way, also the number of neurons in the hidden layers were carefully chosen.

The numerical implementation of the PINN was carried out by using PyTorch [227]. After preliminary tests, n.2000 epochs was identified as the most suitable value for the present work. During the training process the loss function in Eq. (5.30), was optimised by means of Adam, a popular and broadly employed Gradient Descent optimiser [228].

It is worth noting that in small data regime, L2-regularisation and adaptive Learning Rate (LR) might be considered to avoid overfitting effects [229, 230]. The LR is a specific parameter of the NN which establishes the step size of a Gradient Descent optimiser when exploring the domain of the loss function to be minimised [229]. On one hand, higher LR can accelerate the training process, but on the other, it could trap the optimiser at a local minimum, thus preventing the model from refining the predictions of the unseen data. Furthermore, the training of the NN could benefit from a limited LR, particularly in the small dataset regime; this would make the training process computationally more expensive, though. The choice of the LR should also be determined in agreement with the number of training epochs, so a trade-off between all the listed competing factors should be sought.

According to the adopted number of epochs, an adaptive LR was defined by leveraging the best of both sides of the LR spectrum while maintaining an LR globally small to comply with the small dataset regime. Specifically, the initial LR was fixed to 0.001 and held constant until the 1500th epoch. Following, the LR is reduced by 25% every 25 epochs until the 1600th epoch and finally reduced by 75% every 15 epochs. Alongside, L2 regularization with a weight decay as high as 10^{-5} was adopted to further prevent overfitting.

5.5. Results and Discussion

5.5.1. Applicability of SIF Range as a Fatigue Driving Force

Before showing the key results, it is important to assess the suitability of the proposed fatigue driving force parameter, i.e. the normalised SIF range δK. In order to do so, the whole set of fatigue life experimental results were considered and fitted using the power law early referred to as the $\delta K - N$ trend (i.e. Eq. (5.22)), not only for that specific purpose, but also to estimate the S-N and $\Delta K - N$ regression curves, see Figure 5.3. In this particular case study, a few samples were analysed through microscopy to identify the actual defect that triggered the fatigue failure. In those cases, it is unnecessary to consider the first l defects for the regression of the $\delta K - N$ curve and its prediction band. Therefore, in the regression process, a single value of $\delta K - N$ was employed for those samples and expanded l times to give the same weight of the samples in which the killer defect was not identified.

The square root of the estimator for the variance (s) associated with $\log_{10} N$, concerning the prediction band, was evaluated to quantify the scatter of each dataset and assess the buoyancy of the regression. As shown in Figure 5.3, when considering the applied stress range $\Delta\sigma$ as a driving force, the regression provides a good representation of the fatigue behaviour and a prediction band width $s = 0.7$. Instead, this scatter turned out to be significantly higher if the sole ΔK is considered ($s = 1.079$), in contrast with what was reported by Sheridan in his results [65, 64], see Figure 5.3(b). This contrasting result can be due to the dimension of defects that lay within a region where the role of the non-constant ΔK_{th} is relevant. Nonetheless, if the normalised SIF (δK) is deemed to be a representative driving force, the scatter becomes significantly smaller Figure 5.3(c) – although, again, not strikingly evident as Sheridan showed. Therefore, it can be confidently stated that the normalisation approach implemented herein for the first time can provide a more truthful fatigue finite life representation.

5.5.2. PINN Predictions and K-Fold Cross Validation

As mentioned earlier, a K-fold validation test was performed to check the robustness of the presented approach. This test was successfully carried out for 6 different permutations of the training and test datasets (see Figure 5.4(a)-(f)).

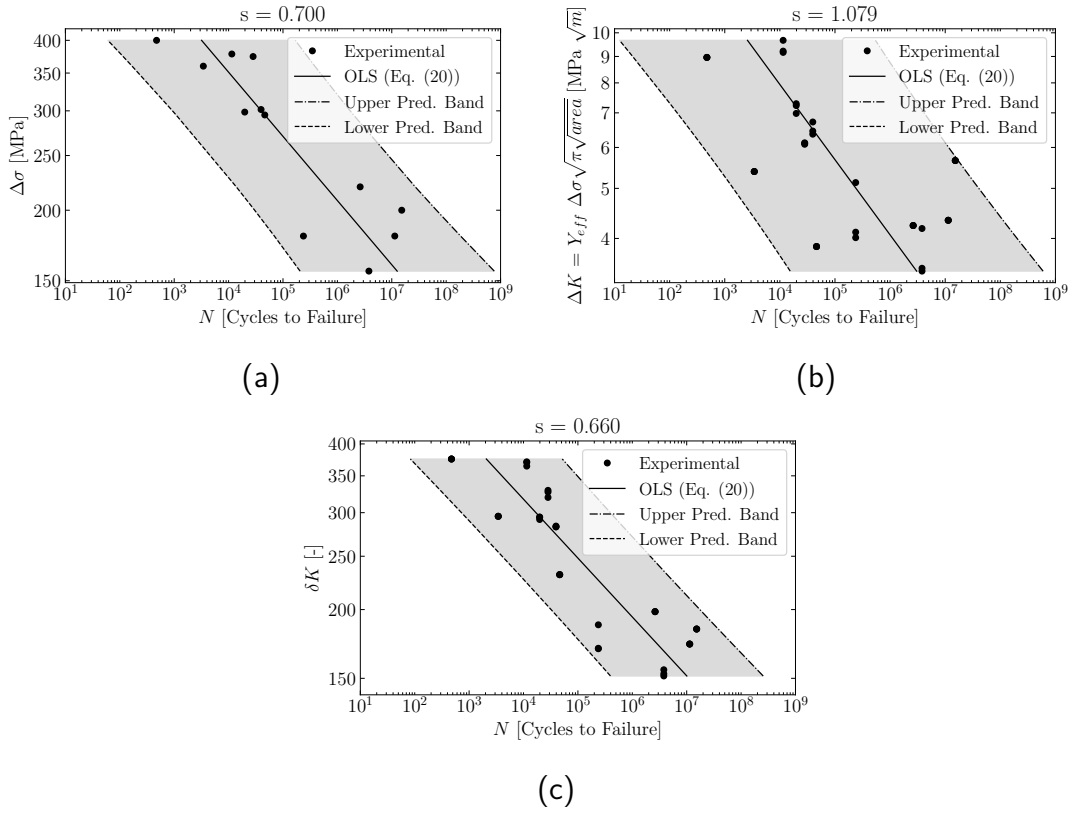

Figure 5.3. Regression curves of fatigue life, prediction bands and square root of the estimator for the variance (s) at 95% confidence level. (a) S-N. (b) $\Delta K - N$. (c) δK.

As far as the training set is concerned, the blue circles in Figure 5.4 are the experimental data, whereas the blue crosses markers are the corresponding predictions. Whilst the test set is labelled using red circles and crosses, respectively for the experimental and associated predictions. The grey-filled region is the prediction band (Eq. (5.20)) enclosed between the associated upper (dot-dashed line) and lower limits (dashed line), respectively. The black solid line is the regression curve obtained from the training dataset through OLS. Additionally, each figure reports the square root of the estimator for the variance computed from the portion of data of the training dataset used to build the regression model (Eq. (5.21). It is very important to mention again that both the prediction band and the regression line are defined using the known experimental data of the fatigued samples employed as training samples, with δK calculated from fractography if present, otherwise from CT scans

as schematically illustrated in Algorithm 2; priority must be given to the fractography data since this information provides a precise identification of the killer defect's traits. On the other hand, the PINN is employed to make predictions exclusively using the data obtained from CT.

Figure 5.4 illustrates the results of the PINN obtained by setting $w_M = 0.015$ and $w_{NN} = 0.985$, which sums to 1 in agreement with Eq. (5.32). These weight values turned out to be appropriate since they equate the contribution of $\mathcal{L}_{M,i}$ and $\mathcal{L}_{NN,i}$. As concerns the early stages of the training a small value of w_M could be particularly suitable. In this instance, the predictions given by the PINN could be forecast far away from the prediction band thus leading excessive values of $\mathcal{L}_{M,i}$ as compared with those of $\mathcal{L}_{NN,i}$.

Although the formulation of the loss function is arbitrary, its peculiar structure defined in Eq. (5.32) allows the user to promptly tune the importance of the physics with respect to the pure NN prediction and vice versa. Extreme instances may be seen if $w_M = 0$, then $w_{NN} = 1$, meaning that the PINN reduces to a standard NN, since the physical constraint is deactivated. Conversely, if $w_M = 1/l$, then $w_{NN} = 0$, therefore the predictive frameworks rely exclusively on the physical constraints.

Another important strength that is worth highlighting is that, in principle, when the PINN is used for prediction purposes, the outcome can be promptly checked with the physics constraints to verify if it complies with the expected range of fatigue life. To this end, it suffices to ascertain whether the predicted point lays inside the prediction band. If so, this point should be accepted. Conversely, it should be rejected.

5.5.3. Assessing the Performance of the PINN

As shown in Figure 5.4, the predictions of the PINN framework and their compliance with phenomenological laws are verified. In fact, the markers indicating the predicted life (i.e. evaluation) lay within the prediction band in all the studied cases. Special attention must be paid to those predictions associated with the "test" samples – those not involved while conducting the PINN training process – which again showed a good prediction. This means that the PINN is capable of satisfactorily estimating the fatigue performance based on the morphological traits and distribution of "killer" defects in the material. Minor mismatches in terms of

the number of cycles (actual vs. predicted) are certainly attributed to those mechanisms involved that are completely neglected in the present study, RS above all. And it is actually for this reason that the employment of semi-empirical law can ensure realistic predictions, rather than seeking the perfect match in terms of the number of cycles which would be impractical if no prior information regarding RS (for example) is known.

It is important to observe that the predictions of the training dataset appear to be located at an intermediate position between the corresponding experimental point and the expected value on the regression line. This could be attributed to the PINN achieving an appropriate trade-off between the model loss $\mathcal{L}_{M,i}$ and the numerical loss $\mathcal{L}_{NN,i}$ during the training process.

For the sake of comparison, the NN counterpart of the PINN is tested. This configuration is obtained by setting $w_M = 0$ and $w_{NN} = 1$ while retaining the same architecture – neurons, layers, and activation functions. The corresponding results are shown in Figure 5.5. In these results it can be seen that some points actually lay outside the prediction band, and the estimate valued of the test samples was less effective; this will be shown shortly.

Besides the qualitative analysis just discussed, it essential to discuss the advantages offered by the PINN over the classic NN in a quantitative manner as well, although one method does not exclude the other. To this end, the results of Figure 5.4 are conveyed into the equivalent, yet concise representation of Figure 5.6, which shows the predicted fatigue life vs the experimental fatigue life exclusively for the test data since these are the independent predictions. Specifically, Figure 5.6(a) reports the results concerning the dataset given by the sole NN, whereas Figure 5.6(b) illustrates those given by the PINN counterpart. Additionally, each figure reports the RMSE (Eq. (5.33) and R^2 (Eq. (5.34)), along with its associated dispersion band for each dataset. The physics-informed side of the PINN provided fundamental and undoubtedly positive support to the NN learning process and avoided overfitting. A remarkable evidence, showing the superior predictive capabilities of the PINN over the NN, can be seen by comparing the values of RMSE and R^2, and obviously the narrower scatter band at the same confidence level (68%).

It worth remarking that in case of even smaller data regime, additional support might be introduced by increasing L2-regularisation or decreasing the LR, limit overfitting.

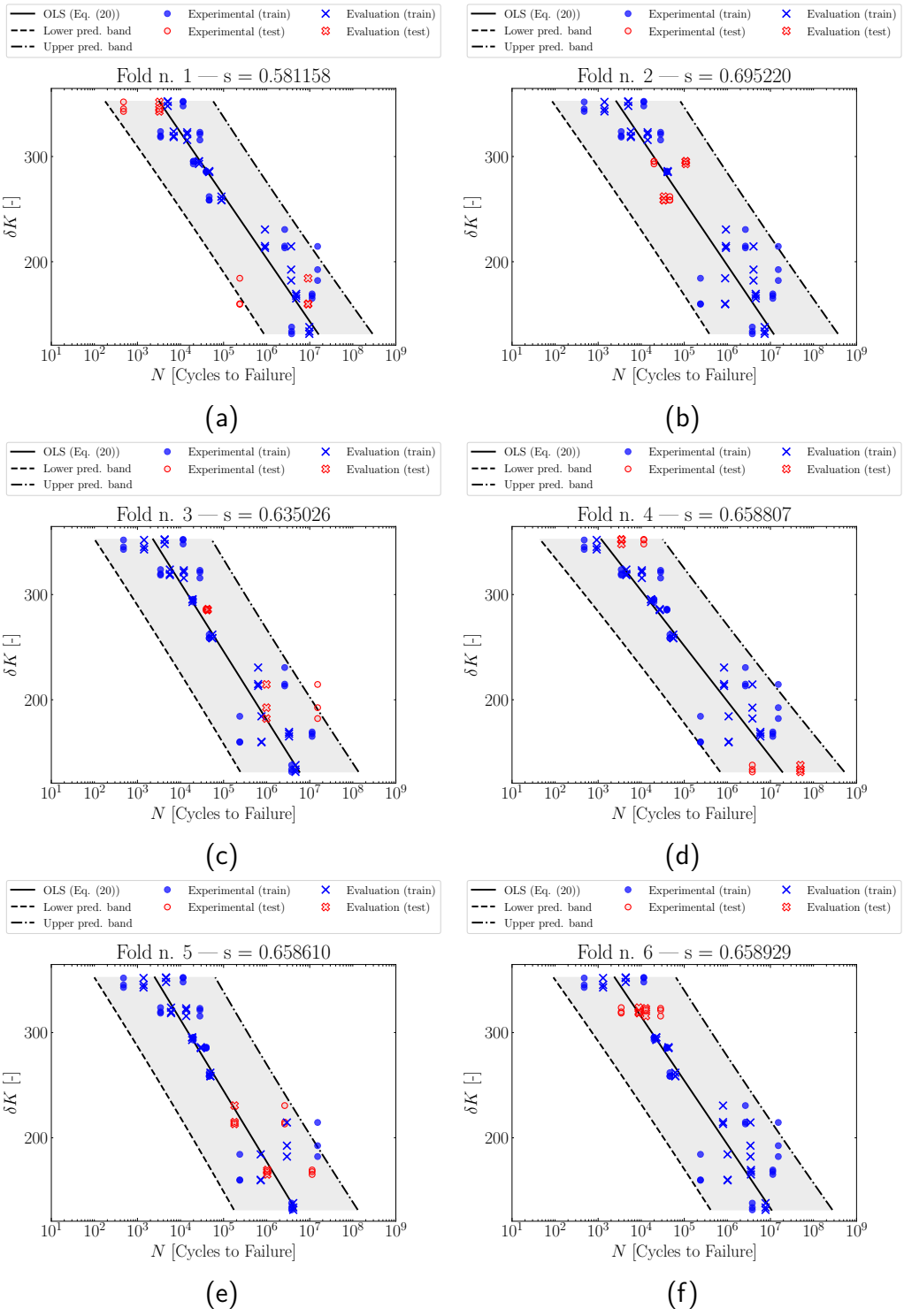

Figure 5.4. Predicted fatigue life overlapped onto the prediction band associated with the considered test samples. Different permutations between test and validations samples are shown (K-fold) (a-f).

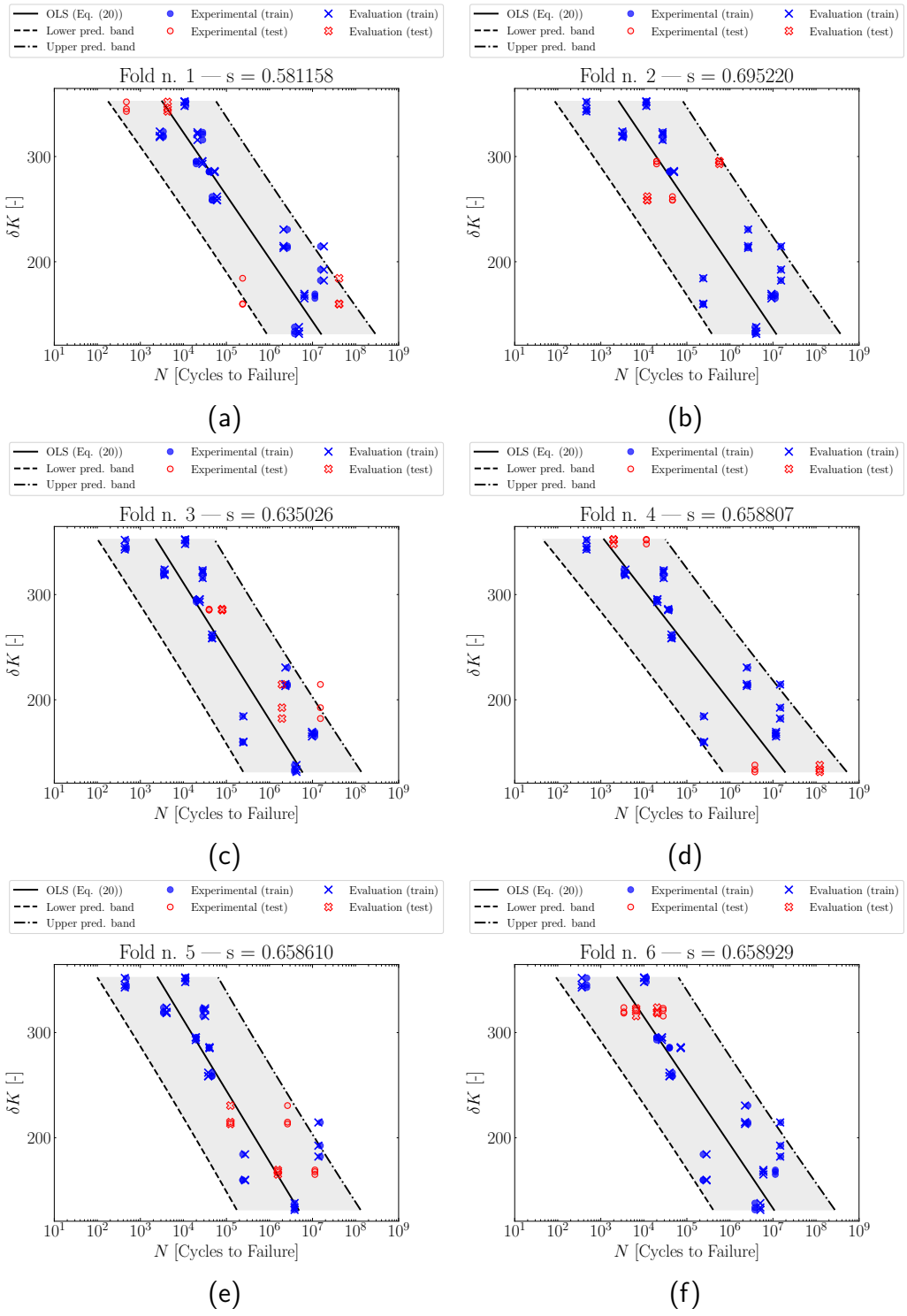

Figure 5.5. Fatigue Life predictions obtained through the NN counterpart of the PINN. Different permutations between test and validations samples are shown (K-fold) (a-f).

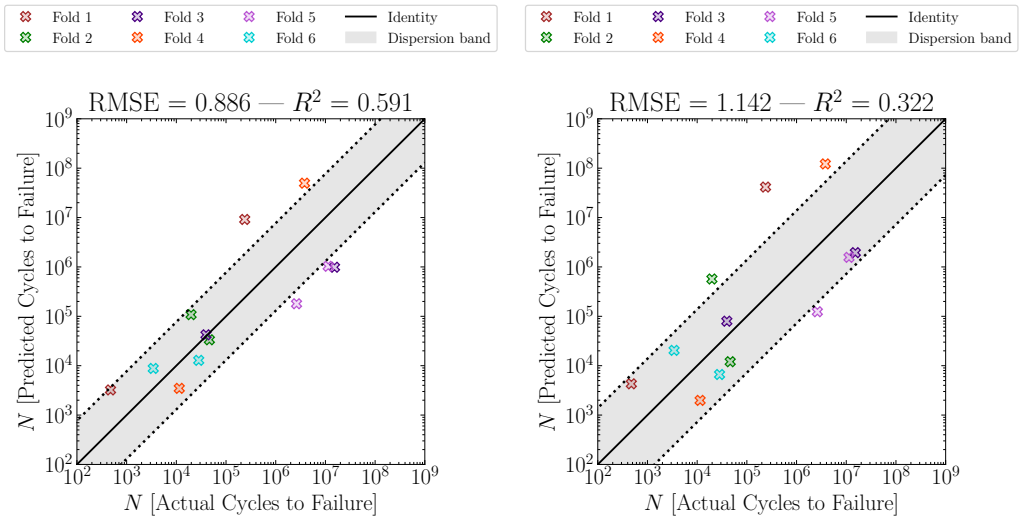

Figure 5.6. Accuracy of the PINN and NN frameworks evaluated through RMSE and R^2. Predicted vs. actual number of cycles for (a) NN and (b) PINN. Dispersion band evaluated at 68% confidence level.

5.6. Conclusions

The present chapter has illustrated the development and implementation of a ML-based prediction tool, constrained by the underlying semi-empirical laws of fatigue finite life, has demonstrated to be highly effective for the accurate prediction of finite fatigue life performance in materials containing flaws.

The validation executed by exploiting experimental results (AlSi10Mg) showed how this approach can account for defect features that could not be taken into account otherwise: defect sphericity and three-dimensional equivalent diameter. The predictions as compared with a purely NN-based predictive tool are improved as demonstrated by the R^2 index that increased by around 83%.

The fundamental idea of using the prediction band, instead of relying upon a deterministic reference curve, allows the model to intrinsically account for other sources of uncertainties that cannot be evaluated, e.g. RS which is certainly present in the analysed samples and may play a significant role.

The PINN framework has proven to be particularly suited for those problems where the dataset is not sufficiently large for reliable prediction using a pure ML technique. Indeed, the lack of data is overcome by introducing phenomenological constraints, i.e. the LEFM model, capable of guaranteeing the physical soundness of predicted outcomes.

By design, the proposed PINN-based approach holds significant versatility as it permits extending the set of defect's characteristics besides those already accounted for, e.g. eccentricity, angularity, solidity [86] if they are thought to play a role in fatigue. Therefore, the accuracy of the method can be further increased, provided that large datasets are available.

In conclusion, the PINN framework has demonstrated an extraordinary capability to make the best out of the two key approaches in fatigue life assessment, namely semi-empirical laws and ML methodologies. This work will pave the way for a new class of predictive tools with unprecedented accuracy and great potential for future developments.

6. Bayesian Evaluation of the Fatigue Endurance Limit of Metallic Alloys

In this chapter, a handy ML probabilistic model is developed to estimate the EH curve of flawed metallic material exclusively using fatigue characterisation and post-mortem fractography as the sole input data. Herein, LR is exploited to turn the phenomenological behaviour of the EH into an ML classification problem, where the likelihood is determined upon the given input data. BI is then seamlessly merged with LR to appropriately inject prior knowledge about the EH curve when insufficient data is provided.

6.1. Introduction

As presented in Section 2.2.2, upon providing defects with a representative crack length, the EH curve is a semi-empirical model that allows practitioners to characterise and visualise the fatigue endurance limit of metallic material. Additionally, it was shown that the EH curve is fully determined by two essential parameters $\Delta K_{th,lc}$ and $\Delta\sigma_w$. This model can be deemed as entrenched across the fatigue & FM community, and, interestingly, it has seen several developments focussed on its extension to the finite fatigue life regime in commercial Inconel 718 [65, 64], and its generalisation to account for propagation and non-propagation crack regimes [231]. It is worth mentioning that a variant of the EH has been proposed by Chapetti to account for closure phenomena and short crack growth [223]. Nevertheless, very little has been done to exploit these models in a probabilistic framework for defect-tolerant design purposes. For instance, a recent study considered a batch of AlSi8Cu3 specimens as a case study, to conceive and apply a probabilistic approach to determining the

EH's model parameters [232]. The experimental campaign of this work permitted $\Delta K_{th,lc}$ and $\Delta\sigma_w$ to be modelled in terms of the survival probability – referred to as Weibull's – of the examined specimens. Another probabilistic method for identifying the EH curve of AM50hp and AZ91hp was developed in [233]. In this instance, a bivariate Weibull distribution embedding the EH model was used to outline the crack propagation region of the examined specimens.

As concerns the inputs required to calibrate the outlined models, the knowledge of $\Delta K_{th,lc}$, $\Delta\sigma_w$ is sometimes difficult to be determined experimentally, especially regarding the latter due to the intrinsic presence of defects in the probed material. Nevertheless, these parameters can be estimated indirectly if a sufficient number of fatigue experimental tests are available at different defect sizes and loading magnitudes – which is one of the key problem addressed herein through the exploitation of ML.

Section 1.2 showed that ML approaches has been extensively employed to forecast the finite fatigue life of metallic alloys upon characterising material's defectivity. Despite this, ML has never been applied to problems dealing with fatigue endurance limit. ML can address these outstanding issues and provide a probabilistic assessment as well. In this respect, datasets similar to that in Figure 2.6 are expected to be available either when experimentally searching for the fatigue endurance limit of a material or in the scientific literature where specimens are labelled as either runout or failed. Since two distinct classes are present, it is thus evident that a dichotomous classification of the dataset can naturally be introduced. As such, this categorisation can be automatically tackled through supervised ML classification methods, amongst which LR as the most suitable, given its probabilistic nature [111].

The present chapter proposes an LR-based probabilistic framework to estimate the EH curve at a given probability of failure. Specifically, the functional form of the EH curve (Eq. (2.27)) is exploited to craft an appropriate decision boundary whose trainable parameters are $\Delta K_{th,lc}$ and $\Delta\sigma_w$. The traditional framework of LR (Section 2.5) requires the unknown parameters of such decision boundary to be trained via ML. Nevertheless, since MLE only provides point estimates of these parameters, MAP is pursued to carry out the training of $\Delta K_{th,lc}$ and $\Delta\sigma_w$ while providing their resulting probability distribution. A Monte Carlo approach is followed by sampling the previously evaluated distributions of $\Delta K_{th,lc}$ and $\Delta\sigma_w$ and computing the associated EH curves accordingly. Finally, a probabilistic post-processing

of the whole set of EH curves is carried out, thus providing the probabilistic EH curve at a given failure probability. The developed LR-MAP method is validated by pursuing a common 80/20 random split of the input dataset. This permit generating the training and test dataset having 80% and 20% the dimension of the input dataset, respectively. LR-MAP is therefore trained on the sole training set and used to predict data belonging to the test set, i.e. the unseen data. To enforce the MAP approach when dealing with lack of information from the available experimental results, numerous datasets that include estimates of $\Delta K_{th,lc}$ and $\Delta\sigma_w$ are gathered herein, or where the identification of the EH curve or KT diagrams was performed, with special attention on those including complete datasets. A few of these datasets were then considered to develop and assess the effectiveness of the proposes method. Finally, the advantages, implications and limitations of the proposed ML approach are widely vetted.

6.2. Machine Learning Probabilistic Design Curves Evaluation

6.2.1. Formulation of the El Haddad Curve

The exploitation of the EH curve necessitates defects to be associated with a representative crack length. To this end, Murakami's approach is followed in agreement with [234]. Specifically, defects are regarded as cracks with a length equal to the renowned $\sqrt{\text{area}}$ [2]. In this instance, it is worth remarking again that $\sqrt{\text{area}}$ is the square root of the projected area of the defect on the plane normal to the loading direction. Additionally, if defects are predominantly loaded under mode I, and limited plasticity effect are involved, LEFM can be invoked, and ΔK (Eq. (5.3)) can be adopted again as the fatigue crack driving force [235, 57]. Accordingly, the related EH curve can be stated by substituting a with $\sqrt{\text{area}}$ in Eq. (2.27):

$$\Delta\sigma = \Delta\sigma_w \sqrt{\frac{\sqrt{\text{area}_0}}{\sqrt{\text{area}_0} + \sqrt{\text{area}}}} \tag{6.1}$$

where $\sqrt{\text{area}_0}$ represents the EH critical defect's length, according to Eq. (2.28):

$$\sqrt{\text{area}_0} = \frac{1}{\pi}\left(\frac{\Delta K_{th,lc}}{Y\,\Delta\sigma_w}\right)^2 \tag{6.2}$$

6.2.2. Logistics Regression Modelling

Before illustrating the theoretical framework of the devised approach it is worth formalising the mathematical structure of the datasets (an example is shown in Figure 2.6). In order to reframe the parameter estimation of the EH curve in terms of $\Delta K_{th,lc}$ and $\Delta\sigma_w$, the dataset of Eq. (2.62) is conveniently adapted as:

$$\mathcal{D} = \left\{\Big((\Delta K_i,\ \Delta\sigma_i), \mathcal{F}_i\Big) \mid \mathcal{F}_i \in \{\text{runout, failed}\}\right\}_{i=1,2,\ldots,\mathsf{N}} \tag{6.3}$$

where N denotes the size of $\mathcal{D}$, ΔK_i was computed using Eq. (5.3) given $\sqrt{\text{area}}_i$, $\Delta\sigma_i$, Y_i. Although $\mathcal{F}_i$ labels the i-th point of the dataset in a descriptive manner, runout and failed are associated with 0 and 1 for the sake of the numerical implementation.

In case of datasets showing defects at different positions with respect to the sample's free surface, multiple values of Y_i must be used for the calculation of the SIF range. So, with the purpose of representing all the samples on a unique diagram, a single $Y_{i,eq}$ is set for the whole dataset while rescaling $\sqrt{\text{area}}_i$ accordingly:

$$\sqrt{\text{area}}_{i,eq} = \frac{Y_i^2}{Y_{i,eq}^2}\sqrt{\text{area}}_i \tag{6.4}$$

which assumes the same SIF for both the equivalent and the original defect. To prove the last relationship, let us write the SIF for the resulting rescaled area $\sqrt{\text{area}}_i$:

$$\Delta K_{i,eq} = Y_{i,eq}\Delta\sigma\sqrt{\text{area}}_{i,eq} \tag{6.5}$$

Equalling the last relationship to Eq. (5.3), i.e. $\Delta K_{i,eq} = \Delta K_i$, leads to:

$$Y_{i,eq}\Delta\sigma\sqrt{\text{area}}_{i,eq} = Y_i\Delta\sigma\sqrt{\text{area}}_i \tag{6.6}$$

which leads to Eq. (6.4) when solved for $Y_{i,eq}$.

Let $\boldsymbol{\theta}$ be the vector of the trainable EH parameters, i.e. $\boldsymbol{\theta} = \begin{bmatrix}\Delta K_{th,lc} & \Delta\sigma_w\end{bmatrix}$. Ad-

ditionally, let us gather the input features into $\mathbf{x} = \begin{bmatrix}\Delta K & \Delta\sigma\end{bmatrix}$. These definitions allow one to model $\mathcal{F}_i$ as a Bernoulli random variable according to Eq. (2.64), and immediately define the decision boundary. Differently from the traditional LR setting, the decision boundary, named as $\mathcal{H}(\mathbf{x}, \boldsymbol{\theta})$ in Section 2.5, is tailored to include the functional form of the EH. Hence, in this case, the decision boundary turns out to be:

$$\mathcal{H}(\mathbf{x}, \boldsymbol{\theta}) = \chi(\mathbf{x}, \boldsymbol{\theta}) \sqrt{\underset{t}{\operatorname{argmin}} \left[(t - \sqrt{\text{area}})^2 + \left(\Delta\sigma - \Delta\sigma_w \sqrt{\frac{\sqrt{\text{area}_0}}{\sqrt{\text{area}_0} + t}} \right)^2 \right]} \tag{6.7}$$

where t is a dummy variable that is sought to find the minimum distance between $\mathbf{x}$ and the EH curve described by $\boldsymbol{\theta}$. Whilst the critical defect dimension ($\sqrt{\text{area}_0}$) can be evaluated through Eq. (6.2), and $\chi(\mathbf{x}, \boldsymbol{\theta})$ determines the sign of the distance:

$$\chi(\mathbf{x}, \boldsymbol{\theta}) = \begin{cases} 1 & \text{if } \mathbf{x} \text{ above EH curve} \\ -1 & \text{if } \mathbf{x} \text{ beneath EH curve} \end{cases} \tag{6.8}$$

Finally, Eq. (6.7) is plugged into the LR equation Eq. (2.66), thus obtaining the probability of failure for $\mathbf{x}$, i.e. $\mathbb{P}[\mathbf{x}|\boldsymbol{\theta}]$. Examining Eq. (2.66) and Eq. (6.7) jointly, it is thus evident that, the higher the $\mathcal{H}(\mathbf{x}, \boldsymbol{\theta})$, the higher the value of $\mathbb{P}[\mathbf{x}|\boldsymbol{\theta}]$. By contrast, the lower the $\mathcal{H}(\mathbf{x}, \boldsymbol{\theta})$, the less the value of $\mathbb{P}[\mathbf{x}|\boldsymbol{\theta}]$ so that the tested point is likely to be runout. Consequently, $\mathcal{F}_i$ is modelled via the following surrogate model which encapsulates the EH curve:

$$\mathcal{F}_i = \mathcal{G}_{\boldsymbol{\theta}}(\mathbf{x}_i) = \frac{1}{1 + \exp\left[-\mathcal{H}(\mathbf{x}_i, \boldsymbol{\theta})\right]} \tag{6.9}$$

according to Eq. (2.29).

6.2.3. Bayesian Parameter Estimation

With reference to Section 2.5, the trainable parameters of the decision boundary are commonly identified utilising MLE (Eq. (2.37)), while employing the Bernoulli likelihood (Eq. (2.67)) as LR handles a classification problem.

Although MLE is a probabilistic strategy to train the parameters, it only provides point estimates. Thus, it cannot ascertain whether potential sources of uncertainty

affect the datasets and it does not accept prior knowledge into the learning process. To overcome this limitation, MAP is used to accomplish the training task. Initially, the likelihood $\mathbb{P}[\boldsymbol{\theta}|\mathcal{D}]$ derived from the given dataset is set. The prior $\mathbb{P}[\boldsymbol{\theta}]$ is prescribed over of the trainable, yet unknown parameters sought to encode prior knowledge while training LR predictor [71]. In this regard, $\Delta K_{th,lc}$ and $\Delta\sigma_w$ are initially hypothesised as independent, hence $\mathbb{P}[\boldsymbol{\theta}] = \mathbb{P}[\Delta K_{th,lc}]\,\mathbb{P}[\Delta\sigma_w]$. Following, $\mathbb{P}[\boldsymbol{\theta}|\mathcal{D}]$ and $\mathbb{P}[\boldsymbol{\theta}]$ are plugged into Bayes' theorem (Eq. (2.32)), and MAP is applied, i.e. Eq. (2.35). In the present case, the evidence is, again, dropped as it is a constant. It is worth mentioning that the term Eq. (2.35) corresponding to the prior becomes:

$$\log \mathbb{P}[\boldsymbol{\theta}] = \log \mathbb{P}[\Delta K_{th,lc}] + \log \mathbb{P}[\Delta\sigma_w] \tag{6.10}$$

Whilst any distribution can be prescribed over $\boldsymbol{\theta}$, Gaussian ($\mathcal{N}$) and Uniform ($\mathcal{U}$) priors were considered herein.

Gaussian priors can be used to introduce strongly informative prior knowledge during the training phase, and at the same time, it acts as a L2-regulariser for $\log \mathbb{P}[\mathbf{x}|\boldsymbol{\theta}]$, thus facilitating the training process and avoiding possible local maxima of the log-likelihood. In this case, let us assume:

$$\Delta K_{th,lc} \sim \mathcal{N}(\mu_{\Delta K}, S_{\Delta K}) \Rightarrow \mathbb{P}[\Delta K_{th,lc}] = \frac{1}{\sqrt{2\pi S_{\Delta K}^2}} \exp\left[-\frac{1}{2}\left(\frac{\Delta K_{th,lc} - \mu_{\Delta K}}{S_{\Delta K}}\right)^2\right] \tag{6.11}$$

$$\Delta\sigma_w \sim \mathcal{N}(\mu_{\Delta\sigma}, S_{\Delta\sigma}) \Rightarrow \mathbb{P}[\Delta\sigma_w] = \frac{1}{\sqrt{2\pi S_{\Delta\sigma}^2}} \exp\left[-\frac{1}{2}\left(\frac{\Delta\sigma_w - \mu_{\Delta\sigma}}{S_{\Delta\sigma}}\right)^2\right] \tag{6.12}$$

where $\mu_{\Delta K}$, $\mu_{\Delta\sigma}$, $S_{\Delta K}$, and $S_{\Delta\sigma}$ are the known mean and the variance of each random variable. Therefore, MAP equation (Eq. (2.36)) turns out to be:

$$\hat{\boldsymbol{\theta}} = \underset{\boldsymbol{\theta}}{\operatorname{argmax}}\left[\log \mathbb{P}[\mathcal{D}|\boldsymbol{\theta}] - \frac{1}{2}\left(\frac{\Delta K_{th,lc} - \mu_{\Delta K}}{S_{\Delta K}}\right)^2 - \frac{1}{2}\left(\frac{\Delta\sigma_w - \mu_{\Delta\sigma}}{S_{\Delta\sigma}}\right)^2 + C\right] \tag{6.13}$$

where C is the constant:

$$C = \log \frac{1}{\sqrt{2\pi S_{\Delta K}^2}} + \log \frac{1}{\sqrt{2\pi S_{\Delta\sigma}^2}} \tag{6.14}$$

and it can be neglected during the maximisation. Eq. (6.13) can be rewritten as follows:

$$\hat{\boldsymbol{\theta}} = \underset{\boldsymbol{\theta}}{\operatorname{argmax}} \left[\log \mathbb{P}[\mathcal{D}|\boldsymbol{\theta}] + \lambda_{\Delta K} \|\Delta K_{th,lc} - \mu_{\Delta K}\|_2^2 + \lambda_{\Delta\sigma} \|\Delta\sigma_w - \mu_{\Delta\sigma}\|_2^2 \right] \tag{6.15}$$

which represents the L2-regularised log-likelihood, where $\lambda_{\Delta K}$, $\lambda_{\Delta\sigma}$ are two independent regularising weights $\lambda_{\Delta K} = -1/2S_{\Delta K}^2$ and $\lambda_{\Delta\sigma} = -1/2S_{\Delta\sigma}^2$, and $\|\cdot\|_2$ denotes the L2-norm.

On the other hand, when none or limited prior knowledge is available, $\mathcal{U}$ priors are preferred. These $\mathcal{U}$ priors do not affect the likelihood, since the corresponding constant term vanishes while maximising Eq. (2.36). For this reason, $\mathcal{U}$ is called a non-informative prior. For instance, if a $\mathcal{U}$ prior is prescribed over $\Delta\sigma_w$, whilst a $\mathcal{N}$ prior is prescribed over $\Delta K_{th,lc}$, Eq. (6.15) transforms into:

$$\hat{\boldsymbol{\theta}} = \underset{\boldsymbol{\theta}}{\operatorname{argmax}} \left[\log \mathbb{P}[\mathcal{D}|\boldsymbol{\theta}] + \lambda_{\Delta K} \|\Delta K_{th,lc} - \mu_{\Delta K}\|_2^2 \right] \tag{6.16}$$

where L2-regularisation acts over the sole random variable $\Delta K_{th,lc}$. Obviously, the same concept applies when a $\mathcal{U}$ prior is imposed on $\Delta K_{th,lc}$:

$$\hat{\boldsymbol{\theta}} = \underset{\boldsymbol{\theta}}{\operatorname{argmax}} \left[\log \mathbb{P}[\mathcal{D}|\boldsymbol{\theta}] + \lambda_{\Delta\sigma} \|\Delta\sigma_w - \mu_{\Delta\sigma}\|_2^2 \right] \tag{6.17}$$

Finally, if $\mathcal{U}$ priors are prescribed over both variables, the log-likelihood is not regularised, and MAP reduces to the mere MLE.

It should be emphasised that the distribution of prior knowledge is generally unknown. Nevertheless, a rational approximation that can be made is the assumption of Gaussian distribution. It is important to state that if a sufficiently large dataset is available, this assumption can be readily checked. The user can actually choose the most appropriate prior to model the distribution of the concerned parameters. In the present work, however, Gaussian priors were adopted to make the calculation more tractable, while easily introducing the most common L2-regularisation for the log-likelihood. Furthermore, hypothesising independent distributions for each element of the prior is typically not restrictive. In fact, this practice is generally advisable rather than erroneously speculating about the underlying relationship amongst the

parameters, thus injecting biased information into the learning stage.

The maximisation of the $\log \mathbb{P}[\boldsymbol{\theta}|\mathbf{x}]$ (Eq. (2.36)) provides the expected value of the parameters, namely $\hat{\boldsymbol{\theta}} = [\Delta\hat{K}_{th,lc} \quad \Delta\hat{\sigma}_w]$ whereby $\sqrt{\hat{\text{area}}_0}$ was evaluated according to Eq. (6.2). Correspondingly, the expected EH curve is determined through Eq. (6.1):

$$\Delta\sigma = \Delta\hat{\sigma}_w \sqrt{\frac{\sqrt{\hat{\text{area}}_0}}{\sqrt{\hat{\text{area}}_0} + \sqrt{\text{area}}}} \tag{6.18}$$

Further operations are required to fully characterise the posterior $\mathbb{P}[\boldsymbol{\theta}|\mathcal{D}]$. According to Bayes' theorem, albeit $\mathbb{P}[\mathcal{D}|\boldsymbol{\theta}]$ and $\mathbb{P}[\boldsymbol{\theta}]$ can promptly be evaluated, the integral of $\mathbb{P}[\mathcal{D}]$ (Eq. (2.33)) is generally intractable, thus $\mathbb{P}[\boldsymbol{\theta}|\mathcal{D}]$ does not possess a closed-form expression. As commonly performed in other contexts of ML methods, Laplace's approximation for the posterior is invoked, see Section 2.3.2. Accordingly, the posterior $\mathbb{P}[\boldsymbol{\theta}|\mathcal{D}]$ turns out to be:

$$\mathbb{P}[\boldsymbol{\theta}|\mathcal{D}] \sim \mathcal{N}(\hat{\boldsymbol{\theta}}, \mathbf{H}^{-1}) \tag{6.19}$$

where $\mathbf{H}^{-1}$ is the inverse of the Hessian matrix of $-\log \mathbb{P}[\boldsymbol{\theta}|\mathcal{D}]$ evaluated at $\hat{\boldsymbol{\theta}}$.

Finally, the marginalisation of Eq. (6.19) allows the distribution of each parameter in $\hat{\boldsymbol{\theta}}$ to be automatically evaluated:

$$\Delta K_{th,lc} \sim \mathcal{N}(\Delta\hat{K}_{th,lc}, \mathbb{V}[\Delta\hat{K}_{th,lc}]) \tag{6.20}$$

$$\Delta\sigma_w \sim \mathcal{N}(\Delta\hat{\sigma}_w, \mathbb{V}[\Delta\hat{\sigma}_w]) \tag{6.21}$$

where $\mathbb{V}[\Delta\hat{K}_{th,lc}] = [\mathbf{H}^{-1}]_{11}$ and $\mathbb{V}[\Delta\hat{\sigma}_w] = [\mathbf{H}^{-1}]_{22}$ correspond to the diagonal terms of $\mathbf{H}^{-1}(\hat{\boldsymbol{\theta}})$, which are in fact the associated variance of each parameter.

6.2.4. Probabilistic Crack Propagation Region

A Monte Carlo simulation exploited the marginal posterior distributions of the parameters to built a probabilistic fatigue endurance limit curve. This approach commences with sampling $\mathcal{N}(\Delta\hat{K}_{th,lc}, \mathbb{V}[\Delta\hat{K}_{th,lc}])$ and $\mathcal{N}(\Delta\hat{\sigma}_w, \mathbb{V}[\Delta\hat{\sigma}_w])$ using Sobol's low-discrepancy sequences via *SALib - Sensitivity Analysis Library in Python* [236–238]. The sampling, therefore, generates M Monte Carlo trials whose j-th element is $\boldsymbol{\theta}^{(j)} = [\Delta K_{th,lc}^{(j)} \quad \Delta\sigma_w^{(j)}]^\top$. Upon computing $\sqrt{\text{area}_0}^{(j)}$ by Eq. (6.2), the j-th EH

curve turns out to be:

$$\mathcal{E}^{(j)} : \Delta\sigma^{(j)} = \Delta\sigma_w^{(j)} \sqrt{\frac{\sqrt{\text{area}_0}^{(j)}}{\sqrt{\text{area}_0}^{(j)} + \sqrt{\text{area}}}} \quad \forall\, j = 1, 2, \ldots, \mathsf{M} \tag{6.22}$$

Let $\overline{\mathcal{E}^{(m)}} = \mathbb{E}[\{\mathcal{E}^{(1)}, \mathcal{E}^{(2)}, \ldots, \mathcal{E}^{(m)}\}]$ be the $\sqrt{\text{area}}$-wise expected value of the history of EH curves up to the m-th trial. If M is sufficiently large, the Central Limit Theorem allows one to readily compute the $\sqrt{\text{area}}$-wise prediction intervals [239]:

$$\mathbb{P}\left[\overline{\mathcal{E}^{(\mathsf{M})}} - \mathcal{P}^{(\mathsf{M})} \leq \mathcal{E}^{(\mathsf{M}+1)} \leq \overline{\mathcal{E}^{(\mathsf{M})}} + \mathcal{P}^{(\mathsf{M})}\right] = \beta \tag{6.23}$$

where β is confidence level and $\mathcal{P}^{(\mathsf{M})}$ is the semi-amplitude of the interval defined as:

$$\mathcal{P}^{(\mathsf{M})} = t_\beta S^{(\mathsf{M})} \sqrt{1 + 1/\mathsf{M}} \tag{6.24}$$

In Eq. (6.24), $S^{(\mathsf{M})} = \sqrt{\mathbb{V}[\{\mathcal{E}^{(1)}, \mathcal{E}^{(2)}, \ldots, \mathcal{E}^{(\mathsf{M})}\}]}$ is the $\sqrt{\text{area}}$-wise standard deviation of the whole history of EH curves, and t_β is the $1 - \beta/2$ percentile of Student's t-distribution with $\mathsf{M} - 1$ degrees of freedom. From a mathematical perspective, Eq. (6.23) is naturally interpreted as the interval, namely $\mathcal{E}^{(\mathsf{M}))} \pm \mathcal{P}^{(\mathsf{M})}$, where the $(\mathsf{M}+1)$-th EH curve is expected to belong, given the collection of trials $\mathcal{E}^{(1)}, \mathcal{E}^{(2)}, \ldots, \mathcal{E}^{(\mathsf{M})}$, for a confidence level β. Such a confidence level is of utmost importance during the structural design process of a mechanical component to define the acceptable level of risk for a specific engineering problem.

In order to monitor the convergence of the Monte Carlo simulation, the following indicator was adopted:

$$\rho^{(j)} = \sqrt{\frac{(\mathcal{E}^{(j)} - \mathcal{E}^{(j-1)})^2}{(\mathcal{E}^{(j)})^2}} \tag{6.25}$$

Essentially, this indicator evaluates the relative residual between two consecutive EH curves $\mathcal{E}^{(j)}$ and $\mathcal{E}^{(j-1)}$.

6.2.5. Computational Algorithm

Algorithm 3 is finally presented to offer a succinct overview of the computational setting illustrated thus far.

Algorithm 3 Computational algorithm for LR in the present study.

— **Logistic Regression** —
Require: Preparation of dataset $\mathcal{D}$ ▷ Eq. (6.3)
Transform data points – if necessary – by SIF equivalence ▷ Eq. (6.4)
Require: Functional form of the decision boundary $\mathcal{H}(\mathbf{x}, \boldsymbol{\theta})$ ▷ Eq. (6.7)
— **Maximum a Posteriori** —
Require: Log-Prior $\log \mathbb{P}[\boldsymbol{\theta}] = \log \mathbb{P}[\Delta K_{th,lc}] + \log \mathbb{P}[\Delta\sigma_w]$ ▷ Eq. (6.10)
Require: Log-likelihood $\mathbb{P}[\mathcal{D}|\boldsymbol{\theta}]$
Build Log-Posterior $\log \mathbb{P}[\boldsymbol{\theta}|\mathcal{D}] = \log \mathbb{P}[\mathcal{D}|\boldsymbol{\theta}] + \log \mathbb{P}[\boldsymbol{\theta}]$
Maximise log-posterior ▷ Eq. (2.36)
Ensure: Optimal parameters $\hat{\boldsymbol{\theta}} = [\Delta\hat{K}_{th,lc} \quad \Delta\hat{\sigma}_w]$
Compute optimal EH curve ▷ Eq. (6.18)
— **Probabilistic Crack Propagation Region** —
Require: Approximated Posterior $\mathbb{P}[\boldsymbol{\theta}|\mathcal{D}] \sim \mathcal{N}(\hat{\boldsymbol{\theta}}, \mathbf{H}^{-1})$
Require: Marginal Posterior $\Delta K_{th,lc} \sim \mathcal{N}(\Delta\hat{K}_{th,lc}, \mathbb{V}[\Delta\hat{K}_{th,lc}])$ ▷ Eq. (6.20)
Require: Marginal Posterior $\Delta\sigma_w \sim \mathcal{N}(\Delta\hat{\sigma}_w, \mathbb{V}[\Delta\hat{\sigma}_w])$ ▷ Eq. (6.21)
— **Monte Carlo Simulation** —
for $i \in \{1, 2, \ldots, \mathsf{M}\}$ **do**
Draw sample from $\Delta K_{th,lc} \sim \mathcal{N}(\Delta\hat{K}_{th,lc}, \mathbb{V}[\Delta\hat{K}_{th,lc}])$ ▷ Eq. (6.20)
Draw sample from $\Delta\sigma_w \sim \mathcal{N}(\Delta\hat{\sigma}_w, \mathbb{V}[\Delta\hat{\sigma}_w])$ ▷ Eq. (6.21)
Compute & collect the j-th EH curve $\mathcal{E}^{(j)}$ ▷ Eq. (6.22)
— **Check convergence** —
if $\rho^{(j)}$ sufficiently small **then** ▷ Eq. (6.25)
Terminate simulation
else
Continue simulation
end if
end for
— **Prediction Intervals** —
Require: Confidence level β
Compute prediction intervals of the collected m EH curves ▷ Eq. (6.23)

6.3. Material Datasets

This section attempts summarising experimental datasets available in the current literature devoted to fatigue tests, on metallic materials containing defects, for the characterisation of fatigue endurance limits. Alongside, this literature survey intends to provide potential practitioners with additional inputs to both support the application of the presented method and achieve more accurate estimates of $\Delta K_{th,lc}$ and $\Delta\sigma_w$. The collected data can refer to the SIF threshold for long cracks $\Delta K_{th,lc}$ and the fatigue limit of a defect-free specimen $\Delta\sigma_w$ when available. In case of tested materials, for instance, using multiple batches or by introducing artificial defects of different nature, Tables 6.1-6.5 indicate ranges for $\Delta K_{th,lc}$ and $\Delta\sigma_w$ using the symbol "$-$". In a few cases, multiple references are specified for a single dataset, meaning that complementary information for the same material can be retrieved from different sources.

The key purpose of this task is the retrieval of relevant information regarding some of most commonly used metallic materials to enforce the lack of necessary information for a univocal evaluation of the EH curve given a certain incomplete experimental dataset. In particular, the present section summarises the data regarding Fe-, Al-, Ti-, Ni-, Mg-based alloys. The results obtained in such a literature survey are summarised in Tables 6.1-6.5, in which all the relevant characteristic conditions are reported alongside, such as the manufacturing conditions, further treatments, type of loading, and stress ratio R. It is worth remarking that a comprehensive review on the fatigue strength characterisation for AMed AlSi10Mg and Ti-6Al-4V can be found in [209]. Alongside, a systematic survey of fatigue properties for many metals, spanning AMed and cast Fe- and Ti-based alloys both, is presented in [240]. While, an exhaustive literature review on the fatigue properties of Mg alloys is given in [241].

Table 6.1. Datasets of Fe-based alloys. Additive manufacturing, wrought, and cast are abbreviated as AM, WR, and CS, respectively. A $*$ denotes data that are not available or indicated in the corresponding references.

Material	Manufacturing details	Loading mode	R	$\Delta K_{th,lc}$ [MPa$\sqrt{\text{m}}$]	$\Delta\sigma_w$ [MPa]	Reference(s)
AISI304	Machined	Rot. Bending	-1	6.44	293 – 297	[242]
	Machined, annealed, polished	Rot. Bending	-1	5.28	296 – 300	
AISI316L	AM (L-PBF)	Tension	-1	9.04	900	[243]
	AM (L-PBF)	Tension	0.1	6.40	511	
AISI316L	AM (L-PBF)	Tension	0.1	2.6 – 3.4	556 – 580	[244, 245]
AISI316L	AM (L-PBF)	Tension	0.1	9.1 – 9.9	$*$	[246, 247]
AISI403	WR (Annealed)	Tension	-1	6.6	780	[248, 249]
X20Cr13 (AISI 420)	WR (Annealed)	Tension	-1	6.6	868	[248–250]
17-4PH (AISI 630)	WR	Tension	-1	6.7	747 – 799	[251]
17-4PH (AISI 630)	WR (PH H1150)	Tension	-1	6.7	1126	[248, 250, 252]
17-4 PH (AISI 630)	AM (L-PBF)	Tension	-1	7.27	2130	[253]
	AM (L-PBF)	Tension	0.1	4.06	$*$	
	AM (L-PBF)	Tension	0.7	2.47	$*$	
25CrMo4	$*$	Tension	-1	14.65	694	[254, 255]
Maraging Steel 300	AM	Tension	-1	6.26	1146	[250]
	AM	Tension		5.69	1776	
	AM	Tension		5.70	1978	
Mild Steel	WR	Bending	-1	10.4	470	[250, 256]
Mild Steel	WR	Bending	-1	12.4	326	[250, 256]
Mild Steel	WR	Tension	-1	13.0	340	[250, 257]
Nodular Cast Iron	CS	Tension	0.1	$*$	360	[258, 259]

Table 6.2. Datasets of Al-based alloys. Additive manufacturing, wrought, and cast are abbreviated as AM, WR, and CS, respectively. A † in "Loading mode" indicates data obtained through fatigue crack growth test, whereas a $*$ denotes data that are not available or indicated in the corresponding references.

Material	Manufacturing details	Loading mode	R	$\Delta K_{th,lc}$ [MPa$\sqrt{\text{m}}$]	$\Delta\sigma_w$ [MPa]	Reference(s)
AlSi10Mg	AM (L-PBF, as built)	Tension	0.1	1.04	155.2	[260]
	AM (L-PBF, machined)	Tension	0.1	1.53	298.2	
AlSi10Mg	AM (L-PBF, as-built)	Bending	0.1	1.41	174	[261]
AlSi10Mg	AM (L-PBF)	Tension	-1	3.2 – 3.6	380 – 420	[212]
AlSi10Mg	AM	Tension	-1	$*$	$*$	[51]
AlSi7Mg0.6	AM (L-PBF)	Tension	-1	0.96 – 1.70	$*$	[262]
AlSi7Mg0.6	AM	Tension	0.1	3.99 – 4.72	400	[263]
A356-T6	CS	Tension	-1	$*$	70 – 90	[264]
	CS	Tension	0	$*$	40 – 75	
	CS	Torsion	-1	$*$	50 – 87	
	CS	Torsion	0	$*$	40 – 73	
	CS	Tension-Torsion	-1	$*$	45 – 68	
	CS	Tension-Torsion	0	$*$	35 – 45	
A357-T6 (+ Sr)	CS	Tension	-1	$*$	214	[265]
	CS	Tension	0.1	$*$	94 – 138	
AlSi8Cu3 T6 Sr	CS	Tension	-1	1.13 – 1.16	84 – 100	[266, 267]
AlSi8Cu3 T6 Sr	CS - HIP	Tension	-1	0.69 – 1.31	122 – 145	[266, 267]
AlSi7Cu0.5Mg T6 Sr	CS	Tension	-1	5.34 – 5.36	69.4 – 113.7	[267, 268]
AlSi7Cu0.5Mg T6 Na	CS	Tension	-1	5.19	47.8 – 71.6	[267, 268]
AlSi7Cu0.5Mg T7 Sr	CS	Tension	-1	4.36 – 5.06	75.0 – 103.5	[267, 268]
AlSi8Cu3 T6	CS - HIP	Tension	-1	3.54	212.8	[232]
AS7G06-T6	CS	Tension	-1	$*$	91	[269]
	CS	Tension	0.1	$*$	66	
2024	T3	Tension	-1	4.8	332	[270]
7075	T6	Tension	-1	4.0	336	[270]
7049	$*$	†	-3,-2,-1	2 – 5	$*$	[271]
6061	Cold-Spray	†	0.1 – 0.7	1.3 – 2.8	$*$	[272]
	Rolled	†	0.1	3.8	$*$	

Table 6.3. Datasets of Ti alloys. Additive manufacturing, wrought, and cast are abbreviated as AM, WR, and CS, respectively. A † in "Loading mode" indicates data obtained through fatigue crack growth test, whereas a $*$ denotes data that are not available or indicated in the corresponding references.

Material	Manufacturing details	Loading mode	R	$\Delta K_{th,lc}$ [MPa$\sqrt{\text{m}}$]	$\Delta\sigma_w$ [MPa]	Reference(s)
Ti-6Al-4V	AM (WAAM)	Tension	0.1	4.5	540	[273]
Ti-6Al-4V	AM (L-PBF)	Tension	-1	2.33	342 – 663	[274]
Ti-6Al-4V	AM	Tension	0.1	$*$	325	[275]
Ti-6Al-4V	AM (EBM)	Tension	-1	6.82	1181	[208, 250]
	AM (L-PBF)	Tension	-1	6.79	1210	
Ti-6Al-4V	Mill annealed bar stock	Tension	0.1	1 – 4.3	450	[276]
Ti-6Al-4V	AM (L-PBF)	Tension	-1	7.3 – 7.5	753.4 – 1086	[277]
Ti-6Al-4V	AM (L-PBF)	Tension	-1	5.6	914 – 1086	[270]
Ti-6Al-4V	$*$	Tension	0.1	3.73 – 5.22	160 – 200	[278]
Ti-6Al-4V	AM (L-PBF)	Tension	-1	3.9	389 – 432	[279]
Ti-6Al-4V	AM (EBM)	Tension	0.1	3.4 – 5.7	$*$	[280]
Ti-6Al-4V	AM (EBM)	Bending	-1	5.5 – 8.4	680 – 1050	[281]
Ti-6Al-4V	AM (L-PBF)	Tension and bending	0.1	2 – 6.7	195 – 221	[282]
Ti-6Al-4V	AM (L-PBF)	†	0.1	1.8–4.1	$*$	[283]
Ti-6Al-4V	AM (LENS)	†	0.1	2.6–4.5	$*$	[284]
	AM (EBM)	†		3.2–5	$*$	
Ti-6Al-4V	AM (L-PBF, as-built)	†	0.1	1.52–1.82	$*$	[285]
	AM (L-PBF, HIP)	†	0.1	3.12–4.53	$*$	
	AM (L-PBF, HT 1020)	†	0.1	6.22–7.29	$*$	
TC21	$*$	Tension	-1	2.8	430	[286]

Table 6.4. Datasets of Ni-based alloys. Additive manufacturing, wrought, and cast are abbreviated as AM, WR, and CS, respectively. A † in "Loading mode" indicates data obtained through fatigue crack growth test, whereas a $*$ denotes data that are not available or indicated in the corresponding references.

Material	Manufacturing details	Loading mode	R	$\Delta K_{th,lc}$ [MPa$\sqrt{\text{m}}$]	$\Delta\sigma_w$ [MPa]	Reference(s)
Inconel 625	AM (L-PBF)	Tension	0.1	7.0	590	[287]
Inconel 625	WR	†	0.1	7.2	$*$	[288]
	AM (L-PBF, annealed)	†	0.1	$7.1 - 10.6$	$*$	
	AM (L-PBF, HIP)	†	0.1	$10.9 - 11.1$	$*$	
Inconel 625	AM (L-PBF)	†	$0.1 - 0.7$	$5 - 10$	$*$	[289]
Inconel 718	AM (L-PBF)	Tension	-1	6	$*$	[64, 65]
	AM (L-PBF)	Tension	0.1	4	$*$	
Inconel 718	AM (L-PBF)	Tension	-1	13.7	$*$	[290]
Inconel 718	AM (L-PBF)	Tension	-1	12	506	[291]
Inconel 718	AM (L-PBF)	Tension	-1	$1.81 - 2.06$	$250 - 325$	[292]
Inconel 718	AM (L-PBF)	Tension	-1	12	946	[293]
Inconel 718	AM (L-PBF)	Tension	0.1	$*$	$*$	[294]
Inconel 718	AM (L-PBF)	†	0.1	1.5	$*$	[295]
Inconel 718	AM (L-PBF)	†	0.1	3.0	$*$	[296]
K418	CS	Tension	-1	13.85	$*$	[297]
	CS	Tension	0.1	12.09	$*$	

Table 6.5. Datasets of Mg-based alloys. Additive manufacturing, wrought, and cast are abbreviated as AM, WR, and CS, respectively. A † in "Loading mode" indicates data obtained through fatigue crack growth test, whereas a $*$ denotes data that are not available or indicated in the corresponding references.

Material	Manufacturing details	Loading mode	R	$\Delta K_{th,lc}$ [MPa$\sqrt{\text{m}}$]	$\Delta\sigma_w$ [MPa]	Reference(s)
AM50hp	Die-CS Conventional	Tension	0.1	1.36 – 1.62	49	[233]
AZ91hp	Die-CS (Conventional)	Tension	0.1	$*$	44	[233]
	Die-CS (Vacural)	Tension	0.1	1.43 – 1.61	62	
AS21hp	CS	†	-1	1.30 – 2.3	$*$	[298]
AZ31	Extruded	Tension	-1	0.85	88	[299]
AZ31	Extruded	Rot. Bending	-1	0.35	$*$	[300]
AZ31B	Extruded	Tension	0.10 – 0.75	0.95 – 2.43	$*$	[301]
AZ31B	Rolled	†	0.1	1.23 – 2.00	$*$	[302]
	Rolled	†	0.5	0.85 – 1.54	$*$	
	Rolled	†	0.75	0.77 – 1.07	$*$	
AZ91D	Die-CS	†	0.1	4	$*$	[303]
AZ61	Extruded	Rot. Bending	-1	0.39	$*$	[304]
AZ61	Extruded	Tension	-1	0.8	140 – 200	[305]
AZ61	WR	†	-1	1.1 – 1.9	$*$	[306]
AM60	Anodised	Tension	0.1	0.86	72	[307]
AM60hp	CS	†	-1	1.40 – 2.4	$*$	[298]
AS21hp	CS	†	-1	1.25 – 2.7	$*$	[298]

Amongst the considerable collection of references presented herein, two metallic alloys were selected to develop and assess the effectiveness of the conceived approach, namely AlSi8Cu3 [232] and AISI316L [243], both tested at $R = -1$ through alternating tensile fatigue tests. Regarding the size of the datasets, i.e. the amount of point data thereof, it is possible to observe that the dataset of the former alloy is about six times smaller than that of the latter; see Figures 6.1(a)-(b). This allowed the proposed method to be tested for two different scenarios, namely small- and large-data regimes. As far as AlSi8Cu3 is concerned, the specimens were cast and underwent T6 heat treatment and machining. The authors of Ref. [232] stated that the defects that supposedly initiate cracks were regraded as surface defects, thus prompting to adopt $Y = 0.65$ for the calculation of the SIF range. Nonetheless, upon machining such surface defects, these turned out to be most akin to opened cracks, thus substantially changing the scenario. For this reason, the authors of the work decided to adopt $Y = 0.73$ for the evaluation of the SIF range [232], and so was adopted herein as well. On the other hand, the AISI316L samples were built using L-PBF along the vertical direction, then machined and polished. The authors of Ref. [243] aimed to assess whether the fatigue response had been sensitive to defects of different nature. To this end, apart from few specimens which did not undergo any further operations, the remaining ones were alternatively subjected to machining & polishing, or pre-corrosion via anodic polarisation, or electrical discharge machining to produce hemispherical defects. Additional analyses revealed that the defects were primarily located near the surface, whereas only a small fraction were classified as internal. In this regard, the SIF range for surface defects was calculated adopting $Y = 0.65$ as per semi-circular cracks, while $Y = 0.5$ was used for internal defects, in agreement to [2]. Given the negligible number of internal defects, in this case these were converted by setting $Y_{eq} = 0.65$ and rescaling the respective $\sqrt{\text{area}}$ to $\sqrt{\text{area}}_{eq}$ using Eq. (6.4).

Figure 6.1(a)-(b) shows the datasets of the chosen metallic alloys. The i-th specimen of each dataset were characterised by $\sqrt{\text{area}_i}$ and $\Delta\sigma_i$. Different markers were used to distinguish failed specimens from those that run out. Additionally, the markers were coloured according to ΔK computed through Eq. (5.3), whose value can be read on the rightmost colour bar.

In agreement with the stages of the LR-MAP approach and the structure of the datasets outlined in Eq. (6.3), the algorithm does not necessitate specific pre-

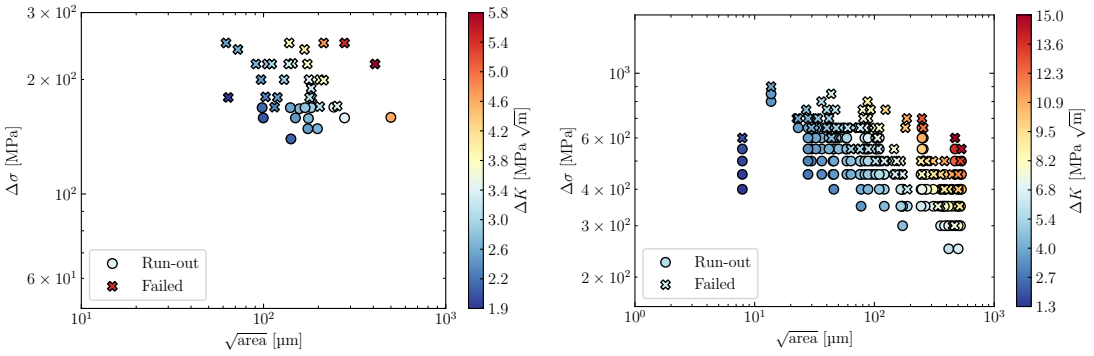

Figure 6.1. Datasets examined for the development of the LR method. (a) AlSi8Cu3 [232]. (b) AISI316L [243]. The specimens of both datasets were subjected to alternating tensile fatigue test at $R = -1$.

processing of the data. Nonetheless, the user is committed to consider transforming $\sqrt{\text{area}}_i$ when defects are characterised by different Y_i. Additionally, the approach handles specimens probed at unique fatigue testing conditions, i.e. same mode and stress ratio.

It is worth pointing out that this probabilistic assessment of the fatigue endurance curve is independent on the distribution of the defect size. In fact, the essential information about the size of the defects observed in the probed material is encoded into the likelihood function whereby the failure probability is modelled (see Eq. (2.65)).

6.4. Application of the Method and Discussion

6.4.1. Small dataset Case-study (AlSi8Cu3)

The first case study presented herein regards an AlSi8Cu3 taken from [232], whose associated dataset is shown in Figure 6.1(a).

Figures 6.2(a)-(c) summarises the contour plots of the log-likelihood, log-prior and log-posterior. Thanks to the opportune parametrisation of $\sqrt{\text{area}}$ (see Section 6.2.2) each contour is a function of $\Delta K_{th,lc}$ and $\Delta\sigma_w$.

The log-likelihood $\log \mathbb{P}[\mathcal{D}|\boldsymbol{\theta}]$ built upon the considered dataset is displayed in Figure 6.2(a). The visual inspection of $\log \mathbb{P}[\mathcal{D}|\boldsymbol{\theta}]$ disclosed the absence of maximum

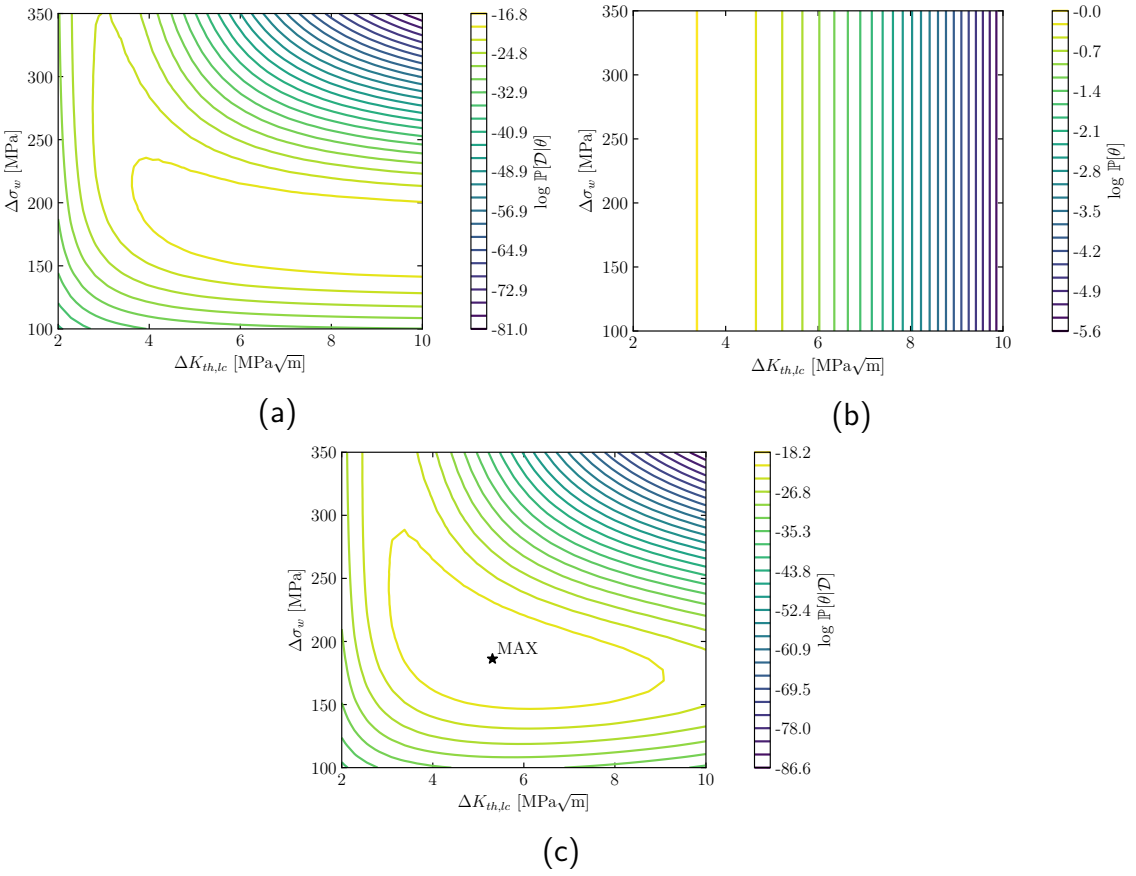

Figure 6.2. The elements of the MAP regarding the AlSi8Cu3 dataset. (a) Log-likelihood (b) Log-prior (c) Log-posterior.

points. As a result, the sole maximisation of the log-likelihood would not have estimated any of the parameters sought. In particular, the optimiser would have moved toward $\Delta\sigma_w \simeq 180\,\text{MPa}$ and $\Delta K_{th,lc} \to +\infty$ indefinitely while seeking the maximum.

Although this preliminary assessment seems to hinder the parameter estimation, it concurs with the conformation of the dataset. A close examination of Figure 6.1(a) revealed that failed and runout specimens can be – almost exactly – separated by a horizontal having intercept $\Delta\sigma_w \simeq 180\,\text{MPa}$. Despite matching the experimental evidence, these results would be unacceptable from an engineering design perspective as they would consider also unrealistic values of $\Delta K_{th,lc}$. A specific choice of priors

allowed for circumventing this issue. Since no information about $\Delta K_{th,lc}$ could be essentially inferred from the dataset, $\Delta K_{th,lc} \sim \mathcal{N}(3.3, 1.4^2)\,\mathrm{MPa}\sqrt{\mathrm{m}}$ was prescribed as a prior, whose parameters are the mean and the variance of the set of $\Delta K_{th,lc}$ obtained by gathering data of similar materials from [266–268]. On the other hand, $\Delta\sigma_w$ was already expected to be around 180 MPa. Therefore, it was sufficient to rely upon the experimental evidence and prescribe a non-informative $\mathcal{U}$ prior for this parameter, hence $\Delta\sigma_w \sim \mathcal{U}$. The resulting log-prior $\log \mathbb{P}[\boldsymbol{\theta}] = \log \mathbb{P}[\Delta K_{th,lc}] + \log \mathbb{P}[\Delta\sigma_w]$ is shown in Figure 6.2(b).

Figure 6.2(c) shows the log-posterior $\log \mathbb{P}[\boldsymbol{\theta}|\mathcal{D}]$ given by the sum of the log-likelihood (Figure 6.2(a)) and the log-prior (Figure 6.2(b)). Herein, it is possible to recognise that $\log \mathbb{P}[\boldsymbol{\theta}|\mathcal{D}]$ peaked at $\hat{\boldsymbol{\theta}} = [\Delta\hat{K}_{th,lc} \quad \Delta\hat{\sigma}_w] = [5.4 \quad 187.1]$, thus providing the expected values of the parameters. Following, these values were exploited to apply Laplace's approximation to $\log \mathbb{P}[\boldsymbol{\theta}|\mathcal{D}]$ and compute the posterior $\mathbb{P}[\boldsymbol{\theta}|\mathcal{D}]$. The subsequent marginalisation of $\mathbb{P}[\boldsymbol{\theta}|\mathcal{D}]$ provided the distributions of the estimated parameter, i.e. $\Delta K_{th,lc} \sim \mathcal{N}(5.4, 1.3^2)\,\mathrm{MPa}\sqrt{\mathrm{m}}$ and $\Delta\sigma_w \sim \mathcal{N}(187.1, 20.4^2)\,\mathrm{MPa}$. Figure 6.3(a) shows the contour plot of $\mathbb{P}[\boldsymbol{\theta}|\mathcal{D}]$, whereas Figure 6.3(b) offers a graphical representation of the marginal distributions of $\Delta K_{th,lc}$ and $\Delta\sigma_w$.

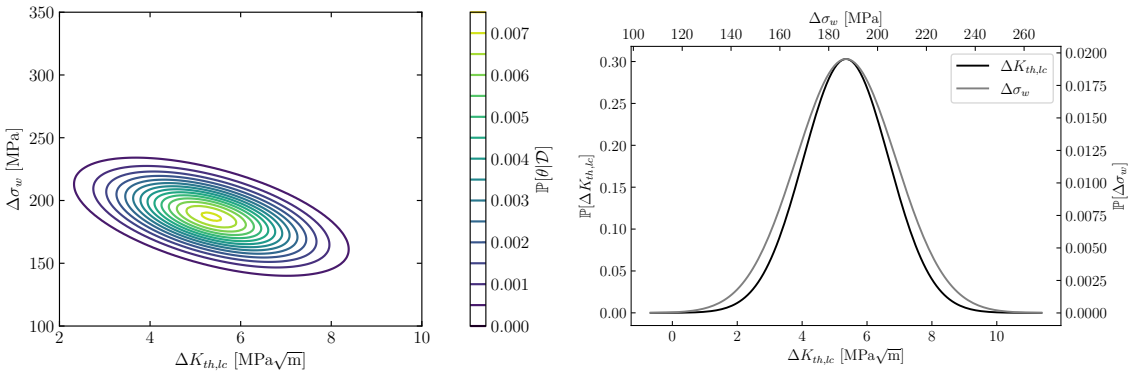

Figure 6.3. Results of the MAP and marginalisation of the posterior (a) Contour plots of the posterior of AlSi8Cu3 dataset. (b) Marginal distributions of $\Delta K_{th,lc}$ and $\Delta\sigma_w$ in black and grey, respectively.

6.4.2. Large dataset Case-study (AISI316L)

It is interesting to note that, even in this case, the log-likelihood did not reveal any maximum point, see Fig 6.4(a). As a consequence, $\Delta K_{th,lc}$ and $\Delta\sigma_w$ would have been, again, unidentifiable unless specific priors had been defined. Moreover, the datasets shown in Figure 6.1(b) did not exhibit any distinctive characteristic, such as preferred values of the parameters whereby the dataset could have been split – similarly to the former case. In order to accomplish the training stage, the following priors $\Delta K_{th,lc} \sim \mathcal{N}(6.8, 0.28^2)\,\text{MPa}\sqrt{\text{m}}$ and $\Delta\sigma_w \sim \mathcal{N}(864.0, 136.8^2)\,\text{MPa}$ were prescribed, again, by gathering data of similar materials from [248–253]. The combinations of these priors computed through Eq. (6.10) is portrayed in Figure 6.4(b). Upon injecting these priors into the learning stage and computing the log-posterior (Figure 6.4(c)), the MAP successfully estimated the expected parameters, $\Delta\hat{K}_{th,lc} = 7.5\,\text{MPa}\sqrt{\text{m}}$ and $\Delta\hat{\sigma}_w = 1003\,\text{MPa}$. Next, Laplace's approximation permitted the posterior to be evaluated, which is displayed in Figure 6.5(a). Finally, the marginal posterior distribution of each parameter was calculated, resulting in $\Delta K_{th,lc} \sim \mathcal{N}(7.5, 0.3^2)\,\text{MPa}\sqrt{\text{m}}$ and $\Delta\sigma_w \sim \mathcal{N}(1003, 146^2)\,\text{MPa}$. Such marginal distribution are displayed in Figure 6.5(b).

6.4.3. Results and Discussion

Table 6.6 succinctly gathers the MAP estimates of $\Delta K_{th,lc}$ and $\Delta\sigma_w$ in terms of 99.7% confidence intervals and the reference values from the literature. Regarding AlSi8Cu3, the reported intervals satisfactorily match the data from the literature for both $\Delta K_{th,lc}$ and $\Delta\sigma_w$ and corroborate the thorough choice of the prior adopted. Nonetheless, the agreement with the literature was only partially achieved as concerns AISI316L. Whilst the interval estimates of $\Delta\sigma_w$ includes its reference counterpart, the analogous estimate for $\Delta K_{th,lc}$ revealed the corresponding reference value to be unlikely. This could be interpreted as being a consequence of the selected prior for $\Delta K_{th,lc}$. In this regard, the data borrowed from the literature appears tightly centred around $6.8\,\text{MPa}\sqrt{\text{m}}$, thus resulting in a limited standard deviation as high as $0.28\,\text{MPa}\sqrt{\text{m}}$. These features biased the posterior by concentrating its distribution around $7.5\,\text{MPa}\sqrt{\text{m}}$ with a relatively small standard deviation of $0.3\,\text{MPa}\sqrt{\text{m}}$, thus reflecting the traits of the prior. Moreover, the $\Delta K_{th,lc}$ value provided by the literature is certainly affected by both epistemic and aleatoric errors that undoubt-

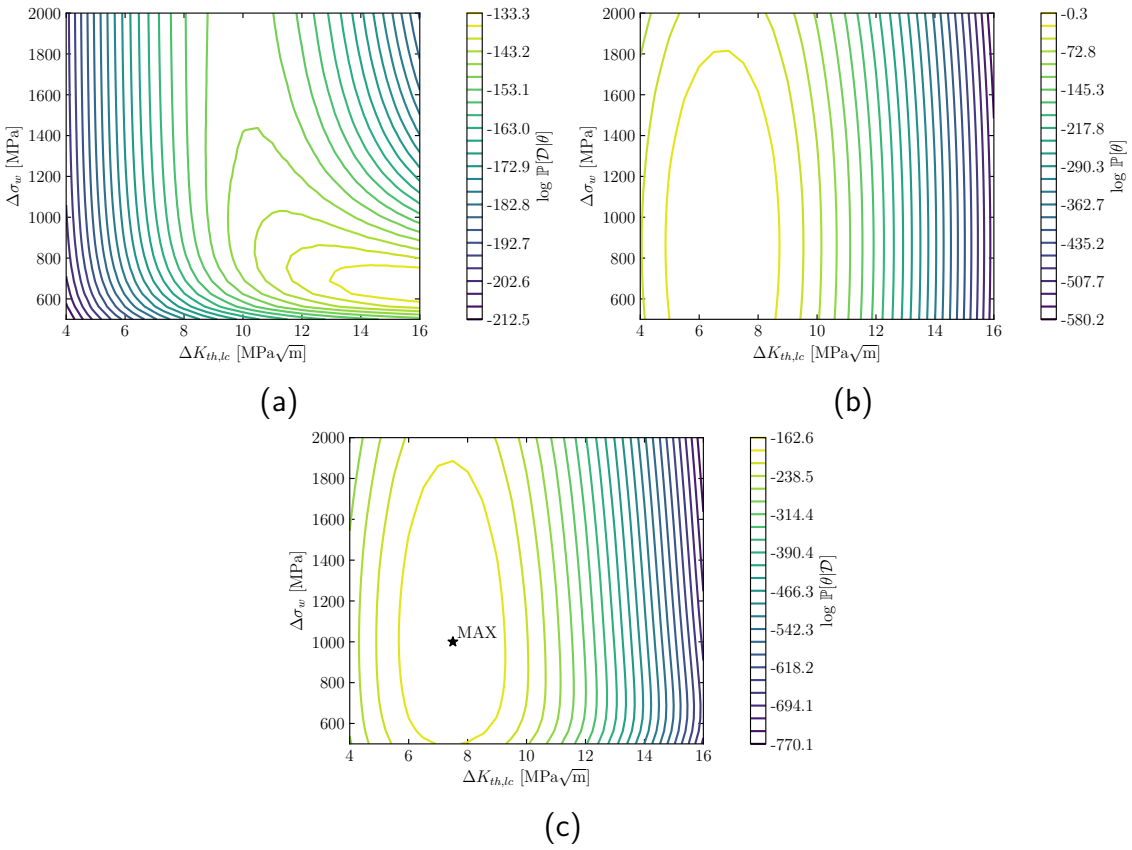

Figure 6.4. The elements of the MAP regarding the AISI316L dataset. (a) Log-likelihood (b) Log-prior (c) Log-posterior.

edly affect its reliability. However, this results and the choice of the priors are not limiting as one can leverage the excellent flexibility of the conceived methodology. Specifically, should further data regarding the characterisation of AISI316L be available, the prior can be readily updated to obtain more and more truthful appraisals of the parameters. Despite this, the estimates are conservative as compared with the reference values so that they can be deemed as acceptable given the restrictive data availability.

It should be mentioned that the microstructure of the material under examination may affect fatigue performance and, consequently, have implications on the evaluated EH parameters. Nevertheless, the results obtained through this method can be compared to other similar materials having the same microstructural characteristics,

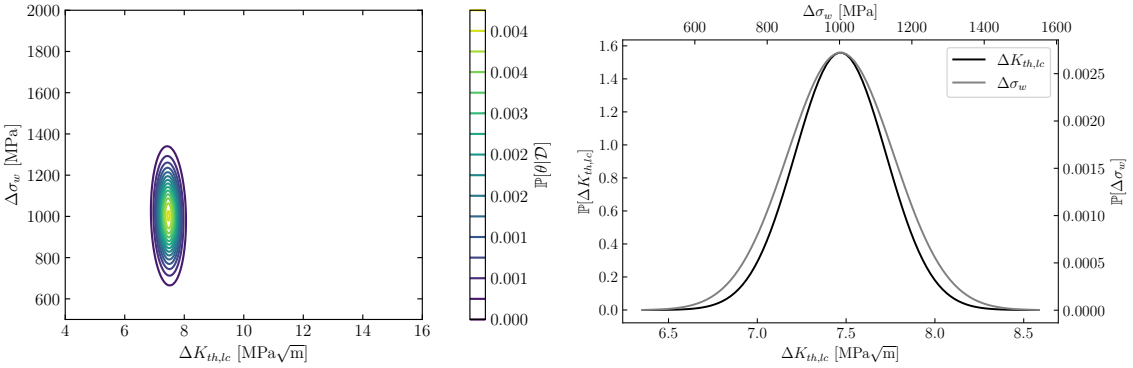

Figure 6.5. Results of the MAP and marginalisation of the posterior (a) Contour plots of the posterior distribution of AISI316L dataset. (b) Marginal distributions of $\Delta K_{th,lc}$ and $\Delta\sigma_w$ in black and grey, respectively.

Table 6.6. 99.7% probabilistic intervals of the estimated parameters and comparison with the literature.

Material	$\Delta\hat{K}_{th,lc} \pm 3\sqrt{\mathbb{V}[\Delta\hat{K}_{th,lc}]}$ [MPa$\sqrt{\text{m}}$]	$\Delta\hat{\sigma}_w \pm 3\sqrt{\mathbb{V}[\Delta\hat{\sigma}_w]}$ [MPa]	$\Delta K_{th,lc}$ Ref. [MPa $\sqrt{\text{m}}$]	$\Delta\sigma_w$ Ref. [MPa]	Ref.
AlSi8Cu3	$5.4 \pm 3 \cdot 1.3$	$187.1 \pm 3 \cdot 20.4$	3.54	212.8	[232]
AISI316L	$7.5 \pm 3 \cdot 0.3$	$1003 \pm 3 \cdot 146$	9.04	900	[243]

i.e. fabricated employing the same manufacturing conditions. Hence, the retrieved EH parameters are exclusively valid for the specific analysed material. In this instance, the sole feature that is meant to vary is the size of the defect where the fatal fatigue crack originated from. On the other hand, it is not possible to characterise the long crack fatigue behaviour unless bespoke experimental would be deployed. In this regard, the intrinsic material defects span (approximately) from 10 µm to 10^3 µm in terms of the defect representative size. To overcome this limitation the proposed methodology exploits literature data to estimated rational interval which the EH parameters should belong to.

The obtained marginal posterior distributions of $\Delta K_{th,lc}$ and $\Delta\sigma_w$ were utilised to conduct a Monte Carlo simulation to determine the probabilistic fatigue endurance

limit curve, following the procedure laid out in Section 6.2.4. The outcomes of the statistical post-processing (see Section 6.2.4) are graphically summarised in Figure 6.6(a) and Figure 6.6(b) for AlSi8Cu3 and AISI316L, respectively. The black solid line indicated in these figures is the evaluated EH curve, i.e. the EH curve given by the expected estimated parameters, whereas the grey solid line is the reference EH curve retrieved from the literature. Additionally, the dot-dashed and dashed lines are the lower ($\mathcal{E}^{(\mathsf{M})} - \mathcal{P}^{(\mathsf{M})}$) and upper ($\mathcal{E}^{(\mathsf{M})} + \mathcal{P}^{(\mathsf{M})}$) bound of the prediction interval computed through Eq.(6.24). For the sake of convenience, each figure reports the related experimental dataset. Besides the mathematical interpretation of the prediction intervals given in Section 6.2.4, $\mathcal{E}^{(\mathsf{M})} \pm \mathcal{P}^{(\mathsf{M})}$ defines the probabilistic crack propagation region. In particular, its lower and upper bounds are regarded as the failure probability thresholds at 2.5% and 97.5% respectively, for the adopted confidence level $\beta = 95\%$ (Eq. (6.24)).

The evaluated EH curves shown in Figure 6.6 concurs well with the corresponding reference ones. This could be attributed the distinctive marginal posterior of each identified parameter. In this respect, the reference values of $\Delta K_{th,lc}$ and $\Delta\sigma_w$ are included within the 99.7% probabilistic interval in Table 6.6, thus resulting likely values with respect to the relative marginal posterior. This however is not fully confirmed when considering $\Delta K_{th,lc}$ of AISI316. Specifically, its reference value falls outside the probability interval so that it appears unlikely. Despite this, the evaluated EH curves can be considered as acceptable, since the scope of this method is estimating the fatigue endurance limit by the sole exploitation of fatigue characterisation and literature data, rather than seeking a perfect match with the reference curves.

The peculiar characteristics of the marginal posterior are reflected on the prediction intervals as well. During the Monte Carlo simulation, samples are drawn from the marginal posterior distributions of $\Delta K_{th,lc}$ and $\Delta\sigma_w$. Consequently, if the reference values belongs to the 99.7% probabilistic interval, these values are likely to be drawn from the marginal posteriors. Also, the closer are the reference values to the mode of the respective marginal posterior the higher the probability of being drawn is. Therefore, the associated EH curve trials are supposed to increasingly approach the corresponding reference EH curve to a certain extent. In particular, if the reference values of $\Delta K_{th,lc}$ and $\Delta\sigma_w$ lays in a sufficiently narrow neighbourhood of the mode, the prediction interval will enclose the reference EH curve with the

confidence level β. This could evidently be seen for AlSi8Cu3 by comparing the values in Table 6.6 and Figure 6.6(a). By contrast, since the evaluated $\Delta K_{th,lc}$ of AISI316 falls outside the probabilistic interval and far away from the mode of the posterior, this property does not hold, see Figure 6.6(b). Further, Figure 6.6(b) also highlight the implication of the chosen prior. In this respect, the limited scatter of the literature values of $\Delta K_{th,lc}$ drastically narrowed the prediction band across the long cracks regime. As briefly mentioned earlier this phenomenon can be mitigated by enriching the prior with data from the literature spanning a wider range of $\Delta K_{th,lc}$.

Furthermore, a rapid critical inspection of the results shown in Figure 6.6 enables one to assess the buoyancy of the EH curves evaluated at different failure probability levels. Particularly, apart from the regions of the diagram where failed and runout specimens coexist, each curve reasonably leaves failed and runout specimens above and beneath the EH curves, according to their respective level of failure probability. As a result, each probabilistic EH curve accommodates the natural conformation of the dataset.

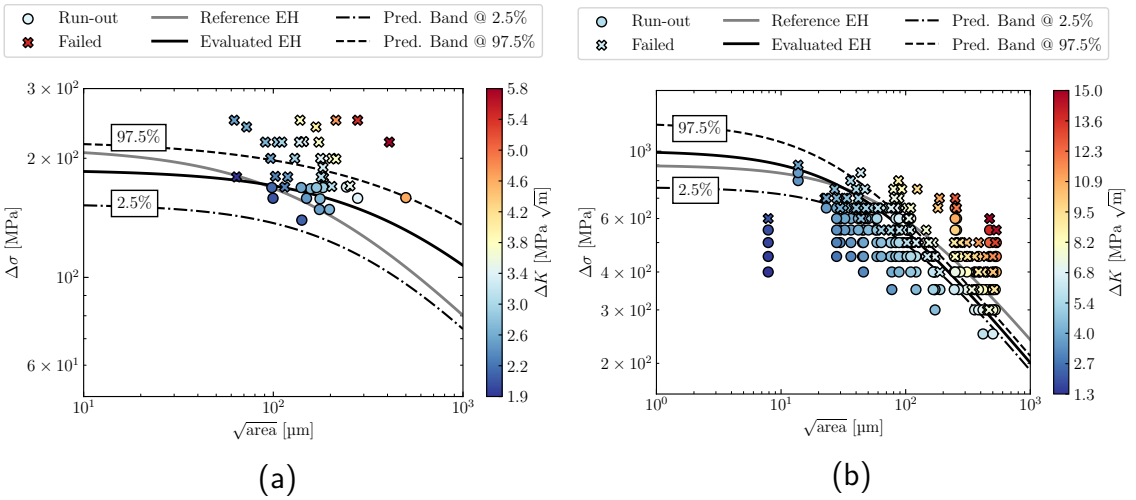

Figure 6.6. Probabilistic fatigue endurance limit at 2.5% and 97.5% failure probability along with the examined datasets (a) AlSi8Cu3 (b) AISI316L.

It is also useful to briefly comment on the behaviour of the convergence indicator ρ_i defined in Eq. (6.25). Except for a few initial fluctuations, ρ_i converged rapidly toward zero. Although the total number of Monte Carlo samples was set to $\mathsf{M} =$

12288, Figure 6.7 suggests that 1000 samples would have sufficed. In fact, after this number of samples, ρ_i stabilised and exhibited negligible oscillation so that the convergence could have been considered as achieved.

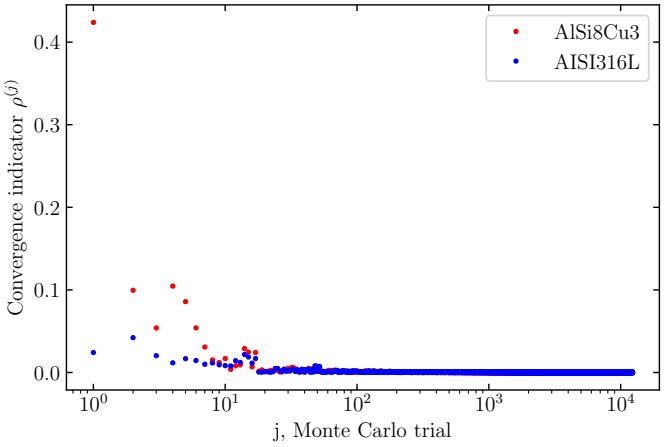

Figure 6.7. Convergence indicator throughout the Monte Carlo simulation.

Figure 6.6 which shows the probabilistic endurance limit curves evaluated using the entire dataset. For the sake of validating the developed LR-MAP framework, the same curves are retrieved splitting the full dataset into the training set $\mathcal{D}_{tr}$, which LR is trained on, and test set $\mathcal{D}_{ts}$, which was held out, such that $\mathcal{D}_{tr} \cup \mathcal{D}_{ts} = D$, $\mathcal{D}_{tr} \cap \mathcal{D}_{ts} = \emptyset$, and $\mathsf{N}_{tr} + \mathsf{N}_{ts} = \mathsf{N}$. Since a typical 80/20 random split was adopted, the training and test dataset were proportionally partitioned as $\mathsf{N}_{tr} = 0.8\,\mathsf{N}$, and $\mathsf{N}_{ts} = 0.2\,\mathsf{N}$. Importantly, the training stage exploited the same priors used earlier.

Table 6.7 reports the identified parameters which approaches those in Table 6.6, thus proving the robustness of the LR-MAP approach.

Figure 6.8 shows the evaluated EH curves at different levels of failure probability obtained by partitioning the dataset. The points belonging to $\mathcal{D}_{tr}$ are indicated in agreement with the markers of Figure 6.6. Whilst, failed and runout specimens belonging to $\mathcal{D}_{ts}$ are denoted by "plus" and triangle markers. It can be noticed once again that each curve divides failed specimens from runout specimens, according to their respective level of failure probability – except for the region were failed and runout may overlap.

Table 6.7. 99.7% probabilistic intervals of the estimated parameters and comparison with the literature. This intervals were retrieved conducting the training stage on the sole $\mathcal{D}_{tr}$.

Material	$\Delta\hat{K}_{th,lc} \pm 3\sqrt{\mathbb{V}[\Delta\hat{K}_{th,lc}]}$ [MPa$\sqrt{\text{m}}$]	$\Delta\hat{\sigma}_w \pm 3\sqrt{\mathbb{V}[\Delta\hat{\sigma}_w]}$ [MPa]	$\Delta K_{th,lc}$ Ref. [MPa $\sqrt{\text{m}}$]	$\Delta\sigma_w$ Ref. [MPa]	Ref.
AlSi8Cu3	$5.2 \pm 3 \cdot 1.3$	$188.6 \pm 3 \cdot 22.3$	3.54	212.8	[232]
AISI316L	$7.3 \pm 3 \cdot 0.26$	$1003 \pm 3 \cdot 107$	9.04	900	[243]

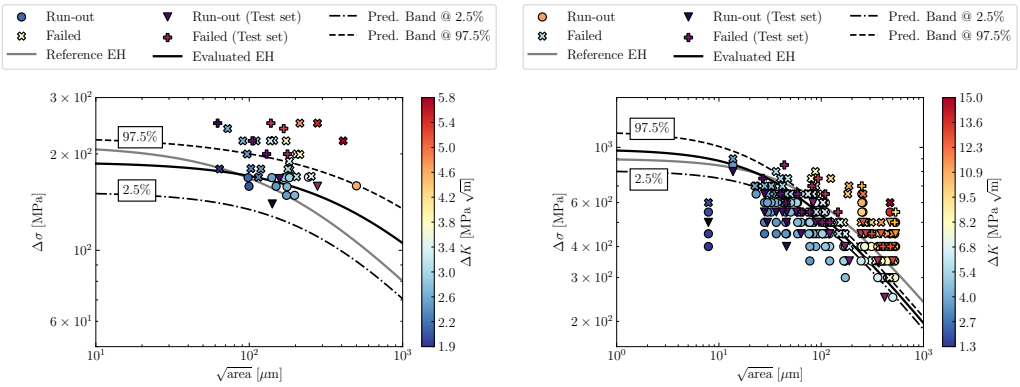

(a) (b)

Figure 6.8. Probabilistic fatigue endurance limit at 2.5% and 97.5% failure probability along with the examined datasets. This curves were retrieved conducting the training stage on the sole $\mathcal{D}_{tr}$ (a) AlSi8Cu3 (b) AISI316L.

6.5. Conclusions

The computational framework proposed herein allows for an accurate probabilistic evaluation of the fatigue endurance limit in metallic materials containing defects. The underlying method relies on the elegant combination of LR and MAP which enables for probabilistically evaluating the EH's parameters ($\Delta K_{th,lc}$ and $\Delta\sigma_w$). This methodology seamlessly merges partial fatigue results of a probed material and the available results taken from the literature that help enforce the physical soundness of the evaluated parameters. Consequently, a relatively limited number of fatigue tests is sufficient to attain a comprehensive fatigue characterisation and curb the

onerousness of its protocol.

The LR-MAP strategy outputs the probability distributions of $\Delta K_{th,lc}$ and $\Delta\sigma_w$. Subsequently, these distribution can be supplied to a Monte Carlo simulation to evaluate the fatigue endurance limit curve for a specified level of failure probability, e.g. 2.5%. This outcome can directly be used when designing engineering structures or components following a probabilistic framework.

Two different metallic alloys, i.e. AlSi8Cu3 and AISI316L, were considered to demonstrate the effectiveness of the LR-MAP appoach. In both examples, the intervention of MAP showed its excellent inclination at incorporating prior knowledge from the literature, thus leading to univocal estimates of the EH parameters. Additionally, a 80/20 random split of the dataset enabled for validating the LR-MAP, while demonstrating its robustness and predictive capabilities.

The LR-MAP method will bring extremely relevant implications in many fatigue design contexts, especially those dealing with defective materials, such as AM. Accurate fatigue endurance curves will increasingly empower the implementation of emerging techniques in numerous advanced engineering applications.

7. Defect-based Prediction of Fatigue Endurance Limit for Metallic Alloys via Bayesian Physics-Guided Neural Networks

This chapter showcases a B-PINN-inspired predictive model to forecast the fatigue endurance limit of metallic materials in the presence of defects. Particularly, an NN is rigorously endowed with BI where the EH is used to infer a prior for NN's parameters, thereby allowing the NN to reproduce the phenomenological behaviour of the EH. Pertinent defect descriptors are collated into a dataset whereby the likelihood is constructed. In agreement with BI, the prior and the likelihood are then cast into Bayes' theorem to compute the posterior of the NN's parameters.

7.1. Introduction

Section 1.2 and Chapter 5 widely discussed how defects massively cause scattered fatigue data, which consequently retain both epistemic and aleatory uncertainty, thus invariably compromising a reliable assessment of fatigue performance [11, 308–310]. Therefore, deterministic data-driven and physics-informed ML models cannot adequately capture this aspect that is of great importance when designing engineering components against fatigue failure. Moreover, these approaches may suffer from small-data regimes. For this reason, the employment of probabilistic approaches is gaining more interest. In fact, another variant of PINNs, referred to as Probabilistic Physics-guided (PPgNN), has emerged alongside to address this drawback [218, 311]. The PPgNN was instructed by fatigue data while reinforcing the training using S-N curves – not strictly defect-based, though. A similar strategy was pursued to pre-

dict the fatigue life of diverse Fe-based materials [312]. Despite being probabilistic, PPgNN are merely frequentist, so they cannot guarantee optimal performance in small-data regimes as well.

Given its potential, BI represents a viable solution to circumvent the limitations of the current deterministic and frequentist ML techniques. Additionally, BI automatically provides a formal probabilistic modelling setting with a built-in uncertainty quantification framework, provided adequate prior domain knowledge [313–315]. Nonetheless, relatively little research has been devoted to applying BI-based methods to problems related to fatigue, e.g. experimental S-N curve fitting [308, 316, 317], ML evaluation of the fatigue endurance limit of metallic alloys [90], prediction of crack nucleation and growth in Ni-based and Ti-based superalloys [318–321].

A potential strategy for predicting the fatigue endurance limit of defect-laden metallic materials while quantifying the associated uncertainty would be the exploitation of B-PINNs, see Section 2.6.2. Nevertheless, the classical B-PINNs primarily focus on PDE-governed problems, as seen in recent engineering application as well [322–324]. Moreover, in this B-PINN framework, the physics governing the problem is injected to modify the likelihood, instead of the prior distribution – which is not formally correct as compared with the Bayesian setting. However, while the likelihood modification approach is more akin to the training for deterministic PINNs, designing priors tailored for a particular application is the natural channel for embedding expert knowledge in BNNs [108, 325, 326]. Crucially, crafting priors resembling the problem's formulation is an essential requirement to obtain good quality uncertainty estimation and a well-calibrated posterior [327]. Thus, further effort must concentrate on synergically merging the settings of PINNs with BI to deal with the present problem while adhering to a rigorous Bayesian treatment. However, it is important to remark that one approach does not exclude the other.

The present chapter borrows the implementation of semi-empirical laws for PINNs from Chapter 5, and complements it with formal BI. Specifically, a standard BNN is initially considered. In agreement with the Bayesian setting, the prior of the BNN is inferred from the selected semi-empirical law. After this stage, the BNN holds the ability to reproduce the phenomenological behaviour of the semi-empirical law, so the BNN morphs into a B-PGNN. Since this particular procedure is not envisaged by the consolidated B-PINNs, the nomenclature "B-PGNN" (where "G" stands for guided) is decidedly employed to make this distinction clearer. However, "informed"

and "guided" seem to be interchangeable in the context of these peculiar NN [328]. Following this preliminary stage, the likelihood is built upon the training dataset, and the posterior is then given by Bayes' theorem (Eq (2.32)). Finally, the posterior is numerically approximated (Section 2.3.2). An overview of the B-PGNN's structure is depicted in Figure 7.1 to clearly emphasise the differences with Figure 2.13.

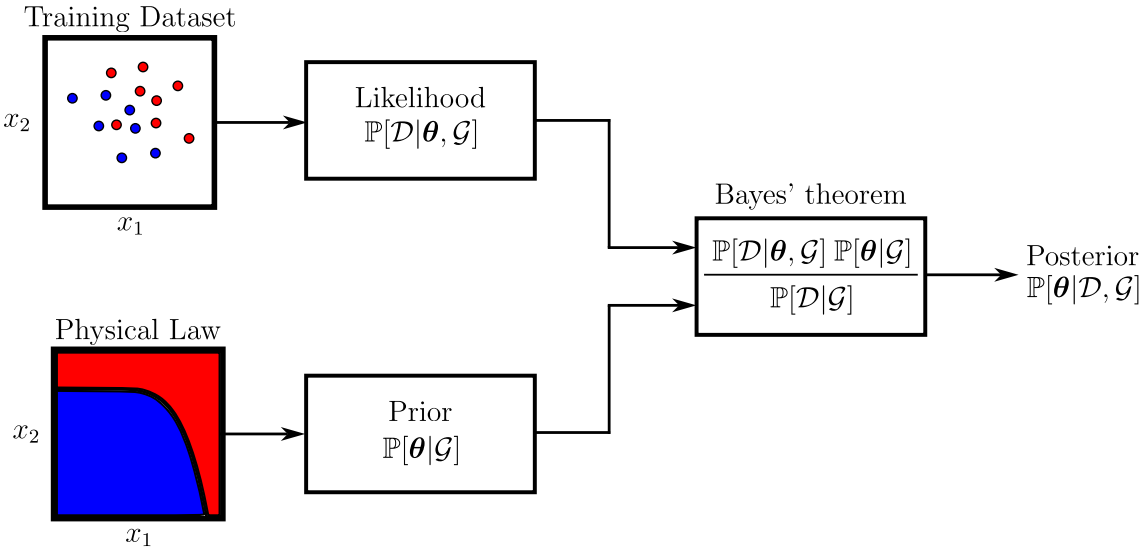

Figure 7.1. Block diagram of the training the B-PGNNs. Herein, $\mathcal{G}$ succinctly denotes the B-PGNN architecture defined according to Eq. (2.68). The prior of the parameters $\boldsymbol{\theta}$, i.e. $\mathbb{P}[\boldsymbol{\theta}|\mathcal{G}]$, is inferred from a "physical" law. Given a training dataset $\mathcal{D}$ the likelihood $\mathbb{P}[\mathcal{D}|\boldsymbol{\theta},\mathcal{G}]$ is built, which is plugged along with the prior into Bayes's theorem. As a result the posterior $\mathbb{P}[\boldsymbol{\theta}|\mathcal{D},\mathcal{G}]$ is computed, alternatively through VI or HMC, allowing for subsequent predictions.

The key objective of the B-PGNN is to predict whether a specimen retaining certain defectivity traits attains a given fatigue life, i.e. the number of cycles, when subjected to a prescribed fatigue load; sometimes referred to as material fatigue limit. The present investigation focusses on the SLM AlSi10Mg literature dataset exploited in Section 5. It is worth recalling that the specimens were tested via alternate tensile fatigue tests, and comprehensive defect descriptors are available from both ante- and post-mortem analysis via CT scan and fractography, respectively. Initially, the fractographic data and further literature information are used to determine the semi-empirical reinforcement of the B-PGNN, i.e. the EH curve of the dataset, following Chapter 6. The retrieved EH curve is then opportunely

generalised to handle the descriptors contained in the CT dataset. The generalised EH curve is then transferred to the parameters (weights & biases) of the B-PGNN as a prior to inform its physical side. Whilst the data-driven side of the B-PGNN is ruled by the likelihood built upon the available experimental CT dataset. Thus, BI is pursued to compute the posterior of the parameters. Consequently, the B-PGNN learns how to predict the failure probability of the samples while providing the uncertainty of such predictions. Furthermore, a K-fold cross-validation is performed to assess the robustness of the B-PGNN and its performance over the BNN counterpart is examined. Alongside, a Bayesian model selection method is presented to identify the optimal B-PGNN architecture amongst many candidate configurations. As an ancillary result, the B-PGNN is exploited to shed light on the correlations between the predictions and descriptors from CT scans, which would not be disclosed if the classic EH model were adopted.

7.2. Materials and Methods

7.2.1. Overview of the Dataset

The present study considers as a case study the literature dataset used in Chapter 5, which was borrowed from [52]. In this instance, the fatigue endurance limit of the dataset was referred to the runout threshold $N_w = 2 \cdot 10^6$. In order to obtain a satisfactory characterisation of the fatigue endurance limit, particular attention was devoted to filtering a sufficient number of runout and failed samples. According to the prescribed runout threshold, the runout and failed specimens are distinguished by $N \geq N_w$ and $N < N_w$, respectively. Table 7.1 summarises the outcomes and the related classification of the samples considered for the development of the B-PGNN approach.

As already described in Chapter 5, each specimen was examined through CT to characterise its defectivity prior to fatigue testing. Herein, a few descriptors employed for the development of the PINN are considered again, for instance, $\sqrt{\text{area}}$, sphericity S (Eq. (5.1)), and equivalent diameter d (Eq. (5.2)). In the present investigation, LEFM is still assumed to hold, and defects are modelled as cracks with length equal to $\sqrt{\text{area}}$. This hypothesis allows ΔK to be adopted as the fatigue crack driving force. Differently from Chapter 5, Y is evaluated through

Table 7.1. Summary of the fatigue test campaign. Samples marked with $*$ underwent prior testing at a lower $\Delta\sigma$.

Sample	$\Delta\sigma$ [MPa]	N [-]	Outcome
1	295.4	46255	`Failed`
2	400.0	474	`Failed`
3	220.0	8889311	`Runout`
3*	360.0	3432	`Failed`
4	156.0	3795336	`Runout`
5	301.6	39538	`Failed`
6	378.3	11465	`Failed`
7	298.5	19806	`Failed`
8	156.0	20000000	`Runout`
9	180.0	11352768	`Runout`
10	220.0	2622640	`Runout`
11	180.0	237485	`Failed`
12	200.0	15242310	`Runout`

pure Murakami's criterion [2], i.e. Eq. (5.6). Amongst numerous acquired defects for each sample, the present research prioritises those yielding the maximum ΔK. These defects are listed in Table 7.2 which indicates the values of the descriptors alongside.

The post-mortem fractography characterised, where detectable, the defects that actually triggered fatigue failure in terms of $\sqrt{\text{area}}$ and, again, the distance h between the defect's centroid and the free-surface of the specimen. Additionally, Murakami's criterion (Eq. (5.6)) was applied to compute Y and the corresponding ΔK. Table 7.3 reports the outcomes of this investigation. The defect pertaining to the twelfth sample of Table 7.3 was originally categorised as sub-surface defect, i.e. $Y = 0.5$. However, EH curve should be referred to a unique class of defect [62]. Eq. (6.4), i.e. the SIF equivalence, was used to convert the original $\sqrt{\text{area}}$ into the equivalent $\sqrt{\text{area}}_{eq} = 440.0\mu\text{m}$ while assigning $Y = 0.65$ to this defect.

Figure 7.2(a) shows the CT dataset given in Table 7.2, where purple circles and yellow cross markers indicates runout and failed samples, respectively. Similarly, Figure 7.2(b) portrays $\sqrt{\text{area}}$ and $\Delta\sigma$ acquired by fractography. Therein, markers

Table 7.2. Defect descriptors acquired via CT-scan yielding the maximum ΔK.

Sample	$\sqrt{\text{area}}$ [µm]	h [µm]	d [–]	S [–]	Y [–]	ΔK [MPa$\sqrt{\text{m}}$]
1	214.2	110.9	186.7	0.35	0.65	5.0
2	275.0	308.8	256.5	0.27	0.65	7.6
3	283.4	134.3	253.0	0.25	0.65	4.3
4	334.5	233.8	227.6	0.32	0.65	3.3
5	379.1	269.5	260.9	0.29	0.65	6.8
6	429.2	222.8	340.6	0.23	0.65	9.0
7	443.3	207.6	401.8	0.21	0.65	7.2
8	458.2	214.2	341.4	0.24	0.65	3.8
9	470.0	222.3	342.6	0.25	0.65	4.5
10	497.8	310.1	418.3	0.17	0.65	5.7
11	568.8	332.0	398.6	0.20	0.65	4.9
12	572.0	373.7	410.2	0.21	0.65	5.5

Table 7.3. Available defect descriptors acquired via fractography.

Sample	$\sqrt{\text{area}}$ [µm]	Y [-]	ΔK [MPa$\sqrt{\text{m}}$]
1	128.8	0.65	3.9
2	378.2	0.65	9.0
3	168.8	0.65	5.4
8	500.0	0.65	2.6
9	437.4	0.65	4.3
10	271.5	0.65	4.2
12	440.0	0.65	4.2

are coloured according to the associated ΔK whose value can be read from the rightmost colour bar.

7.2.2. El Haddad's Curve of the Fractography Dataset

The EH curve illustrated in Section 2.2.2 is considered to build the physical constraint of the B-PGNN. In this instance, the EH is referred to the aforementioned

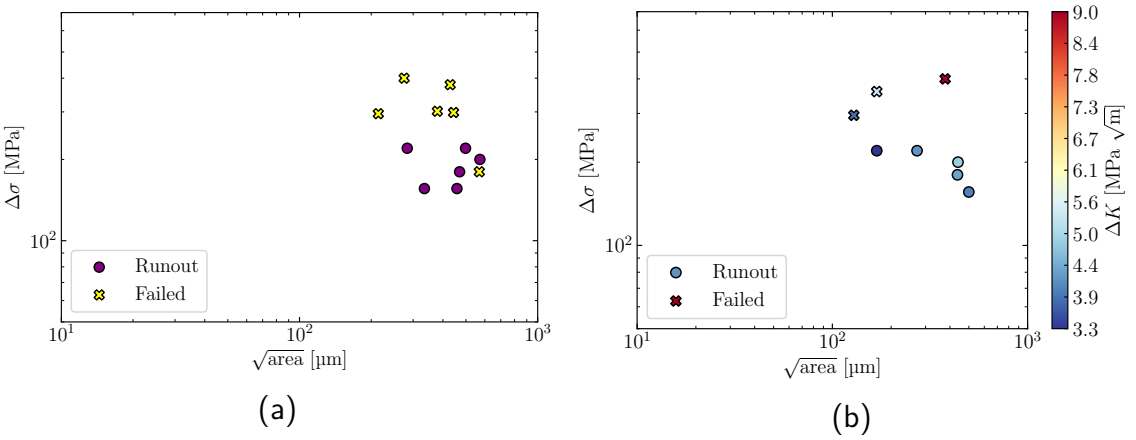

Figure 7.2. (a) CT dataset (b) Fractography dataset.

runout threshold N_w to outline the fatigue endurance limit of the examined material. Furthermore, the EH is restated in terms of $\sqrt{\text{area}}$. Consequently, the formulation shown in Eq. (6.1) is assumed herein as well as the EH critical length of Eq. (6.2) [62, 234]. In the following, the generic EH curve will concisely be denoted as $\mathcal{E}$.

The identification of the EH parameters, i.e. $\Delta K_{th,lc}$ and $\Delta\sigma_w$, is carried out using the MAP approach comprehensively described in Chapter 6. In this instance, it is worth structuring the fractographic dataset:

$$\mathcal{D}_H = \{(\mathbf{x}_i, \mathcal{F}_i) : \mathbf{x}_i = \left[\sqrt{\text{area}}_i \quad \Delta\sigma_i\right], i = 1, 2, 3, 8, 9, 10, 12\} \tag{7.1}$$

where $\mathcal{F}_i$ is determined according to:

$$\mathcal{F}_i = \begin{cases} 0 & \text{if } N \geq N_w \\ 1 & \text{if } N < N_w \end{cases} \tag{7.2}$$

where 0 and 1 stand for runout and failed, respectively. For the sake of the identification, the input vector was equivalently restated as $\mathbf{x}_i = \left[\Delta K_i, \Delta\sigma_i\right]$ using Eq. (2.16). Whilst for the remainder of the implementation, the input vector is assumed as $\mathbf{x}_i = \left[\sqrt{\text{area}}_i \quad \Delta\sigma_i\right]$ as per Eq. (7.1). Results from the literature were used to inform independent priors $\mathbb{P}[\Delta K_{th,lc}] = \mathcal{N}(4.9, 1.6^2)\,\text{MPa}\sqrt{\text{m}}$ and $\mathbb{P}[\Delta\sigma_w] = \mathcal{N}(330.7, 10.4^2)\,\text{MPa}$ for the EH parameters [212, 260–263]. MAP

was then pursued to compute the corresponding marginal posterior distributions $\mathbb{P}[\Delta K_{th,lc}|\mathcal{D}_H]$, and $\mathbb{P}[\Delta\sigma_w|\mathcal{D}_H]$, whose expected values $\Delta\hat{K}_{th,lc}$ and $\Delta\hat{\sigma}_w$ are the EH parameters sought. The EH curve referred to these values will be denoted as $\hat{\mathcal{E}}$.

7.2.3. Learning El Haddad's Curve

The primary objective of this framework is to surrogate the following model:

$$\mathcal{F}_i = \mathcal{G}_{\boldsymbol{\theta}}(\mathbf{x}'_i) \tag{7.3}$$

by a B-PGNN whose architecture is defined in Eq. (2.68), where $\boldsymbol{\theta}$ are the B-PGNN's parameters, which obey BI. Whilst $\mathbf{x}'_i$ is a generic vector gathering all the relevant defect's descriptors as shown shortly. The first step necessary for the application of the B-PGNN framework to the present problem aims to encode the EH curve into the prior of the BNN. Although BNNs are flexible models that can tightly approximate any smooth function, they are characterised by a non-linear relationship between the distribution placed on the weights and the resulting functional form of their output. Therefore, the EH curve cannot be analytically encoded. Nevertheless, as highlighted in the following, a method for accurate encoding of the prior can be designed through a combination of synthetic data generation, learning, and posterior tempering by relying on the concept of catalytic priors [326, 329].

In the specific problem analysed herein, the set of problem descriptors considered thus far is initially extended. In fact, the application of ML allows for considering features whose relationships with the predictor are already well-understood physically, but also descriptors that potentially hold complementary information. Specifically, beside $\sqrt{\text{area}}$ and already considered in the EH curve, the vector representing the BNN input, $\mathbf{x}_i$, is expanded as:

$$\mathbf{x}'_i = \begin{bmatrix} \sqrt{\text{area}}_i & d_i & S_i & \Delta\sigma_i \end{bmatrix} \tag{7.4}$$

Intuitively, the feature $\sqrt{\text{area}}$ allows the B-PGNN to account for the extension of the defects, whereas the combination of $\sqrt{\text{area}}$ and d (Eq. (5.2)) indirectly encode the influence of the defect's thickness. Additionally, S (Eq. (5.1)) was selected as a shape parameter since it introduces the functional dependence on three-dimensional morphological traits. Specifically, S can allow for spheroidal defects (e.g. gas pores)

to be distinguished from those being more crack-like (e.g. lack-of-fusion) when $S \to 1$ and $S \to 0$, respectively. As opposed to the set of inputs used in Chapter 5, h was not included in the model since Murakami's criterion (Eq. (5.6)) categorises all the instances of Table 7.2 as surface defects. Thanks to the flexibility of the present framework, any other available descriptors relevant to the problem can be potentially included in $\mathbf{x}'_i$.

To encode the EH curve in the BNN, the catalytic prior framework [326, 329] is pursued. A synthetic dataset is generated such that it encapsulates the behaviour of the EH curve in a discretised fashion. In order to do so, a uniform grid over the entries of $\mathbf{x}_i$ is defined – this step only affects $\sqrt{\text{area}_i}$ and $\Delta\sigma_i$. Whilst the additional descriptors specific to the BNN are sampled from a Gaussian distribution with mean and variance set according to the experimental data listed in Table 7.2:

$$\begin{bmatrix} d_i & S_i \end{bmatrix} \sim \mathcal{N}(\boldsymbol{\mu} = \begin{bmatrix} 320 & 0.25 \end{bmatrix}, \boldsymbol{\Sigma} = \text{diag} = (80^2, 0.05^2)) \tag{7.5}$$

With the resulting samples a synthetic dataset is built as follows:

$$\mathcal{D}_S = \{(\mathbf{x}'_i, \mathcal{F}_i) : \mathbf{x}'_i = \begin{bmatrix} \sqrt{\text{area}}_i & d_i & S_i & \Delta\sigma_i \end{bmatrix}, i = 1, 2, \ldots, \mathsf{M}\} \tag{7.6}$$

where $\mathcal{F}_i$ depends only on the EH input descriptors.

In short, the catalytic prior is learnt through the BNN from the synthetic dataset $\mathcal{D}_S$. Formally, a standard Gaussian distribution is initially placed over the weight, $\mathbb{P}[\boldsymbol{\theta}|\mathcal{G}]$ so that the catalytic prior is retrieved from a straightforward application of the Bayesian formula:

$$\mathbb{P}[\boldsymbol{\theta}|\mathcal{D}_S, \mathcal{G}] = \frac{\mathbb{P}[\mathcal{D}_S|\boldsymbol{\theta}, \mathcal{G}]^\tau \, \mathbb{P}[\boldsymbol{\theta}|\mathcal{G}]}{\mathbb{P}[\mathcal{D}_S|\mathcal{G}]} \tag{7.7}$$

which is approximated using VI and the implementation is carried out through *Pyro* [330]. Differently from the standard Bayes' theorem (Eq. (2.32)), Eq. (7.7) implements an additional parameter τ, called *temperature* [327]. In the current application, τ balances the relative weight between the importance given to the physics and that given to the observed dataset. Specifically, τ is chosen as suggested in Ref. [326, 329] such that $\tau = p/\mathsf{M}$; where $\mathsf{M} = \max\{400, 4p\}$ (Eq. (7.6)) and p is the number of B-PGNN's parameters. The influence of τ shall be clarified later in regard to the present problem. Furthermore, Eq. (7.7) is not yet the learning

stage of the final B-PGNN, but only its first step encoding the physics information into the BNN model. Before discussing this aspect, however, a Bayesian method to identify a suitable architecture of $\mathcal{G}$ is illustrated.

7.2.4. Model Selection

The design of the BNN prior to reproduce the EH curve has been discussed without referring to any specific architecture $\mathcal{G}$. The present section addresses the issue of selecting the optimal architecture from a given set of configurations by exploiting Bayesian model selection presented in Section 2.6.5.

Consider the CT dataset given in Table 7.2, formally:

$$\mathcal{D}_N = \{(\mathbf{x}'_i, \mathcal{F}_i) : \mathbf{x}'_i = \left[\sqrt{\text{area}}_i \quad d_i \quad S_i \quad \Delta\sigma_i\right], i = 1, 2, \ldots, 12\}. \tag{7.8}$$

where $\mathcal{F}_i$ refers to the ground-truth label obtained by combining the data in Table 7.1 and Eq. (7.2). The first step consists in dividing the dataset into a training set, $\mathcal{D}_T$, and a validation one, $\mathcal{D}_V$, which reserves one-third of the data for the latter. In addition, a train-test K-fold split is performed thrice so that each data point is included in the validation set once. This results in the definition of three K-fold pairs which are denoted by $\mathcal{D}_T^{(K)}$ and $\mathcal{D}_V^{(K)}$ for $K = 1, 2, 3$. The resulting folds are graphically depicted in Figure 7.3.

In order to perform model selection, one is meant to consider a finite dataset of possible configurations. In this instance, fully-connected NN architectures with tanh activation functions are considered [81, 312]:

$$\mathcal{D}_C = \{\mathcal{G}_{m,n} : m \in \{1, 2\},\ n \in \{16, 32, 64\}\}, \tag{7.9}$$

where m is the number of hidden layers L, whereas n denotes the neurons belonging to the first hidden layer N_1. If $m = 2$, then $N_2 = N_1/2$ neurons are assigned to the second hidden layer. In any case, the dimension of the input vector $\mathbf{x}'_i$ automatically determines the size of the input layer.

In agreement with Section 2.6.5, model selection is performed by selecting the specific architecture that maximises the model evidence for each specific fold K:

$$\mathbb{P}[\mathcal{D}_T^{(K)}|\mathcal{G}_{m,n}] = \int_{\boldsymbol{\theta}} \mathbb{P}[\mathcal{D}_T^{(K)}|\boldsymbol{\theta}, \mathcal{G}_{m,n}]\mathbb{P}[\boldsymbol{\theta}|\mathcal{G}_{m,n}]d\boldsymbol{\theta} \tag{7.10}$$

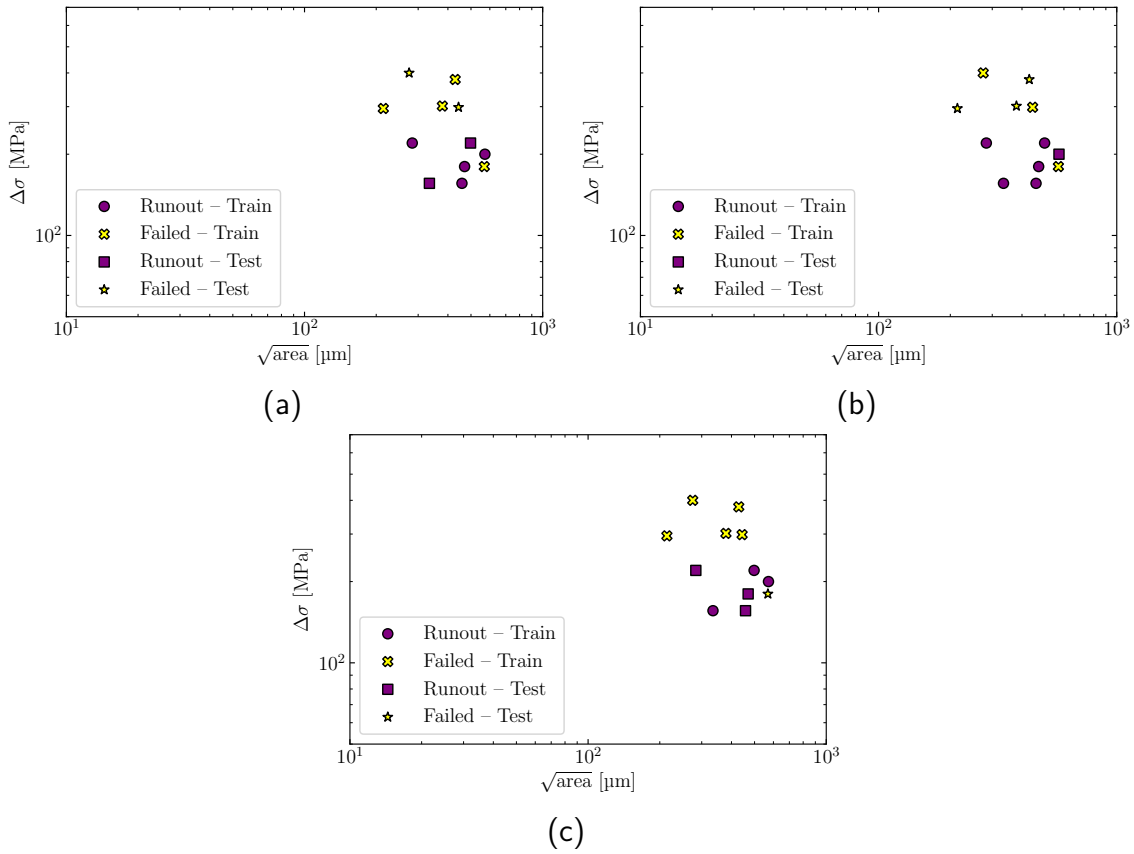

Figure 7.3. K-folds adopted to conduct model selection.

Since the above integral is in general analytically intractable, it can be numerically approximated, by Eq. (2.81). Finally, the optimal architecture for each K-fold is selected as:

$$\mathcal{G}^* = \max_{\mathcal{G}_{m,n} \in \mathcal{D}_C;\ K \in \{1,2,3\}} \mathbb{P}[\mathcal{D}_T^{(K)} | \mathcal{G}_{m,n}] \tag{7.11}$$

analogously to Eq. (2.82).

7.2.5. Training on CT data

The final stage of the learning entails the computation of the posterior of the B-PGNN for each optimal architecture and prior designed over the EH curve. In particular, given the catalytic prior $\mathbb{P}[\boldsymbol{\theta}|\mathcal{D}_S, \mathcal{G}]$ of Eq. (7.7), the optimal model archi-

tecture $\mathcal{G}^*$ is selected as explained in the previous section. The likelihood over the fold training set, $\mathcal{D}_T^{(K)}$, is then computed and used to evaluate the posterior of the B-PGNN according to Equation (2.32). The resulting posterior is approximated using HMC. In this instance, n.8 Markov chains having n.100 samples of $\boldsymbol{\theta}$ randomly explore the parameter space, whereas n.200 samples are dedicated to sample the posterior once the Markov's chains converge. The implementation of HMC was conducted utilising, again, *Pyro* [330]. The resulting posterior distribution $\mathbb{P}[\boldsymbol{\theta}|\mathcal{D}_T^{(K)}, \mathcal{G}^*]$ is finally employed to make predictions as per Eq. (2.52).

7.2.6. Computational Algorithm

Algorithm 4 is presented herein concisely outlines the steps of the application of the conceived B-PGNN framework.

Algorithm 4 Computational algorithm of the B-PGNN.

— **EH curve** —
Require: Fractography dataset $\mathcal{D}_H$ ▷ Eq. (7.1)
Require: Priors for EH parameters $\mathbb{P}[\Delta K_{th,lc}]$ and $\mathbb{P}[\Delta\sigma_w]$
Perform MAP ▷ Chapter 6
Compute $\mathbb{P}[\Delta K_{th,lc}|\mathcal{D}_H]$ and $\mathbb{P}[\Delta\sigma_w|\mathcal{D}_H]$
Compute EH curve of $\mathcal{D}_H$
— **EH Catalytic Prior & Model Selection** —
Require: EH curve of $\mathcal{D}_H$
Require: Dataset $\mathcal{D}_N$ ▷ Eq.(7.8)
Require: K-fold split of $\mathcal{D}_N$, i.e. $\mathcal{D}_T^{(K)}$ and $\mathcal{D}_V^{(K)}$
Require: NN architectures $\mathcal{G}_{m,n}$ ▷ Eq. (7.9)
for $m \in \{1, 2\}$ **do**
for $n \in \{16, 32, 64\}$ **do**
Generate synthetic Dataset $\mathcal{D}_S$ ▷ Eq. (7.6)
Learn the Catalytic prior through VI
for $K \in \{1, 2, 3\}$ **do**
Compute the evidence of $\mathcal{G}_{m,n}$ on $\mathcal{D}_T^{(K)}$ ▷ Eq.(7.10)
end for
end for
end for
Select the optimal architectures $\mathcal{G}^*$ for each K-fold
— **Training on CT data** —
Require: K-folds of $\mathcal{D}_N$, i.e. $\mathcal{D}_T^{(K)}$ and $\mathcal{D}_V^{(K)}$
Require: Optimal architectures $\mathcal{G}^*$
for Each optimal architecture **do**
Prescribe the catalytic prior over $\boldsymbol{\theta}$
Train B-PGNN through HMC on $\mathcal{D}_T^{(K)}$
Make predictions ▷ Eq. (2.52)
end for

7.3. Result and Discussion

7.3.1. Identified EH Curve

The application of MAP provided the expected values of the EH parameters $\Delta\hat{K}_{th,lc} = 6.6\,\text{MPa}\sqrt{\text{m}}$ and $\Delta\hat{\sigma}_w = 349.2\,\text{MPa}$, which univocally identify the EH curve through Eq. (6.1)-(6.2). Figure 7.4 displays $\Delta\sigma$ alongside $\sqrt{\text{area}}$, and the identified EH curve $\hat{\mathcal{E}}$. A visual examination indicates $\hat{\mathcal{E}}$ to be correctly located at an intermediate position between failed and runout specimens, thus partitioning the dataset $\mathcal{D}_H$, precisely. This result, therefore, substantiates the judicious selection of the adopted prior distributions, i.e. $\mathbb{P}[\Delta K_{th,lc}]$ and $\mathbb{P}[\Delta\sigma_w]$.

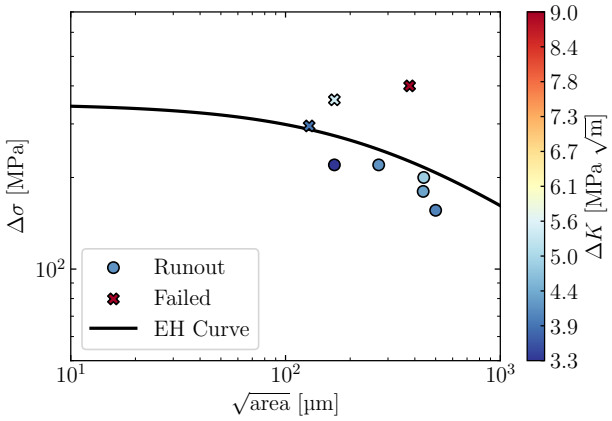

Figure 7.4. Graphical representation of the dataset $\mathcal{D}_H$ (Table 7.3) along with the identified EH curve $\hat{\mathcal{E}}$.

7.3.2. Functional Prior of the Selected Architectures

The implementation of model selection and the guidelines in Ref. [326, 329] appointed $\mathcal{G}_{1,16}$ as the optimal architecture for each K-fold $\mathcal{D}_T^{(K)}$. Specifically, $\mathcal{G}_{1,16}$ possess n.1 hidden layer with n.16 neurons totalising $p = 114$ parameters. Correspondingly, this strategy automatically determined the number of training points, i.e. $\mathsf{M} = 484$, required to form the synthetic dataset $\mathcal{D}_S^{(K)}$ (Eq. (7.6)). Alongside, the value of the temperature parameter turned out be $\tau = 0.236$. The section of $\mathcal{D}_S^{(K)}\ \forall\, K = 1, 2, 3$ – which is identical for each K-fold – taken on $\sqrt{\text{area}} - \Delta\sigma$ plane

is portrayed in Figure 7.5. Therein, runout and failed samples of $\mathcal{D}_S^{(K)}$ are denoted by blue and red circle dots, respectively, whereas the solid black line is $\hat{\mathcal{E}}$. It is worth remarking that the descriptors not shown in Figure 7.5 follow the normal distribution defined in Eq. (7.5).

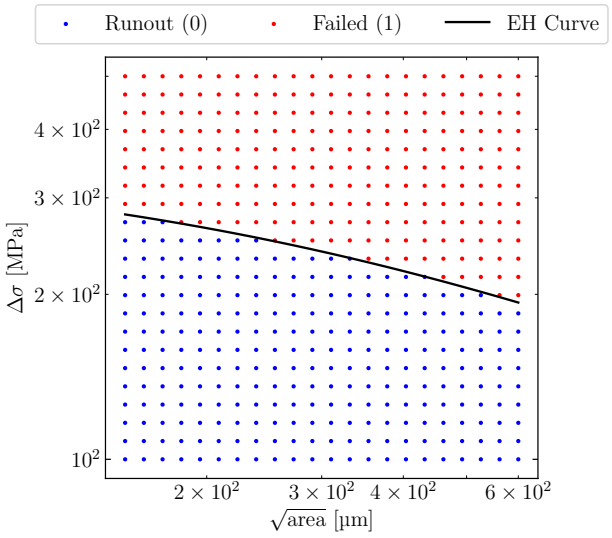

Figure 7.5. Section of $\mathcal{D}_S^{(K)}$ taken on $\sqrt{\text{area}} - \Delta\sigma$ plane. This section is identical for each K-fold, whereas the hidden descriptors obey to the distribution of Eq. (7.5).

VI was applied on three distinct instances of $\mathcal{G}_{1,16}$ to compute the related the variational approximation of the catalytic prior $\mathbb{P}[\boldsymbol{\theta}|\mathcal{D}_S^{(K)}|\mathcal{G}_{1,16}]$ $\forall\, K = 1, 2, 3$. To qualitatively assess the buoyancy of this stage, Figure 7.6 presents the contours of the predictive posterior in terms of the expected value $\mathbb{E}[\mathcal{F}_i]$ and uncertainty $\sqrt{\mathbb{V}[\mathcal{F}_i]}$ of the forecast class $\mathcal{F}_i$. Each figure also depicts failed and runout specimens belonging to the training and test set, i.e. $\mathcal{D}_T^{(K)}$ and $\mathcal{D}_V^{(K)}$ $\forall\, K = 1, 2, 3$, for the sake of convenience. The combination of these contours can be interpreted as the probabilistic fatigue endurance limit of the examined batch of samples. Apart from modest oscillations ensuing from the random hidden descriptors, the contours bear a close resemblance to one another. A graphical inspection reveals that $\mathcal{G}_{1,16}$ satisfactorily surrogates the EH curve as the contour lines of the predictive posterior globally track the functional form of $\hat{\mathcal{E}}$. Nevertheless, a substantial broadening of the contour lines of $\mathbb{E}[\mathcal{F}_i]$ and a general increase of $\sqrt{\mathbb{V}[\mathcal{F}_i]}$ can be observed along

$\hat{\mathcal{E}}$ for approximately $\sqrt{\text{area}} < 150$ MPa and $\sqrt{\text{area}} > 600$ MPa. Therein, $\mathcal{G}_{1,16}$ supposedly extrapolates more than it would do across the sub-domain of the plane where the synthetic training points are concentrated, i.e. $[150, 600] \times [100, 500]$. In contrast, $\mathcal{G}_{1,16}$ achieve greater performance across the interior of this region as the contour lines of $\mathbb{E}[\mathcal{F}_i]$ tightly surround $\hat{\mathcal{E}}$ while showing relatively lower levels of uncertainty.

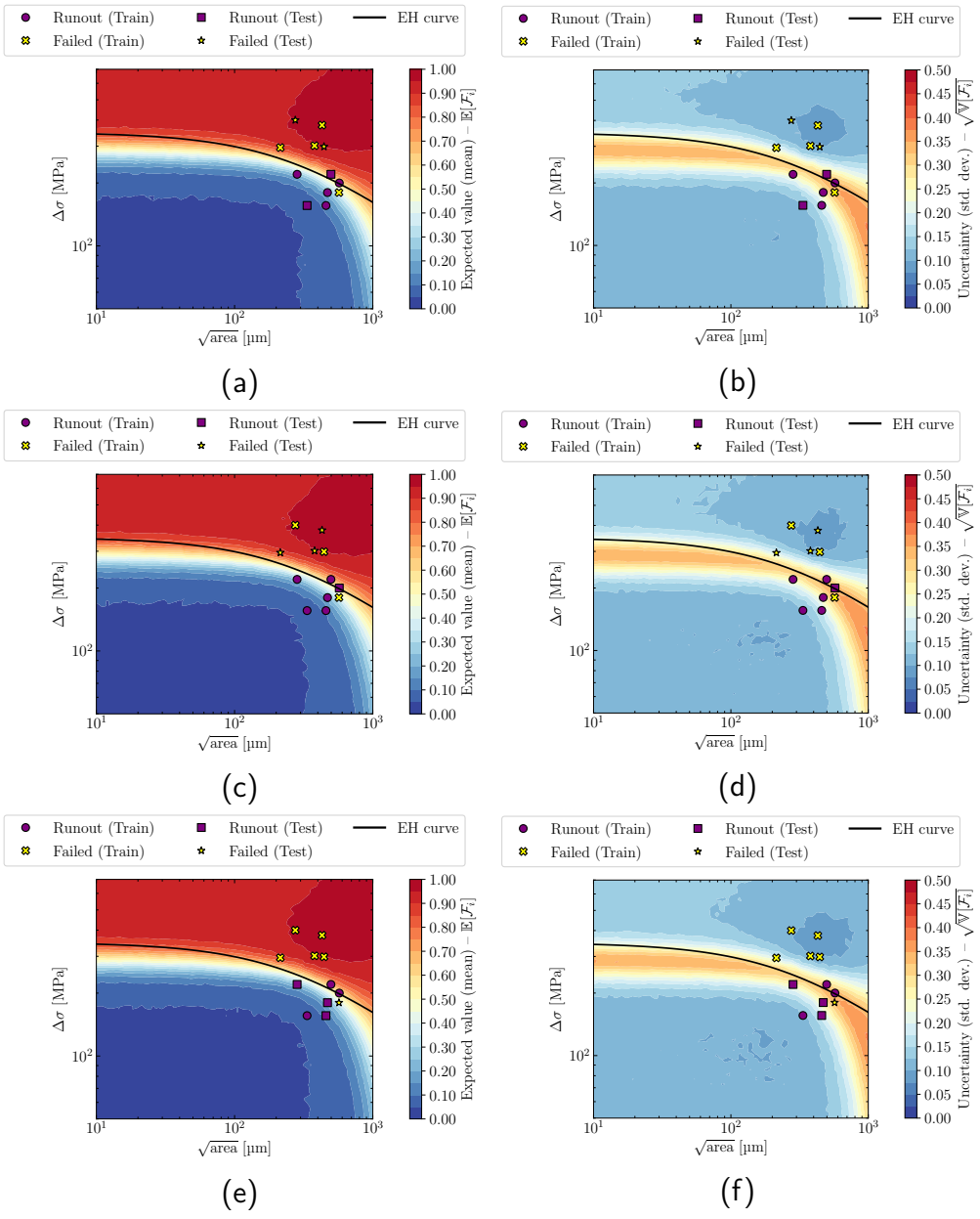

Figure 7.6. Contours of the catalytic prior for $\mathcal{D}_S^{(K)}\ \forall\, K = 1, 2, 3$ obtained through VI (a)-(c)-(e) Expected value $\mathbb{E}[\mathcal{F}_i]$. (b)-(d)-(f) Uncertainty $\sqrt{\mathbb{V}[\mathcal{F}_i]}$. The contours are grouped row-wise with respect to the K-folds. (a)-(b) $K = 1$. (c)-(d) $K = 2$. (e)-(f) $K = 3$.

7.3.3. Assessing B-PGNN Predictions

Each $\mathcal{G}_{1,16}$ was subsequently trained on $\mathcal{D}_T^{(K)}$ through HMC upon prescribing the functional prior $\mathbb{P}[\boldsymbol{\theta}|\mathcal{D}_S^{(K)}|\mathcal{G}_{1,16}]$ $\forall\, K = 1, 2, 3$. As a result of the training, the final posterior distribution $\mathbb{P}[\boldsymbol{\theta}|\mathcal{D}_T^{(K)}, \mathcal{H}_{1,16}]$ was computed. Figure 7.7 illustrates the contours of $\mathbb{E}[\mathcal{F}_i]$ and $\sqrt{\mathbb{V}[\mathcal{F}_i]}$ of the predictive posterior of each $\mathcal{G}_{1,16}$. For each examined K-fold, the contours ostensibly retain the trend seen in Figure 7.6. This finding demonstrates that each B-PGNN preserved the physical knowledge assimilated during VI. Interestingly, the contours attempt to accommodate the conformation of the training datasets. As concerns K-folds n.1, this effect is barely perceptible in Figure 7.6(a) since the arrangement of the training points already seem to concur well with the underlying phenomenological law. Nonetheless, the B-PGNN becomes more confident about its predictions in the neighbouring regions of the CT training data. Therein the uncertainty is reduced thanks to the additional training information ensued from CT data, as it can be noticed in Figure 7.7(b). The adaptation of the contours to the CT training data is more evident in regards to K-folds n.2. The group five of runouts in $\mathcal{D}_T^{(2)}$ appears as prevailing so that the contours of $\mathbb{E}[\mathcal{F}_i]$ and $\sqrt{\mathbb{V}[\mathcal{F}_i]}$ are shifted downwards on the rightmost portion of the plot (Figure 7.7(c)-(d)). Similarly to K-fold n.1, the uncertainty diminishes around the CT training data, see Figure 7.7(d). With particular regard to K-fold n.3, the predominant presence of four failed training specimens above $\hat{\mathcal{E}}$ drastically pushes the contours upwards, see Figure 7.7(d). Intriguingly, the peculiar collocation of the CT training points suffices to reduce the uncertainty over the entire failed side of the contours.

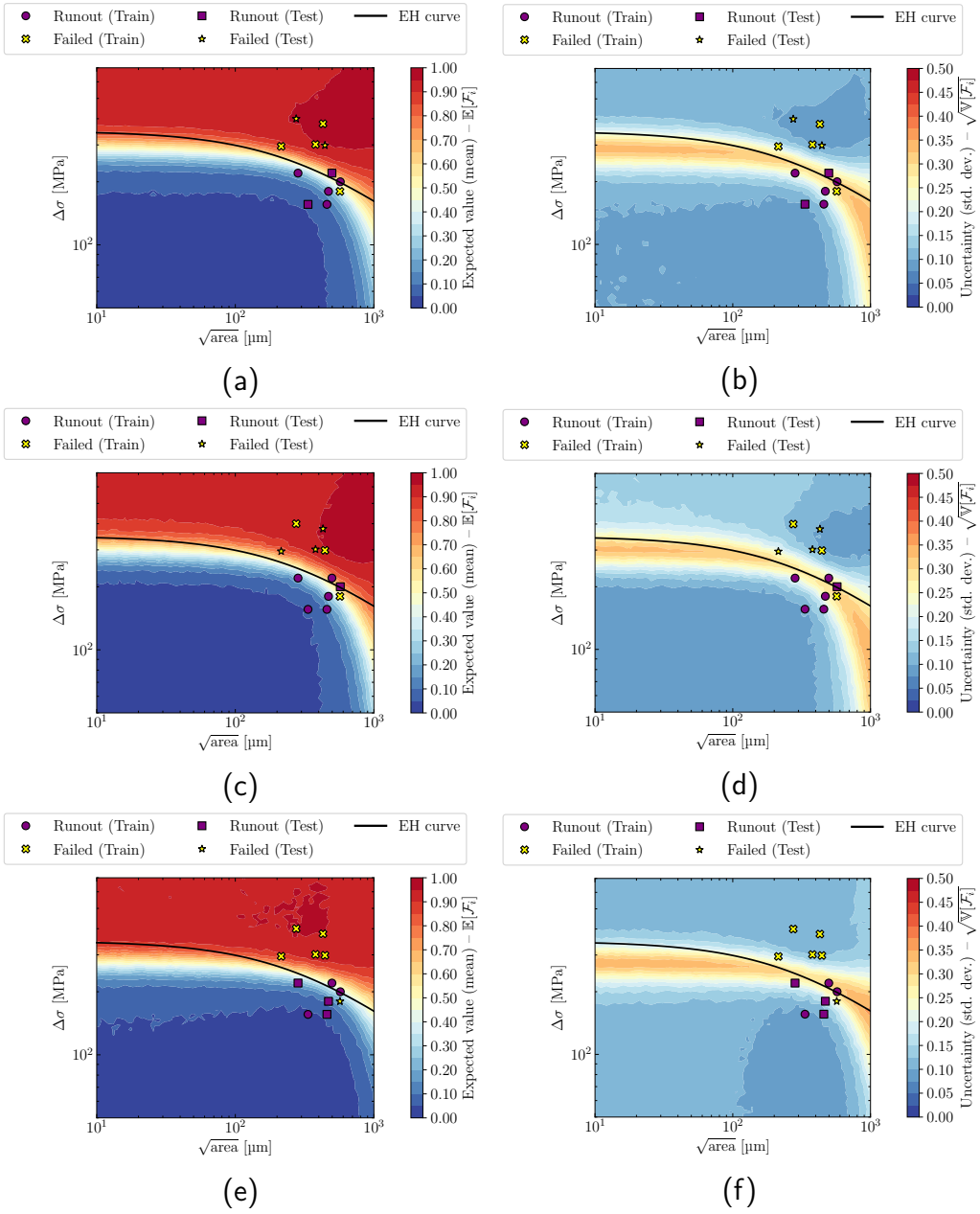

Figure 7.7. Contours of the predictive posterior obtained by training $\mathcal{G}_{1,16}$ on $\mathcal{D}_T^{(K)}\ \forall\, K = 1, 2, 3$ through HMC (a)-(c)-(e) Expected value $\mathbb{E}[\mathcal{F}_i]$. (b)-(d)-(f) Uncertainty $\sqrt{\mathbb{V}[\mathcal{F}_i]}$. The contours are grouped row-wise with respect to the K-folds. (a)-(b) $K = 1$. (c)-(d) $K = 2$. (e)-(f) $K = 3$.

Box & whisker plots are presented in Figure 7.8 to quantitatively assess the obtained predictions. The box spans the interquartile ranges, whereas the whiskers decidedly cover 95% confidence interval. Besides training and test points, the figure reports the median as a short black horizontal line, whilst the expected value of the predictions are denoted as blue triangle markers. The samples are sorted as per Table 7.2. Except for limited variations, the B-PGNNs achieve similar predictions for samples 1-9. Indeed, this predictions satisfactorily match the experimental expectation for both the training and test datasets. By contrast, little inconsistency is observed with regard to specimens 10-12. These are closely located to $\hat{\mathcal{E}}$ where $\mathbb{E}[\mathcal{F}_i]$ attains values about 0.5 and $\sqrt{\mathbb{V}[\mathcal{F}_i]}$ is relatively high. Therefore, the B-PGNNs cannot exactly distinguish which class the samples belong to. Much attention should be devoted to the eleventh sample of the third K-fold (Figure 7.7(c)). In this instance, let $\mathbf{x}'_{11}$ its representative point. Contrary to expectations, the B-PGNN probabilistically classify $\mathbf{x}'_{11}$ as a runout. The apparent lack of matching can attributed to the pathological location of this sample. Focusing on the sole prior knowledge (Figure 7.6(e)), $\mathbf{x}'_{11}$ is positioned beneath $\hat{\mathcal{E}}$, where runouts are supposed to lay in. Further, the sample is surrounded by runouts training points which not only prompt the B-PGNN to classify $\mathbf{x}'_{11}$ as runout, but also make the B-PGNN more confident. Certainly, further experimental data surrounding $\mathbf{x}'_{11}$ can compensate for this little inaccuracy. In conclusion, $\mathbf{x}'_{11}$ should essentially be treated as an outlier. Conversely, regarding K-fold n.1 and n.2, $\mathbf{x}'_{11}$ acts as a training point, and it allows one to highlight an interesting property of the B-PGNN. Specifically, the B-PGNN recognise $\mathbf{x}'_{11}$ not complying with the EH semi-empirical law. Consequently, since the B-PGNN becomes unsure about handling this exception, it increases the uncertainty around $\mathbf{x}'_{11}$ to compensate for this apparent mismatch. Therefore, the B-PGNN classifies $\mathbf{x}'_{11}$ with higher uncertainty, and this valuable information would not have been appreciated with frequentist training, or by training without a physics-guided prior. Although this performance is not ideal, overall, the robustness of the B-PGNNs across the examined K-fold is verified, given the limited number of processed samples.

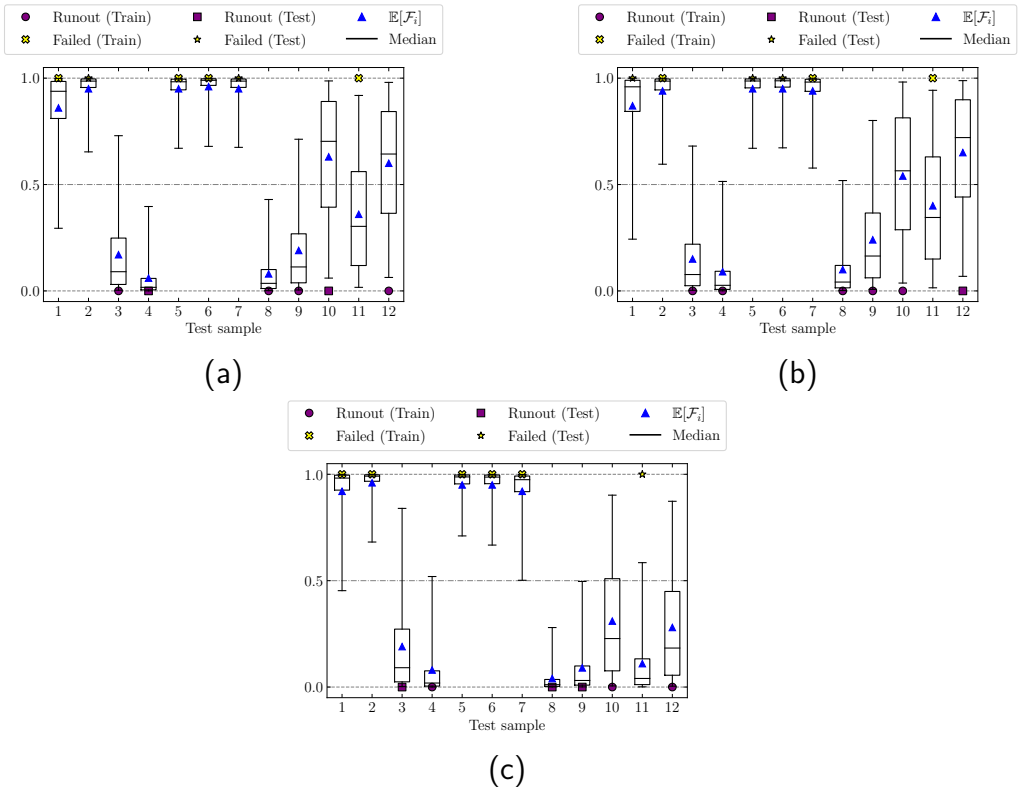

Figure 7.8. Box-plots for each K-Fold. The predictions are provided by the B-PGNN after HMC training which exploited the functional prior (a) $K = 1$ (b) $K = 2$. (c) $K = 3$.

7.3.4. Performance of the B-PGNN for Engineering Practice

It is worth emphasising that the examined sample are positioned nearby the $\hat{\mathcal{E}}$, where considerable uncertainty is present. Nevertheless, in order to ensure sufficiently reliable parts, engineering design against fatigue failure requires samples to be located sufficiently distant from $\hat{\mathcal{E}}$. To this end, the performance of the B-PGNNs is probed in such regions upon generating an additional synthetic dataset $\mathcal{D}_P$ which is shown in Figure 7.9. The dataset is characterised by points remotely located with respect to $\hat{\mathcal{E}}$. Each point belonging to $\mathcal{D}_P$ is assumed to possess $d = 320\,\mu\text{m}$ and $S = 0.25$, in agreement with the mean values of the distribution in Eq. (7.5). Accordingly, the box & whisker plot in Figure 7.10 gives the associated predictions. Therein, the samples are sorted by $\sqrt{\text{area}}$ as in Figure 7.9. The box-plot clearly demonstrates that the B-PGNN attains accurate predictions on $\mathcal{D}_P$ and proves the suitability of the conceived approach to designing against fatigue failure.

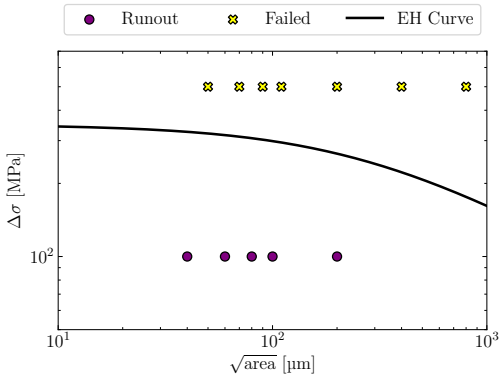

Figure 7.9. Synthetic dataset generated to probe the predictions of the B-PGNN far away from $\hat{\mathcal{E}}$.

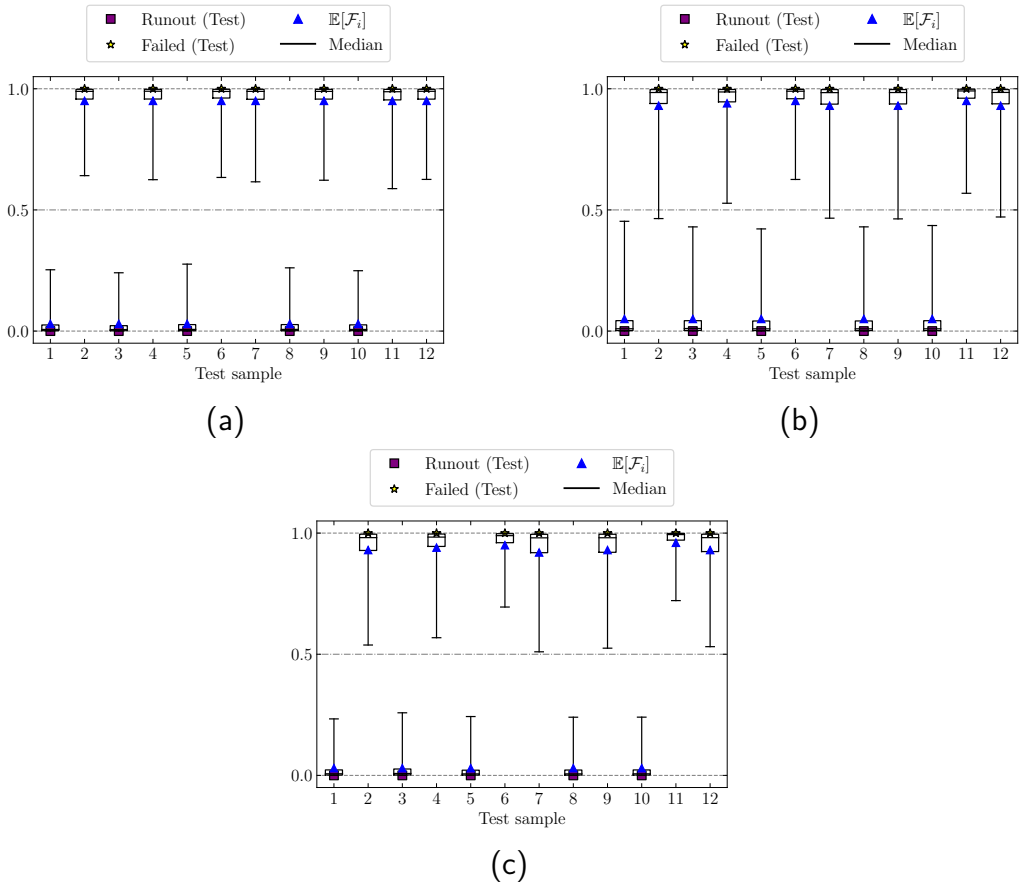

Figure 7.10. Box-plot for the predictions of $\mathcal{D}_P$ (a) $K = 1$ (b) $K = 2$. (c) $K = 3$.

7.3.5. Influence of the temperature

In this context, it is worth commenting on the function of τ (Eq. (7.7)) across the different stages of the training. Specifically, τ intervenes as factor weighting the influence of the functional prior, i.e. $\mathbb{P}[\boldsymbol{\theta}|\mathcal{D}_S^{(K)}, \mathcal{G}_{m,n}]$, and the likelihood ensued from $\mathcal{D}_T^{(K)}$ involved in HMC, i.e. $\mathbb{P}[\mathcal{D}_T^{(K)}|\boldsymbol{\theta}, \mathcal{G}_{m,n}]$. Hence, τ balances the contribution of the physical model and the training data from the CT dataset. As far as the extreme instances of τ are concerned, if τ conceptually approaches zero, the physical side of the B-PGNN dominates the posterior. In contrast, if τ becomes increasingly larger, the contribution of the functional prior is progressively purged. Lastly, if $\tau = 1$ the prior and the likelihood are equally balanced.

Additionally, to assess the sensitivity of the temperature parameter on the final predictions, τ is drastically amplified, thus giving $\tau_{\min} = 0.2\,\tau$ and $\tau_{\max} = 5\,\tau$. Figure 7.11 summarises the results obtained through VI upon training on the synthetic dataset in terms of the predictive posterior. As concern the former case, the contours seems to approach those pertaining to the mere data-driven strategy as $\tau_{\min}$ weakens the prior knowledge inherited from the $\hat{\mathcal{E}}$. Conversely, in the latter instance the physical branch of the B-PGNN is strengthened, thus tightening the contours along $\hat{\mathcal{E}}$.

The choice of τ has direct implication for the final predictions, as shown in Figure 7.12. Specifically, the lack of physical knowledge ensuing from $\tau_{\min}$ broadened both the interquartile ranges and the confidence intervals. Hence, an overall increase of uncertainty is observed. The opposite behaviour is obtained for $\tau_{\max}$, which considerably enhances the confidence of the B-PGNN. As concerns Figure 7.12, $\mathbf{x}'_{11}$ seems to be, again, probabilistically classified as a runout, notwithstanding the reduced value of τ. Therefore, in order to include the possibility for $\mathbf{x}'_{11}$ to be a failed samples, one ought to decrease τ further. Nevertheless, this would lead to an unjustified broadening of the interquartile ranges and confidence intervals of the remaining samples. By contrast, the adoption of $\tau_{\max}$ confirms $\mathbf{x}'_{11}$ to be a runout. This is mathematically reasonable as $\mathbf{x}'_{11}$ would initially belong to the region where the expected value ranges from 0.3 to 0.4. As previously mentioned, $\mathbf{x}'_{11}$ ought to be treated as an outlier so that its predictions needs to be interpreted with caution.

Additionally, it is expected that finely tuning $\tau \in [\tau_{\min}, \tau_{\max}]$ would partly address this issue, but not completely solve it. Furthermore, it is worth noting that the limitations in identifying potential outliers, such as $\mathbf{x}_{11} \in \mathcal{D}_T^{(3)}$, may also stem from

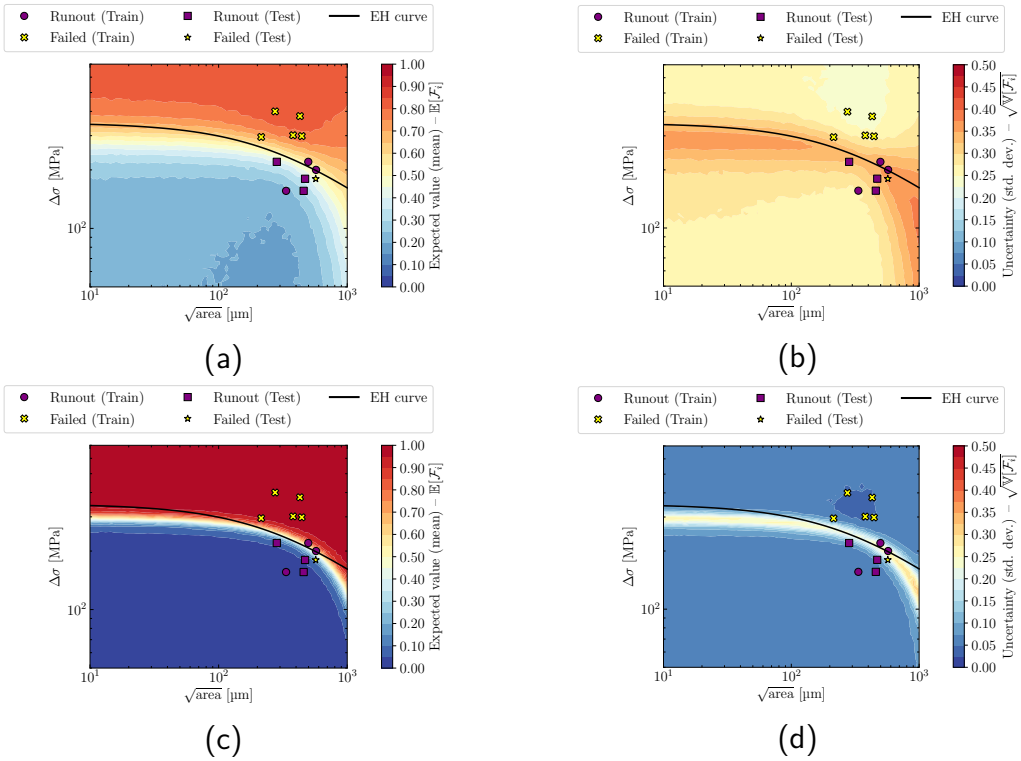

Figure 7.11. Contours of the predictive posterior obtained by training $\mathcal{G}_{1,16}$ on $\mathcal{D}_S^{(3)}$ through VI. (a)-(c) Expected value $\mathbb{E}[\mathcal{F}_i]$. (b)-(d) Uncertainty $\sqrt{\mathbb{V}[\mathcal{F}_i]}$. The contours are grouped row-wise with respect to τ. (a)-(b) τ_{min}. (c)-(d) τ_{max}.

the retrieved $\hat{\mathcal{E}}$ and the insufficient corresponding training points, see Figure 7.4. With a more comprehensive training dataset it would have been possible to establish a more suitable curve for the subsequent training stages, potentially assisting with the detection of outliers. However, the constraints on data availability restricted the possibility of fully addressing this concern.

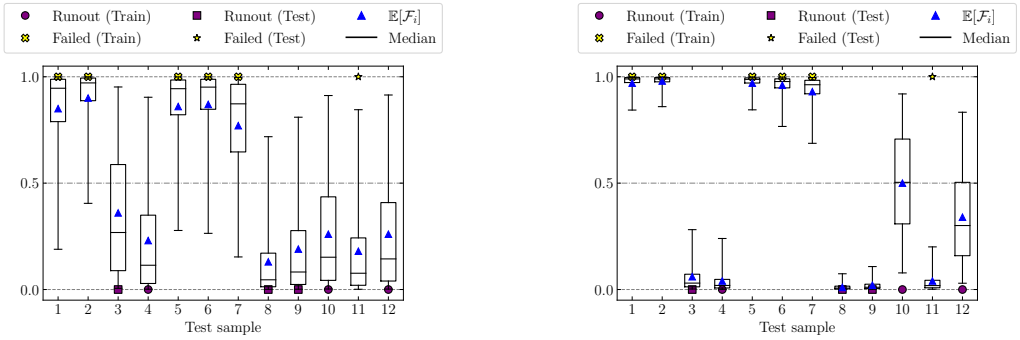

Figure 7.12. The predictions provided by the B-PGNN after HMC (a) τ_{min} (b) τ_{max}.

7.3.6. Predictive posterior of the non-guided B-PGNN

In order to demonstrate the capabilities of the B-PGNN over the BNN counterpart having the same architecture, HMC was repeated without prescribing the catalytic prior. As concerns the implementation, VI was foregone, and HMC pursued with $\tau = 1$ and a non-informative prior over the parameters. Therefore, this configuration completely neglects the physical knowledge that the catalytic prior brought about earlier. The related results are reported in Figure 7.13. In this case, the contours of $\mathbb{E}[\mathcal{F}_i]$ qualitatively capture the configuration of each dataset, but they do not follow the functional shape of the EH curve. Examining Figure 7.13(a), however, one can claim little similarity the contour in Figure 7.7(a) and Figure 7.7(c). Again, this is fortuitously due to the intrinsic distribution of the training points. Nevertheless, the quantitative predictions are far from being adequate.

Further evidence is provided by the box-plots in Figure 7.14 whose box and whiskers span, again, the interquartile range and the 95% confidence interval, respectively. A graphical inspection reveals that the B-PGNN yields more consistent predictions except for the specimens located in the vicinity of the EH which may inherit higher uncertainty from the catalytic prior (see Figure 7.6). Apart from these peculiar specimens, the B-PGNN's predictions considerably approach the ground-truth more than the BNN does. In fact, BNN's $\mathbb{E}[\mathcal{F}_i]$ appears to oscillate just within [0.3, 0.6] – considerably deviating from the ground truth value. Moreover, the larger interaquartile range and confidence intervals prevent one from inferring precise information about the predicted class. Since the BNN may provide predictions significantly differing from the actual value, a prospective practitioner would pursue more conservative approaches to tolerate this higher uncertainty in the predictions. Whilst, a more performance-oriented can be adopted by exploiting the superior accuracy of the B-PGNN.

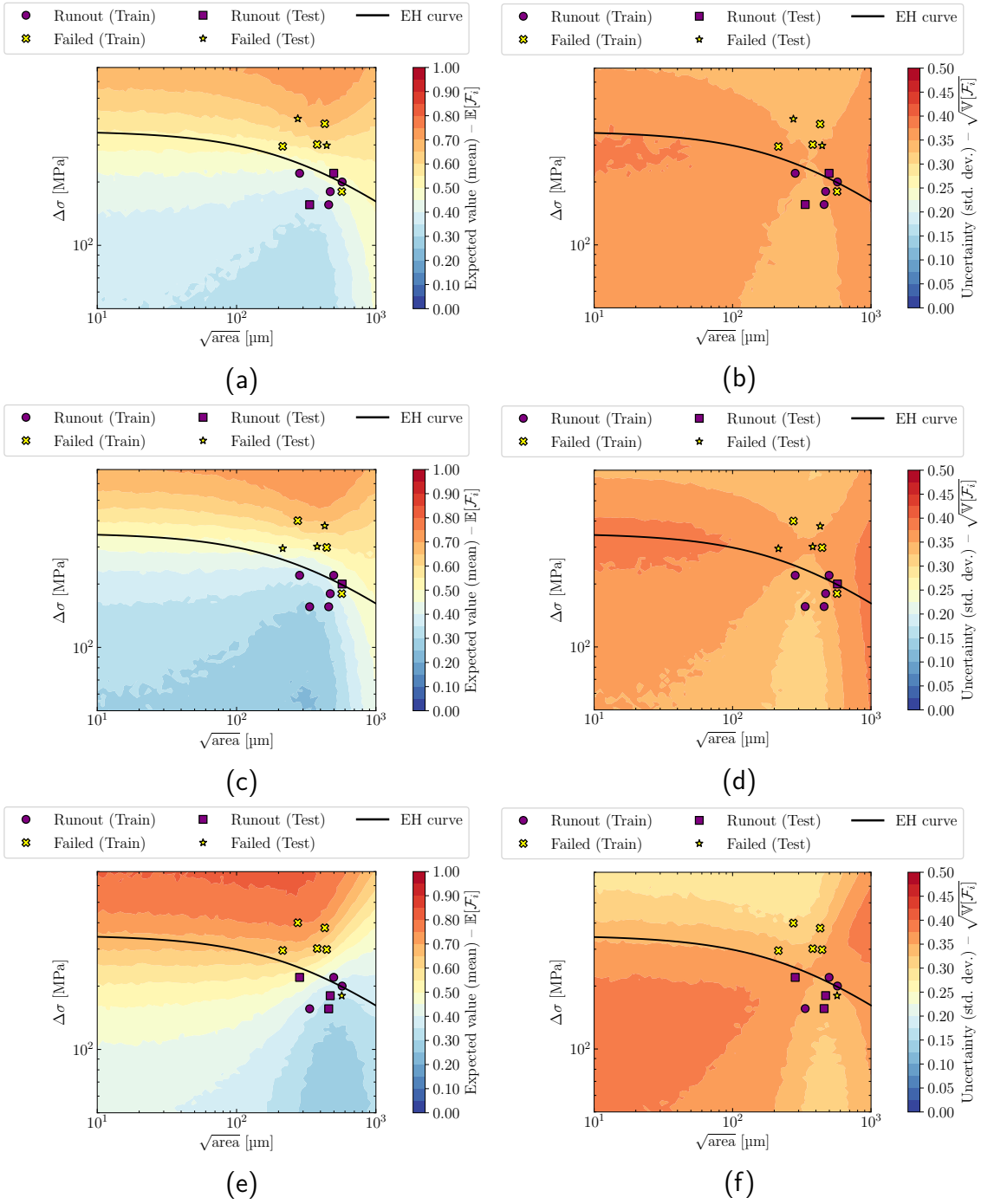

Figure 7.13. Contours of the predictive posterior obtained by training $\mathcal{G}_{1,16}$ on $\mathcal{D}_T^{(K)}$ $\forall\, K = 1, 2, 3$ without prescribing the functional prior. (a)-(c)-(e) Expected value $\mathbb{E}[\mathcal{F}_i]$. (b)-(d)-(f) Uncertainty $\sqrt{\mathbb{V}[\mathcal{F}_i]}$. The contours are grouped row-wise with respect to the K-folds. (a)-(b) $K = 1$. (c)-(d) $K = 2$. (e)-(f) $K = 3$.

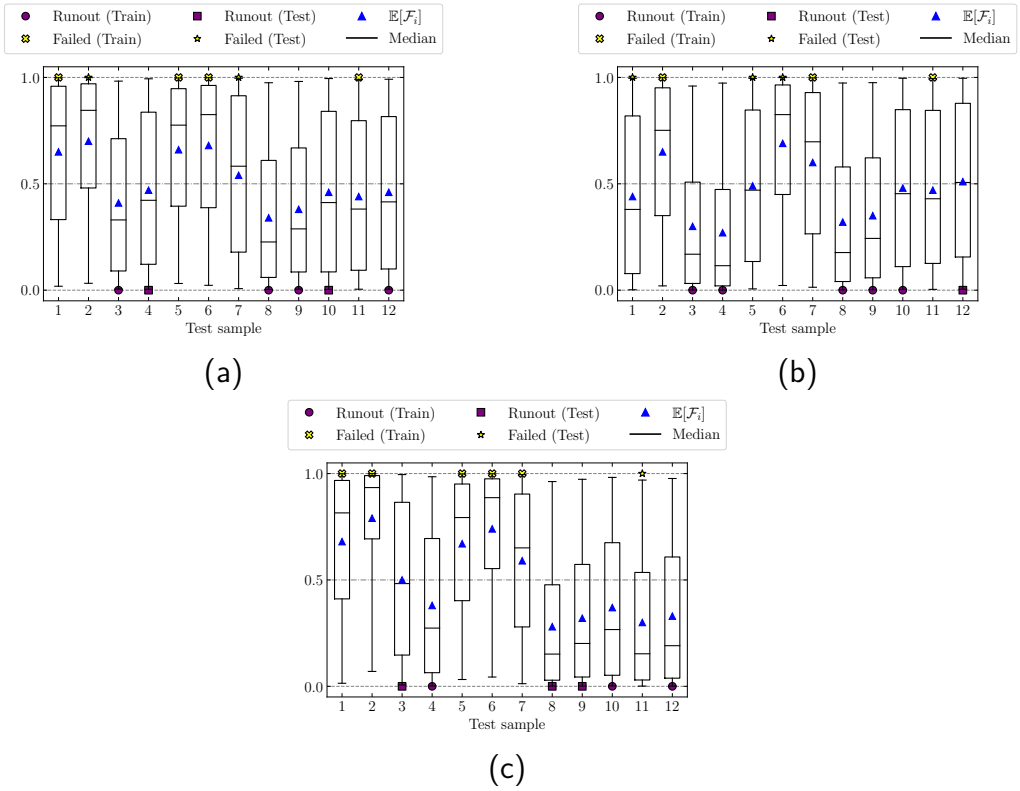

Figure 7.14. The predictions provided by the BNN after HMC training without prescribing the functional prior (a) $K = 1$ (b) $K = 2$. (c) $K = 3$.

7.3.7. Investigation of Latent Relationships

Unlike the classical EH model which exclusively concentrates on $\sqrt{\text{area}}$ and $\Delta\sigma$, the obtained B-PGNNs allow for unveiling potential latent correlations between $\mathcal{F}_i$ and the additional defect descriptors. This can provide insights into phenomena governing fatigue failures. The features were considered in pairs and permuted to study all the possible planes of the input domain, other than $\Delta\sigma - \sqrt{\text{area}}$ already discussed. This investigation was carried out with regard to the third K-fold ($\mathcal{D}_T^{(3)}$) only, for the sake of brevity. Figure 7.15 visually summarises the outcomes of this analysis. Particularly, Figure 7.15(a) discloses a positive correlation between $\sqrt{\text{area}}$ and d, i.e. if these features jointly increase the failure probability increases as well. This appears reasonable since large defects are more likely to trigger fatigue collapse. Unexpectedly, Figure 7.15(b) suggest that $\sqrt{\text{area}}$ and S are positively correlated, which seems, in a word, counterintuitive. In fact, one would suppose that spheroidal defects, i.e. $S \to 1$, yield a minor influence on fatigue failure. Nonetheless, Figure 7.15(b) recalls some of the traits of the EH curve. Presumably, this can be ascribed to the presence of $\sqrt{\text{area}}$ whose behaviour was previously informed by the EH model. However, as concerns Figure 7.15(c), a neat correlation is scarcely distinguishable. Figure 7.15(g) indicates that $\Delta\sigma$ generally controls the predictions, although a mild positive correlation can be recognised. In other words, for increasing d, $\mathbb{E}[\mathcal{F}_i]$ increases, which is in line with theoretical expectations. Still, an arguable negative correlation can be noticed in Figure 7.15(i) with regard to S, similarly to that observed in Figure 7.15(c). Therefore, defects having $S \to 0$ ought to possess a crack-like shape, thus more detrimental to fatigue. In any case, the information contained in $\mathcal{D}_T^{(3)}$ allowed the B-PGNN to enhance its predictions. The rightmost panels of Figure 7.15 witnesses diminished uncertainty in the neighbouring region of the training points. It should be mentioned that these sections are partly, or even completely (Figure 7.15(e)-(f)), non-informed by the physical branch. As a result, the patterns that the B-PGNN acquired were inferred from mere data, which corroborates the arrangement of the contours. Potentially, the existing observed discrepancies might be mitigated should further data is provided.

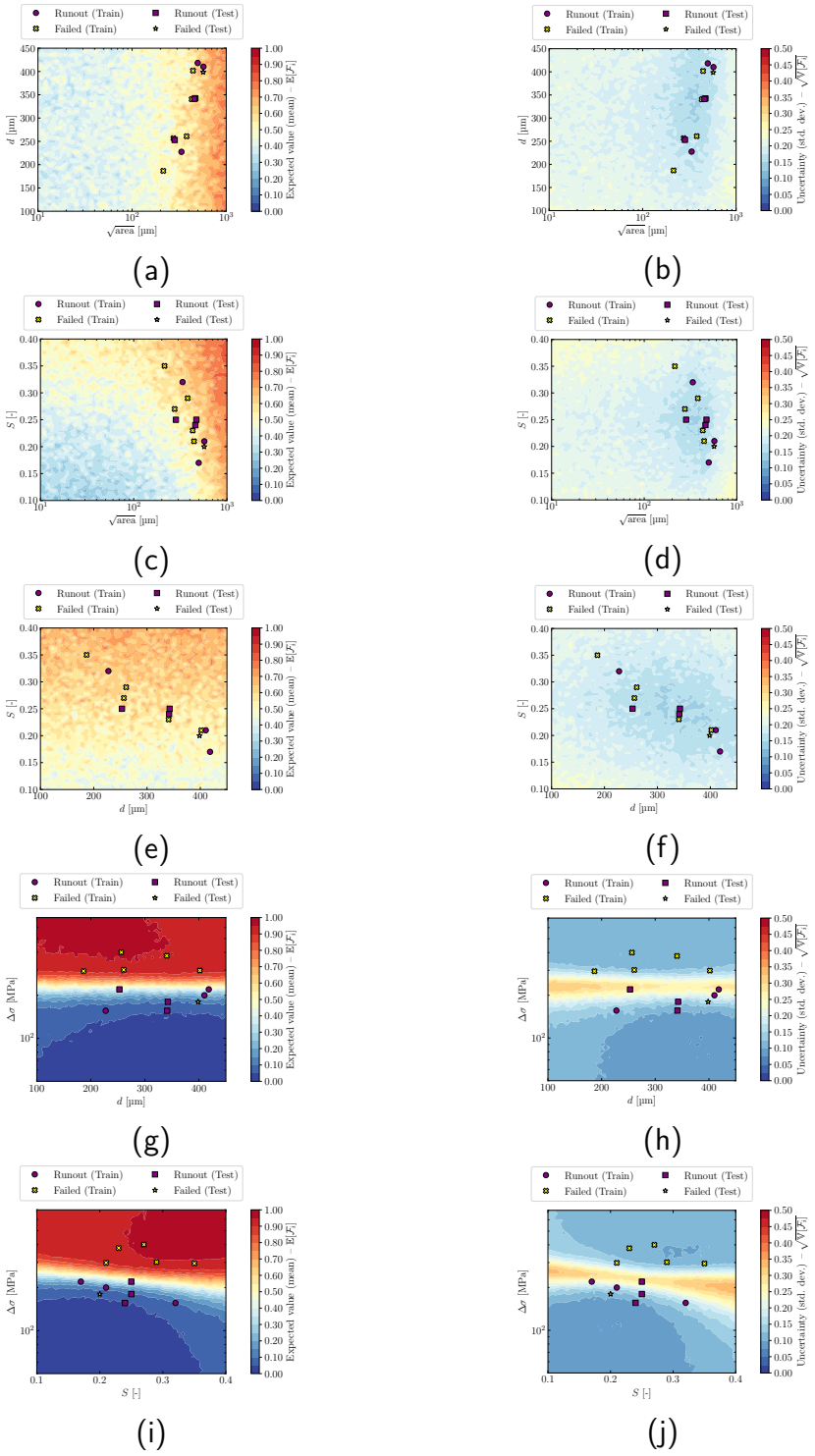

Figure 7.15. Contours of the predictive posterior obtained by training $\mathcal{G}_{1,16}$ on $\mathcal{D}_T^{(3)}$ (the third K-fold) through HMC. Other sections.

7.4. Conclusions

B-PGNN framework to probabilistically forecast whether metallic defect-laden materials experience fatigue failure when subjected to uniaxial fatigue loads has been presented herein. A rigorous Bayesian framework was developed to train the B-PGNNs by inferring a prior knowledge incoming from the data-associated semi-empirical El Haddad curve following a previously proposed procedure. The training culminates with the introduction of experimental evidence from CT data to account for a set of defect descriptors. A selection technique based on model evidence was illustrated to effectively select the most appropriate NN architecture. This approach ensures a full Bayesian treatment of the problem and eliminates the user's arbitrariness on choice NN structure, i.e. layers and neurons.

To test this approach, a literature dataset of SLM AlSi10Mg specimens was considered as a case study. A K-fold split was employed to assess the robustness of the predictions offered by the developed method. Additionally, it was seen that the B-PGNN outperformed the non-informed BNN counterpart whose training did not involve the prescription of the prior. The tested case-study confirmed that out-of-distribution experimental data might affect the accuracy of the predictions – in extremely small datasets – however the results shown herein are more than satisfactory.

Based on the considered case-study, the developed B-PGNN model allowed for the exploration of potential latent correlations between the prediction and the input descriptors.

The proposed B-PGNN framework makes the most of advanced computational tools and fracture mechanics concepts to establish an unprecedentedly accurate probabilistic predictive model – even for scarce experimental datasets – to efficiently support the design against fatigue failure of defect-laden materials.

8. Conclusions

8.1. Synopsis

In this final chapter, I condense the conclusions of the dissertation with particular attention to the objectives, key findings, implications, and future directions. The research elucidated the effect of two critical features influencing fatigue, namely RS and manufacturing defects, and examined their impact on structural integrity. Accordingly, several outstanding issues were addressed, encompassing RS evaluation and fatigue characterisation & modelling, with the unique aim of establishing an all-round probabilistic framework for designing against fatigue failure. To fulfil the objectives set, several advanced ML techniques were exploited while prioritising probabilistic aspects to build extremely robust predictive tools and ascertain their accuracy. I feel this work will hold the promise of a comprehensive setting for the probabilistic design against fatigue failure with highly relevant implications from both research and industrial perspectives.

8.2. Residual Stress Evaluation

As concerns RS, the focus was drawn on a relatively recent evaluation technique, namely the CM. This choice was motivated by the CM's potential and its cost-effectiveness, making it particularly appealing to effectively integrate RS evaluations into fatigue assessments. Nevertheless, the original formulation of the CM unveiled a few weak points worth investigating. In particular, the spline-fitting involved in the CM renders the pre-processing of the input displacement data rather cumbersome. This crucial limitation became overwhelming when the RS was assessed in the FSW and HYB joints (Chapter 3). In doing so, the optimal spline parameters were selected upon the existing guidelines, thus eventually attaining a satisfactory

interpolation. Nonetheless, finer parameter adjustments were required to adequately capture the gradients of the input data without smoothing it excessively.

This experience showed how users are generally committed to surveying a considerable number of splines, which can be extremely time-consuming. Consequently, this downside underscored the need for more systematic data-fitting strategies and pointed out the arbitrariness of this stage. Moreover, quantifying the uncertainty stemming from the selection of the spline parameters was recognised as crucial to the soundness of the entire CM evaluation. Besides, attention was paid to modelling the uncertainty due to the measurement noise embedded into the input data. The literature, however, offered a potential uncertainty quantification framework to tackle this caveat. Although such a framework might be practical to some extent, it lacks robustness, and its application is highly dependent on the user's experience and confidence.

Chapter 4 showed how this framework was elegantly redefined by implementing GPR, which replaced the splines during the fitting stage. The striking capabilities of GPR enabled the optimal fitting parameters to be stochastically identified, thus minimising the user's intervention. Notably, the GPR automatically condensed the uncertainty due to the interpolation *per se* and measurement noise into a single indicator. As an additional benefit, since these uncertainties were no longer treated as separated, a single Monte Carlo simulation was required to propagate them in terms of RS. Consequently, the overall computational requirements were drastically reduced.

8.3. Defect-based Fatigue Modelling

Regarding fatigue, the research addressed two categories of problems related to defect-laden metallic alloys, i.e. the prediction of the finite fatigue life and the estimation of the fatigue endurance limit. It was extensively vetted that the state-of-the-art models revealed their inadequacy in the context of today's manufacturing scenario. In particular, traditional LEFM-based fatigue models hinder the full exploitation of the numerous defect features obtained by CT and fractographic investigations. Although ML paradigms have been applied to address this limitation, they did not leverage the knowledge offered by traditional fatigue models. Therefore, guaranteeing the robustness of such ML models for a wide range of conditions

seemed hardly attainable.

With particular regard to finite fatigue life, Chapter 5 harnessed the PINN setting to significantly ameliorate the accuracy of the current defect-based finite fatigue models by accounting for additional geometric & morphological features. The PINN resorted to prior information from a semi-empirical Basquin-like generalised by concepts from FM to account for defectivity. Whilst the PINN received defect descriptors retrieved from CT. The semi-empirical model permitted constraining the training stage to ensure the physical consistency of the predictions, thus resulting in remarkable robustness. The PINN inherited from this add-on feature the natural inclination to handle the provided small dataset. This was demonstrated by benchmarking against the mere NN, which showed peculiar symptoms of overfitting and prediction deviating from the semi-empirical law. It is worth emphasising that the Basquin-like law was complemented with prediction intervals, which enabled tailoring a particular physics loss function while intrinsically accounting for latent sources of uncertainty – RS, for instance, which was neglected in the analysis.

Although ML has widely tackled the prediction of finite fatigue life, a crucial deficit was recognised regarding the evaluation of the fatigue endurance limit of flawed metallic material. Amongst many available semi-empirical models, the research focussed on the EH curve given its extensive use across the literature, as Chapter 6 witnessed. The chapter proposed a probabilistic MAP-supported framework to indirectly estimate the peculiar parameters of the EH curve from fatigue and post-mortem fractographic data. The key point of this approach was to inject prior information from the literature when handling small or incomplete datasets. This feature makes the method appealing since it allows for reducing the required test and, consequently, the related onerousness. Furthermore, MAP automatically provides practitioners with a probabilistic appraisal of the parameters rather than their point-valued estimation. This renders the methodology incredibly attractive in order to engineer mechanical parts against fatigue failure within a probabilistic setting.

In Chapter 7, a B-PGNN framework was developed to predict the fatigue endurance limit of defective metallic alloys. Specifically, the B-PGNN predicts the failure probability of fatigued samples upon the characterisation of relevant defect descriptors. BI was strictly followed to pursue the training. This B-PGNN method is particularly attractive since it made the most out of the physical consistency

of PINN and BI, which, in turn, minimises the dependency on the data regime and provides a built-in uncertainty quantification framework. Although a few obtained results might have contradicted the experimental evidence at first glance, it is worth noting the B-PGNN allowed this little inconsistency to be detected. Whilst a deterministic or frequentist approach would not have captured it. The work also addressed a major concern often encountered amongst the ML community, that is, selecting the architecture of the NN. Therein, by exploiting BI, a selection criterion was devised, thus circumventing user arbitrariness and ensuring a full Bayesian treatment of the problem.

8.4. Future Perspectives

The presented findings and proposed methods contribute to advancing the current state-of-the-art of the Contour Method and predictive models for the design against fatigue failure and indeed foreshadow further developments for future work.

Although RS and fatigue were considered independent problems, the scientific literature actually proves the opposite. Thus, future efforts must be devoted to including RS evaluation data into the devised ML fatigue models to account for the influence of RS along with that due to defects. Since residual stress (RS) locally modifies the stress state, deviations from the expected stress due to fatigue loading may occur, leading to alterations in the average stress and stress ratio surrounding defects. Therefore, future developments should strive to incorporate simulated or experimentally evaluated residual stress descriptors, or leverage prior knowledge from mechanistic models, in surrogate ML models. In this way, it would possible to enhance the predictive accuracy and reliability of fatigue predictions. Furthermore, the research conducted on the CM by utilising GPR has apparently broader implications for other RS evaluation methods. GPR performs the data regularisation required in those RS assessment techniques that entail back-calculations or integral methods [16, 331]. Interestingly, the GPR has recently shown its capabilities in the context of hole drilling [332]. This encouraging result hints that GPR appears suitable for the regularisation for other RS evaluation methods – for instance, FIB-DIC would be a potential candidate.

The logical extension of the two defect-based predictive models would be their seamless fusion to constitute an all-round setting to both estimate the fatigue en-

durance limit as well as the finite fatigue life of defective metallic material. In this way, one can initially evaluate the fatigue endurance limit of a given material using the EH model via the MAP-based method upon fractographic data. Next, the samples can be processed using the B-PGNN to ascertain whether they collapse based on CT investigations. If a sample collapses, it will be possible to estimate its finite fatigue life using the PINN approach. Additionally, it will be worth investigating how to enrich the proposed PINN framework by incorporating BI analogously to the proposed B-PGNN. In this case, the objective would be different, since the aim is to establish a formal probabilistic regression model for finite fatigue life. Presently, this work has preliminary been addressed in a recently published paper [333], albeit from a frequentist perspective. The published work focussed on the uncertainty quantification and sensitivity analysis of the PINN (formerly developed in Chapter 5) by utilising Monte Carlo simulations to characterise the fatigue output distributions under various input distribution scenarios. Although this approach is well suited for analysing the uncertainty owing to defect's descriptors, its applications requires speculating about the input distributions. Conversely, BI would automatically capture the sources of uncertainty affecting such descriptors as well as those not explicitly accounted for, such as the influence of RS.

Another point that merits attention is the generalised version of the EH curve for targeted fatigue life applications, whereby iso-fatigue life EH curves can be modelled. In this regard, the scientific literature has already proposed diverse strategies [64, 231]. It is essential to recognise that these generalised models embed fatigue crack propagation laws, posing significant ML implementation challenges. However, they offer inherited physical consistency for prospective physics-informed ML approaches. Therefore, their integration into the probabilistic ML-based framework thus far would be highly advantageous and undoubtedly impactful.

References

[1] Norman E. Dowling. *Mechanical Behavior of Materials: Engineering Methods for Deformation, Fracture, and Fatigue*. Pearson, 2013.

[2] Yukitaka Murakami. *II - Metal Fatigue: Effects of Small Defects and Nonmetallic Inclusions*. Elsevier, 2019.

[3] G. S. Campbell and R. Lahey. A survey of serious aircraft accidents involving fatigue fracture. *International Journal of Fatigue*, 6(1):25–30, January 1984. doi: 10.1016/0142-1123(84)90005-7.

[4] P. Paris and F. Erdogan. A Critical Analysis of Crack Propagation Laws. *Journal of Basic Engineering*, 85(4):528–533, December 1963. doi: 10.1115/1.3656900.

[5] André Pineau, David L. McDowell, Esteban P. Busso, and Stephen D. Antolovich. Failure of metals II: Fatigue. *Acta Materialia*, 107:484–507, April 2016. doi: 10.1016/j.actamat.2015.05.050.

[6] A. Pineau, A.A. Benzerga, and T. Pardoen. Failure of metals I: Brittle and ductile fracture. *Acta Materialia*, 107:424–483, April 2016. doi: 10.1016/j.actamat.2015.12.034.

[7] D.L. McDowell and F.P.E. Dunne. Microstructure-sensitive computational modeling of fatigue crack formation. *International Journal of Fatigue*, 32(9):1521–1542, September 2010. doi: 10.1016/j.ijfatigue.2010.01.003.

[8] Mohammadreza Yaghoobi, Krzysztof S. Stopka, Aaditya Lakshmanan, Veera Sundararaghavan, John E. Allison, and David L. McDowell. PRISMS-Fatigue computational framework for fatigue analysis in polycrystalline metals and alloys. *npj Computational Materials*, 7(1):38, March 2021. doi: 10.1038/s41524-021-00506-8.

[9] Gustavo M. Castelluccio and David L. McDowell. Mesoscale modeling of microstructurally small fatigue cracks in metallic polycrystals. *Materials Science and Engineering: A*, 598:34–55, March 2014. doi: 10.1016/j.msea.2014.01.015.

[10] Zahra S. Hosseini, Mohsen Dadfarnia, Brian P. Somerday, Petros Sofronis, and Robert O. Ritchie. On the theoretical modeling of fatigue crack growth. *Journal of the Mechanics and Physics of Solids*, 121:341–362, December 2018. doi: 10.1016/j.jmps.2018.07.026.

[11] Yukitaka Murakami, Toshio Takagi, Kentaro Wada, and Hisao Matsunaga. Essential structure of S-N curve: Prediction of fatigue life and fatigue limit of defective materials and nature of scatter. *International Journal of Fatigue*, 146:106138, May 2021. doi: 10.1016/j.ijfatigue.2020.106138.

References

[12] S. Nishida. *Failure analysis in engineering applications*. Butterworth-Heinemann, 1992.

[13] Yee Mey Goh, Julian Booker, and Chris McMahon. A Comparison of Methods in Probabilistic Design Based on Computational and Modelling Issues. In Alan Bramley, Daniel Brissaud, Daniel Coutellier, and Chris McMahon, editors, *Advances in Integrated Design and Manufacturing in Mechanical Engineering*, pages 109–122. Springer-Verlag, 2005. doi: 10.1007/1-4020-3482-2_9.

[14] Gary S. Schajer, editor. *Practical residual stress measurement methods*. Wiley, 2013.

[15] P.J. Withers and H.K.D.H. Bhadeshia. Residual stress. Part 2 – Nature and origins. *Materials Science and Technology*, 17(4):366–375, April 2001. doi: 10.1179/026708301101510087.

[16] G. S. Schajer, M. B. Prime, and P. J. Withers. Why Is It So Challenging to Measure Residual Stresses ? *Experimental Mechanics*, 62(9):1521–1530, November 2022. doi: 10.1007/s11340-022-00879-x.

[17] Eckard Macherauch. Introduction to Residual Stress. In A. Niku-lari, editor, *Residual Stresses*, pages 1–36. Pergamon, January 1987. doi: 10.1016/B978-0-08-034062-3.50011-2.

[18] P.J. Withers and H.K.D.H. Bhadeshia. Residual stress. Part 1 – Measurement techniques. *Materials Science and Technology*, 17(4):355–365, April 2001. doi: 10.1179/026708301101509980.

[19] Enrico Salvati, Hongjia Zhang, Kai Soon Fong, Xu Song, and Alexander M. Korsunsky. Separating plasticity-induced closure and residual stress contributions to fatigue crack retardation following an overload. *Journal of the Mechanics and Physics of Solids*, 98:222–235, January 2017. doi: 10.1016/j.jmps.2016.10.001.

[20] M.N. James, D.J. Hughes, Z. Chen, H. Lombard, D.G. Hattingh, D. Asquith, J.R. Yates, and P.J. Webster. Residual stresses and fatigue performance. *Engineering Failure Analysis*, 14(2):384–395, March 2007. doi: 10.1016/j.engfailanal.2006.02.011.

[21] P J Withers. Residual stress and its role in failure. *Reports on Progress in Physics*, 70(12):2211–2264, December 2007. doi: 10.1088/0034-4885/70/12/R04.

[22] Y. Yamada and J. C. Newman. Crack closure under high load-ratio conditions for Inconel-718 near threshold behavior. *Engineering Fracture Mechanics*, 76(2):209–220, January 2009. doi: 10.1016/j.engfracmech.2008.09.009.

[23] Christopher J. Lammi and Diana A. Lados. Effects of residual stresses on fatigue crack growth behavior of structural materials: Analytical corrections. *International Journal of Fatigue*, 33(7):858–867, July 2011. doi: 10.1016/j.ijfatigue.2011.01.019.

[24] Raghawendra Sisodia, Marek Weglowski, and Piotr Sliwinski. In situ localised post-weld heat treatment with electron beam welding of S690QL steel. *Journal of Advanced Joining Processes*, 9:100182, June 2024. ISSN 2666-3309. doi: 10.1016/j.jajp.2023.100182.

[25] Bin Qiang, Yunjie Xie, Qiang Xie, Jingyu Shi, Xinran Liu, Changrong Yao, and Yadong Li. Influence of post-weld heat treatment on welding residual stress in U-rib-to-deck joint. *Thin-Walled Structures*, 196:111550, March 2024. ISSN 0263-8231. doi: 10.1016/j.tws.2023.111550.

[26] Nurul Syahida Mohd Nasir. REVIEW ON WELDING RESIDUAL STRESS. *ARPN Journal of Engineering and Applied Sciences*, 11(9):10, 2016.

[27] Micheal Kattoura, Seetha Ramaiah Mannava, Dong Qian, and Vijay K. Vasudevan. Effect of laser shock peening on residual stress, microstructure and fatigue behavior of ATI 718Plus alloy. *International Journal of Fatigue*, 102:121–134, September 2017. doi: 10.1016/j.ijfatigue.2017.04.016.

[28] S. Keller, M. Horstmann, N. Kashaev, and B. Klusemann. Crack closure mechanisms in residual stress fields generated by laser shock peening: A combined experimental-numerical approach. *Engineering Fracture Mechanics*, 221:106630, November 2019. doi: 10.1016/j.engfracmech.2019.106630.

[29] U. Zerbst, M. Madia, C. Klinger, D. Bettge, and Y. Murakami. Defects as a root cause of fatigue failure of metallic components. III: Cavities, dents, corrosion pits, scratches. *Engineering Failure Analysis*, 97:759–776, March 2019. doi: 10.1016/j.engfailanal.2019.01.034.

[30] Majid Laleh, Esmaeil Sadeghi, Reynier I. Revilla, Qi Chao, Nima Haghdadi, Anthony E. Hughes, Wei Xu, Iris De Graeve, Ma Qian, Ian Gibson, and Mike Y. Tan. Heat treatment for metal additive manufacturing. *Progress in Materials Science*, 133:101051, March 2023. doi: 10.1016/j.pmatsci.2022.101051.

[31] R. C. McCLUNG. A literature survey on the stability and significance of residual stresses during fatigue. *Fatigue & Fracture of Engineering Materials & Structures*, 30(3):173–205, 2007. ISSN 1460-2695. doi: 10.1111/j.1460-2695.2007.01102.x.

[32] Richard G. Budynas and J. Keith Nisbett. *Shigley's mechanical engineering design*. McGraw-Hill series in mechanical engineering. McGraw-Hill, 9th ed edition, 2011.

[33] G Sendeckyj. Constant life diagrams — a historical review. *International Journal of Fatigue*, 23(4):347–353, April 2001. doi: 10.1016/S0142-1123(00)00077-3.

[34] E. Salvati and A.M. Korsunsky. An analysis of macro- and micro-scale residual stresses of Type I, II and III using FIB-DIC micro-ring-core milling and crystal plasticity FE modelling. *International Journal of Plasticity*, 98:123–138, November 2017. doi: 10.1016/j.ijplas.2017.07.004.

[35] Ali Tabatabaeian, Ahmad Reza Ghasemi, Mahmood M. Shokrieh, Bahareh Marzbanrad, Mohammad Baraheni, and Mohammad Fotouhi. Residual Stress in Engineering Materials: A Review. *Advanced Engineering Materials*, page 2100786, November 2021. doi: 10.1002/adem.202100786.

[36] Andrzej Nycz, Yousub Lee, Mark Noakes, Deo Ankit, Christopher Masuo, Srdjan Simunovic, Jeff Bunn, Lonnie Love, Victor Oancea, Andrew Payzant, and Chris M. Fancher. Effective residual stress prediction validated with neutron diffraction method for metal large-scale additive manufacturing. *Materials & Design*, 205:109751, July 2021. doi: 10.1016/j.matdes.2021.109751.

[37] Yilan Kang, Yu Qiu, Zhenkun Lei, and Ming Hu. An application of Raman spectroscopy on the measurement of residual stress in porous silicon. *Optics and Lasers in Engineering*, 43

(8):847–855, August 2005. doi: 10.1016/j.optlaseng.2004.09.005.

[38] M. D. Olson, A. T. DeWald, and M. R. Hill. Precision of Hole-Drilling Residual Stress Depth Profile Measurements and an Updated Uncertainty Estimator. *Experimental Mechanics*, 61 (3):549–564, March 2021. doi: 10.1007/s11340-020-00679-1.

[39] Michele Barsanti, Marco Beghini, Ciro Santus, Alessio Benincasa, and Lorenzo Bertelli. Integral method coefficients for the ring-core technique to evaluate non-uniform residual stresses. *The Journal of Strain Analysis for Engineering Design*, 53(4):210–224, May 2018. doi: 10.1177/0309324718760438.

[40] E. Salvati, L. Romano-Brandt, M.Z. Mughal, M. Sebastiani, and A.M. Korsunsky. Generalised residual stress depth profiling at the nanoscale using focused ion beam milling. *Journal of the Mechanics and Physics of Solids*, 125:488–501, April 2019. doi: 10.1016/j.jmps.2019.01.007.

[41] Michael Prime. Cross-Sectional Mapping of Residual Stresses by Measuring the Surface Contour After a Cut. *Journal of Engineering Materials and Technology*, 123:162–168, May 2001. doi: 10.1115/1.1345526.

[42] Alexander Jg Lunt, Nikolaos Baimpas, Enrico Salvati, Igor P Dolbnya, Tan Sui, Siqi Ying, Hongjia Zhang, Annette K Kleppe, Jiri Dluhoš, and Alexander M Korsunsky. A state-of-the-art review of micron-scale spatially resolved residual stress analysis by FIB-DIC ring-core milling and other techniques. *The Journal of Strain Analysis for Engineering Design*, 50(7):426–444, October 2015. doi: 10.1177/0309324715596700.

[43] Gary S. Schajer and Clayton O. Ruud. Overview of Residual Stresses and Their Measurement. In *Practical Residual Stress Measurement Methods*, pages 1–27. John Wiley & Sons, Ltd, 2013. doi: 10.1002/9781118402832.ch1.

[44] G. F. Bocchini. The Influences of Porosity on the Characteristics of Sintered Materials. *SAE Transactions*, 95:790–805, 1986.

[45] Anirudh Sampath Madhvacharyula, Araveeti V. Sai Pavan, Subrahmanyam Gorthi, Srihari Chitral, N. Venkaiah, and Degala Venkata Kiran. In situ detection of welding defects: a review. *Welding in the World*, 66(4):611–628, April 2022. doi: 10.1007/s40194-021-01229-6.

[46] Niloofar Sanaei and Ali Fatemi. Defects in additive manufactured metals and their effect on fatigue performance: A state-of-the-art review. *Progress in Materials Science*, 117:100724, April 2021. doi: 10.1016/j.pmatsci.2020.100724.

[47] Wayne E. King, Holly D. Barth, Victor M. Castillo, Gilbert F. Gallegos, John W. Gibbs, Douglas E. Hahn, Chandrika Kamath, and Alexander M. Rubenchik. Observation of keyhole-mode laser melting in laser powder-bed fusion additive manufacturing. *Journal of Materials Processing Technology*, 214(12):2915–2925, December 2014. doi: 10.1016/j.jmatprotec.2014.06.005.

[48] Ross Cunningham, Cang Zhao, Niranjan Parab, Christopher Kantzos, Joseph Pauza, Kamel Fezzaa, Tao Sun, and Anthony D. Rollett. Keyhole threshold and morphology in laser melting revealed by ultrahigh-speed x-ray imaging. *Science*, 363(6429):849–852, February 2019. doi:

10.1126/science.aav4687.

[49] Stephen J. Mashl. Hot Isostatic Pressing of Castings. In Srinath Viswanathan, Diran Apelian, Raymond J. Donahue, Babu DasGupta, Michael Gywn, John L. Jorstad, Raymond W. Monroe, Mahi Sahoo, Thomas E. Prucha, and Daniel Twarog, editors, *Casting*, volume 15, page 0. ASM International, December 2008. doi: 10.31399/asm.hb.v15.a0005293.

[50] William E. Frazier. Metal Additive Manufacturing: A Review. *Journal of Materials Engineering and Performance*, 23(6):1917–1928, June 2014. doi: 10.1007/s11665-014-0958-z.

[51] Xiaopeng Niu, Shun-Peng Zhu, Jin-Chao He, Ding Liao, José A. F. O. Correia, Filippo Berto, and Qingyuan Wang. Defect tolerant fatigue assessment of AM materials: Size effect and probabilistic prospects. *International Journal of Fatigue*, 160:106884, July 2022. doi: 10.1016/j.ijfatigue.2022.106884.

[52] S. Romano, A. Brückner-Foit, A. Brandão, J. Gumpinger, T. Ghidini, and S. Beretta. Fatigue properties of AlSi10Mg obtained by additive manufacturing: Defect-based modelling and prediction of fatigue strength. *Engineering Fracture Mechanics*, 187:165–189, January 2018. doi: 10.1016/j.engfracmech.2017.11.002.

[53] S. Romano, A. Abel, J. Gumpinger, A.D. Brandão, and S. Beretta. Quality control of AlSi10Mg produced by SLM: Metallography versus CT scans for critical defect size assessment. *Additive Manufacturing*, 28:394–405, August 2019. doi: 10.1016/j.addma.2019.05.017.

[54] U. Zerbst, M. Madia, C. Klinger, D. Bettge, and Y. Murakami. Defects as a root cause of fatigue failure of metallic components. II: Non-metallic inclusions. *Engineering Failure Analysis*, 98:228–239, April 2019. doi: 10.1016/j.engfailanal.2019.01.054.

[55] U. Zerbst, M. Madia, C. Klinger, D. Bettge, and Y. Murakami. Defects as a root cause of fatigue failure of metallic components. I: Basic aspects. *Engineering Failure Analysis*, 97: 777–792, March 2019. doi: 10.1016/j.engfailanal.2019.01.055.

[56] Bi Zhang, Yongtao Li, and Qian Bai. Defect Formation Mechanisms in Selective Laser Melting: A Review. *Chinese Journal of Mechanical Engineering*, 30(3):515–527, May 2017. doi: 10.1007/s10033-017-0121-5.

[57] Yukitaka Murakami. Material defects as the basis of fatigue design. *International Journal of Fatigue*, 41:2–10, August 2012. doi: 10.1016/j.ijfatigue.2011.12.001.

[58] E. Maire and P. J. Withers. Quantitative X-ray tomography. *International Materials Reviews*, 59(1):1–43, January 2014. doi: 10.1179/1743280413Y.0000000023.

[59] T. DebRoy, H. L. Wei, J. S. Zuback, T. Mukherjee, J. W. Elmer, J. O. Milewski, A. M. Beese, A. Wilson-Heid, A. De, and W. Zhang. Additive manufacturing of metallic components – Process, structure and properties. *Progress in Materials Science*, 92:112–224, March 2018. doi: 10.1016/j.pmatsci.2017.10.001.

[60] Walter Schütz. A history of fatigue. *Engineering Fracture Mechanics*, 54(2):263–300, May 1996. doi: 10.1016/0013-7944(95)00178-6.

[61] Weicheng Cui. A state-of-the-art review on fatigue life prediction methods for metal

structures. *Journal of Marine Science and Technology*, 7(1):43–56, June 2002. doi: 10.1007/s007730200012.

[62] M. H. El Haddad, K. N. Smith, and T. H. Topper. Fatigue Crack Propagation of Short Cracks. *Journal of Engineering Materials and Technology*, 101(1):42–46, January 1979. doi: 10.1115/1.3443647.

[63] H. Kitagawa. Applicability of fracture mechanics to very small cracks or the cracks in the early stage. *Proc. of 2nd ICM, Cleveland, 1976*, pages 627–631, 1976.

[64] Luke Sheridan. A modified El-Haddad model for versatile defect tolerant design. *International Journal of Fatigue*, 145:106062, April 2021. doi: 10.1016/j.ijfatigue.2020.106062.

[65] Luke Sheridan, Joy E. Gockel, and Onome E. Scott-Emuakpor. Stress-defect-life interactions of fatigued additively manufactured alloy 718. *International Journal of Fatigue*, 143:106033, February 2021. doi: 10.1016/j.ijfatigue.2020.106033.

[66] Zhengkai Wu, Shengchuan Wu, Jianguang Bao, Weijian Qian, Suleyman Karabal, Wei Sun, and Philip J. Withers. The effect of defect population on the anisotropic fatigue resistance of AlSi10Mg alloy fabricated by laser powder bed fusion. *International Journal of Fatigue*, 151:106317, October 2021. doi: 10.1016/j.ijfatigue.2021.106317.

[67] Klas Solberg, Shuai Guan, Nima Razavi, Torgeir Welo, Kang Cheung Chan, and Filippo Berto. Fatigue of additively manufactured 316L stainless steel: The influence of porosity and surface roughness. *Fatigue & Fracture of Engineering Materials & Structures*, 42(9): 2043–2052, 2019. doi: 10.1111/ffe.13077.

[68] N.S. Matloff. *Statistical Regression and Classification: From Linear Models to Machine Learning*. Chapman & Hall/CRC Texts in St. CRC Press, Taylor & Francis Group, 2017.

[69] Alexander L. Fradkov. Early History of Machine Learning. *IFAC-PapersOnLine*, 53(2): 1385–1390, 2020. doi: 10.1016/j.ifacol.2020.12.1888.

[70] Christopher M. Bishop. *Pattern recognition and machine learning*. Information science and statistics. Springer, 2006.

[71] Kevin P. Murphy. *Machine learning: a probabilistic perspective*. Adaptive computation and machine learning series. MIT Press, 2012.

[72] Zoubin Ghahramani. Probabilistic machine learning and artificial intelligence. *Nature*, 521 (7553):452–459, May 2015. ISSN 1476-4687. doi: 10.1038/nature14541.

[73] Farshid Jafarian, Hossein Amirabadi, and Mehdi Fattahi. Improving surface integrity in finish machining of Inconel 718 alloy using intelligent systems. *The International Journal of Advanced Manufacturing Technology*, 71(5):817–827, March 2014. doi: 10.1007/s00170-013-5528-2.

[74] Hasan Jafari, Hadi Mansouri, and Mohammad Honarpisheh. Investigation of residual stress distribution of dissimilar Al-7075-T6 and Al-6061-T6 in the friction stir welding process strengthened with SiO2 nanoparticles. *Journal of Manufacturing Processes*, 43:145–153, July 2019. doi: 10.1016/j.jmapro.2019.05.023.

[75] Jing Ying Zhang, Steven Y. Liang, Guowei Zhang, and David Yen. Modeling of Residual Stress Profile in Finish Hard Turning. *Materials and Manufacturing Processes*, 21(1):39–45, January 2006. doi: 10.1081/AMP-200060608.

[76] J. P. B. A. Sembiring, A. Amanov, and Y. S. Pyun. Artificial neural network-based prediction model of residual stress and hardness of nickel-based alloys for UNSM parameters optimization. *Materials Today Communications*, 25:101391, December 2020. doi: 10.1016/j.mtcomm.2020.101391.

[77] D. Umbrello, G. Ambrogio, L. Filice, and R. Shivpuri. A hybrid finite element method–artificial neural network approach for predicting residual stresses and the optimal cutting conditions during hard turning of AISI 52100 bearing steel. *Materials & Design*, 29 (4):873–883, January 2008. doi: 10.1016/j.matdes.2007.03.004.

[78] Q. Wu, T. Mukherjee, A. De, and T. DebRoy. Residual stresses in wire-arc additive manufacturing – Hierarchy of influential variables. *Additive Manufacturing*, 35:101355, October 2020. doi: 10.1016/j.addma.2020.101355.

[79] Minghui Cheng, Li Jiao, Pei Yan, Lvchen Feng, Tianyang Qiu, Xibin Wang, and Baorong Zhang. Prediction of surface residual stress in end milling with Gaussian process regression. *Measurement*, 178:109333, June 2021. doi: 10.1016/j.measurement.2021.109333.

[80] Jie Chen and Yongming Liu. Fatigue modeling using neural networks: A comprehensive review. *Fatigue & Fracture of Engineering Materials & Structures*, 45(4):945–979, 2022. doi: 10.1111/ffe.13640.

[81] Lanyi Wang, Shun-Peng Zhu, Changqi Luo, Ding Liao, and Qingyuan Wang. Physics-guided machine learning frameworks for fatigue life prediction of AM materials. *International Journal of Fatigue*, page 107658, March 2023. doi: 10.1016/j.ijfatigue.2023.107658.

[82] N.S. Johnson, P.S. Vulimiri, A.C. To, X. Zhang, C.A. Brice, B.B. Kappes, and A.P. Stebner. Invited review: Machine learning for materials developments in metals additive manufacturing. *Additive Manufacturing*, 36:101641, December 2020. doi: 10.1016/j.addma.2020.101641.

[83] Seunghyun Moon, Ruimin Ma, Ross Attardo, Charles Tomonto, Mark Nordin, Paul Wheelock, Michael Glavicic, Maxwell Layman, Richard Billo, and Tengfei Luo. Impact of surface and pore characteristics on fatigue life of laser powder bed fusion Ti–6Al–4V alloy described by neural network models. *Scientific Reports*, 11(1):20424, December 2021. doi: 10.1038/s41598-021-99959-6.

[84] Xin Peng, Shengchuan Wu, Weijian Qian, Jianguang Bao, Yanan Hu, Zhixin Zhan, Guangping Guo, and Philip J. Withers. The potency of defects on fatigue of additively manufactured metals. *International Journal of Mechanical Sciences*, 221:107185, May 2022. doi: 10.1016/j.ijmecsci.2022.107185.

[85] Hongyixi Bao, Shengchuan Wu, Zhengkai Wu, Guozheng Kang, Xin Peng, and Philip J. Withers. A machine-learning fatigue life prediction approach of additively manufactured metals. *Engineering Fracture Mechanics*, 242:107508, February 2021. doi: 10.1016/j.

engfracmech.2020.107508.

[86] Anyi Li, Shaharyar Baig, Jia Liu, Shuai Shao, and Nima Shamsaei. Defect criticality analysis on fatigue life of L-PBF 17-4 PH stainless steel via machine learning. *International Journal of Fatigue*, 163:107018, October 2022. doi: 10.1016/j.ijfatigue.2022.107018.

[87] Jun Li, Zhengmao Yang, Guian Qian, and Filippo Berto. Machine learning based very-high-cycle fatigue life prediction of Ti-6Al-4V alloy fabricated by selective laser melting. *International Journal of Fatigue*, 158:106764, May 2022. doi: 10.1016/j.ijfatigue.2022.106764.

[88] E. Maleki, S. Bagherifard, S.M.J. Razavi, M. Bandini, A. du Plessis, F. Berto, and M. Guagliano. On the efficiency of machine learning for fatigue assessment of post-processed additively manufactured AlSi10Mg. *International Journal of Fatigue*, 160:106841, July 2022. doi: 10.1016/j.ijfatigue.2022.106841.

[89] Andrea Tridello, Alberto Ciampaglia, Filippo Berto, and Davide Salvatore Paolino. Assessment of the Critical Defect in Additive Manufacturing Components through Machine Learning Algorithms. *Applied Sciences*, 13(7):4294, March 2023. doi: 10.3390/app13074294.

[90] Lei He, Zhilei Wang, Yuki Ogawa, Hiroyuki Akebono, Atsushi Sugeta, and Yoshiichirou Hayashi. Machine-learning-based investigation into the effect of defect/inclusion on fatigue behavior in steels. *International Journal of Fatigue*, 155:106597, February 2022. doi: 10.1016/j.ijfatigue.2021.106597.

[91] Linwei Dang, Xiaofan He, Dingcheng Tang, Yuhai Li, and Tianshuai Wang. A fatigue life prediction approach for laser-directed energy deposition titanium alloys by using support vector regression based on pore-induced failures. *International Journal of Fatigue*, 159:106748, June 2022. doi: 10.1016/j.ijfatigue.2022.106748.

[92] Linwei Dang, Xiaofan He, Dingcheng Tang, Bin Wu, and Yuhai Li. A fatigue life posterior analysis approach for laser-directed energy deposition Ti-6Al-4V alloy based on pore-induced failures by kernel ridge. *Engineering Fracture Mechanics*, 289:109433, September 2023. doi: 10.1016/j.engfracmech.2023.109433.

[93] Y.W. Luo, B. Zhang, X. Feng, Z.M. Song, X.B. Qi, C.P. Li, G.F. Chen, and G.P. Zhang. Pore-affected fatigue life scattering and prediction of additively manufactured Inconel 718: An investigation based on miniature specimen testing and machine learning approach. *Materials Science and Engineering: A*, 802:140693, January 2021. doi: 10.1016/j.msea.2020.140693.

[94] Liu Yang, Xuhui Meng, and George Em Karniadakis. B-PINNs: Bayesian physics-informed neural networks for forward and inverse PDE problems with noisy data. *Journal of Computational Physics*, 425:109913, January 2021. doi: 10.1016/j.jcp.2020.109913.

[95] Foroogh Hosseinzadeh, P. Bouchard, and Jan Kowal. Towards good practice guidelines for the contour method of residual stress measurement. *Journal of Engineering*, 2014, July 2014. doi: 10.1049/joe.2014.0134.

[96] N. Naveed. Guidelines to select suitable parameters for contour method stress measurements. *Archives of Mechanics*, 72(1):39–58, February 2020. doi: 10.24423/aom.3378.

[97] E. Salvati and A.M. Korsunsky. Micro-scale measurement & FEM modelling of residual stresses in AA6082-T6 Al alloy generated by wire EDM cutting. *Journal of Materials Processing Technology*, 275:116373, January 2020. doi: 10.1016/j.jmatprotec.2019.116373.

[98] M. D. Olson, A. T. DeWald, M. B. Prime, and M. R. Hill. Estimation of Uncertainty for Contour Method Residual Stress Measurements. *Experimental Mechanics*, 55(3):577–585, March 2015. doi: 10.1007/s11340-014-9971-2.

[99] M. B. Prime, R. J. Sebring, J. M. Edwards, D. J. Hughes, and P. J. Webster. Laser surface-contouring and spline data-smoothing for residual stress measurement. *Experimental Mechanics*, 44(2):176–184, April 2004. doi: 10.1007/BF02428177.

[100] OH Basquin. The Exponential Law of Endurance Tests. *Copyright of Key Engineering Materials is the property of Trans Tech Publications*, 1910.

[101] E08 Committee. Practice for Statistical Analysis of Linear or Linearized Stress-Life (S-N) and Strain-Life (-N) Fatigue Data. Technical report, ASTM International, 2008.

[102] Carl Edward Rasmussen and Christopher K. I. Williams. *Gaussian processes for machine learning*. Adaptive computation and machine learning. MIT Press, 2006.

[103] Alex Graves. Practical Variational Inference for Neural Networks. In *Advances in Neural Information Processing Systems*, volume 24. Curran Associates, Inc., 2011.

[104] David Wingate and Theophane Weber. Automated Variational Inference in Probabilistic Programming, January 2013.

[105] Benyamin Ghojogh, Ali Ghodsi, Fakhri Karray, and Mark Crowley. Factor Analysis, Probabilistic Principal Component Analysis, Variational Inference, and Variational Autoencoder: Tutorial and Survey, May 2022.

[106] Rajesh Ranganath, Sean Gerrish, and David M. Blei. Black Box Variational Inference, December 2013.

[107] Michael I. Jordan, Zoubin Ghahramani, Tommi S. Jaakkola, and Lawrence K. Saul. An Introduction to Variational Methods for Graphical Models. In Michael I. Jordan, editor, *Learning in Graphical Models*, pages 105–161. Springer Netherlands, 1998. doi: 10.1007/978-94-011-5014-9_5.

[108] Radford M. Neal. *Bayesian Learning for Neural Networks*. Springer New York, 1996. doi: 10.1007/978-1-4612-0745-0.

[109] Radford M. Neal. MCMC Using Hamiltonian Dynamics. In *Handbook of Markov Chain Monte Carlo*. Chapman and Hall/CRC, 2011.

[110] Jie Wang. An Intuitive Tutorial to Gaussian Processes Regression. *arXiv:2009.10862 [cs, stat]*, February 2021.

[111] Nicolas Bacaër. *A Short History of Mathematical Population Dynamics*. Springer London, 2011. doi: 10.1007/978-0-85729-115-8.

[112] Stephan Dreiseitl and Lucila Ohno-Machado. Logistic regression and artificial neural network classification models: a methodology review. *Journal of Biomedical Informatics*, 35(5):352–

359, October 2002. doi: 10.1016/S1532-0464(03)00034-0.

[113] C.M. Bishop. *Neural Networks for Pattern Recognition*. Advanced Texts in Econometrics. Clarendon Press, 1995.

[114] Yann Lecun. A theoretical framework for back-propagation. *Proceedings of the 1988 Connectionist Models Summer School, CMU, Pittsburg, PA*, pages 21–28, 1988.

[115] M. Raissi, P. Perdikaris, and G.E. Karniadakis. Physics-informed neural networks: A deep learning framework for solving forward and inverse problems involving nonlinear partial differential equations. *Journal of Computational Physics*, 378:686–707, February 2019. doi: 10.1016/j.jcp.2018.10.045.

[116] George Em Karniadakis, Ioannis G. Kevrekidis, Lu Lu, Paris Perdikaris, Sifan Wang, and Liu Yang. Physics-informed machine learning. *Nature Reviews Physics*, 3(6):422–440, June 2021. doi: 10.1038/s42254-021-00314-5.

[117] Salvatore Cuomo, Vincenzo Schiano Di Cola, Fabio Giampaolo, Gianluigi Rozza, Maziar Raissi, and Francesco Piccialli. Scientific Machine Learning Through Physics–Informed Neural Networks: Where we are and What's Next. *Journal of Scientific Computing*, 92(3):88, July 2022. doi: 10.1007/s10915-022-01939-z.

[118] David J. C. MacKay. Information-Based Objective Functions for Active Data Selection. *Neural Computation*, 4(4):590–604, July 1992. doi: 10.1162/neco.1992.4.4.590.

[119] David J C Mackay. Probable networks and plausible predictions — a review of practical Bayesian methods for supervised neural networks. *Network: Computation in Neural Systems*, 6(3):469–505, January 1995. doi: 10.1088/0954-898X_6_3_011.

[120] David J C MacKay. *Information Theory, Inference, and Learning Algorithms*. Cambridge University Press, 2003.

[121] Jouko Lampinen and Aki Vehtari. Bayesian approach for neural networks—review and case studies. *Neural Networks*, 14(3):257–274, April 2001. doi: 10.1016/S0893-6080(00)00098-8.

[122] Ethan Goan and Clinton Fookes. Bayesian Neural Networks: An Introduction and Survey. In Kerrie L. Mengersen, Pierre Pudlo, and Christian P. Robert, editors, *Case Studies in Applied Bayesian Data Science: CIRM Jean-Morlet Chair, Fall 2018*, Lecture Notes in Mathematics, pages 45–87. Springer International Publishing, 2020. doi: 10.1007/978-3-030-42553-1_3.

[123] Laurent Valentin Jospin, Hamid Laga, Farid Boussaid, Wray Buntine, and Mohammed Bennamoun. Hands-On Bayesian Neural Networks - A Tutorial for Deep Learning Users. *IEEE Computational Intelligence Magazine*, 17(2):29–48, May 2022. doi: 10.1109/MCI.2022.3155327.

[124] Hyeongwoon Lee and Jongsoo Lee. Neural network prediction of sound quality via domain Knowledge-Based data augmentation and Bayesian approach with small data sets. *Mechanical Systems and Signal Processing*, 157:107713, August 2021. doi: 10.1016/j.ymssp.2021.107713.

[125] Hayrettin Okut. Bayesian Regularized Neural Networks for Small n Big p Data. In Joao

Luis Garcia Rosa, editor, *Artificial Neural Networks - Models and Applications*. InTech, October 2016. doi: 10.5772/63256.

[126] David Barber. *Bayesian Reasoning and Machine Learning*. Cambridge University Press, 1 edition, June 2012. doi: 10.1017/CBO9780511804779.

[127] Jie Ding, Vahid Tarokh, and Yuhong Yang. Model Selection Techniques: An Overview. *IEEE Signal Processing Magazine*, 35(6):16–34, November 2018. doi: 10.1109/MSP.2018.2867638.

[128] Wayne Cai, Glenn Daehn, Anupam Vivek, Jingjing Li, Haris Khan, Rajiv S. Mishra, and Mageshwari Komarasamy. A State-of-the-Art Review on Solid-State Metal Joining. *Journal of Manufacturing Science and Engineering*, 141(3):031012, March 2019. doi: 10.1115/1.4041182.

[129] R.S. Mishra and Z.Y. Ma. Friction stir welding and processing. *Materials Science and Engineering: R: Reports*, 50(1-2):1–78, August 2005. doi: 10.1016/j.mser.2005.07.001.

[130] J. S. Jesus, J. M. Costa, A. Loureiro, and J. M. Ferreira. Assessment of friction stir welding aluminium T-joints. *Journal of Materials Processing Technology*, 255:387–399, May 2018. doi: 10.1016/j.jmatprotec.2017.12.036.

[131] Dhanesh G Mohan and S Gopi. A Review on Friction Stir Welded T-Joint. *International Journal of Science Technology & Engineering*, 2(07):7, 2016.

[132] M.T. Milan, W.W. Bose Filho, J.R. Tarpani, A.M.S. Malafaia, C.P.O. Silva, B.C. Pellizer, and L.E. Pereira. Residual Stress Evaluation of AA2024-T3 Friction Stir Welded Joints. *Journal of Materials Engineering and Performance*, 16(1):86–92, February 2007. doi: 10.1007/s11665-006-9013-z.

[133] Lucjan Śnieżek, Robert Kosturek, Marcin Wachowski, and Bogusz Kania. Microstructure and Residual Stresses of AA2519 Friction Stir Welded Joints under Different Heat Treatment Conditions. *Materials*, 13(4):834, February 2020. doi: 10.3390/ma13040834.

[134] Huseyin Uzun, Claudio Dalle Donne, Alberto Argagnotto, Tommas Ghidini, and Carla Gambaro. Friction stir welding of dissimilar Al 6013-T4 To X5CrNi18-10 stainless steel. *Materials & Design*, 26(1):41–46, February 2005. doi: 10.1016/j.matdes.2004.04.002.

[135] A. Yazdipour and A. Heidarzadeh. Effect of friction stir welding on microstructure and mechanical properties of dissimilar Al 5083-H321 and 316L stainless steel alloy joints. *Journal of Alloys and Compounds*, 680:595–603, September 2016. doi: 10.1016/j.jallcom.2016.03.307.

[136] P L Threadgill, A J Leonard, H R Shercliff, and P J Withers. Friction stir welding of aluminium alloys. *International Materials Reviews*, 54(2):49–93, March 2009. doi: 10.1179/174328009X411136.

[137] Ø. Grong. Recent advances in solid-state joining of aluminum. *Welding Journal*, 91(1):26–33, 2012.

[138] Øystein Grong, Lise Sandnes, and Filippo Berto. A Status Report on the Hybrid Metal Extrusion & Bonding (HYB) Process and Its Applications. *Material Design & Processing Communications*, 1:e41, February 2019. doi: 10.1002/mdp2.41.

[139] Lise Sandnes, Luca Romere, Øystein Grong, Filippo Berto, and Torgeir Welo. Assessment of the Mechanical Integrity of a 2 mm AA6060-T6 Butt Weld Produced Using the Hybrid Metal Extrusion & Bonding (HYB) Process – Part II: Tensile Test Results. *Procedia Structural Integrity*, 17:632–642, 2019. doi: 10.1016/j.prostr.2019.08.085.

[140] Lise Sandnes, Luca Romere, Filippo Berto, Torgeir Welo, and Øystein Grong. Assessment of the Mechanical Integrity of a 2 mm AA6060-T6 Butt Weld Produced Using the Hybrid Metal Extrusion & Bonding (HYB) Process – Part I: Bend Test Results. *Procedia Manufacturing*, 34:147–153, 2019. doi: 10.1016/j.promfg.2019.06.132.

[141] Lise Sandnes, Øystein Grong, Torgeir Welo, and Filippo Berto. Fatigue properties of AA6060-T6 butt welds made by hybrid metal extrusion & bonding. *Fatigue & Fracture of Engineering Materials & Structures*, 43(10):2349–2358, October 2020. doi: 10.1111/ffe.13302.

[142] Alessia Greco, Emanuele Sgambitterra, and Franco Furgiuele. A new methodology for measuring residual stress using a modified Berkovich nano-indenter. *International Journal of Mechanical Sciences*, 207:106662, October 2021. doi: 10.1016/j.ijmecsci.2021.106662.

[143] Fatih Uzun and Alexander M Korsunsky. On the identification of eigenstrain sources of welding residual stress in bead-on-plate inconel 740H specimens. *International Journal of Mechanical Sciences*, 145:231–245, September 2018. doi: 10.1016/j.ijmecsci.2018.07.007.

[144] A. Kouadri-Henni, C. Seang, B. Malard, and V. Klosek. Residual stresses induced by laser welding process in the case of a dual-phase steel DP600: Simulation and experimental approaches. *Materials & Design*, 123:89–102, June 2017. doi: 10.1016/j.matdes.2017.03.022.

[145] Jazeel Rahman Chukkan, Guiyi Wu, Michael E. Fitzpatrick, Steve Jones, and Joe Kelleher. An iterative technique for the reconstruction of residual stress fields in a butt-welded plate from experimental measurement, and comparison with welding process simulation. *International Journal of Mechanical Sciences*, 160:421–428, September 2019. doi: 10.1016/j.ijmecsci.2019.07.001.

[146] Hamed Jamshidi Aval. Microstructure and residual stress distributions in friction stir welding of dissimilar aluminium alloys. *Materials & Design*, 87:405–413, December 2015. doi: 10.1016/j.matdes.2015.08.050.

[147] M. Peel, A. Steuwer, M. Preuss, and P.J. Withers. Microstructure, mechanical properties and residual stresses as a function of welding speed in aluminium AA5083 friction stir welds. *Acta Materialia*, 51(16):4791–4801, September 2003. doi: 10.1016/S1359-6454(03)00319-7.

[148] Enrico Salvati, Joris Everaerts, Koji Kageyama, and Alexander M. Korsunsky. Transverse fatigue behaviour and residual stress analyses of double sided FSW aluminium alloy joints. *Fatigue & Fracture of Engineering Materials & Structures*, 42(9):1980–1990, September 2019. doi: 10.1111/ffe.13068.

[149] T-S. Jun, K. Dragnevski, and A.M. Korsunsky. Microstructure, residual strain, and eigenstrain analysis of dissimilar friction stir welds. *Materials & Design*, 31:S121–S125, June 2010. doi: 10.1016/j.matdes.2009.11.042.

[150] A.P Reynolds, Wei Tang, T Gnaupel-Herold, and H Prask. Structure, properties, and resid-

ual stress of 304L stainless steel friction stir welds. *Scripta Materialia*, 48(9):1289–1294, May 2003. doi: 10.1016/S1359-6462(03)00024-1.

[151] Meysam Haghshenas, M. A. Gharghouri, V. Bhakhri, R. J. Klassen, and A. P. Gerlich. Assessing residual stresses in friction stir welding: neutron diffraction and nanoindentation methods. *The International Journal of Advanced Manufacturing Technology*, 93(9-12):3733–3747, December 2017. doi: 10.1007/s00170-017-0759-2.

[152] Madhumanti Bhattacharyya. Evaluation of residual stresses in isothermal friction stir welded 304L stainless steel plates. *Materials Science and Engineering: A*, page 39, 2021.

[153] M Prime, T Gnaupelherold, J Baumann, R Lederich, D Bowden, and R Sebring. Residual stress measurements in a thick, dissimilar aluminum alloy friction stir weld. *Acta Materialia*, 54(15):4013–4021, September 2006. doi: 10.1016/j.actamat.2006.04.034.

[154] Chuan Liu and Xiang Yi. Residual stress measurement on AA6061-T6 aluminum alloy friction stir butt welds using contour method. *Materials & Design*, 46:366–371, April 2013. doi: 10.1016/j.matdes.2012.10.030.

[155] Pierpaolo Carlone and Gaetano S. Palazzo. Longitudinal Residual Stress Analysis in AA2024-T3 Friction Stir Welding. *The Open Mechanical Engineering Journal*, 7(1):18–26, August 2013. doi: 10.2174/1874155X01307010018.

[156] Chengcong Zhang and Amir A. Shirzadi. Measurement of residual stresses in dissimilar friction stir-welded aluminium and copper plates using the contour method. *Science and Technology of Welding and Joining*, 23(5):394–399, July 2018. doi: 10.1080/13621718.2017.1402846.

[157] I. Alinaghian, M. Honarpisheh, and S. Amini. The influence of bending mode ultrasonic-assisted friction stir welding of Al-6061-T6 alloy on residual stress, welding force and macrostructure. *The International Journal of Advanced Manufacturing Technology*, 95(5-8):2757–2766, March 2018. doi: 10.1007/s00170-017-1431-6.

[158] Iman Alinaghian, Saeid Amini, and Mohammad Honarpisheh. Residual stress, tensile strength, and macrostructure investigations on ultrasonic assisted friction stir welding of AA 6061-T6. *The Journal of Strain Analysis for Engineering Design*, 53(7):494–503, October 2018. doi: 10.1177/0309324718789768.

[159] Sumair Sunny, Ritin Mathews, Glenn Gleason, Arif Malik, and Jeremiah Halley. Effect of metal additive manufacturing residual stress on post-process machining-induced stress and distortion. *International Journal of Mechanical Sciences*, 202-203:106534, July 2021. doi: 10.1016/j.ijmecsci.2021.106534.

[160] Ritin Mathews, Sumair Sunny, Arif Malik, and Jeremiah Halley. Coupling between inherent and machining-induced residual stresses in aluminum components. *International Journal of Mechanical Sciences*, page 106865, October 2021. doi: 10.1016/j.ijmecsci.2021.106865.

[161] Dong-yang Yan, Ai-ping Wu, Juergen Silvanus, and Qing-yu Shi. Predicting residual distortion of aluminum alloy stiffened sheet after friction stir welding by numerical simulation. *Materials & Design*, 32(4):2284–2291, April 2011. doi: 10.1016/j.matdes.2010.11.032.

[162] Weiliang He, Jinglin Liu, Wei Hu, Gongdong Wang, and Wenjing Chen. Controlling residual stress and distortion of friction stir welding joint by external stationary shoulder. *High Temperature Materials and Processes*, 38(2019):662–671, February 2019. doi: 10.1515/htmp-2019-0005.

[163] Wanchuck Woo, Hahn Choo, Donald W. Brown, Zhili Feng, and Peter K. Liaw. Angular distortion and through-thickness residual stress distribution in the friction-stir processed 6061-T6 aluminum alloy. *Materials Science and Engineering: A*, 437(1):64–69, November 2006. doi: 10.1016/j.msea.2006.04.066.

[164] Lise Sandnes, Gisle Rørvik, Inge Kulbotten, Øystein Grong, and Filippo Berto. Qualification of the Hybrid Metal Extrusion & Bonding (HYB) Process for Welding of Aluminium Offshore Structures. *Material Design & Processing Communications*, June 2020. doi: 10.1002/mdp2.194.

[165] Francesco Leoni, Øystein Grong, Lise Sandnes, and Filippo Berto. High temperature tensile properties of AA6082 filler wire used for solid-state joining. *Procedia Structural Integrity*, 25:348–354, 2020. doi: 10.1016/j.prostr.2020.04.039.

[166] HuiHuan Ma, Quanchao Hou, Zhiwei Yu, and Pengpeng Ni. Stability of 6082-T6 aluminum alloy columns under axial forces at high temperatures. *Thin-Walled Structures*, 157:107083, December 2020. doi: 10.1016/j.tws.2020.107083.

[167] Xiaonong Guo, Lei Tao, Shaojun Zhu, and Shaohan Zong. Experimental Investigation of Mechanical Properties of Aluminum Alloy at High and Low Temperatures. *Journal of Materials in Civil Engineering*, 32(2):06019016, February 2020. doi: 10.1061/(ASCE)MT.1943-5533.0003002.

[168] Nina Kristin Langhelle and Jørgen Amdahl. Experimental and Numerical Analysis of Aluminium Columns Subjected to Fire. *The International Society of Offshore and Polar Engineers*, 2001.

[169] Ole Runar Myhr, Øystein Grong, and Carmen Schäfer. An Extended Age-Hardening Model for Al-Mg-Si Alloys Incorporating the Room-Temperature Storage and Cold Deformation Process Stages. *Metallurgical and Materials Transactions A*, 46(12):6018–6039, December 2015. doi: 10.1007/s11661-015-3175-y.

[170] Christophe Geuzaine and Jean-François Remacle. Gmsh: A 3-D finite element mesh generator with built-in pre- and post-processing facilities. *International Journal for Numerical Methods in Engineering*, 79(11):1309–1331, 2009. doi: https://doi.org/10.1002/nme.2579.

[171] Electricité de France. Finite element code_aster, Analysis of Structures and Thermomechanics for Studies and Research, 1989–2024. URL www.code-aster.org.

[172] M. B. Toparli and M. E. Fitzpatrick. Development and Application of the Contour Method to Determine the Residual Stresses in Thin Laser-Peened Aluminium Alloy Plates. *Experimental Mechanics*, 56(2):323–330, February 2016. doi: 10.1007/s11340-015-0100-7.

[173] S.W. Williams and A. Steuwer. Residual stresses in friction stir welding. In *Friction Stir Welding*, pages 215–244. Elsevier, 2010. doi: 10.1533/9781845697716.2.215.

[174] Francesco Leoni, Øystein Grong, Lise Sandnes, Torgeir Welo, and Filippo Berto. Finite element modelling of the filler wire feeding in the hybrid metal extrusion & bonding (HYB) process. *Journal of Advanced Joining Processes*, 1:100006, March 2020. doi: 10.1016/j.jajp.2020.100006.

[175] Lise Sandnes, Øystein Grong, Jan Torgersen, Torgeir Welo, and Filippo Berto. Exploring the hybrid metal extrusion and bonding process for butt welding of Al–Mg–Si alloys. *The International Journal of Advanced Manufacturing Technology*, 98(5-8):1059–1065, September 2018. doi: 10.1007/s00170-018-2234-0.

[176] Bernd-Arno Behrens, Jens Gibmeier, Kai Brunotte, Hendrik Wester, Nicola Simon, and Christoph Kock. Investigations on Residual Stresses within Hot-Bulk-Formed Components Using Process Simulation and the Contour Method. *Metals*, 11(4):566, March 2021. doi: 10.3390/met11040566.

[177] H. K. Kim, S. S. Carlson, M. L. Stanfield, S. Paddea, F. Hosseinzadeh, and P. J. Bouchard. Mitigating Cutting-Induced Plasticity Errors in the Determination of Residual Stress at Cold Expanded Holes Using the Contour Method. *Experimental Mechanics*, August 2021. doi: 10.1007/s11340-021-00756-z.

[178] M. B. Toparli, N. E. Kılınçdemir, S. Yurtdaş, B. Tanrıkulu, and U. İnce. Residual Stress Measurements of Cold-Forged Ball Studs by the Contour Method. *Experimental Techniques*, November 2021. doi: 10.1007/s40799-021-00521-w.

[179] A. Evans, G. Johnson, A. King, and P. J. Withers. Characterization of laser peening residual stresses in Al 7075 by synchrotron diffraction and the contour method. *Journal of Neutron Research*, 15(2):147–154, June 2007. doi: 10.1080/10238160701372653.

[180] Michael B. Prime. Contour Method Advanced Applications: Hoop Stresses in Cylinders and Discontinuities. In Tom Proulx, editor, *Engineering Applications of Residual Stress, Volume 8*, Conference Proceedings of the Society for Experimental Mechanics Series, pages 13–28. Springer, 2011. doi: 10.1007/978-1-4614-0225-1_2.

[181] Daulton D. Isaac, Michael B. Prime, and Nagaraj Arakere. Residual Stress Measurement of Full-Scale Jet-Engine Bearing Elements Using the Contour Method. In Simon Quinn and Xavier Balandraud, editors, *Residual Stress, Thermomechanics & Infrared Imaging, Hybrid Techniques and Inverse Problems, Volume 9*, Conference Proceedings of the Society for Experimental Mechanics Series, pages 69–81. Springer International Publishing, 2017. doi: 10.1007/978-3-319-42255-8_10.

[182] F. Hosseinzadeh and P. J. Bouchard. Mapping Multiple Components of the Residual Stress Tensor in a Large P91 Steel Pipe Girth Weld Using a Single Contour Cut. *Experimental Mechanics*, 53(2):171–181, February 2013. doi: 10.1007/s11340-012-9627-z.

[183] Y. Zhang, S. Ganguly, V. Stelmukh, M.E. Fitzpatrick, and L. Edwards. Validation of the Contour Method of Residual Stress Measurement in a MIG 2024 Weld by Neutron and Synchrotron X-ray Diffraction. *Journal of Neutron Research*, 11(4):181–185, December 2003. doi: 10.1080/10238160410001726594.

[184] Daniel F. O. Braga, Harry E. Coules, Thilo Pirling, Valentin Richter-Trummer, Paul Colegrove, and Paulo M. S. T. de Castro. Assessment of residual stress of welded structural steel plates with or without post weld rolling using the contour method and neutron diffraction. *Journal of Materials Processing Technology*, 213(12):2323–2328, December 2013. doi: 10.1016/j.jmatprotec.2013.07.004.

[185] Fatih Uzun, Joris Everaerts, León Romano Brandt, Mehmet Kartal, Enrico Salvati, and Alexander M. Korsunsky. The inclusion of short-transverse displacements in the eigenstrain reconstruction of residual stress and distortion in in740h weldments. *Journal of Manufacturing Processes*, 36:601–612, December 2018. doi: 10.1016/j.jmapro.2018.10.047.

[186] Qiang Wang, Yue Zhao, Tianyi Zhao, Dongyang Yan, Guoqing Wang, and Aiping Wu. Influence of restraint conditions on residual stress and distortion of 2219-T8 aluminum alloy TIG welded joints based on contour method. *Journal of Manufacturing Processes*, 68:796–806, August 2021. doi: 10.1016/j.jmapro.2021.05.065.

[187] Hao Jiang, Junjun Liu, Zhenkun Lei, Ruixiang Bai, Zhenfei Guo, Jianchao Zou, Honggang Dong, and Wenwen Feng. Noise-insensitive contour method for residual stress measurement in laser butt welding. *Thin-Walled Structures*, 165:107861, August 2021. doi: 10.1016/j.tws.2021.107861.

[188] M. D. Olson, A. T. DeWald, and M. R. Hill. Validation of a Contour Method Single-Measurement Uncertainty Estimator. *Experimental Mechanics*, 58(5):767–781, June 2018. doi: 10.1007/s11340-018-0385-4.

[189] Shu-cai Li, Peng He, Li-ping Li, Shao-shuai Shi, Qian-qing Zhang, Jian Zhang, and Jie Hu. Gaussian process model of water inflow prediction in tunnel construction and its engineering applications. *Tunnelling and Underground Space Technology*, 69:155–161, October 2017. doi: 10.1016/j.tust.2017.06.018.

[190] Guoshao Su, Lifeng Peng, and Lihua Hu. A Gaussian process-based dynamic surrogate model for complex engineering structural reliability analysis. *Structural Safety*, 68:97–109, September 2017. doi: 10.1016/j.strusafe.2017.06.003.

[191] Odin Gramstad, Christian Agrell, Elzbieta Bitner-Gregersen, Bingjie Guo, Eivind Ruth, and Erik Vanem. Sequential sampling method using Gaussian process regression for estimating extreme structural response. *Marine Structures*, 72:102780, July 2020. doi: 10.1016/j.marstruc.2020.102780.

[192] Ehsan Momeni, Mohammad Bagher Dowlatshahi, Fereydoon Omidinasab, Harnedi Maizir, and Danial Jahed Armaghani. Gaussian Process Regression Technique to Estimate the Pile Bearing Capacity. *Arabian Journal for Science and Engineering*, 45(10):8255–8267, October 2020. doi: 10.1007/s13369-020-04683-4.

[193] Clement Kweku Arthur, Victor Amoako Temeng, and Yao Yevenyo Ziggah. Novel approach to predicting blast-induced ground vibration using Gaussian process regression. *Engineering with Computers*, 36(1):29–42, January 2020. doi: 10.1007/s00366-018-0686-3.

[194] John Jackson, Luca Laurenti, Eric Frew, and Morteza Lahijanian. Synergistic Offline-Online

Control Synthesis via Local Gaussian Process Regression. In *2021 60th IEEE Conference on Decision and Control (CDC)*, pages 2232–2239, December 2021. doi: 10.1109/CDC45484.2021.9683557.

[195] Fabian Pedregosa, Gael Varoquaux, Alexandre Gramfort, Vincent Michel, Bertrand Thirion, Olivier Grisel, Mathieu Blondel, Peter Prettenhofer, Ron Weiss, Vincent Dubourg, Jake Vanderplas, Alexandre Passos, and David Cournapeau. Scikit-learn: Machine Learning in Python. *Journal of Machine Learning Research*, page 6, 2011.

[196] Charles A. Micchelli, Yuesheng Xu, and Haizhang Zhang. Universal Kernels. *Journal of Machine Learning Research*, 7(95):2651–2667, 2006.

[197] Anders Logg, Kent-Andre Mardal, and Garth Wells, editors. *Automated Solution of Differential Equations by the Finite Element Method*, volume 84 of *Lecture Notes in Computational Science and Engineering*. Springer Berlin Heidelberg, 2012. doi: 10.1007/978-3-642-23099-8.

[198] Martin Alnæs, Jan Blechta, Johan Hake, August Johansson, Benjamin Kehlet, Anders Logg, Chris Richardson, Johannes Ring, Marie E. Rognes, and Garth N. Wells. The FEniCS Project Version 1.5. *Archive of Numerical Software*, 3(100), December 2015. doi: 10.11588/ans.2015.100.20553.

[199] M. R. Hill and M. D. Olson. Repeatability of the Contour Method for Residual Stress Measurement. *Experimental Mechanics*, 54(7):1269–1277, September 2014. doi: 10.1007/s11340-014-9867-1.

[200] Jikai Liu, Andrew T. Gaynor, Shikui Chen, Zhan Kang, Krishnan Suresh, Akihiro Takezawa, Lei Li, Junji Kato, Jinyuan Tang, Charlie C. L. Wang, Lin Cheng, Xuan Liang, and Albert. C. To. Current and future trends in topology optimization for additive manufacturing. *Structural and Multidisciplinary Optimization*, 57(6):2457–2483, June 2018. doi: 10.1007/s00158-018-1994-3.

[201] J. P. Oliveira, T. G. Santos, and R. M. Miranda. Revisiting fundamental welding concepts to improve additive manufacturing: From theory to practice. *Progress in Materials Science*, 107:100590, January 2020. doi: 10.1016/j.pmatsci.2019.100590.

[202] X. Cui, S. Zhang, C. Wang, C. H. Zhang, J. Chen, and J. B. Zhang. Effects of stress-relief heat treatment on the microstructure and fatigue property of a laser additive manufactured 12CrNi2 low alloy steel. *Materials Science and Engineering: A*, 791:139738, July 2020. doi: 10.1016/j.msea.2020.139738.

[203] E. Salvati, A. J. G. Lunt, S. Ying, T. Sui, H. J. Zhang, C. Heason, G. Baxter, and A. M. Korsunsky. Eigenstrain reconstruction of residual strains in an additively manufactured and shot peened nickel superalloy compressor blade. *Computer Methods in Applied Mechanics and Engineering*, 320:335–351, June 2017. doi: 10.1016/j.cma.2017.03.005.

[204] Erfan Maleki, Sara Bagherifard, Michele Bandini, and Mario Guagliano. Surface post-treatments for metal additive manufacturing: Progress, challenges, and opportunities. *Additive Manufacturing*, 37:101619, January 2021. doi: 10.1016/j.addma.2020.101619.

[205] Yunhui Chen, Samuel J. Clark, Chu Lun Alex Leung, Lorna Sinclair, Sebastian Marussi,

Margie P. Olbinado, Elodie Boller, Alexander Rack, Iain Todd, and Peter D. Lee. In-situ Synchrotron imaging of keyhole mode multi-layer laser powder bed fusion additive manufacturing. *Applied Materials Today*, 20:100650, September 2020. doi: 10.1016/j.apmt.2020.100650.

[206] Chu Lun Alex Leung, Sebastian Marussi, Robert C. Atwood, Michael Towrie, Philip J. Withers, and Peter D. Lee. In situ X-ray imaging of defect and molten pool dynamics in laser additive manufacturing. *Nature Communications*, 9(1):1355, April 2018. doi: 10.1038/s41467-018-03734-7.

[207] Majid Laleh, Anthony E. Hughes, Sam Yang, Jiangting Wang, Jianli Li, A. Matt Glenn, Wei Xu, and Mike Y. Tan. A critical insight into lack-of-fusion pore structures in additively manufactured stainless steel. *Additive Manufacturing*, 38:101762, February 2021. doi: 10.1016/j.addma.2020.101762.

[208] Hiroshige Masuo, Yuzo Tanaka, Shotaro Morokoshi, Hajime Yagura, Tetsuya Uchida, Yasuhiro Yamamoto, and Yukitaka Murakami. Influence of defects, surface roughness and HIP on the fatigue strength of Ti-6Al-4V manufactured by additive manufacturing. *International Journal of Fatigue*, 117:163–179, December 2018. doi: 10.1016/j.ijfatigue.2018.07.020.

[209] S. Beretta and S. Romano. A comparison of fatigue strength sensitivity to defects for materials manufactured by AM or traditional processes. *International Journal of Fatigue*, 94:178–191, January 2017. doi: 10.1016/j.ijfatigue.2016.06.020.

[210] Y.N. Hu, S.C. Wu, P.J. Withers, J. Zhang, H.Y.X. Bao, Y.N. Fu, and G.Z. Kang. The effect of manufacturing defects on the fatigue life of selective laser melted Ti-6Al-4V structures. *Materials & Design*, 192:108708, July 2020. doi: 10.1016/j.matdes.2020.108708.

[211] G. Meneghetti, D. Rigon, and C. Gennari. An analysis of defects influence on axial fatigue strength of maraging steel specimens produced by additive manufacturing. *International Journal of Fatigue*, 118:54–64, January 2019. doi: 10.1016/j.ijfatigue.2018.08.034.

[212] S. Romano, L. Patriarca, S. Foletti, and S. Beretta. LCF behaviour and a comprehensive life prediction model for AlSi10Mg obtained by SLM. *International Journal of Fatigue*, 117:47–62, December 2018. doi: 10.1016/j.ijfatigue.2018.07.030.

[213] S. Tammas-Williams, P. J. Withers, I. Todd, and P. B. Prangnell. The Influence of Porosity on Fatigue Crack Initiation in Additively Manufactured Titanium Components. *Scientific Reports*, 7(1):7308, August 2017. doi: 10.1038/s41598-017-06504-5.

[214] S. Beretta. More than 25 years of extreme value statistics for defects: Fundamentals, historical developments, recent applications. *International Journal of Fatigue*, 151:106407, October 2021. doi: 10.1016/j.ijfatigue.2021.106407.

[215] S. Romano, S. Miccoli, and S. Beretta. A new FE post-processor for probabilistic fatigue assessment in the presence of defects and its application to AM parts. *International Journal of Fatigue*, 125:324–341, August 2019. doi: 10.1016/j.ijfatigue.2019.04.008.

[216] Anton du Plessis, Ina Yadroitsava, and Igor Yadroitsev. Effects of defects on mechanical properties in metal additive manufacturing: A review focusing on X-ray tomography insights. *Materials & Design*, 187:108385, February 2020. doi: 10.1016/j.matdes.2019.108385.

[217] Rui Liu, Sen Liu, and Xiaoli Zhang. A physics-informed machine learning model for porosity analysis in laser powder bed fusion additive manufacturing. *The International Journal of Advanced Manufacturing Technology*, 113(7-8):1943–1958, April 2021. doi: 10.1007/s00170-021-06640-3.

[218] Jie Chen and Yongming Liu. Probabilistic physics-guided machine learning for fatigue data analysis. *Expert Systems with Applications*, 168:114316, April 2021. doi: 10.1016/j.eswa.2020.114316.

[219] Chun-Teh Chen and Grace X. Gu. Learning hidden elasticity with deep neural networks. *Proceedings of the National Academy of Sciences*, 118(31):e2102721118, August 2021. doi: 10.1073/pnas.2102721118.

[220] Hiroshige Masuo, Yuzo Tanaka, Shotaro Morokoshi, Hajime Yagura, Tetsuya Uchida, Yasuhiro Yamamoto, and Yukitaka Murakami. Effects of Defects, Surface Roughness and HIP on Fatigue Strength of Ti-6Al-4V manufactured by Additive Manufacturing. *Procedia Structural Integrity*, 7:19–26, January 2017. doi: 10.1016/j.prostr.2017.11.055.

[221] Yoichi Yamashita and Yukitaka Murakami. Small crack growth model from low to very high cycle fatigue regime for internal fatigue failure of high strength steel. *International Journal of Fatigue*, 93:406–414, December 2016. doi: 10.1016/j.ijfatigue.2016.04.016.

[222] S. Suresh and R. O. Ritchie. Propagation of short fatigue cracks. *International Metals Reviews*, 29(1):445–475, January 1984. doi: 10.1179/imtr.1984.29.1.445.

[223] M Chapetti. Fatigue propagation threshold of short cracks under constant amplitude loading. *International Journal of Fatigue*, 25(12):1319–1326, December 2003. doi: 10.1016/S0142-1123(03)00065-3.

[224] B. Künkler, O. Düber, P. Köster, U. Krupp, C.-P. Fritzen, and H.-J. Christ. Modelling of short crack propagation – Transition from stage I to stage II. *Engineering Fracture Mechanics*, 75(3-4):715–725, February 2008. doi: 10.1016/j.engfracmech.2007.02.018.

[225] Yukitaka Murakami and Masahiro Endo. Effects of hardness and crack geometries on delta k sub th of small cracks emanating from small defects. *Mechanical Engineering Publications, The Behaviour of Short Fatigue Cracks,*, pages 275–293, 1986.

[226] Steven De Gryze, Ivan Langhans, and Martina Vandebroek. Using the correct intervals for prediction: A tutorial on tolerance intervals for ordinary least-squares regression. *Chemometrics and Intelligent Laboratory Systems*, 87(2):147–154, June 2007. doi: 10.1016/j.chemolab.2007.03.002.

[227] Adam Paszke, Sam Gross, Francisco Massa, Adam Lerer, James Bradbury, Gregory Chanan, Trevor Killeen, Zeming Lin, Natalia Gimelshein, Luca Antiga, Alban Desmaison, Andreas Köpf, Edward Yang, Zach DeVito, Martin Raison, Alykhan Tejani, Sasank Chilamkurthy, Benoit Steiner, Lu Fang, Junjie Bai, and Soumith Chintala. PyTorch: An Imperative Style, High-Performance Deep Learning Library. *arXiv:1912.01703 [cs, stat]*, December 2019.

[228] Yanzhao Wu, Ling Liu, Juhyun Bae, Ka-Ho Chow, Arun Iyengar, Calton Pu, Wenqi Wei, Lei Yu, and Qi Zhang. Demystifying Learning Rate Policies for High Accuracy Training of

Deep Neural Networks, October 2019.

[229] Leslie N. Smith. A disciplined approach to neural network hyper-parameters: Part 1 – learning rate, batch size, momentum, and weight decay, April 2018.

[230] Twan van Laarhoven. L2 Regularization versus Batch and Weight Normalization, June 2017.

[231] M Ciavarella and F Monno. On the possible generalizations of the Kitagawa–Takahashi diagram and of the El Haddad equation to finite life. *International Journal of Fatigue*, 28 (12):1826–1837, December 2006. doi: 10.1016/j.ijfatigue.2005.12.001.

[232] R. Aigner, S. Pusterhofer, S. Pomberger, M. Leitner, and M. Stoschka. A probabilistic Kitagawa-Takahashi diagram for fatigue strength assessment of cast aluminium alloys. *Materials Science and Engineering: A*, 745:326–334, February 2019. doi: 10.1016/j.msea.2018.12.108.

[233] B. Köhler, H. Bomas, W. Leis, and L. Kallien. Endurance limit of die-cast magnesium alloys AM50hp and AZ91hp depending on type and size of internal cavities. *International Journal of Fatigue*, 44:51–60, November 2012. doi: 10.1016/j.ijfatigue.2012.05.011.

[234] Uwe Zerbst, Giovanni Bruno, Jean-Yves Buffière, Thomas Wegener, Thomas Niendorf, Tao Wu, Xiang Zhang, Nikolai Kashaev, Giovanni Meneghetti, Nik Hrabe, Mauro Madia, Tiago Werner, Kai Hilgenberg, Martina Koukolíková, Radek Procházka, Jan Džugan, Benjamin Möller, Stefano Beretta, Alexander Evans, Rainer Wagener, and Kai Schnabel. Damage tolerant design of additively manufactured metallic components subjected to cyclic loading: State of the art and challenges. *Progress in Materials Science*, 121:100786, August 2021. doi: 10.1016/j.pmatsci.2021.100786.

[235] Y. Murakami and M. Endo. Effects of defects, inclusions and inhomogeneities on fatigue strength. *International Journal of Fatigue*, 16(3):163–182, April 1994. doi: 10.1016/0142-1123(94)90001-9.

[236] I. M Sobol'. On the distribution of points in a cube and the approximate evaluation of integrals. *USSR Computational Mathematics and Mathematical Physics*, 7(4):86–112, January 1967. doi: 10.1016/0041-5553(67)90144-9.

[237] Jon Herman and Will Usher. SALib: An open-source Python library for Sensitivity Analysis. *The Journal of Open Source Software*, 2(9), January 2017. doi: 10.21105/joss.00097.

[238] Takuya Iwanaga, William Usher, and Jonathan Herman. Toward SALib 2.0: Advancing the accessibility and interpretability of global sensitivity analyses. *Socio-Environmental Systems Modelling*, 4:18155, May 2022. doi: 10.18174/sesmo.18155.

[239] William Q. Meeker, Gerald J. Hahn, and Luis A. Escobar. *Statistical Intervals: A Guide for Practitioners and Researchers*. Wiley Series in Probability and Statistics. John Wiley & Sons, Inc., March 2017. doi: 10.1002/9781118594841.

[240] D. Rigon and G. Meneghetti. Engineering estimation of the fatigue limit of wrought and defective additively manufactured metals for different load ratios. *International Journal of Fatigue*, 154:106530, January 2022. doi: 10.1016/j.ijfatigue.2021.106530.

[241] B. J. Wang, S. D. Wang, D. K. Xu, and E. H. Han. Recent progress in fatigue behavior of Mg alloys in air and aqueous media: A review. *Journal of Materials Science & Technology*, 33(10):1075–1086, October 2017. doi: 10.1016/j.jmst.2017.07.017.

[242] M. Kuroda and T. J. Marrow. Modelling the effects of surface finish on fatigue limit in austenitic stainless steels. *Fatigue & Fracture of Engineering Materials & Structures*, 31(7): 581–598, July 2008. doi: 10.1111/j.1460-2695.2008.01223.x.

[243] Pierre Merot, Franck Morel, Etienne Pessard, Linamaria Gallegos Mayorga, Paul Buttin, and Thierry Baffie. Fatigue strength and life assessment of L-PBF 316L stainless steel showing process and corrosion related defects. *Engineering Fracture Mechanics*, page 108883, October 2022. doi: 10.1016/j.engfracmech.2022.108883.

[244] Olivier Andreau, Etienne Pessard, Imade Koutiri, Jean-Daniel Penot, Corinne Dupuy, Nicolas Saintier, and Patrice Peyre. A competition between the contour and hatching zones on the high cycle fatigue behaviour of a 316L stainless steel: Analyzed using X-ray computed tomography. *Materials Science and Engineering: A*, 757:146–159, May 2019. doi: 10.1016/j.msea.2019.04.101.

[245] Olivier Andreau, Etienne Pessard, Imade Koutiri, Patrice Peyre, and Nicolas Saintier. Influence of the position and size of various deterministic defects on the high cycle fatigue resistance of a 316L steel manufactured by laser powder bed fusion. *International Journal of Fatigue*, 143:105930, February 2021. doi: 10.1016/j.ijfatigue.2020.105930.

[246] Jyoti Suryawanshi, K.G. Prashanth, and U. Ramamurty. Mechanical behavior of selective laser melted 316L stainless steel. *Materials Science and Engineering: A*, 696:113–121, June 2017. doi: 10.1016/j.msea.2017.04.058.

[247] Xiaoyu Liang, Anis Hor, Camille Robert, Feng Lin, and Franck Morel. Effects of building direction and loading mode on the high cycle fatigue strength of the laser powder bed fusion 316L. *International Journal of Fatigue*, 170:107506, May 2023. doi: 10.1016/j.ijfatigue.2023.107506.

[248] Bernd M. Schönbauer and Herwig Mayer. Effect of small defects on the fatigue strength of martensitic stainless steels. *International Journal of Fatigue*, 127:362–375, October 2019. doi: 10.1016/j.ijfatigue.2019.06.021.

[249] Bernd M. Schönbauer and Stefanie E. Stanzl-Tschegg. Influence of environment on the fatigue crack growth behaviour of 12% Cr steel. *Ultrasonics*, 53(8):1399–1405, December 2013. doi: 10.1016/j.ultras.2013.02.007.

[250] Daniele Rigon and Giovanni Meneghetti. An engineering estimation of fatigue thresholds from a microstructural size and Vickers hardness: application to wrought and additively manufactured metals. *International Journal of Fatigue*, 139:105796, October 2020. doi: 10.1016/j.ijfatigue.2020.105796.

[251] Bernd M. Schönbauer, Keiji Yanase, and Masahiro Endo. The influence of various types of small defects on the fatigue limit of precipitation-hardened 17-4PH stainless steel. *Theoretical and Applied Fracture Mechanics*, 87:35–49, February 2017. doi: 10.1016/j.tafmec.2016.10.

003.

[252] Bernd M. Schönbauer, Stefanie E. Stanzl-Tschegg, Andrea Perlega, Ronald N. Salzman, Neville F. Rieger, Alan Turnbull, Shengqi Zhou, Mikolaj Lukaszewicz, and David Gandy. The influence of corrosion pits on the fatigue life of 17-4PH steam turbine blade steel. *Engineering Fracture Mechanics*, 147:158–175, October 2015. doi: 10.1016/j.engfracmech.2015.08.011.

[253] Simone Romano, P. D. Nezhadfar, Nima Shamsaei, Mohsen Seifi, and Stefano Beretta. High cycle fatigue behavior and life prediction for additively manufactured 17-4 PH stainless steel: Effect of sub-surface porosity and surface roughness. *Theoretical and Applied Fracture Mechanics*, 106:102477, April 2020. doi: 10.1016/j.tafmec.2020.102477.

[254] J. Maierhofer, H. P. Gänser, and R. Pippan. Modified Kitagawa–Takahashi diagram accounting for finite notch depths. *International Journal of Fatigue*, 70:503–509, January 2015. doi: 10.1016/j.ijfatigue.2014.07.007.

[255] S. C. Wu, Y. Luo, Z. Shen, L. C. Zhou, W. H. Zhang, and G. Z. Kang. Collaborative crack initiation mechanism of 25CrMo4 alloy steels subjected to foreign object damages. *Engineering Fracture Mechanics*, 225:106844, February 2020. doi: 10.1016/j.engfracmech.2019.106844.

[256] Yoshikazu Nakai and Keisuke Tanaka. Grain Size Effect on Growth Threshold for Small Surface-Cracks and Long Through-Cracks Under Cyclic Loading. *Proceedings of The Japan Congress on Materials Research*, pages 106–112, 1980.

[257] S. Usami and S. Shida. Elastic–Plastic Analysis of the Fatigue Limit for a Material with Small Flaws. *Fatigue & Fracture of Engineering Materials & Structures*, 1(4):471–481, 1979. doi: 10.1111/j.1460-2695.1979.tb01334.x.

[258] Yves Nadot. Fatigue from Defect: Influence of Size, Type, Position, Morphology and Loading. *International Journal of Fatigue*, 154:106531, January 2022. doi: 10.1016/j.ijfatigue.2021.106531.

[259] A. Nasr, Ch. Bouraoui, R. Fathallah, and Y. Nadot. Probabilistic high cycle fatigue behaviour of nodular cast iron containing casting defects. *Fatigue & Fracture of Engineering Materials & Structures*, 32(4):292–309, 2009. doi: 10.1111/j.1460-2695.2009.01330.x.

[260] S. Beretta, L. Patriarca, M. Gargourimotlagh, A. Hardaker, D. Brackett, M. Salimian, J. Gumpinger, and T. Ghidini. A benchmark activity on the fatigue life assessment of AlSi10Mg components manufactured by L-PBF. *Materials & Design*, 218:110713, June 2022. doi: 10.1016/j.matdes.2022.110713.

[261] S. Beretta, M. Gargourimotlagh, S. Foletti, A. du Plessis, and M. Riccio. Fatigue strength assessment of "as built" AlSi10Mg manufactured by SLM with different build orientations. *International Journal of Fatigue*, 139:105737, October 2020. doi: 10.1016/j.ijfatigue.2020.105737.

[262] Timothy D. Piette, Robert J. Warren, Anthony G. Spangenberger, Edward J. Hummelt, and Diana A. Lados. Microstructure evolution, fatigue crack growth, and ultrasonic fatigue in As-fabricated laser powder bed and conventionally cast Al–10Si-0.4Mg: A mechanistic

understanding and integrated flaw-sensitive fatigue design methods. *Materials Science and Engineering: A*, 825:141892, September 2021. doi: 10.1016/j.msea.2021.141892.

[263] M. Bonneric, C. Brugger, N. Saintier, A. Castro Moreno, and B. Tranchand. Contribution of the introduction of artificial defects by additive manufacturing to the determination of the Kitagawa diagram of Al-Si alloys. *Procedia Structural Integrity*, 38:141–148, 2022. doi: 10.1016/j.prostr.2022.03.015.

[264] Mohamed Iben Houria, Yves Nadot, Raouf Fathallah, Matthew Roy, and Daan M. Maijer. Influence of casting defect and SDAS on the multiaxial fatigue behaviour of A356-T6 alloy including mean stress effect. *International Journal of Fatigue*, 80:90–102, November 2015. doi: 10.1016/j.ijfatigue.2015.05.012.

[265] Antonio Rotella, Yves Nadot, Mickaël Piellard, Rémi Augustin, and Michel Fleuriot. Fatigue limit of a cast Al-Si-Mg alloy (A357-T6) with natural casting shrinkages using ASTM standard X-ray inspection. *International Journal of Fatigue*, 114:177–188, September 2018. doi: 10.1016/j.ijfatigue.2018.05.026.

[266] C. Garb, M. Leitner, and F. Grün. Effect of elevated temperature on the fatigue strength of casted AlSi8Cu3 aluminium alloys. *Procedia Structural Integrity*, 7:497–504, 2017. doi: 10.1016/j.prostr.2017.11.118.

[267] Christian Garb, Martin Leitner, Bernhard Stauder, Dirk Schnubel, and Florian Grün. Application of modified Kitagawa-Takahashi diagram for fatigue strength assessment of cast Al-Si-Cu alloys. *International Journal of Fatigue*, 111:256–268, June 2018. doi: 10.1016/j.ijfatigue.2018.01.030.

[268] C. Garb, M. Leitner, and F. Grün. Application of $\sqrt{area}$-concept to assess fatigue strength of AlSi7Cu0.5Mg casted components. *Engineering Fracture Mechanics*, 185:61–71, November 2017. doi: 10.1016/j.engfracmech.2017.03.018.

[269] P. Mu, Y. Nadot, C. Nadot-Martin, A. Chabod, I. Serrano-Munoz, and C. Verdu. Influence of casting defects on the fatigue behavior of cast aluminum AS7G06-T6. *International Journal of Fatigue*, 63:97–109, June 2014. doi: 10.1016/j.ijfatigue.2014.01.011.

[270] C. Santus and D. Taylor. Physically short crack propagation in metals during high cycle fatigue. *International Journal of Fatigue*, 31(8):1356–1365, August 2009. doi: 10.1016/j.ijfatigue.2009.03.002.

[271] M. da Fonte, F. Romeiro, M. de Freitas, S. E. Stanzl-Tschegg, E. K. Tschegg, and A. K. Vasudévan. The effect of microstructure and environment on fatigue crack growth in 7049 aluminium alloy at negative stress ratios. *International Journal of Fatigue*, 25(9):1209–1216, September 2003. doi: 10.1016/S0142-1123(03)00150-6.

[272] Anastasios G. Gavras, Diana A. Lados, Victor K. Champagne, and Robert J. Warren. Effects of processing on microstructure evolution and fatigue crack growth mechanisms in cold-spray 6061 aluminum alloy. *International Journal of Fatigue*, 110:49–62, May 2018. doi: 10.1016/j.ijfatigue.2018.01.006.

[273] Romali Biswal, Xiang Zhang, Abdul Khadar Syed, Mustafa Awd, Jialuo Ding, Frank

Walther, and Stewart Williams. Criticality of porosity defects on the fatigue performance of wire + arc additive manufactured titanium alloy. *International Journal of Fatigue*, 122: 208–217, May 2019. doi: 10.1016/j.ijfatigue.2019.01.017.

[274] Etienne Pessard, Manon Lavialle, Pascal Laheurte, Paul Didier, and Myriam Brochu. High-cycle fatigue behavior of a laser powder bed fusion additive manufactured Ti-6Al-4V titanium: Effect of pores and tested volume size. *International Journal of Fatigue*, 149:106206, August 2021. doi: 10.1016/j.ijfatigue.2021.106206.

[275] G. Léopold, Y. Nadot, T. Billaudeau, and J. Mendez. Influence of artificial and casting defects on fatigue strength of moulded components in Ti-6Al-4V alloy. *Fatigue & Fracture of Engineering Materials & Structures*, 38(9):1026–1041, 2015. doi: 10.1111/ffe.12326.

[276] J. O Peters and R. O Ritchie. Influence of foreign-object damage on crack initiation and early crack growth during high-cycle fatigue of Ti–6Al–4V. *Engineering Fracture Mechanics*, 67(3):193–207, October 2000. doi: 10.1016/S0013-7944(00)00045-X.

[277] M. Benedetti and C. Santus. Building the Kitagawa-Takahashi diagram of flawed materials and components using an optimized V-notched cylindrical specimen. *Engineering Fracture Mechanics*, 224:106810, February 2020. doi: 10.1016/j.engfracmech.2019.106810.

[278] Chretien Gaëlle, Sarrazin-Baudoux Christine, Leost Laurie, and Hervier Zeline. Near-threshold fatigue propagation of physically short and long cracks in Titanium alloy. *Procedia Structural Integrity*, 2:950–957, 2016. doi: 10.1016/j.prostr.2016.06.122.

[279] Y. N. Hu, S. C. Wu, Z. K. Wu, X. L. Zhong, S. Ahmed, S. Karabal, X. H. Xiao, H. O. Zhang, and P. J. Withers. A new approach to correlate the defect population with the fatigue life of selective laser melted Ti-6Al-4V alloy. *International Journal of Fatigue*, 136:105584, July 2020. doi: 10.1016/j.ijfatigue.2020.105584.

[280] Theo Persenot, Alexis Burr, Guilhem Martin, Jean-Yves Buffiere, Remy Dendievel, and Eric Maire. Effect of build orientation on the fatigue properties of as-built Electron Beam Melted Ti-6Al-4V alloy. *International Journal of Fatigue*, 118:65–76, January 2019. doi: 10.1016/j.ijfatigue.2018.08.006.

[281] Punit Kumar and Upadrasta Ramamurty. High cycle fatigue in selective laser melted Ti-6Al-4V. *Acta Materialia*, 194:305–320, August 2020. doi: 10.1016/j.actamat.2020.05.041.

[282] L. Barricelli, L. Patriarca, A. du Plessis, and S. Beretta. Orientation-dependent fatigue assessment of Ti6Al4V manufactured by L-PBF: Size of surface features and shielding effect. *International Journal of Fatigue*, page 107401, November 2022. doi: 10.1016/j.ijfatigue.2022.107401.

[283] M. Tarik Hasib, Halsey E. Ostergaard, Qian Liu, Xiaopeng Li, and Jamie J. Kruzic. Tensile and fatigue crack growth behavior of commercially pure titanium produced by laser powder bed fusion additive manufacturing. *Additive Manufacturing*, 45:102027, September 2021. doi: 10.1016/j.addma.2021.102027.

[284] Yuwei Zhai, Haize Galarraga, and Diana A. Lados. Microstructure, static properties, and fatigue crack growth mechanisms in Ti-6Al-4V fabricated by additive manufacturing: LENS

and EBM. *Engineering Failure Analysis*, 69:3–14, November 2016. doi: 10.1016/j.engfailanal.2016.05.036.

[285] M. Tarik Hasib, Halsey E. Ostergaard, Xiaopeng Li, and Jamie J. Kruzic. Fatigue crack growth behavior of laser powder bed fusion additive manufactured Ti-6Al-4V: Roles of post heat treatment and build orientation. *International Journal of Fatigue*, 142:105955, January 2021. doi: 10.1016/j.ijfatigue.2020.105955.

[286] Baohua Nie, Zihua Zhao, Yongzhong Ouyang, Dongchu Chen, Hong Chen, Haibo Sun, and Shu Liu. Effect of Low Cycle Fatigue Predamage on Very High Cycle Fatigue Behavior of TC21 Titanium Alloy. *Materials*, 10(12):1384, December 2017. doi: 10.3390/ma10121384.

[287] J. R. Poulin, A. Kreitcberg, P. Terriault, and V. Brailovski. Fatigue strength prediction of laser powder bed fusion processed Inconel 625 specimens with intentionally-seeded porosity: Feasibility study. *International Journal of Fatigue*, 132:105394, March 2020. doi: 10.1016/j.ijfatigue.2019.105394.

[288] J. R. Poulin, V. Brailovski, and P. Terriault. Long fatigue crack propagation behavior of Inconel 625 processed by laser powder bed fusion: Influence of build orientation and post-processing conditions. *International Journal of Fatigue*, 116:634–647, November 2018. doi: 10.1016/j.ijfatigue.2018.07.008.

[289] Xiaoan Hu, Zhiyuan Xue, TingTing Ren, Yun Jiang, ChengLi Dong, and Fencheng Liu. On the fatigue crack growth behaviour of selective laser melting fabricated Inconel 625: Effects of build orientation and stress ratio. *Fatigue & Fracture of Engineering Materials & Structures*, 43(4):771–787, 2020. doi: 10.1111/ffe.13181.

[290] Yoichi Yamashita, Takao Murakami, Rei Mihara, Masami Okada, and Yukitaka Murakami. Defect analysis and fatigue design basis for Ni-based superalloy 718 manufactured by selective laser melting. *International Journal of Fatigue*, 117:485–495, December 2018. doi: 10.1016/j.ijfatigue.2018.08.002.

[291] W. B. Li, J. C. Pang, H. Zhang, S. X. Li, and Z. F. Zhang. The high-cycle fatigue properties of selective laser melted Inconel 718 at room and elevated temperatures. *Materials Science and Engineering: A*, 836:142716, March 2022. doi: 10.1016/j.msea.2022.142716.

[292] Jayaraj Radhakrishnan, Punit Kumar, Shihao Li, Yakai Zhao, and Upadrasta Ramamurty. Unnotched fatigue of Inconel 718 produced by laser beam-powder bed fusion at 25 and 600°C. *Acta Materialia*, 225:117565, February 2022. doi: 10.1016/j.actamat.2021.117565.

[293] Kun Yang, Qi Huang, Qingyuan Wang, and Qiang Chen. Competing crack initiation behaviors of a laser additively manufactured nickel-based superalloy in high and very high cycle fatigue regimes. *International Journal of Fatigue*, 136:105580, July 2020. doi: 10.1016/j.ijfatigue.2020.105580.

[294] Nicola Cersullo, Jon Mardaras, Philippe Emile, Katja Nickel, Vitus Holzinger, and Christian Hühne. Effect of Internal Defects on the Fatigue Behavior of Additive Manufactured Metal Components: A Comparison between Ti6Al4V and Inconel 718. *Materials*, 15(19):6882, January 2022. doi: 10.3390/ma15196882.

References

[295] R. Konecná, L. Kunz, G. Nicoletto, and A. Baca. Fatigue crack growth behavior of Inconel 718 produced by selective laser melting. *Frattura ed Integrità Strutturale*, 10(35):31–40, December 2015. doi: 10.3221/IGF-ESIS.35.04.

[296] R. Konečná, L. Kunz, G. Nicoletto, and A. Bača. Long fatigue crack growth in Inconel 718 produced by selective laser melting. *International Journal of Fatigue*, 92:499–506, November 2016. doi: 10.1016/j.ijfatigue.2016.03.012.

[297] Xiaolong Li, Wei Li, Muhammad Imran Lashari, Tatsuo Sakai, Ping Wang, Liang Cai, Xiaoming Ding, and Usama Hamid. Fatigue failure behavior and strength prediction of nickel-based superalloy for turbine blade at elevated temperature. *Engineering Failure Analysis*, 136:106191, June 2022. doi: 10.1016/j.engfailanal.2022.106191.

[298] M. Papakyriacou, H. Mayer, U. Fuchs, S. E. Stanzl-Tschegg, and R. P. Wei. Influence of atmospheric moisture on slow fatigue crack growth at ultrasonic frequency in aluminium and magnesium alloys. *Fatigue & Fracture of Engineering Materials & Structures*, 25(8-9): 795–804, 2002. doi: 10.1046/j.1460-2695.2002.00571.x.

[299] Md.Shahnewaz Bhuiyan and Mutoh Yoshiharu. Two stage S-N curve in corrosion fatigue of extruded magnesium alloy AZ31. *Songklanakarin Journal of Science and Technology*, 31, September 2009.

[300] Sotomi Ishihara, Zhenyu Nan, and Takahito Goshima. Effect of microstructure on fatigue behavior of AZ31 magnesium alloy. *Materials Science and Engineering: A*, 468-470:214–222, November 2007. doi: 10.1016/j.msea.2006.09.124.

[301] Sanlong Zheng, Qin Yu, and Yanyao Jiang. An experimental study of fatigue crack propagation in extruded AZ31B magnesium alloy. *International Journal of Fatigue*, 47:174–183, February 2013. doi: 10.1016/j.ijfatigue.2012.08.010.

[302] Duke Culbertson and Yanyao Jiang. An experimental study of the orientation effect on fatigue crack propagation in rolled AZ31B magnesium alloy. *Materials Science and Engineering: A*, 676:10–19, October 2016. doi: 10.1016/j.msea.2016.08.088.

[303] P Venkateswaran, S Ganesh Sundara Raman, S. D Pathak, Y Miyashita, and Y Mutoh. Fatigue crack growth behaviour of a die-cast magnesium alloy AZ91D. *Materials Letters*, 58 (20):2525–2529, August 2004. doi: 10.1016/j.matlet.2004.03.014.

[304] S. Ishihara, S. Kitagawa, M. R. Qi, H. Shibata, and T. Goshima. Evaluation of distribution of fatigue lives of the extruded magnesium alloy AZ61. *Acta Mechanica*, 224(6):1251–1260, June 2013. doi: 10.1007/s00707-013-0872-8.

[305] M Bhuiyan, Y Mutoh, T Murai, and S Iwakami. Corrosion fatigue behavior of extruded magnesium alloy AZ61 under three different corrosive environments. *International Journal of Fatigue*, 30(10-11):1756–1765, October 2008. doi: 10.1016/j.ijfatigue.2008.02.012.

[306] U. Karr, B.M. Schönbauer, and H. Mayer. Near-threshold fatigue crack growth properties of wrought magnesium alloy AZ61 in ambient air, dry air, and vacuum. *Fatigue & Fracture of Engineering Materials & Structures*, 41(9):1938–1947, September 2018. doi: 10.1111/ffe.12832.

[307] Sabrina Alam Khan, Yukio Miyashita, Yoshiharu Mutoh, and Toshikatsu Koike. Effect of anodized layer thickness on fatigue behavior of magnesium alloy. *Materials Science and Engineering: A*, 474(1):261–269, February 2008. doi: 10.1016/j.msea.2007.04.078.

[308] Davide Leonetti, Johan Maljaars, and H. H. (Bert) Snijder. Fitting fatigue test data with a novel S-N curve using frequentist and Bayesian inference. *International Journal of Fatigue*, 105:128–143, December 2017. doi: 10.1016/j.ijfatigue.2017.08.024.

[309] Daniel Sandberg, Rami Mansour, and Mårten Olsson. Fatigue probability assessment including aleatory and epistemic uncertainty with application to gas turbine compressor blades. *International Journal of Fatigue*, 95:132–142, February 2017. doi: 10.1016/j.ijfatigue.2016.10.001.

[310] L. Patriarca, S. Beretta, S. Foletti, A. Riva, and S. Parodi. A probabilistic framework to define the design stress and acceptable defects under combined-cycle fatigue conditions. *Engineering Fracture Mechanics*, 224:106784, February 2020. doi: 10.1016/j.engfracmech.2019.106784.

[311] Jie Chen and Yongming Liu. Fatigue property prediction of additively manufactured Ti-6Al-4V using probabilistic physics-guided learning. *Additive Manufacturing*, 39:101876, March 2021. doi: 10.1016/j.addma.2021.101876.

[312] Taotao Zhou, Shan Jiang, Te Han, Shun-Peng Zhu, and Yinan Cai. A Physically Consistent Framework for Fatigue Life Prediction using Probabilistic Physics-Informed Neural Network. *International Journal of Fatigue*, page 107234, September 2022. doi: 10.1016/j.ijfatigue.2022.107234.

[313] Daniel McNeish. On Using Bayesian Methods to Address Small Sample Problems. *Structural Equation Modeling: A Multidisciplinary Journal*, 23(5):750–773, September 2016. doi: 10.1080/10705511.2016.1186549.

[314] S Ghiasi, A Patane, A Greco, L Laurenti, Ep Scilingo, and M Kwiatkowska. Gaussian Processes with Physiologically-Inspired Priors for Physical Arousal Recognition. In *2020 42nd Annual International Conference of the IEEE Engineering in Medicine & Biology Society (EMBC)*, pages 54–57. IEEE, July 2020. doi: 10.1109/EMBC44109.2020.9176437.

[315] Shadi Ghiasi, Andrea Patane, Luca Laurenti, Claudio Gentili, Enzo Pasquale Scilingo, Alberto Greco, and Marta Kwiatkowska. Physiologically-Informed Gaussian Processes for Interpretable Modelling of Psycho-Physiological States. *IEEE Journal of Biomedical and Health Informatics*, pages 1–10, 2022. doi: 10.1109/JBHI.2022.3224775.

[316] G. Edwards and L.A. Pacheco. A Bayesian method for establishing fatigue design curves. *Structural Safety*, 2(1):27–38, January 1984. doi: 10.1016/0167-4730(84)90005-5.

[317] Ivo Babuška, Zaid Sawlan, Marco Scavino, Barna Szabó, and Raúl Tempone. Bayesian inference and model comparison for metallic fatigue data. *Computer Methods in Applied Mechanics and Engineering*, 304:171–196, June 2016. doi: 10.1016/j.cma.2016.02.013.

[318] Hidetoshi Fujii, D. J. C. Mackay, and H. K. D. H. Bhadeshia. Bayesian Neural Network Analysis of Fatigue Crack Growth Rate in Nickel Base Superalloys. *ISIJ International*, 36

(11):1373–1382, 1996. doi: 10.2355/isijinternational.36.1373.

[319] R.J. Grylls. Mechanical properties of a high-strength cupronickel alloy-Bayesian neural network analysis. *Materials Science and Engineering: A*, 234-236:267–270, August 1997. doi: 10.1016/S0921-5093(97)00174-3.

[320] Andrea Rovinelli, Michael D. Sangid, Henry Proudhon, Yoann Guilhem, Ricardo A. Lebensohn, and Wolfgang Ludwig. Predicting the 3D fatigue crack growth rate of small cracks using multimodal data via Bayesian networks: In-situ experiments and crystal plasticity simulations. *Journal of the Mechanics and Physics of Solids*, 115:208–229, June 2018. doi: 10.1016/j.jmps.2018.03.007.

[321] Maxwell Pinz, George Weber, Jean Charles Stinville, Tresa Pollock, and Somnath Ghosh. Data-driven Bayesian model-based prediction of fatigue crack nucleation in Ni-based superalloys. *npj Computational Materials*, 8(1):1–15, March 2022. doi: 10.1038/s41524-022-00727-5.

[322] Kevin Linka, Amelie Schäfer, Xuhui Meng, Zongren Zou, George Em Karniadakis, and Ellen Kuhl. Bayesian Physics Informed Neural Networks for real-world nonlinear dynamical systems. *Computer Methods in Applied Mechanics and Engineering*, 402:115346, December 2022. doi: 10.1016/j.cma.2022.115346.

[323] Luning Sun and Jian-Xun Wang. Physics-constrained bayesian neural network for fluid flow reconstruction with sparse and noisy data. *Theoretical and Applied Mechanics Letters*, 10 (3):161–169, March 2020. doi: 10.1016/j.taml.2020.01.031.

[324] Luka Malashkhia, Dehao Liu, Yanglong Lu, and Yan Wang. Physics-Constrained Bayesian Neural Network for Bias and Variance Reduction. *Journal of Computing and Information Science in Engineering*, 23(011012), November 2022. doi: 10.1115/1.4055924.

[325] Eric Thomas Nalisnick. *On Priors for Bayesian Neural Networks*. PhD thesis, UC Irvine, 2018. URL https://escholarship.org/uc/item/1jq6z904.

[326] Dongming Huang, Feicheng Wang, Donald B. Rubin, and S. C. Kou. Catalytic Priors: Using Synthetic Data to Specify Prior Distributions in Bayesian Analysis, August 2022.

[327] Florian Wenzel, Kevin Roth, Bastiaan S. Veeling, Jakub Swiatkowski, Linh Tran, Stephan Mandt, Jasper Snoek, Tim Salimans, Rodolphe Jenatton, and Sebastian Nowozin. How good is the bayes posterior in deep neural networks really? In *Proceedings of the 37th International Conference on Machine Learning*, volume 119 of *ICML'20*, pages 10248–10259. JMLR.org, July 2020.

[328] Wei Li, Martin Z. Bazant, and Juner Zhu. A physics-guided neural network framework for elastic plates: Comparison of governing equations-based and energy-based approaches. *Computer Methods in Applied Mechanics and Engineering*, 383:113933, September 2021. doi: 10.1016/j.cma.2021.113933.

[329] Dongming Huang, Nathan Stein, Donald B. Rubin, and S. C. Kou. Catalytic prior distributions with application to generalized linear models. *Proceedings of the National Academy of Sciences*, 117(22):12004–12010, June 2020. doi: 10.1073/pnas.1920913117.

[330] Eli Bingham, Jonathan P. Chen, Martin Jankowiak, Fritz Obermeyer, Neeraj Pradhan, Theofanis Karaletsos, Rohit Singh, Paul Szerlip, Paul Horsfall, and Noah D. Goodman. Pyro: Deep Universal Probabilistic Programming. *Journal of Machine Learning Research*, 20(28):1–6, 2019.

[331] M. Beghini, T. Grossi, M.B. Prime, and C. Santus. Ill-Posedness and the Bias-Variance Tradeoff in Residual Stress Measurement Inverse Solutions. *Experimental Mechanics*, 63(3): 495–516, March 2023. doi: 10.1007/s11340-022-00928-5.

[332] Claudia Barile, Simone Carone, Caterina Casavola, and Giovanni Pappalettera. Implementation of Gaussian Process Regression to strain data in residual stress measurements by hole drilling. *Measurement*, 211:112590, April 2023. doi: 10.1016/j.measurement.2023.112590.

[333] Emanuele Avoledo, Alessandro Tognan, and Enrico Salvati. Quantification of uncertainty in a defect-based Physics-Informed Neural Network for fatigue evaluation and insights on influencing factors. *Engineering Fracture Mechanics*, 292:109595, November 2023. doi: 10.1016/j.engfracmech.2023.109595.